

N° d'ordre : 4302

THÈSE

présentée à

L'UNIVERSITÉ BORDEAUX 1

ÉCOLE DOCTORALE DE MATHÉMATIQUES ET INFORMATIQUE

par **Damiano Lombardi**

POUR OBTENIR LE GRADE DE

DOCTEUR

SPÉCIALITÉ : **Mathématiques Appliquées**

Problèmes Inverses pour les modèles de croissance tumorale

Soutenue le 9 septembre 2011 à l'Institut de Mathématiques de Bordeaux

Devant la commission d'examen composée de :

M. Angelo Iollo	Université de Bordeaux 1	Directeur de thèse
M. Thierry Colin	Institut Polytechnique Bordeaux	Co-directeur de thèse
M. Jean-Frédéric Gerbeau	INRIA Rocquencourt	Rapporteur
Mme Florence Hubert	LAPT Marseille	Rapporteur
M. Nicholas Ayache	INRIA Sophia Antipolis	Président
M. Jean Palussière	Institut Bergonié	Examineur
M. Olivier Saut	CNRS, IMB Bordeaux	Examineur

École doctorale de Mathématiques
et Informatique de Bordeaux
U.F.R de Mathématiques Informatique
Bat A33, 1er étage, 352, cours de la
Libération -F 33405 TALENCE cedex

Abstract

Cette thèse porte sur la thématique de la modélisation de la croissance tumorale. L'objectif n'est pas d'étudier des nouveaux modèles mais plutôt de comprendre si on peut calibrer les modèles en telle sorte qu'ils arrivent à reproduire l'évolution de la pathologie dans un patient spécifique. La nature des modèles considérés est phénoménologique car une modélisation basée sur des principes premiers n'est pas faisable. Les modèles sont paramétriques et les paramètres, ainsi que les conditions initiales et les conditions au bords en général ne sont pas connus *a priori*. Comme ils doivent être déterminés et on ne peut pas les mesurer, on cherche à les identifier en utilisant des problèmes inverses, dont la source d'information est l'imagerie médicale.

Dans la première partie de ce travail on s'occupe de la numérique associée aux problèmes inverses. Une technique classique de sensibilité est étudiée. Afin de réduire le coût computationnel une technique réduite est décrite, basée sur la Proper Orthogonal Decomposition. Ces deux approches ont été validées par des cas test artificiels et ensuite appliquées à des cas cliniques, étudiés en collaboration avec l'Institut Bergonié (un institut d'oncologie sur Bordeaux).

Des nécessités à niveau d'imagerie médicale ont fait en sorte qu'on s'intéresse au transport optimale et ce problème fait l'objet de la deuxième partie de la thèse. En particulier on s'intéresse à la numérique du problème de Monge-Kantorovich L^2 . Une famille des méthodes lagrangiennes est définie. Des applications et une perspective concernant la réduction de modèle concluent cette partie.

Mots-clefs modélisation de la croissance tumorale, assimilation des données, problèmes inverses, sensibilité, modèles réduits, analyse des composantes principales, transport optimal, problème de Monge-Kantorovich.

Abstract

This thesis deals with tumor growth modeling and it may be divided in two parts. The objective is not to set up novel models but, instead, to understand if a general framework may be set up to calibrate existing models to a specific ongoing pathology. The models nature is phenomenological, since a first principle based modeling is not affordable. As consequence, all the models are parametrical and parameters (as well as initial and boundary conditions) are not known *a priori*. In order to simulate a specific tumor growth all these unknown elements have to be found. They can not be measured directly, instead, they are identified by means of inverse problems, the data coming from medical imagery.

In the first part of this work the numerics about inverse problems is investigated. A sensitivity technique is studied first. In order to decrease its cost a reduced order approach is devised based on Proper Orthogonal Decomposition. Both the approaches are validated through artificial numerical tests and then applied to some realistic clinical cases, studied in collaboration with Institut Bergonié, (oncology institute in Bordeaux).

When dealing with medical images several practical needs emerge concerning the pre-processing of the images. This pushed us to be interested in Optimal Transport and an independent study on this topic is presented in the second part of this work. The numerics about the L^2 Monge-Kantorovich problem is studied. A family of lagrangian methods is proposed. Several applications and a perspective on model reduction conclude the work.

Keywords tumor growth modeling, data assimilation, inverse problems, sensitivity techniques, reduced order modeling, proper orthogonal decomposition, optimal transport, Monge-Kantorovich problem

Remerciements

Je tiens en premier lieu à remercier mon directeur, Angelo Iollo, pour m'avoir proposé ce travail de thèse et des défis toujours très passionnants, qui m'ont fait aimer tous les différents aspects du calcul scientifique. Je lui exprime toute ma gratitude pour ces trois années magnifiques, pour toutes les idées et les conseils.

Je remercie mon codirecteur Thierry Colin pour m'avoir proposé de travailler sur la croissance tumorale, pour ses idées profondes en modélisation EDP et pour l'énergie qui sait communiquer.

Mes remerciements s'adressent à Olivier Saut avec lequel j'ai travaillé constamment pendant ces trois années de thèse et qui a rendu possible ce travail. Merci pour le soutien et les conseils, et pour m'avoir énormément appris en informatique!

J'exprime ma reconnaissance à Jean-Frédéric Gerbeau et Florence Hubert pour avoir accepté de corriger mon manuscrit de thèse et avoir contribué à l'améliorer. Je remercie Nicolas Ayache pour avoir accepté de présider mon jury et avoir porté beaucoup d'intérêt à mon travail. Un remerciement spécial à Jean Palussière qui a accepté de collaborer avec nous: c'est grâce à lui et au groupe de Bergonié si on a pu mettre en place une collaboration entre disciplines aussi différentes.

À l'occasion je remercie tous les participants au CEMRACS 2009 et en particulier mes encadrants Marc Thiriet et Philippe Poncet pour le travail très intéressant sur les écoulements diphasiques. Un remerciement spécial à ma collègue Séverine avec laquelle j'ai eu la chance de travailler aussi dans d'autres occasions.

Je remercie tout le groupe MC2 pour l'ambiance extraordinaire, qui m'a permis de travailler dans les meilleures conditions. Merci à Michel, Clair, Lisl, Heloise, Thomas, Vincent, Yannick, Jessica, Brigitte, Patricia, Anne-Laure.

Merci aux doctorants et ingénieurs avec lesquels j'ai partagé ces trois années, pour les conversations très enrichissantes et pour les moments de détente: Michele, Cedric, Johana, Marco, Frank, Alice, Jean Baptiste, Peng, Adrien, Frederic, Aurelie, Jade, Karen, Alberto, Denis, Xiong, Xin.

Enfin les remerciements les plus personnels. Je remercie Fabio, Sebastiano, Marco et Beatrice pour leur amitié.

Un gros merci à Elisa pour avoir enrichi ma vie et avoir été à mon côté, malgré la distance qui nous a séparés.

Merci à ma famille pour m'avoir soutenu pendant toutes ses années, sans eux rien aurait été possible.

It is not the knowledge, but the learning, not the possession, but the earning, not the being there, but the getting there, which gives us the greatest pleasure.

C.F. Gauss

Contents

1	Introduction (français)	11
1.1	Motivation	12
1.2	Contribution de ce travail	13
1.3	Résultats d'applications cliniques	19
1.4	Structure de la thèse	22
2	Introduction	27
2.1	Motivation	28
2.2	Overview of the present contribution	30
2.3	Paradigmatic results of clinical applications	35
2.4	Structure of the present work	39
3	Tumor growth modeling and applications	43
3.1	Cancer biological nature and development	44
3.1.1	Phases of tumor invasion	46
3.1.2	Classification of tumors	48
3.2	Modeling tumor growth	49
3.2.1	ODE models	50
3.2.2	Discrete models	52
3.2.3	Continuous models	54
3.2.4	Hybrid models	57
3.3	Toward realistic applications	58
3.3.1	Medical imaging techniques	60
3.3.2	Image-driven inverse problems	62
4	Models and Computational Framework adopted	67
4.1	Two species Darcy-type model	68

4.2	Regularized Darcy-type model	71
4.3	A one specie incompressible model	73
4.4	Computational Framework	74
4.5	Direct simulations	76
4.6	Dealing with medical images	78
5	Sensitivity Technique	81
5.1	Sensitivity on ODE models	82
5.1.1	A logistic-type model inspired by Darcy model	82
5.1.2	Realistic cases	85
5.2	Sensitivity on 2D regularized Darcy-type model	89
5.2.1	Layer structure tests	90
5.2.2	Extending the control by harmonics	96
5.3	Testing other models	98
6	Residual Based Approach	101
6.1	Preliminary inverse problems	102
6.1.1	Identification of porosity	102
6.1.2	Simplified logistic-type model: identifying porosity and hypoxia function	104
6.2	Regularization by Proper Orthogonal Decomposition	105
6.3	Reduced Order Technique	108
6.3.1	Time interpolation	111
6.4	Analytical testcases	112
6.4.1	Far blood vessel	114
6.4.2	In vitro-like tumor: spherical growth	120
6.5	Comparison with Sensitivity	124
6.5.1	Layer structure test	124
6.5.2	Extended control	127
6.5.3	Costs and Summary	127
6.6	Realistic tests	127
6.6.1	Fast rate growth	128
6.6.2	Slow rate growth	129
6.6.3	Two nodules	131

7	Optimal Transport	135
7.1	Optimal transport theory	136
7.2	The L^2 Monge problem	138
7.3	The Angenent-Haker-Tannenbaum (AHT) gradient flow	139
7.4	Action minimization	142
7.5	Mass transport along straight lines	143
7.5.1	Reconstruction of the initial condition	144
7.5.2	Potential velocity field and reconstruction of the final condition	145
7.6	Preliminary numerical tests	146
7.6.1	Recovering a wavy density distribution	147
7.6.2	Mass splitting: recovering a one-dimensional exact map	150
7.6.3	Two-dimensional mass splitting	151
7.6.4	Application to medical imagery	153
7.6.5	A three-dimensional application	156
7.7	A preliminary investigation on the multilevel approach	160
7.8	Application of Wasserstein distance to model reduction	162
7.8.1	Technique definition	163
7.8.2	Normalization of the embedding when a sampling of an optimal transport is considered	165
7.8.3	Baricenter of the space	167
7.8.4	Ideal vortex scattering	168
7.8.5	2D cylinder vortex shedding	173
8	Conclusions et Perspectives (français)	177
9	Conclusions and Perspectives	183

List of Figures

1.1	Schema conceptuel de problème inverse: deux images sont disponibles, aux temps $t=0$ et $t=1$; l'évolution est décrite par un modèle qui doit être calibré de façon à minimiser l'erreur de fitting.	14
1.2	Scans: a) Novembre 2005, b) Octobre 2007, c) Juillet 2008, d) Avril 2009 .	20
1.3	Surface de la tumeur un fonction du temps: la ligne continue représente la simulation, les cercles noirs les données, les carrés rouges les prédictions. .	20
1.4	a) Quatrième image b) Simulation	21
1.5	Distribution de densité au temps a) $T=0$, b) $T=1$	22
1.6	Coupes de la densité finale: a) plan XZ b) Z planes.	23
2.1	Conceptual scheme of an inverse problem: two images are available at $t = 0$ and $t = 1$, evolution is described by a model which has to be calibrated in sort that the fitting error is low.	31
2.2	Scans: a) November 2005, b) October 2007, c) July 2008, d) April 2009 . .	36
2.3	Area as function of time for the slow rate growth. Solid line represents the simulation results, black circles are the data used for the identification, red squares the predictions.	37
2.4	a) Fourth scan b) Simulation	37
2.5	Density distribution at time a) $T=0$, b) $T=1$	38
2.6	Slices of the final density distribution: a) XZ plane b) Z planes.	39
3.1	Phases of the cell cycle; from www.nature.com	45
3.2	Evolution of tumor, from left to right: avascular stage, angiogenesis, tumor invasion; from www.gene.com	47
4.1	a) MAC discretization b) Penalization on cartesian grid	75

4.2	a) Direct simulations as function of three parameters (α, C_{hyp}, ξ): sphere radius is proportional to the average tumor volume, color scale renders aggressivity (norm of the indicators). b) First indicator (f) plotted on three orthogonal slices and isocontours (30 lines between maximum and minimum).	77
5.1	Identification for BEN case performed with a) 2 b) 3 c) 4 Data. Solid line represents the simulation results, black circles are the data used for the identification, red squares are the predictions.	87
5.2	Identification for FER case performed with a) 2 b) 3 c) 4 Data	87
5.3	Identification in the BEN case performed with a) 2 b) 3 c) 4 Data and the Simeoni model	89
5.4	Scans: a) November 2005, b) October 2007, c) July 2008, d) April 2009 . .	92
5.5	Curve of the evolution of the tumor area: identification with a) 2 images b) 5 images	93
5.6	Contours of the difference between the scans and the simulation at time corresponding to a) the second image b) the last image. 40 isolines are plotted between the maximum and the minimum.	94
5.7	Contours of the difference between the scans and the simulation at time corresponding to a) the second image b) the last image. 40 isolines are used between the maximum and the minimum.	97
5.8	FER-II dataset analysis: a) Volume curve with respect to months b) Contours of the difference between scans and images for the first prediction, that is the fourth scan.	99
6.1	Eigenfunctions for the oxygen field (above) and for proliferating cells (below): a) First b) Second c) Third	107
6.2	L^2 representation with respect to the number of used modes for a) oxygen and b) proliferating cells density; the database for the Darcy model was used. 107	
6.3	Solution of the Stokes-type flow in the case of a far blood vessel, at: a) $T=0$; b) $T=20$; contour lines represent oxygen concentration in the tissue. .	115
6.4	Tumor mass Y for the Stokes flow (upper row) and for the Darcy flow (below) : a) $T=5$ b) $T=10$ c) $T=15$; Color scale ranges from 0 (blue) to 1 (red)	116
6.5	Relative error when identification time is $T=5$, with linear interpolation. a) volume error; b) centre of mass position error	117

6.6	Relative volume error when $\Delta t = 5$, varying interpolations. a) $T=5$; b) $T=10$	118
6.7	Relative volume error when $T = 10$, varying Δt with . a) Linear interpolation; b) Exponential interpolation	119
6.8	Tumor mass Y for the Stokes flow (upper row) and for the Darcy flow (below) : a) $T=5$ b) $T=10$ c) $T=15$	120
6.9	Solution of the Stokes-type flow in the case of a in vitro-like tumor at: a) $T=0$; b) $T=20$; contour lines represent the oxygen concentration levels	121
6.10	Tumor mass Y for the Stokes flow (upper row) and for the Darcy flow (below) : a) $T=5$ b) $T=10$ c) $T=15$	122
6.11	Relative error when identification time is $T=5$, with linear interpolation. a) volume error; b) centre of mass position error	123
6.12	Relative volume error when $\Delta t = 5$, varying interpolations in the case: a) $T = 5$; b) $T = 10$	123
6.13	Area as function of time, for the Reduced Order Model (black line) and for the Sensitivity approach (blue line).	126
6.14	Difference between the third scan and the solution when the identification is performed by a) Sensitivity b) ROM	126
6.15	Fast growing tumor: scan at a) june 2008 b) september 2008 c) december 2008	128
6.16	Results: a) Superposition of simulation and geomtry b) Volume curve with respect to days	129
6.17	a) Fourth scan b) Simulation	130
6.18	Area as function of time for the slow rate growth. Solid line represents the simulation results, black circles are the data used for the identification, red squares the predictions.	131
6.19	Nodule 1 (upper row) and Nodule 2(lower row) at: a) June 2008 b) April 2009 c) July 2009	132
6.20	Volulme curve for: a) Nodule 1 and b) Nodule 2.	132
7.1	Conceptual scheme of Optimal Transport	136
7.2	Density distribution at time a) $T=0$, b) $T=1$	147
7.3	Relative error on the final density distribution. Resolution: a) 200×100 , b) 400×200	149
7.4	Density distribution at time a) $T=0$, b) $T=1$. The grid resolution is $N=80$	151
7.5	Reference density distributions, resolution 200×100 , at time a) $T=0$, b) $T=1$	152

7.6	a) Density at time $T=1$ for the computed optimal solution b) relative error on the final image.	152
7.7	Thorax image scan at a) $T=0$, b) $T=1$ (corresponding to an evolution of six months); Courtesy Institute Bergonié, Bordeaux.	154
7.8	On the left: optimal transport result at $T=1$; On the right the true image at the same time.	155
7.9	Residual of the final image in the case of a) Thorax non-rigid registration, b) Tissue mapping for a regressing tumor.	155
7.10	Tissue scan at a) $T=0$, b) $T=1$ (corresponding to an evolution of three months; Courtesy Institute Bergonié, Bordeaux.	156
7.11	On the left: Monge result at $T=1$; On the right the true image at the same time.	157
7.12	Density distribution at time a) $T=0$, b) $T=1$	158
7.13	Slices of the final density distribution: a) XZ planes b) Z planes.	158
7.14	a) Contour lines of the residual distribution in the X plane; b) Contours of residual in YZ planes	159
7.15	Three different scattering, trajectories of vortex cores for: a) $l = 1.5, \beta = 0.5, f = 0.25$ b) $l = 1.0, \beta = 0.75, f = 0.15$ c) $l = 2.0, \beta = 0.15, f = 0.30$.	170
7.16	First case: a) the singular values of the embedding matrix in logarithmic; in b) the first two eigenvectors are represented in a phase plane plot. . . .	171
7.17	Second case: a) the singular values of the embedding matrix in logarithmic scale; in b) the first two eigenvectors represented in a phase plane plot. . .	172
7.18	Third case: a) the singular values of the embedding matrix in logarithmic scale; in b) the first eigenvector	172
7.19	Kinetic energy of the flow around a circular cylinder: a) singular values in logarithmic scale b) phase plot of the first two eigenvectors	173
7.20	Baricentral density for the kinetic energy of the flow around a circular cylinder: isocontours, 30 lines between the maximum and the minimum . .	174
7.21	Isocontours of the base mappings: 30 lines between the maximum ($1.25e - 3$) and the minimum $-1.25e - 3$	175
7.22	Isocontours (30 lines between the maximum and the minimum) of the reconstruction (upper line) and the simulation (lower line) for a) $t = 0$ and for $t = 1/8$	175

List of Tables

5.1	Data set and results for BEN case, Darcy-type model: 5 volumes measures are taken from 3D MRI, resolution $3.0mm$	86
5.2	Data set and results for FER case, Darcy-type model: 5 volumes measures are taken from 2D scan, resolution $1.25mm$	86
5.3	Data set and results for BEN case, Simeoni model: 5 volumes measures are taken from 3D MRI, resolution $3.0mm$	88
5.4	Data set and results for FER-II case, Regularized: 6 volumes measures are taken from 2D scans, resolution $1.25mm$	93
5.5	Data set and results for FER-II case, One specie incompressible model: 6 volumes measures are taken from 2D scans, resolution $1.25mm$	99
6.1	Relative projection error as a function of the number of POD modes N_P and of the time instant considered T	113
6.2	Data set and results for FER-II case, fitted with the parameters identified by ROM: 6 volumes measures are taken from 2D scans, resolution $1.25mm$	125
7.1	Resolution 100×50 . ϵ_0 is the L^2 relative error on the initial density distribution, ϵ_T on the final. N_i is the number of iterations to minimize \mathcal{E} , <i>i.e.</i> , such that the gradient norm variation is below $1.0e - 4$	148
7.2	Resolution 200×100	149
7.3	Resolution 400×200	150
7.4	N_p is the number of particles, ℓ is the kernel length, ϵ_T is the error computed on the actual grid, ϵ_a is the error computed with respect to the exact solution, and E_p is the error on the mapping, <i>i.e.</i> , on the gradient of the exact potential. The regularization was set to $\beta = 5e - 4$	153

- 7.5 Table representing the cost of the multilevel algorithm: the cost in equivalent iterations is shown for three different resolutions of the grid and as function of the number of levels adopted. The parameter $a_R^{(m)} = \frac{c_m}{c_0}$ quantifies the acceleration obtained when m levels are used for a problem originally formulated of a grid of resolution R^2 161

Chapter 1

Introduction (français)

1.1 Motivation

Le cancer a été étudié dans un cadre multidisciplinaire, ainsi que d'autres phénomènes biologiques, notamment la dynamique de l'ADN et des protéines ou l'évolution d'écosystèmes. Les majeurs contributions proviennent de la physique, de mathématiques et de l'informatique, qui cherchent à établir un cadre théorique pour donner une description de ces phénomènes complexes. Le terme *in silico* a été inventé pour définir les expériences numériques capables de simuler le comportement des systèmes biologiques, et qui représentent une nouveauté par rapport aux méthodes traditionnellement utilisées en biologie, les expériences *in vitro* et *in vivo*.

Ce travail porte sur la modélisation de la croissance tumorale. En particulier l'objectif n'est pas de mettre au point de nouveaux modèles mais, plutôt, d'étudier si et comment il est possible de les utiliser dans des applications réalistes. On cherche un cadre général tel que l'on peut appliquer à différents modèles qui décrivent des contextes variés comme par exemple différents types de cancer.

Concrètement, le but est d'être capable d'utiliser une série d'images médicales afin de comprendre et déduire les caractéristiques les plus importantes de la pathologie, du point de vue quantitatif. Etant données les images prises au cours d'une série d'exams d'un patient, on cherche à définir un instrument qui extrait les informations et donne une prognose. La difficulté principale est d'être capable de travailler en n'utilisant que les informations qui sont disponibles dans la pratique médicale courante.

En ce qui concerne la modélisation, un tel instrument permettrait de valider et de comparer différents modèles en utilisant des données expérimentales (*in vitro* ainsi que *in vivo*), permettant de comprendre lesquels arrivent à donner une meilleure description des différentes pathologies ou aspects de la croissance tumorale. Le but est de décrire la propagation *in vivo*, pour commencer à appliquer les modèles dans un contexte clinique.

Plusieurs perspectives ont motivé cette étude. Par exemple, un outil numérique pourrait être utilisé afin de définir un filtre fusionné avec les techniques d'imagerie médicale. Améliorer les techniques d'imagerie permettrait de limiter les cas de faux positifs et faux négatifs. Une autre application est le design (et la planification) des protocoles cliniques et l'évaluation de l'efficacité du traitement. Par exemple, dans les cas où la tumeur grossit très lentement, une prédiction de la croissance pourrait corroborer la décision d'attendre sans commencer des traitements spécifiques ou, au contraire, aider dans la décision d'utiliser un traitement par radiofréquence ou une thérapie moléculaire.

Une possible application serait aussi la simulation de l'effet placebo. Dans les tests cliniques deux groupes des patients (auxquels le même cancer a été diagnostiqué) sont

traités, un avec un médicament (chimiothérapie) et l'autre avec un placebo. Du moment que plusieurs examens sont disponibles avant de commencer le traitement, le groupe placebo peut être simulé numériquement (ce serait en quelque sorte un groupe de test virtuel).

Pour ce qui concerne l'efficacité du traitement, on pourrait déterminer si le patient est en train de réagir positivement au traitement ou si la tumeur a réussi à développer une résistance au médicament et a commencé à envahir à nouveau les organes. Un modèle calibré sur l'évolution de la maladie avant le commencement du traitement pourrait simuler comment la tumeur grossirait en l'absence de traitement. L'évolution de la maladie serait donc comparée avec la simulation. Le contrôle de la thérapie n'est pas traité dans ce travail et sera l'objet de travaux ultérieurs.

Des études statistiques et un cadre probabiliste sont utiles afin de comprendre s'il y a des corrélations entre des caractéristiques distinctives de la pathologie et certains paramètres physiologiques associés aux patients ainsi que pour étudier de façon quantitative la fiabilité des outils numériques proposés. Cependant l'intérêt est d'être capable de calibrer les modèles sur une évolution spécifique et pas de chercher des distributions ou des valeurs moyennes des paramètres sur une population d'individus.

Dans ce travail, après avoir validé les méthodes par des expériences numériques sur des données fictives, on commencera à tester les outils sur des cas réalistes. En collaboration avec l'Institut Bergonié (Institut d'oncologie sur Bordeaux), différents cas cliniques concernant l'évolution de métastases pulmonaires ont été étudiés. Ce type de métastases représente un défi du point de vue de la diagnose car certains évoluent très rapidement alors que d'autres ont un comportement quasi stationnaire. Pour ceux qui sont très agressives un traitement doit être envisagé (par exemple par chimiothérapie), pour ceux qui ne grossissent pas un contrôle, sans traitement spécifique, pourrait être suffisant.

Les cas d'évolutions lentes présentent un intérêt du point de vue de la techniques parce que plus de données sont disponibles avant de commencer le traitement et a permettent d'étudier le comportement de l'outil numérique sur une échelle temporelle plus longue.

1.2 Contribution de ce travail

Trois éléments sont nécessaires afin de définir un outil qui ait toute les caractéristiques souhaitées, (i.e. qui permettrait de construire un modèle personnalisé):

- Un modèle de croissance tumorale,

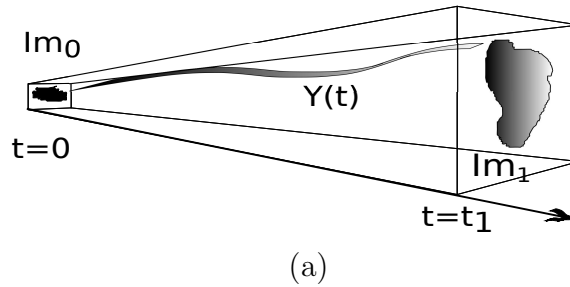


Figure 1.1: Schema conceptuel de problème inverse: deux images sont disponibles, aux temps $t=0$ et $t=1$; l'évolution est décrite par un modèle qui doit être calibré de façon à minimiser l'erreur de fitting.

- Un ensemble de données concernant un patient,
- Un problème inverse qui calibre le modèle.

Dans cette section les différents aspects et étapes de ce travail sont mentionnés et décrits de façon synthétique. Une description détaillée sera faite dans les chapitres suivants.

Le premier point important est un modèle capable de décrire l'évolution des tissus et en particulier les phénomènes associés à la croissance tumorale. Tous les modèles proposés dans la littérature se basent sur des considérations d'ordre phénoménologique, car une modélisation basée sur des principes premiers n'est pas faisable. Par conséquent, les paramètres qui apparaissent dans tous ces modèles n'ont pas une signification biologique ou physique bien précise et même s'ils l'avaient, on pourrait très rarement les mesurer de façon non-invasive sur un patient spécifique.

Afin de calibrer le modèle en telle sorte que la pathologie du patient soit décrite au mieux, les paramètres doivent être identifiés. Pour cela, on utilise les données qui sont disponibles grâce à l'imagerie médicale et on identifie les paramètres en résolvant des problèmes inverses. Un point très important qui s'impose lors que l'on veut résoudre des problèmes inverses en partant des mesures réalistes est la définition du rapport entre ce que l'on modélise et ce que l'on mesure. Ce rapport n'est pas facile à trouver pour des systèmes décrits par des principes phénoménologiques.

Des stratégies variées ont été proposées dans la littérature afin d'analyser et de résoudre des problèmes inverses ([92, 21]). Comme on ne cherche pas à retrouver des distributions statistiques on se place dans un cadre déterministe. Des considérations probabilistes deviennent nécessaires lors que l'on souhaite analyser la fiabilité des instruments proposés.

On décrit en détail le contexte mathématique pour le fitting d'un ensemble des données, la dynamique du système étant décrite par un système d'équation sous la forme:

$$\dot{X} = f(X, Y, \pi_j), \quad j = 0, \dots, N_p, \quad (1.1)$$

$$\dot{Y} = g(X, Y, \pi_j), \quad j = 0, \dots, N_p, \quad (1.2)$$

où X est la variable d'état et π_j le j -ème paramètre. Y est le vecteur des quantités mesurées (on l'appellera l'observable dans la suite). L'observable ne coïncide pas en général avec la variable d'état, et sa dynamique est déterminée par une fonction non-linéaire de l'observable elle-même, de la variable d'état et des paramètres. Une telle équation décrit l'évolution de ce qui est mesuré. Afin de fermer le système les conditions initiales et les conditions aux bords, si nécessaires, doivent être fixées. Certaines paramètres et aussi certaines conditions initiales (ou aux bords) ne sont pas connus *a priori*. On doit les identifier en telle sorte que le système reproduit au mieux un ensemble des données (c'est-à-dire un ensemble des mesures).

On note avec Im le valeur des champs qui sont expérimentalement mesurés. On définit une erreur qui quantifie la qualité du fitting:

$$\mathcal{E}^2 = \int_{\Omega \times [0, T]} \|Im - Y\|^2 dx dt, \quad (1.3)$$

ce qui est la norme L^2 de la différence en espace et en temps entre l'observable mesuré et simulé. Dans le cas de la croissance tumorale, les mesures disponibles sont discrètes en temps, et donc l'intégrale en temps se réduit à une somme, comme dans le cas montré à titre d'exemple en Fig.1.1.

L'objectif est de minimiser l'erreur par rapport au set de control choisi, c'est-à-dire l'ensemble des paramètres qui apparaissent dans le modèle et les conditions (initiales ou aux bords) inconnues. Cette minimisation peut être envisagée de plusieurs manières : la première, utilisée dans [89] consiste à utiliser l'opérateur adjoint. Cette technique a l'avantage de calculer la direction de descente pour l'erreur en utilisant seulement la simulation directe et celle du système adjoint. Cette méthode peut s'écrire avec le formalisme des multiplicateurs de Lagrange:

$$c = \arg \min_{\tilde{c}} \left\{ \int_{\Omega} \int_0^T (Im - Y)^2 - \lambda(\dot{Y} - g(X)) - \mu(\dot{X} - f(X, \tilde{c})) dx dt \right\}, \quad (1.4)$$

où c est le contrôle, λ, μ les multiplicateurs de Lagrange. Les équations d'Euler-Lagrange associées à cette fonctionnelle nous permettent de dériver le système adjoint pour les

variables λ, μ et la direction de descente. A ce stade tous les algorithmes de descente peuvent être appliqués.

Même si c'est plus coûteux du point de vue des calculs, une approche du type sensibilité (voir [138] pour les détails) est simple à mettre en place et facile à paralléliser. Ces sont les raisons qui nous ont poussé à préférer cette approche pour ce travail.

On calcule le gradient de la fonctionnelle qui décrit l'erreur Eq.2.3 par rapport à un élément générique du set de contrôle c_j :

$$\frac{\partial \mathcal{E}}{\partial c_j} = \int_{\Omega} \int_0^T 2(Im - Y) \frac{\partial Y}{\partial c_j} dx dt, \quad (1.5)$$

où la quantité $Z_j := \frac{\partial Y}{\partial c_j}$ est la sensibilité de Y par rapport au j -ème élément de l'ensemble de contrôle. La direction de descente est proportionnelle au produit scalaire L^2 entre l'erreur et la sensibilité. Les équations pour la variable Z_j sont écrites en utilisant la règle de dérivation des fonctions composées:

$$\frac{\partial}{\partial c_j} \dot{Y} = \frac{\partial}{\partial c_j} g(Y, X; c) \Rightarrow \dot{Z}_j = \frac{\partial g}{\partial Y} Z_j + \frac{\partial g}{\partial X} \frac{\partial X}{\partial c_j} + \frac{\partial g}{\partial c} \frac{\partial c}{\partial c_j}, \quad (1.6)$$

$$Z_j(0) = \frac{\partial Y(0)}{\partial c_j}. \quad (1.7)$$

Dans l'équation pour Z_j , qui est la seule variable d'intérêt afin de calculer la direction de descente, aussi $W_j := \frac{\partial X}{\partial c_j}$ apparaît et doit être calculé. Son équation et les conditions initiales associées sont trouvées avec la même procédure appliquée aux équations qui décrivent l'évolution de l'état du système:

$$\dot{W}_j = \frac{\partial f}{\partial X} W_j + \frac{\partial f}{\partial c_j}, \quad (1.8)$$

$$W_j(0) = \frac{\partial X(0)}{\partial c_j}. \quad (1.9)$$

Le système peut s'écrire proprement comme suit:

$$\dot{Z}_j = \frac{\partial g}{\partial Y} Z_j + \frac{\partial g}{\partial X} W_j + \frac{\partial g}{\partial c_j}. \quad (1.10)$$

Cette équation montre que, dans une approche de sensibilité, afin de calculer la direction de descente il est nécessaire de calculer $N_c + 1$ simulations directes, où N_c est le nombre d'éléments dans l'ensemble de contrôle. Si on calcule la solution du système adjoint on

peut calculer la matrice Hessienne de la fonctionnelle et utiliser un algorithme du type Newton, dont la convergence est plus rapide que celle des méthodes du type gradient.

L'algorithme du gradient s'écrit de la manière suivante:

$$c_j^{n+1} = c_j^n - \beta \left(\sum_i^{N_o} \int_{\Omega} (Im_i(x) - Y(x; t_i))(-Z_j(x; t_i)) dx \right), \quad (1.11)$$

où N_o est le nombre des mesures disponible et β est le pas, qui est un paramètre libre et doit être fixé pour chaque cas. Si on écrit cette équation de manière plus compacte on trouve:

$$c_j^{n+1} = c_j^n + \beta \left(\sum_i^{N_o} \langle \mathcal{E}(x, t_i), Z_j(x; t_i) \rangle_{\Omega} dx \right). \quad (1.12)$$

L'inconvénient le plus important de toutes les méthodes basées sur l'optimisation est le coût computationnel. Pour cette raison une technique d'ordre réduit a été mise à point, en cherchant à préserver un certain pouvoir de prédiction. En particulier, dans ce travail, la Proper Orthogonal Decomposition (POD, voir [147]) a été appliquée aux modèles de croissance tumorale.

Cette technique utilise un ensemble des solutions du système d'EDP en variant les éléments de l'ensemble de contrôle, afin de décrire les solutions elles-mêmes comme éléments d'un espace de dimension finie et si possible, petite. L'avantage d'une telle représentation n'est pas seulement lié à la réduction du nombre d'inconnues au niveau discret mais aussi à un effet de régularisation.

Un point critique des toutes méthodes d'optimisation est leur initialisation. En général du moment que plusieurs minima locaux peut exister différentes initialisations ont été faites dans certains intervalles de l'ensemble de contrôle. Pour déterminer les intervalles des simulations directes ont été faites en sorte d'identifier les bornes supérieures et inférieures, correspondantes à des croissances en volume raisonnables.

Nous Décrivons maintenant comment l'état X et l'observable Y sont modélisés. Les modèles de croissance tumorale d'intérêt dans le cas présent sont des systèmes paramétriques d'EDP construits à partir de trois hypothèses principales : un ensemble d'équations décrit la dynamique des populations cellulaires, des équations prennent en compte la mécanique du tissu et d'autres décrivent la manière dont l'énergie est fournie aux cellules, *i.e.* les nutriments.

Le modèle étudié est diphasique pour ce qui concerne la composition de la tumeur : la densité P représente le nombre des cellules tumorales actives par unité de volume, Q celle des cellules nécrosées. Le tissu sain est une phase distincte, notée par S . Les équations

décrivant la dynamique des populations cellulaires sont:

$$\frac{\partial P}{\partial t} + \nabla \cdot (\mathbf{v}P) = (2\gamma - 1)P, \quad (1.13)$$

$$\frac{\partial Q}{\partial t} + \nabla \cdot (\mathbf{v}Q) = (1 - \gamma)P, \quad (1.14)$$

$$\frac{\partial S}{\partial t} + \nabla \cdot (\mathbf{v}S) = 0. \quad (1.15)$$

où la vitesse \mathbf{v} décrit la déformation du tissu et γ (appelée seuil d'hypoxie) est une fonction scalaire de la concentration des nutriments et sera définie plus précisément dans la suite. S'il y a assez de nutriment $\gamma = 1$ et la tumeur prolifère, autrement elle meure. Le tissu sain évolue selon une équation de conservation.

En assumant que $P + Q + S = 1$ en chaque point du domaine on peut dériver une équation pour la divergence de la vitesse. Couplée avec une loi de Darcy, elle permet de décrire complètement la mécanique du système:

$$\nabla \cdot \mathbf{v} = \gamma P, \quad (1.16)$$

$$\mathbf{v} = -k(P, Q)\nabla\Pi. \quad (1.17)$$

La fonction scalaire Π joue le rôle d'une pression (ou d'un potentiel) et k est la perméabilité, qui satisfait:

$$k = k_1 + (k_2 - k_1)(P + Q), \quad (1.18)$$

où k_1 est la constante de perméabilité du tissu sain et k_2 celle du tissu tumorale. L'équation qui décrit les nutriment a la forme suivante:

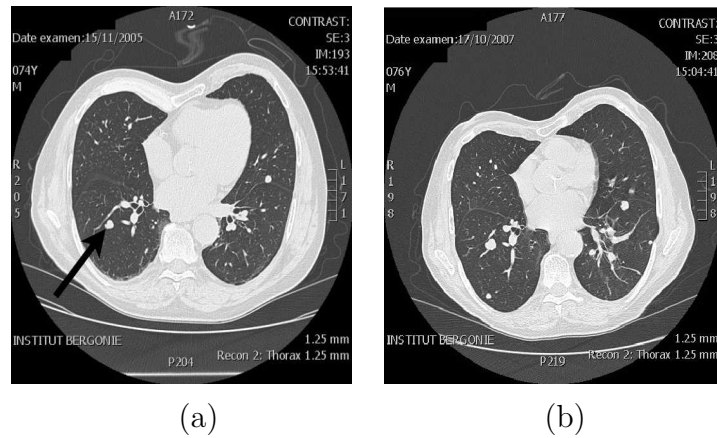
$$-\nabla \cdot (D(P, Q)\nabla C) = -\alpha PC - \lambda C, \quad (1.19)$$

où α est le taux de consommation d'oxygène (le seul nutriment considéré) des cellules proliférantes, λ est la consommation du tissu sain, $D(P, Q)$ la diffusivité. Les conditions aux bords et les sources sont déterminées en cherchant à prendre en compte la nature de l'organe. La diffusivité peut s'écrire:

$$D = D_{max} - K(P + Q). \quad (1.20)$$

Le lien entre la concentration des nutriments et la dynamique des populations est fourni par :

$$\gamma = \frac{1 + \tanh(R(C - C_{hyp}))}{2}, \quad (1.21)$$



où R est un coefficient et C_{hyp} est le seuil d'hypoxie.

Pour ce simple modèle $X = P, Q, C, \Pi$. L'observable $Y = P + Q$ a été choisi après une discussion avec les médecins sur ce qui est mesuré par des CT scans dans le cas des métastases pulmonaires. Sa signification est simple : avec les rayons X on ne peut pas distinguer différents phénotypes à l'intérieur de la tumeur, mais uniquement la masse tumorale par rapport au tissu sain. L'ensemble de contrôle est constitué par tous les paramètres scalaires et les conditions initiales pour la variable P .

Les conditions aux bords pour l'oxygène et la pression, ainsi que les sources seront précisées proprement pour chaque cas analysé.

1.3 Résultats d'applications cliniques

Quelques résultats obtenus dans des cas réalistes sont présentés comme exemple d'application potentielle de l'outil numérique développé.

In Fig. 1.2 quatre scans qui couvrent une période de 45 mois sont montrés, concernant des métastases pulmonaires. Ce patient a plusieurs métastases, mais seulement celle qui est encadrée dans la Fig.2.2.a) a été étudiée. Il s'agit d'une métastase qui évolue de façon quasi-statique et qui nécessite seulement d'être mis sous monitoring.

Les résultats obtenus par la technique de sensibilité sont présentés dans le cas où seulement deux scans sont utilisés comme ensemble de données pour résoudre le problème inverse et trouver l'ensemble de contrôle. La simulation directe a été faite et le résultat comparé aux examens suivants. En Fig.1.3 le volume des scans est comparé aux simulations directes. La ligne continue est la surface de la tumeur simulée, les cercles noirs sont les scans utilisés dans le processus d'identification et les carrés rouges les scans qu'on

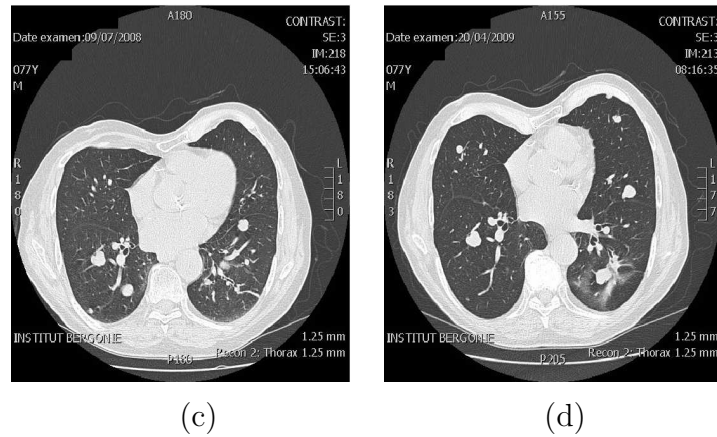


Figure 1.2: Scans: a) Novembre 2005, b) Octobre 2007, c) Juillet 2008, d) Avril 2009

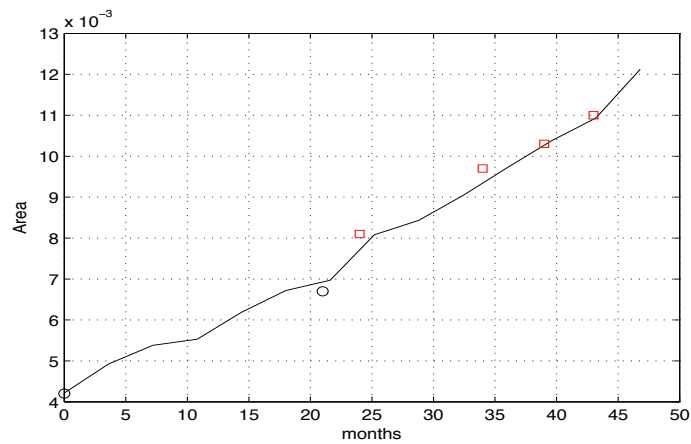


Figure 1.3: Surface de la tumeur un fonction du temps: la ligne continue représente la simulation, les cercles noirs les données, les carrés rouges les prédictions.

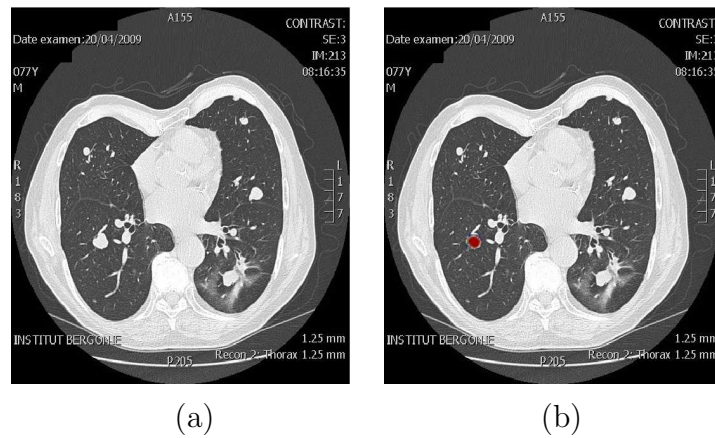


Figure 1.4: a) Quatrième image b) Simulation

souhaite prévoir.

Le résultat est très prometteur et représente en quelque sorte la meilleure prédiction qu'on espère obtenir par l'outil défini dans notre travail. En Fig.1.4 le quatrième scan est comparé à l'image correspondante (simulée) : l'accord est plutôt satisfaisant.

Les premiers travaux qui ont commencé à envisager des applications réalistes étaient basés sur des modèles du type EDO. Les résultats obtenus par des modèles EDP montrent un possible avantage de ces modèles par rapport aux modèles EDO, qui sont plus simples et moins coûteux mais qui ne peuvent pas utiliser toute l'information disponible et qui donnent une description forcément moins riche du phénomène.

Quand on traite des applications réalistes, des problèmes divers d'ordre pratique doivent être résolus afin de traiter les images et de les adapter à la définition d'un problème inverse. La première opération est la segmentation. La tumeur doit être séparée du reste de l'organe. Cette tâche devient extrêmement critique lorsqu'on ne peut pas définir les bords de la tumeur, comme par exemple dans toutes les pathologies caractérisées par des phénotypes diffus.

Les organes sont souvent très déformables ce qui signifie que des facteurs externes influencent ce qui est observé sur les images. Dans ce travail tous ces problèmes d'imagerie ont été traités de manière standard mais ils ont fait en sorte qu'on s'intéresse aux processus de recalage non-rigide pour les tissus biologiques.

Les aspects numériques de l'intégration du problème de Monge-Kantorovich L^2 ont été étudiés afin de comprendre s'il pouvait être utilisé en tant que outil géométrique pour les problèmes inverses. Le problème de transport optimal consiste à trouver le mapping dont l'énergie est minimale tel qu'une densité de départ est transportée en une densité

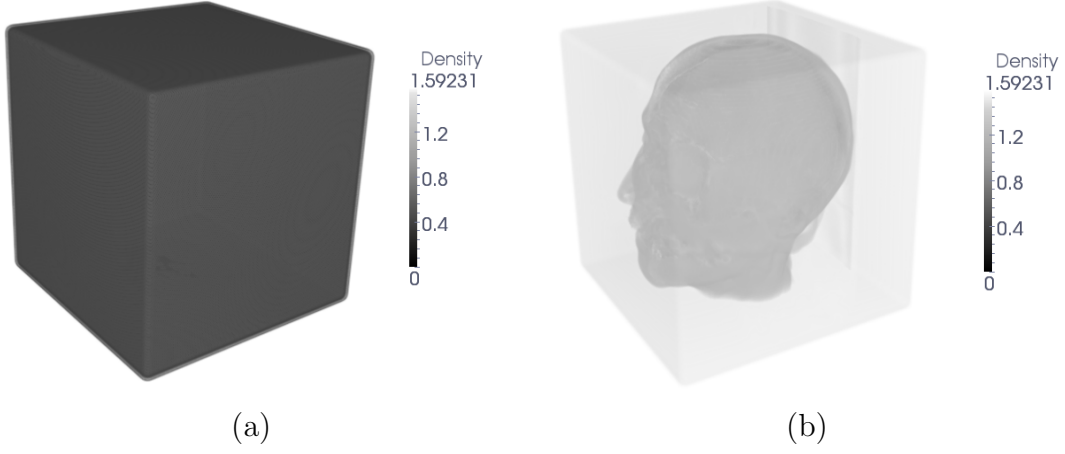


Figure 1.5: Distribution de densité au temps a) $T=0$, b) $T=1$.

d'arrivée, les deux étant données. Les équations qui gouvernent ce transport sont définies par un principe variationnel:

$$X(\xi) = \arg \min_{\tilde{X}} \left\{ \int_{\Omega_0} \rho_0(\xi) |\tilde{X}(\xi) - \xi|^p d\xi \right\}, \quad (1.22)$$

avec la contrainte:

$$\rho_0(\xi) = \rho_T(X(\xi)) \det(\nabla_{\xi} X), \quad (1.23)$$

où X est le mapping inconnu, ρ_0 et ρ_T les densités initiale et finale. Un résultat 3D est montré, qui représente le mapping d'un cube de densité, uniforme, dans la densité normalisée qui correspond à l'IRM d'une tête humaine. La complexité de la géométrie est bien reconstruite.

1.4 Structure de la thèse

Cette thèse peut être divisée en deux parties, qui sont relativement indépendantes l'une de l'autre. Dans la première on décrit l'étude concernant les problèmes inverses, dans la seconde les aspects numériques du transport optimal L^2 .

Modèles de croissance tumorale et applications. Dans ce chapitre on présente l'état de l'art de la modélisation de la croissance tumorale dans le but de définir le contexte dans lequel ce travail a été développé. En particulier on pose l'accent sur la nature phénoménologique de la modélisation de la croissance tumorale. Dans une perspective

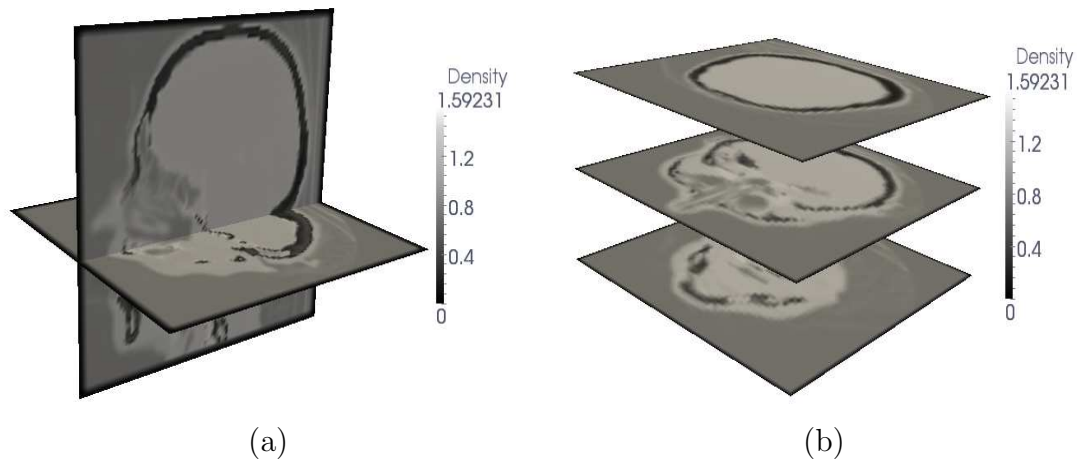


Figure 1.6: Coupes de la densité finale: a) plan XZ b) Z planes.

historique on commence par décrire les modèle EDO, qui ont été les premiers à être développés. Les principes généraux de ce type de modélisation sont montrés, suivis par des exemples. La croissance tumorale est fortement influencée par les propriétés spatiales des tissus : une description basée uniquement sur des propriétés intégrales n'est pas satisfaisante dans la plupart des cas. C'est pourquoi des modèles qui prennent en compte l'évolution spatio-temporelle ont été proposés. On peut les diviser du point de vue conceptuel en deux catégories : les modèles discrets et continus. Leurs caractéristiques principales ainsi que les avantages et les défauts sont décrit, en donnant les motivations du choix des modèles continus pour ce travail. Ce survol des modèles est complété par une brève description des modèles hybrides, qui cherchent à combiner les avantages des deux et qui représentent un domaine actif de recherche en modélisation de la croissance tumorale. Dans la deuxième partie de ce chapitre on décrit les travaux concernant des applications réalistes. Les premières ont été proposées en utilisant les modèles EDO. Des perspectives diverses sont commentées. Dans la littérature on trouve très peu de travaux concernant l'application des modèles spatiaux à la réalité clinique. Ces travaux seront commentés plus en détail (en particulier ceux qui se proposent d'utiliser l'imagerie médicale comme source d'information).

Modèles adoptés et stratégie computationnelle. Dans ce chapitre on donne une description des modèles qu'on a utilisé dans ce travail. Le modèle de référence est un modèle à deux espèces du type Darcy. Il consiste en un système d'EDPs paramétriques qui est déterminé à partir de modèles plus complexes qui ont été proposé dans la littérature.

Ensuite, on présente une version régularisée qui cherche à améliorer le conditionnement lorsque l'on souhaite résoudre des problèmes inverses. Un autre modèle proposé dans la littérature est étudié, qui représente une simplification du modèle de Darcy adopté. Après avoir décrit les modèles on introduit les méthodes d'intégration qui ont été utilisées. On commente une analyse préliminaire des simulations directes et des résultats qu'on obtient en variant les éléments de l'ensemble de contrôle. Le chapitre se termine avec une description très synthétique des opérations de pre-processing qui sont nécessaires afin d'utiliser les images médicales comme données (segmentation et recalage).

Technique de sensibilité. Dans ce chapitre on décrit plus en détail les résultats concernant une approche de sensibilité. D'abord on analyse des problèmes inverses lorsque les modèles sont du type EDO et la technique est une sensibilité exacte. Un modèle qui est une version 0-D du modèle de Darcy est proposé et testé. Les aspects les plus critiques des modèles EDO sont soulignés et illustrés par des exemples. On commente les résultats obtenus en utilisant des modèles EDP, en variant les éléments de l'ensemble de contrôle ainsi que le modèle utilisé. Après avoir validé les outils numériques par des expériences abstraites on les teste sur des cas réalistes concernant l'évolution des métastases dans les poumons. La condition initiale pour la distribution des cellules proliférantes modélise une structure en couches (un hypothèse bien acceptée en biologie). On conclue ce chapitre par une comparaison entre les performances des modèles EDO et EDP.

Approche Réduite. La réduction du coût des calculs est une nécessité dans ce genre de problème. Une approche basée sur le résidu de l'équation à différents instants est décrite. Des tests préliminaires montrent que le problème peut être sous-déterminé et que une régularisation doit être adoptée. La solution est de chercher dans un espace engendré par une base construite par la technique de Proper Orthogonal Decomposition (POD). Cette approche a été validée par des cas tests. Ensuite des cas réalistes sont étudiés et les avantages et les défaut de cette technique sont commentés en détail.

Transport Optimal La seconde partie de ce travail est dédiée au problème du transport optimale et en particulier à la numérique du problème de Monge-Kantorovich L^2 . Une introduction décrit synthétiquement les contributions majeures sur le plan théorique, en soulignant en particulier les propriétés utiles lors que l'on cherche à approcher la solution de ce problème. Ensuite, les techniques numériques proposées dans la littérature sont commentées. En utilisant les propriétés des équations de Hamilton-Jacobi associées à

une formulation Eulerienne de ce problème une famille de méthodes lagrangiennes est dérivée. On propose une méthode particulière pour intégrer les équations. Une étape de validation a été mis en place avec des cas test, dans lesquels on montre que l'algorithme proposé est robuste dans une série de phénomènes critiques, tels que la fragmentation et la coalescence. On commente quelques résultats concernant l'application de cette technique au recalage non-rigide des images de tissus biologiques (en 2D et 3D). Les test montrent qu'il y a une super-linéarité dans le coût de l'algorithme, liée à la nature du problème de transport. Une accélération multi-niveau est proposée pour limiter ces effets. Le chapitre se termine par une perspective concernant l'utilisation de la distance de Wasserstein pour la réduction de modèle. L'objectif est d'utiliser le fait que la distance de Wasserstein est définie naturellement par un transport. Cette caractéristique pourrait résoudre les problèmes de la POD et des techniques d'analyse en composantes principales en présence d'advection des structures cohérentes concentrées.

Chapter 2

Introduction

2.1 Motivation

Recently, cancer has been studied in a multidisciplinary framework, as well as a broad variety of other biological phenomena, ranging from DNA and protein dynamics to biosystems and ecology. The main contributions coming from physics, mathematics and computer science try to set up theoretical frameworks to describe such complex phenomena. The term *in silico* has been created to define numerical experiments that are able to emulate biological systems behaviors, in contrast to *in vitro* or *in vivo* experiments, which are the traditional tools in biological research.

The present work deals with tumor growth modeling. In particular, the goal is not to set up novel models but, instead, to investigate if and whether it is possible to utilize them in realistic applications. A general framework is sought, such that it can be applied to different models and to all possible contexts, *i.e.* to different kind of cancers, attacking all sort of tissues.

Concretely, the objective is to be able to exploit a set of medical images in order to infer the main features of an undergoing pathology from a quantitative point of view. Roughly speaking, given the images taken during the first two medical exams of a patient, a tool is sought that it can extract useful informations and give an approximated prognosis. One of the main challenges is to be able to work with the informations that are available in the current clinical practice, without requiring additional medical exams.

For what concerns theoretical and modeling issues, such a tool would allow to validate and compare models with respect to experimental data sets (coming from both *in vivo* or *in vitro* systems), thus permitting to understand which models perform better in describing different pathologies or aspects of the growth. The interest is, of coarse, to better describe *in vivo* tumor propagations. Indeed, this allow to investigate the applications of mathematical modeling to realistic clinical practice.

Several needs and perspectives motivate this study. For instance, a numerical tool may be set up and fused with the present medical imaging techniques to act as a filter. Improving the diagnosis stage would allow to decrease the number of false positive and false negative cases. Furthermore, such a numerical tool would be helpful in designing clinical protocols, since it might suggest when a novel medical exam would be helpful to monitor the critical stages of the progression.

For the oncologists the development of predictive tools could be of interest in the planning and in the evaluation of an anti-tumoral treatment. For example with slowly evolving tumors, a prediction of growth could reinforce the decision of waiting without specific treatment or on the contrary to help in the decision of starting radiofrequency

thermal ablation or molecular targeted therapy.

A possible outcome of this tool would be the placebo effect simulation. In clinical tests two sets of patients (to whom the same cancer has been diagnosed) are treated, one with a chemotherapeutic and the other with a placebo. Since several images are available before the treatment starts, the placebo may be numerically simulated (a sort of *in silico* test group).

Yet another possible application concerns the treatment efficacy evaluation. For instance, informations might be provided on whether a patient is positively reacting to the treatment or if tumor has managed to become resistant to the therapy and it is starting spreading again. Indeed, a model calibrated on the evolution of the disease before the beginning of the therapy may simulate how the tumor would grow in absence of any treatment. Then, the simulated evolution might be compared to the observed one. Therapy control is not treated in this work and it is one of the perspectives of the proposed framework.

Statistical studies and some probability are useful and fundamental to understand if there are correlations between some distinctive feature of the pathology and some physiological parameters of the patients and to study the reliability of the numerical tools proposed. However, for all these applications becoming possible, as said, the interest is to be able to calibrate models onto a specific patient pathology, not to find some statistical results or probability distributions describing the mean evolution of the disease over a population of individuals.

For the present work, after having validated the proposed methods by means of numerical testcases, we started applying them to clinical cases. Lung metastases have been studied as a first realistic application. In collaboration with oncologists from Institut Bergonié (the cancerology institute of Bordeaux) several realistic cases have been studied and discussed. These metastases are secondary tumors that detached from a primary tumor (growing in some other organ) and attack the lungs. They are a therapeutic challenge because some are fast evolving and are good candidates for trials with molecular targeted therapies, but other are slowly evolving and it is difficult to decide when to treat them.

Several scans may hence be available for a slowly evolving nodule and this occurrence is important in our case since it allows a validation of the assimilation technique on a long time horizon.

2.2 Overview of the present contribution

Three main elements are necessary in order to set up a tool fulfilling the requirements described in the previous section, *i.e.* a patient based prognostic model:

- A model describing tumor growth;
- A set of data concerning a patient pathology;
- An inverse problem in order to calibrate the model on the specific case.

In this section the different aspects and stages of the work are mentioned and described in a synthetic way. A detailed description is postponed to the following chapters.

The first building block is a model describing the evolution of the tissues and in particular tumor invasion. For all the models studied in the literature, a classical first principles based modeling is not affordable, thus obliging to adopt some phenomenological assumptions in order to target specific portions of the evolution. Hence, the parameters appearing in all these models arise from the lack of modeling of some of the scales involved in the natural evolution and therefore they do not have a precise physical meaning or, if they have it, they could hardly be measured on a specific patient.

In order to calibrate the model in such a way that the patient pathology is reproduced as good as possible, the model parameters have to be found. To this end, data coming from medical imagery are used to recover the parameters value by means of an inverse problem. A key point arising in inverse problems driven from realistic measurements consists in defining the relationship between modeled and measured quantities. This is far from being obvious for systems described by means of phenomenological equations.

Different frameworks were proposed in the literature to analyze and to solve inverse problems (see [92, 21]). Since we are not interested in recovering statistical distributions of the parameters, a deterministic approach is chosen for the present work. As already stated, further investigation of probability distributions of parameters are useful to study the reliability of the tool.

Let us describe in detail the context for a case in which a fitting of data is sought, the dynamics being determined by a system of equations. In Fig.2.1 all the elements of inverse problems which are of interest for this work are represented. In all the treated problems the state variables of the system (*i.e.* all the variables which are needed and sufficient to describe uniquely its configuration) are described by governing laws of the form:

$$\dot{X} = f(X, Y, \pi_j), \quad j = 0, \dots, N_p, \quad (2.1)$$

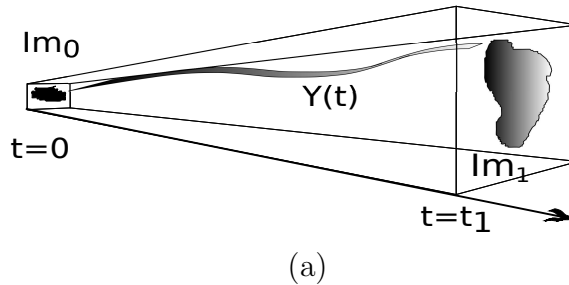


Figure 2.1: Conceptual scheme of an inverse problem: two images are available at $t = 0$ and $t = 1$, evolution is described by a model which has to be calibrated in sort that the fitting error is low.

$$\dot{Y} = g(X, Y, \pi_j), \quad j = 0, \dots, N_p, \quad (2.2)$$

where X is the state, and π_j is the j -th parameter. Y is the vector of measured quantities (it will be called *observable* in the following). The observable does not coincide in general with the state of the system and its dynamics depends on a non-linear function of the observable itself, of the state and of parameters. Such an equation describes the evolution of what is measured. In order to close the system, initial and boundary conditions (if there are PDEs that require them) have to be imposed. Some parameters and possibly some of the initial or boundary conditions are not known *a priori*. They need to be identified in such a way that the system fits at best a given set of data, that is, a collection of measurements.

Let us denote by Im the value of the fields that are experimentally measured.

An error is defined, which quantifies how the model fits the data:

$$\mathcal{E}^2 = \int_{\Omega \times [0, T]} \|Im - Y\|^2 dx dt, \quad (2.3)$$

which is the L^2 norm of the difference in space and time of the measured and the simulated observable. In the case of tumor growth a set of measurements is available, which is discrete in time, so that the integral in time reduces to a finite sum, as depicted in Fig.2.1, where only two images are taken.

The goal is to minimize the error with respect to a *control set*, that is, the parameters appearing in the model and the unknown initial and boundary conditions.

The minimization can be carried out in different ways: the first one, as used in [89], consists in using an adjoint technique. This has the advantage of computing the descent direction for the error by requiring only the simulation of the adjoint system. The system

can be written in a Lagrange multiplier formulation as follows:

$$c = \arg \min_{\tilde{c}} \left\{ \int_{\Omega} \int_0^T (Im - Y)^2 - \lambda(\dot{Y} - g(X)) - \mu(\dot{X} - f(X, \tilde{c})) \, dx \, dt \right\}, \quad (2.4)$$

where c is the control, λ, μ the lagrangian multipliers. Euler-Lagrange equations associated to this functional allow to derive the adjoint system in λ, μ and the descent direction. Any descent algorithm can be applied to find the minimizer.

Even if it is more expensive from a computational standpoint, a sensitivity approach (see [138] for details) is simple to set up and easy to parallelize. These are the main reasons why in this work a sensitivity approach is chosen and studied.

Let us compute the gradient of the error functional Eq.2.3, with respect to the generic element c_j of the control set:

$$\frac{\partial \mathcal{E}}{\partial c_j} = \int_{\Omega} \int_0^T 2(Im - Y) \frac{\partial Y}{\partial c_j} \, dx \, dt, \quad (2.5)$$

where the quantity $Z_j := \frac{\partial Y}{\partial c_j}$ is the sensitivity of Y with respect to the j -th element of the control set. The descent direction is proportional to the L^2 scalar product between the error and the sensitivity. The equations for Z_j are written by applying the chain rule:

$$\frac{\partial}{\partial c_j} \dot{Y} = \frac{\partial}{\partial c_j} g(Y, X; c) \Rightarrow \dot{Z}_j = \frac{\partial g}{\partial Y} Z_j + \frac{\partial g}{\partial X} \frac{\partial X}{\partial c_j} + \frac{\partial g}{\partial c} \frac{\partial c}{\partial c_j}, \quad (2.6)$$

$$Z_j(0) = \frac{\partial Y(0)}{\partial c_j}. \quad (2.7)$$

In the equation for Z_j , which is the only variable of interest to compute the descent direction, also $W_j := \frac{\partial X}{\partial c_j}$ appears and has to be computed. Its equation, including initial conditions, is found exactly by the same procedure, leading to:

$$\dot{W}_j = \frac{\partial f}{\partial X} W_j + \frac{\partial f}{\partial c_j}, \quad (2.8)$$

$$W_j(0) = \frac{\partial X(0)}{\partial c_j}. \quad (2.9)$$

Recasting properly the system, the following expression is obtained for the Z_j sensitivity:

$$\dot{Z}_j = \frac{\partial g}{\partial Y} Z_j + \frac{\partial g}{\partial X} W_j + \frac{\partial g}{\partial c_j}. \quad (2.10)$$

This highlights the fact that, in a sensitivity approach, in order to compute the descent direction, $N_c + 1$ simulations are needed, where N_c is the number of elements in the control

set. If an adjoint computation is added, the Hessian matrix for the error functional could be computed, allowing to perform a Newton-type algorithm, whose convergence is faster than normal gradient based methods.

A gradient descent algorithm for the error minimization reads:

$$c_j^{n+1} = c_j^n - \beta \left(\sum_i^{N_o} \int_{\Omega} (Im_i(x) - Y(x; t_i)) (-Z_j(x; t_i)) dx \right), \quad (2.11)$$

where N_o is the number of available volume measures and β is the step, which is a free parameter and has to be fixed for each case. Recasting it in a more compact form, the following update is obtained for the control set:

$$c_j^{n+1} = c_j^n + \beta \left(\sum_i^{N_o} \langle \mathcal{E}(x, t_i), Z_j(x; t_i) \rangle_{\Omega} dx \right). \quad (2.12)$$

The main drawback of all the methods based on an optimization framework for PDEs systems is the computational cost. That is why some reduced order technique has been investigated in order to decrease it as much as possible, with the hope that the prediction capability is not too much corrupted. In particular, in the present work, Proper Orthogonal Decomposition (see [147] for details) was applied to tumor growth models. This technique uses a set of solutions of the system of PDEs, varying the elements of the control set, in order to describe the solutions themselves as elements of a space of finite small dimension. The advantage of such a representation is not merely linked to the reduction of the number of unknowns at discrete level but also to a regularization effect.

One critical point of all the optimization methods is their initialization. In general, since local minima may arise, several initializations are done in a certain range of the control set. To determine this, direct simulations are used in such a way that the upper boundary of the control set corresponds to a set of parameters such that the simulated tumor increase its volume of a reasonable factor in a given time interval.

Let us briefly introduce how the state X and the observable Y are modeled in the present case. Tumor models which are of interests for our purposes are systems of parametric partial differential equations in which three main modeling hypothesis appear: a set of equations describing the tissue composition (*i.e.* healthy tissue, tumor mass etc.), a set of equation describing the mechanical evolution of the phases and then nutrients equations, accounting for the energy supply necessary for the cellular activities.

Concerning the model used for the present work, the tumoral tissue is composed by two different phases (called phenotypes in the following), denoted by P and Q . The density

P represents the number of dividing cells per unit volume, Q is that of the necrotic cells. The healthy tissue is the phase denoted by S . Equations for P , Q and S reads:

$$\frac{\partial P}{\partial t} + \nabla \cdot (\mathbf{v}P) = (2\gamma - 1)P, \quad (2.13)$$

$$\frac{\partial Q}{\partial t} + \nabla \cdot (\mathbf{v}Q) = (1 - \gamma)P, \quad (2.14)$$

$$\frac{\partial S}{\partial t} + \nabla \cdot (\mathbf{v}S) = 0. \quad (2.15)$$

where the velocity \mathbf{v} renders in some sort the tissue deformation and γ (called the hypoxia threshold) is a scalar function of the nutrient concentration that is more precisely defined later on. If enough nutrients are available then $\gamma = 1$ and the tumor cells proliferate, otherwise they die. The healthy tissue evolves through a pure conservation equation.

Assuming that $P + Q + S = 1$ in every point of the domain, a condition for the divergence of the velocity field is derived that, coupled with a Darcy law allows to describe the mechanics of the system:

$$\nabla \cdot \mathbf{v} = \gamma P, \quad (2.16)$$

$$\mathbf{v} = -k(P, Q)\nabla\Pi. \quad (2.17)$$

The scalar function Π plays the role of a pressure (or of the potential), and k is a permeability field, satisfying:

$$k = k_1 + (k_2 - k_1)(P + Q), \quad (2.18)$$

where k_1 represents the constant porosity of the healthy tissue and k_2 is the porosity of the tumor tissue.

The equation describing the nutrients has the following form:

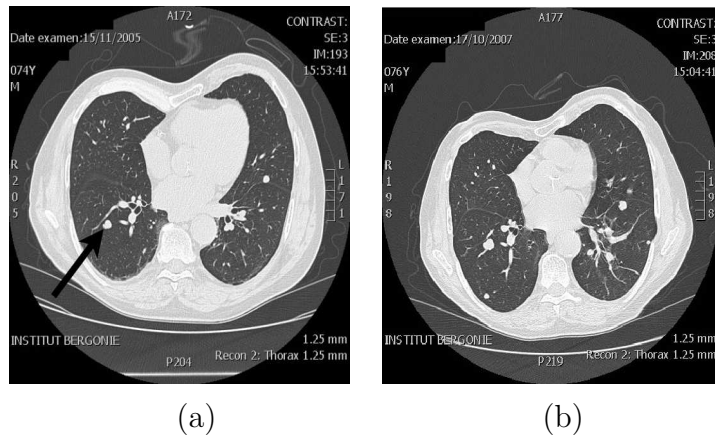
$$-\nabla \cdot (D(P, Q)\nabla C) = -\alpha PC - \lambda C, \quad (2.19)$$

where α is the oxygen consumption rate for the proliferating cells, λ is the oxygen consumption coefficient of healthy tissue and $D(P, Q)$ is the diffusivity. Boundary conditions and sources are set up according to the nature of the organs considered and will be detailed later on. The diffusivity may be written as:

$$D = D_{max} - K(P + Q). \quad (2.20)$$

The link between the nutrients concentration and the population dynamics is provided by:

$$\gamma = \frac{1 + \tanh(R(C - C_{hyp}))}{2}, \quad (2.21)$$



where R is a coefficient and C_{hyp} is called the hypoxia threshold. The resulting hypoxia function thus satisfies $0 \leq \gamma \leq 1$.

For this simple model the state is $X = \{P, Q, C, \Pi\}$. The observable $Y = P + Q$ is the result of a discussion with medical doctors about what is measured by CT scans in the case of lung metastasis. Its meaning is simply that one can not distinguish on images the cell phenotypes composing the tumor, but only the tumor mass. The control set consists in all the undetermined scalar parameters describing tissue properties (such as k_1, k_2, D_{max}, K), the tumor activities (nutrient consumptions α, λ , and C_{hyp}), and the fields describing the initial non-observed conditions needed to integrate the system ($P(x, 0)$). Furthermore boundary conditions (and additional sources) potentially enter in the control set. The latter play a fundamental role and it will be detailed for each test presented in the following chapters.

2.3 Paradigmatic results of clinical applications

In this section some results obtained in a realistic application are presented as an example of potential outcome of the framework which has been synthetically outlined in the previous section.

In Fig.2.2 four scans covering an evolution over 45 months are presented of some lung metastases of a primary tumor affecting the thyroid (Courtesy Institut Bergonié). Even though this patient is affected by several metastases, only the study of the one marked in Fig.2.2.a) will be presented. It is a quasi-steady metastasis, which grows very slowly and thus need only to be monitored. The results obtained by means of a sensitivity technique are presented, when only the first two scans were used in order to identify the system.

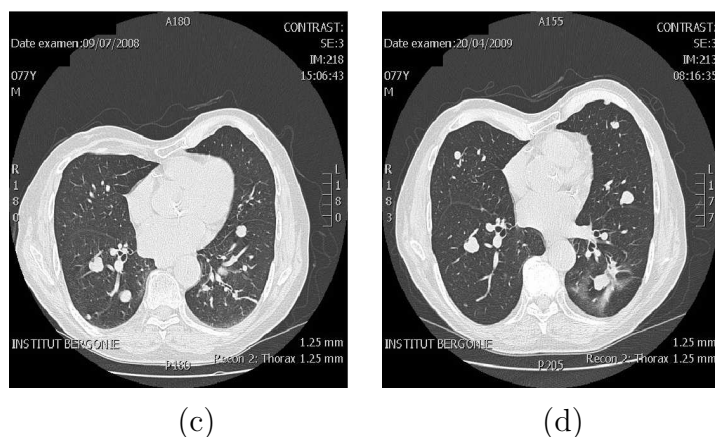


Figure 2.2: Scans: a) November 2005, b) October 2007, c) July 2008, d) April 2009

This means that the first two images were used as data set to solve the inverse problem and find the set of control. Then, the direct simulation were performed covering the entire evolution and the result has been compared to the data of the subsequent exams.

The computational set up is detailed in the following chapters. In Fig.2.3 the volume of the scans is compared to the direct simulation. The solid line is the area of the simulated tumor (seen on a 2D slice), the black circles represent the area of the scans used as data and the red squares represent the predictions. This is a very promising result and it will be analyzed in detail. However this represents in some sort the best that may be achieved by a prognosis tool driven by medical imagery. In Fig.2.4 the fourth scan and the corresponding image are compared, showing a good agreement.

The first works considering realistic applications for tumor growth were based on ordinary differential equations. The presented results highlights one of the advantage of using models based on partial differential equations with respect to models based on ordinary differential equations. The latter, albeit simple and cheap from a computational standpoint, are not able to exploit all the available informations concerning the pathology, thus providing a less rich description of the phenomenon.

When targeting realistic applications several fundamental practical problems have to be tackled in order to set up a reliable tool. In particular, as it will be clear later on, images have to be preprocessed to be suitable for inverse problems. The first issue is segmentation: tumor and the surroundings have to be distinguished as well as the organ boundaries. This task may be very difficult in the case in which a tumor boundary is hardly defined and phenotypes are very diffused. Moreover, organs are often very deformable, which means that several external factors may influence what is observed on

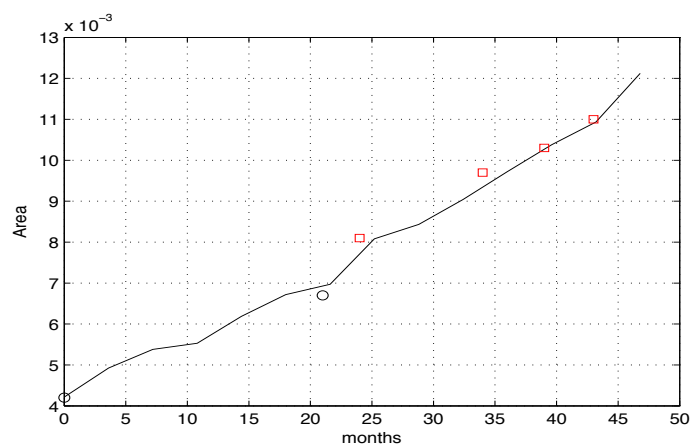


Figure 2.3: Area as function of time for the slow rate growth. Solid line represents the simulation results, black circles are the data used for the identification, red squares the predictions.

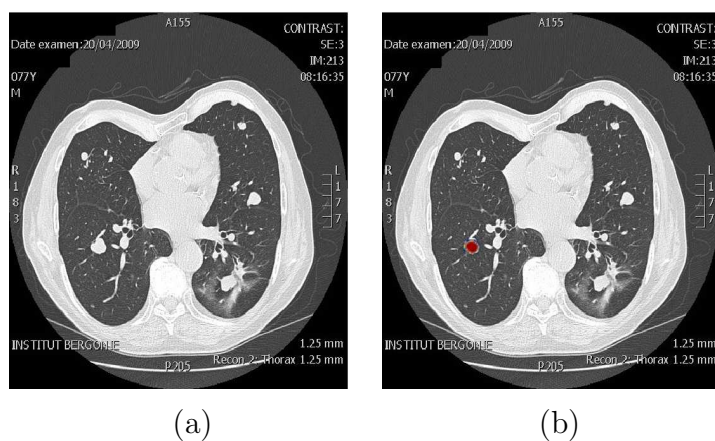


Figure 2.4: a) Fourth scan b) Simulation

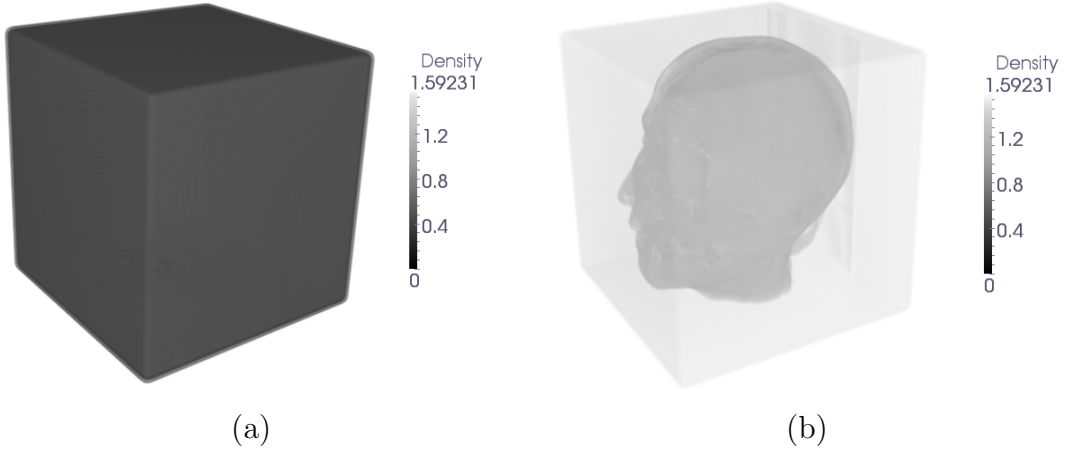


Figure 2.5: Density distribution at time a) $T=0$, b) $T=1$.

images. These problems were treated by means of standard techniques in this work but they pushed us to consider non-linear registration processes for biological tissues.

We investigated numerical aspects of the integration of the L^2 optimal transport problem, aiming at understanding if it may be used as a geometrical tool for inverse problem or as an estimator of several quantities. This problem consists in finding the minimal energy mapping between two given density distributions. A study was carried out which is relatively independent from that of inverse problems for tumor growth and it is presented in the last part of this work.

The equations governing the transport are defined through a variational principle:

$$X(\xi) = \arg \min_{\tilde{X}} \left\{ \int_{\Omega_0} \rho_0(\xi) |\tilde{X}(\xi) - \xi|^p d\xi \right\}, \quad (2.22)$$

subject to the constraint:

$$\rho_0(\xi) = \rho_T(X(\xi)) \det(\nabla_{\xi} X), \quad (2.23)$$

where X is the unknown mapping, ρ_0 and ρ_T are the initial and the final density distribution respectively. A 3D result is shown hereafter, which is the mapping between a uniform cube (*i.e.* $\rho_0 = 1$ over a cubic domain) and the density which corresponds to the normalized image of the MRI of a human head. In Fig.2.5 the initial and the final density are represented. In Fig.2.6 slices of the result of the mapping (taken parallel to coordinate planes) are shown to highlight the complexity of the geometrical configuration recovered.

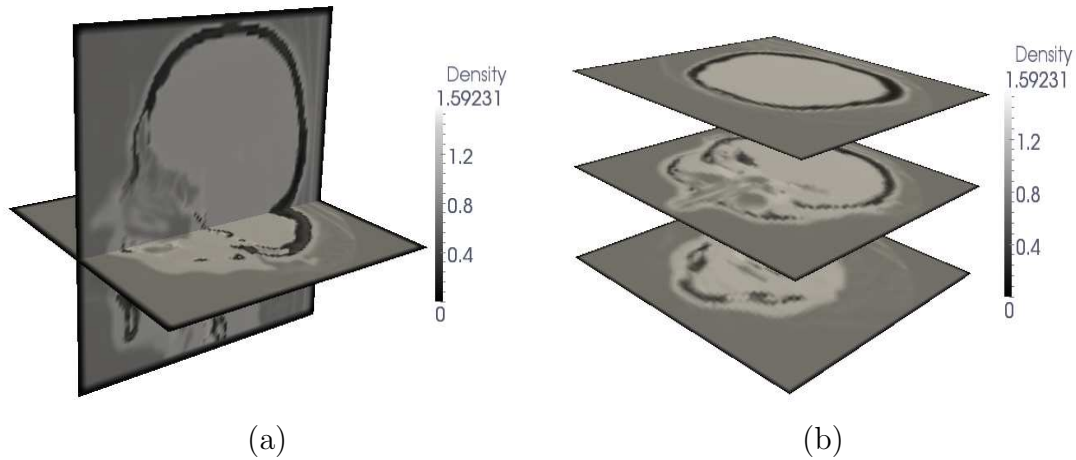


Figure 2.6: Slices of the final density distribution: a) XZ plane b) Z planes.

2.4 Structure of the present work

The structure of the present work is as follows. It may be divided into two parts, which are relatively independent: the first one deals with inverse problems while the second one treats the numerics of the L^2 Monge-Kantorovich problem.

Tumor growth modeling and applications In this chapter the state of the art of tumor growth modeling is presented aiming at defining the context in which the present work was developed. In particular, the phenomenological nature of the models is underlined. In an historical perspective, models based on ordinary differential equations (ODEs in the following) are described, which were the first ones to be set up. The general principles of the ODE modeling are commented and some examples are provided. Tumor growth is highly influenced by spacial properties of tissues: a mere integral quantities description is not satisfactory. This motivated the study of space models based on partial differential equations (PDEs). They may be thought as divided into two classes: the discrete and the continuous models. Their main features as well as their advantages and drawbacks are discussed, motivating the choice of using continuous models for the present work. To complete the review of the models the hybrid class is described, that tries to combine the advantages of the two and represents a front of research in tumor growth modeling.

In the second part of the chapter the works concerning realistic applications of the models are described. The first applications adopt ODEs based models. Several appli-

cations ranging from inverse problems to population and therapy control are discussed. Few works are devoted on applications involving PDEs models. These works will be commented in greater detail focusing in particular on those ones proposing an image driven framework.

Models and computational framework adopted In this chapter the models which were adopted for all the computations carried out in this work are presented. A first model, which is the reference one for this work, is a two species Darcy-type model. It is a continuous model resulting from a simplification of more complex models presented in the literature. All the hypothesis made are commented and justified. Then, a regularized version is introduced to satisfy in a better way some inverse problems needs. Another model presented in the literature is commented, which may be considered a simplification of the Darcy model presented.

After this description of the models, a synthetic overview on the integration method of the direct system is outlined, concentrating on the distinctive features of the numerical methods implemented. An example of direct computation and a preliminary analysis of the simulation results with respect to the parameters value is provided.

The chapter ends with a synthetic comment and description on the preprocessing operations which are necessary in order to use realistic medical images as data. In particular two operations have to be performed: segmentation and registration.

Sensitivity technique In this chapter some results concerning a sensitivity approach are detailed. First, ODE models are analyzed by means of an exact sensitivity procedure. A model inspired by the continuous Darcy model is proposed, validated and compared to a widely used existing model. Some critical points concerning the use of ODE models are discussed and supported by some examples.

Then, the results obtained with PDEs are discussed, both varying the model and the control set. The main part consists in the study of the regularized Darcy model. After having validated the procedure by means of a synthetic experiment, a realistic case is studied concerning lung metastases. The initial condition is parametrized in order to reproduce a layer structure of the tumor, which is a well accepted biological hypothesis. A comparison of the performances of ODEs and PDEs based approaches is detailed.

Reduced order approach The cost reduction is mandatory when dealing with these kind of problems. A residual based strategy is proposed aiming at considering the resid-

ual of the equations at discrete times instead of integrating the PDEs system. Several preliminary tests show that the problem become underdetermined, thus requiring a regularization. The latter is sought by means of a Proper Orthogonal Decomposition (POD in the following) approach. The elements of the procedure are discussed and the approach is validated by means of artificial tests.

Then, the performance of such an approach is compared to the one of the sensitivity approach when the two works in exactly the same conditions. A realistic clinical case is considered for this study.

In the end of the chapter some results concerning several realistic applications are presented. The advantages and the limitations of the proposed technique are highlighted and some conclusion is presented.

Optimal Transport The second part of the work consists in the numerics about the Monge-Kantorovich L^2 mass transfer problem. A brief introduction accounts for the main theoretical contributions on the subject focusing on the properties which are helpful when a numerical integration is sought.

Then, a review of the existing methods is provided and their computational cost is discussed. Using the properties of the characteristics of the Hamilton-Jacobi equation resulting from the minimization of the functional that defines the problem, a lagrangian family of numerical methods is derived. A particle based method is proposed in order to integrate it.

A validation stage is performed through synthetic testcases, in which several critical phenomena like fragmentation and coalescence are studied. The applications on non-rigid registration of biological tissues are described and discussed for both 2D and 3D cases.

The tests performed highlighted some difficulties and superlinearity appearing in the computational costs of the methods: a preliminary investigation on a multilevel acceleration is detailed, aiming at overcoming these problems.

The chapter ends with a perspective concerning the use of Wasserstein distance for model reduction. The aim is to exploit the remarkable property that Wasserstein distance naturally implies a transport. This feature may overcome some problems pertinent to POD and global modes principal component analysis when trying to describe the advection of concentrated coherent structures.

Chapter 3

Tumor growth modeling and applications

3.1 Cancer biological nature and development

Cancer has a particularly complex, not yet understood nature. Its origin is mainly due to the effect of genetic mutations, giving a certain cellular phenotype an advantage from a micro-evolutionary standpoint (see [5]). Cancer cells are mainly featured by two properties: the ability to reproduce without control and to colonize tissues which are normally occupied by other kind of cells. A tumor (*i.e.* a group of proliferative abnormal cells) become a cancer only if it is malignant.

The so called *monoclonal* hypothesis is well accepted in the medical community: cancer starts from the mutation of a single cell ([15] for a detailed overview). Throughout the life of an individual, billions of mutations occur: they are not dangerous as long as they do not allow a group of cells to disrupt the equilibrium of the population and multiply in an uncontrolled manner. Mutations can be induced by several factors: chemical, environmental or even by viruses and, except for the *teratocarcinoma*, their origin is not epigenetic, that is, they are not caused by the wrong order of transcriptions of genes ([5]). Studies of preneoplastic cells suggest that cancer develops through a continuous process of mutation and selection. The mechanism that allows a phenotype to survive and to increase the number of its individuals is called proliferation.

Natural human cells have a proliferative capacity that is much higher than what is normally required to preserve tissues; in a healthy population the proliferation is controlled and limited ([15]). The lack of these control mechanisms, exerted during the cell cycle, and a combination of other factors, cause cancer.

A single cell life (represented in Fig.3.1) is characterized by a cycle (see [5, 15]), in which four distinct phases take place, two of them are called functional (S, M) and the others preparatory (G1,G2):

- G1: it has a variable length (ranging from 6 hours to several days); the cells prepare the material for the S phase. The variability of the cell cycle time is mainly due to the variability of this phase. At the end, an important check point takes place: if the micro-environmental conditions are favorable to proliferate, the cell starts the S phase, otherwise it enters a state called G0, or *quiescence*, in which it can remain until the conditions are favorable. The transition from G0 to G1 and then S is regulated by two other check points: the competence and restriction ones (R). In tumor cells, this mechanism is altered in a significant way.
- S: it is the phase of duplication of the genetic material, and its duration is about 8 hours in human body. The DNA duplication occurs with a precise and controlled

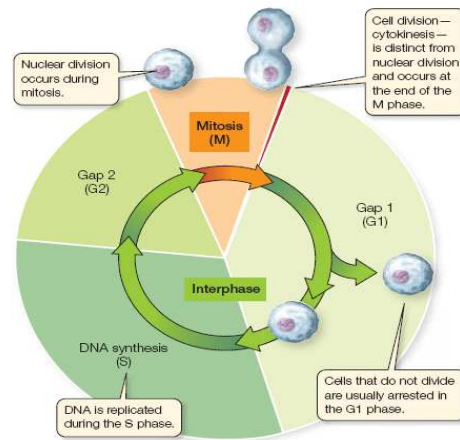


Figure 3.1: Phases of the cell cycle; from www.nature.com

time schedule (see [5]).

- G2: cells increase their size to prepare to mitosis process. In this phase there is another important check point; the cell can undergo to mitosis if the DNA duplication is successfully completed and if the cell size is sufficient.
- M: it is the mitosis, and it can be divided into 5 sub-phases (prophase, prometaphase, metaphase, anaphase, telophase), it starts with the formation of the mitotic spindle, the subsequent division of the nucleus and it ends with the cytokinesis, that is, the division of the cytoplasm. At the end two daughter cells are created.

The cell cycle is governed by biochemical groups called cyclins: they regulate and promote different phases of the cycle ([15]). In order to guarantee that the cycle is correctly performed, some molecules exert a control function, preventing the transition from a phase to the subsequent one if not all the necessary tasks have been completed.

Sometimes errors occur in the genes transcription, leading to mutations. Let us briefly describes which elements modified by mutations can transform a normal phenotype into a malignant one.

Errors in the genes that regulate proliferation alter frequently the first stages of the cycle, in particular the transition between the phase G1 and the phase S ([5]). This results in an augmented capacity to proliferate: cells become able to avoid quiescence even if micro-environmental conditions are not favorable. Moreover, growth and proliferation are promoted or inhibited by several growth factors, which are molecules (proteins, aminoacids, nucleotides) that combine with membrane receptors to translate a signal from

the cell neighborhood. Frequently, in cancers, the chain that allow a signal to be received and actuated by a cell is compromised. Different pathologies can be associated to different errors in genes transcription and in the transduction chain.

Another important element in understanding cancer causes is the alteration of the *apoptosis* (see [135] for a detailed description of this mechanism), which is the programmed death of the cell. In particular, mutations activate anti-apoptotic genes or suppress the expression of pro-apoptotic genes, resulting in an augmented cellular survival. Two features are peculiar of tumor pathologies: genetic instability and incapacity to undergo to apoptosis when DNA errors occur ([5] for an overview), even if they are detected by proteins devoted to the control of the DNA replication.

Cancer does not derive merely on the frequency of division of cells. Indeed, a major role is played in many cancers by cell differentiation mechanism ([15]). In normal healthy tissues a group of factors regulate the equilibrium between proliferation and differentiation, in such a way that tissues are repaired and maintained. A disfunction of the transcription factors prevent cells to be differentiated. All cancers involving stem cells (as skin cancers, leukemias, carcinomas of uterine cervix) are characterized by an excess of immature, non-differentiated cells, that proliferate continuously, leading to a neoplastic mass.

Mutations that allow the mutation rate to increase affect the rate of propagation and the nature of the disease ([5]). As a matter of fact, they are related to the machinery controlling DNA replication and repairing, thus, being transmitted to their heritage, they cause a great instability in the kariotype. This phenomenon is widely used in tumor diagnosis and analysis. It is also related to therapy strategies to be adopted. Especially in chemotherapy, drugs are used that are able to kill proliferative cells, but rarely they succeed in kill all the malignant cells. Since cell population evolves rapidly through continuous process of mutations and selections, some cells develop a resistance to the drug used and to other drugs (multidrug resistance) of the same kind.

3.1.1 Phases of tumor invasion

Tumor growth have an enormous intra and inter individual variability, so that it is difficult to state a unique universal phenomenology. However, for solid tumors, three phases can be identified, characterizing the evolution of the pathology.

The first one is the avascular growth ([5, 15, 71]). In the first stage tumor starts proliferating consuming the nutrients which are nearby (see Fig.3.1.1). The size of the tumor in this phase normally does not exceed $1mm$ and its activity is limited by the

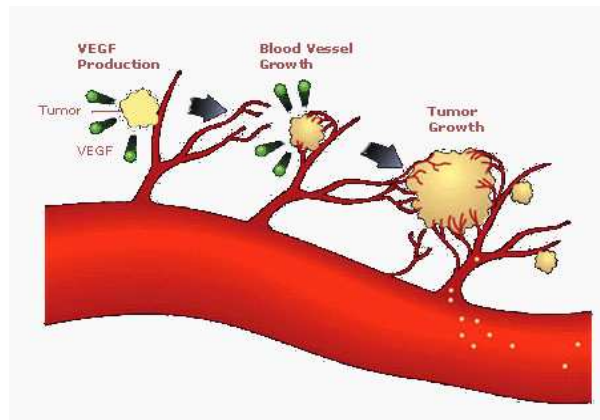


Figure 3.2: Evolution of tumor, from left to right: avascular stage, angiogenesis, tumor invasion; from www.gene.com

quantity of available nutrients. It may happen that carcinomas which are not able to recruit nutrients remain dormant and do not cause disease in the patient, since they are rarely metastatic; most of them are not diagnosed during the patient life (see [71]). This does not mean that in avascular tumor cells proliferate at a slow rate, but that a critical size is reached. The core of the tumor cannot receive a proper nutrient uptake, thus a certain number of cells undergo to apoptosis. When cell proliferation is balanced by apoptosis, the growth become quasi-steady. The differences between the size reached in the avascular stage is determined by the ability to survive to different degrees of hypoxia. For instance, the average diffusion length of oxygen in tissues is about $100\mu m$ ($85\mu m$ for a typical human melanoma, $110\mu m$ for prostate carcinoma): at a greater distance from a blood vessel, cells become hypoxic and then apoptotic (see [71]). In tumors in which particular mutations occur some cells can survive even if they are at a greater distance, but the latter actually do not exceed $200\mu m$.

Normal cells that mutate (hence becoming neoplastic) are not automatically angiogenic, that is, they are not able to induce the production of new blood vessels to bring their own nutrients. To do so, other mutations have to occur and cells have to switch to angiogenic type. In [71] a review of studies on angiogenesis is outlined. When cells become angiogenic they increase the expression of proteins such as VEGF (Vascular Endothelial Growth Factor) and bFGF (basic Fibroblast Growth Factor). Furthermore the tumor is able to decrease angiogenesis inhibitors and to induce stromal cells to express proteins which help angiogenesis. Moreover, a recruitment of bone-marrow happen. In this way tumor manage to attract endothelial cells of the host and start building its own

vascular network (capillary sprout), after having corrupted the basal membrane that normally surrounds it and separates it from the capillary vessels. Therapeutical strategies have been set up in order to inhibit the angiogenesis process and prevent the tumor to receive a constant nutrient uptake and potentially reach every other part of the body.

When tumor has reached a certain size, it starts invading tissues ([99]). This process is called metastasis and it is the terminal phase of the evolution of the pathology, often catastrophic. Angiogenesis is a fundamental precursor of this phase, since tumor needs blood vessels in order to be connected to the rest of the body. The processes of invasion and metastasis kill the host by locally invading the tissue and by colonizing distant organs. Tumors prevent the organs to work properly by attacking or compressing them. The pathology cannot be treated locally anymore. The metastatic process is complex and involves multiple tumor-host interactions (see [99] for a detailed description). Again, the natural selection of subpopulations plays a fundamental role: metastasis process is highly selective, only 0.01% of cells that enter the vascular or lymphatic tree give rise to a metastasis focus. The distribution of metastases is not deterministic, but frequently cells colonize the first capillary or lymphatic bed they encounter while circulating. This explain why the most probable locations for metastases are liver and lungs. Several hypothesis were proposed on the mechanism of selection of the organ to be attacked by a tumor: metastases uniformly span the organs of the human body but they grow preferentially on certain organs, or, maybe, they are selectively attracted by certain organs.

From this global albeit synthetic picture the multiscale nature of cancer can be inferred. In this idealized conceptual framework, three scales may be distinguished:

- *microscopic*: it is the intracellular level, where mutations and regulatory network take place. Carcinogenesis is mainly related to this scale.
- *mesoscopic*: it is the intercellular level, where biochemical signals are exchanged by cells and the extracellular matrix. At this scale population dynamics arise.
- *macroscopic*: it is the tissue level, where mechanical interactions occur as well as nutrient macroscopic transport and invasion.

3.1.2 Classification of tumors

A large number of type of cancer exists; a common classification is performed according to the tissue attacked and the kind of cells that become proliferating. Other names are given according to the region of the body affected and also for historical reasons. As

previously stated, tumor is called a cancer only if it is malignant (*i.e.* if it is able to spread and invade the organs, preventing them to accomplish their normal functions); for each malignant tumor denomination corresponds its counter benign one (in [5] examples are found).

Cancer that derives from *epithelial* cells (the cells composing the membranous tissue covering all the cavities of the body as well as many glands) is called *carcinoma*. It is the most common kind of cancer, about 90% of cancers are carcinomas; it is probably due to the number of epithelial cells and their localization in region sensitive to proliferation.

Tumors attacking connective tissue (fibrous tissue composing for instance tendons, bones, cartilage) or muscles are called *sarcomas*.

Hemopoietic cells (*i.e.* the ones composing blood) are linked to a cancer called *leukemia*, which is not a solid tumor, but a cell suspension.

Cancers, such as *gliomas*, attack the nervous tissues, which are different from all the other tissues.

Other kind of classifications are used by medical doctors. One concerns the progression of the pathology: the stage, a number ranging from 1 to 4. When a pathology is at the very beginning it is labelled by 1, a terminal one by 4. The aggressiveness of tumor is denoted by another parameter, which is the grade. An elevated grade means that cancerous cells are very active in attacking healthy tissues and colonize them.

3.2 Modeling tumor growth

Tumor growth and development has an intrinsic multiscale nature. According to its complexity a wide variety of models were proposed in the literature.

Mathematical modeling gives a valuable contribution in understanding quantitatively such a complex biological system (see [17, 40, 72] for reviews). Reaching biological insight allows to target novel experiments, validating hypothesis and trying to set up tools for realistic clinical applications.

Since the phenomenon is very difficult to be represented as a whole, several approaches were developed, concentrating on different aspects or phases of the growth. In [141, 60, 160] the avascular stage is considered while [6, 13, 23, 155, 33, 47, 94, 103] were devoted to the description of the angiogenesis process, and the vasculogenesis in general. An overview of the different phases and related mathematical models is provided in the work of Chaplain (see [44]).

Moreover, cancer shows a broad variety of behaviors, depending on the organ attacked,

the age of the patient and several environmental factors. At present it is not possible to set up a model describing all the kind of cancers at once. In general, some phenomenological guidelines are used to build models adapted to a specific kind of propagation. For example [151, 96] treat brain tumors, in [20, 154] a model for the description of tumor cords is developed, [159] deal with lung tumors, in [78] breast cancer is taken into account.

In this section a brief review is outlined aiming at presenting the state of the art of tumor growth modeling. First, the ODEs (*Ordinary Differential Equations*) models are presented. Second, models taking the space evolution into account by means of PDEs (*Partial Differential Equations*) are described according to a conceptual classification: discrete single cell-based models are presented followed by continuous type models. Finally hybrid models are detailed.

3.2.1 ODE models

Gompertz proposed a model for human mortality in 1825, [83]. It was intended to describe the incidence of accidental causes of death in a human population. The Gompertz model is used to describe population dynamics and it assumes that the rate of growth is proportional to the logarithm of the inverse of the size of the population itself, that is:

$$\dot{n}(t) = \alpha \log \left(\frac{K}{n(t)} \right) n(t). \quad (3.1)$$

This model is suitable to describe the global behavior of a population when a limited quantity of nutrients is available (see for instance the work of Brunton [38]). K , called carrying capacity, represents the asymptotic population size for a given nutrient uptake. This model is successfully used to fit tumor dynamics in simple experiments. In order to take more complex effects and dynamics into account several models were proposed; a review and a general framework is proposed by d'Onofrio in [57]. The most basic models arising in the description of populations are the exponential and the logistic ones; in general, competition phenomena between subpopulation are modeled through Lotka-Volterra systems of equations.

ODE models used to describe tumor growth aim at describing integral properties characterizing the tissue evolution: in all these models two elements are fundamental: the total size of the population (expressed as number of individuals or volume or weight), and the nutrient dynamics. In the following two models are detailed.

In the paper of Simeoni ([109]) a simple model is proposed to fit experiments, in the case of chemotherapy treatment. In particular a three parameters model is used to

described the non treated tumor dynamics, while two additional parameters are added to take the therapy into account. A first exponential phase is followed by a linear phase. This dynamics actually mimics the first two stages of a Gompertzian growth. The authors set up a regularization, such that the right hand side of the population dynamics equation is a differentiable function. The state variable is the tumor weight (w) and the model (without treatment) reads:

$$\dot{w} = \frac{\lambda_0 w}{\left[1 + \left(\frac{\lambda_0}{\lambda_1} w\right)^\psi\right]^{1/\psi}}. \quad (3.2)$$

For large values of the parameter ψ exhibits the growth described above. λ_0 and λ_1 represents the exponential and the linear growth rate respectively, their ratio being the switching point between the two regimes. In order to take therapy effect into account a subpopulation model is proposed and interpreted as a perturbation of the base one, adding terms corresponding to the effect of the drug on the subpopulation.

The coupling between nutrients uptake and population dynamics is detailed in the works of Hahnfeldt (see for instance [144, 86]). The starting point is the Gompertz model for the tumor volume, but instead of considering the carrying capacity as a constant parameter, an equation is provided, linking the capacity to the vasculature and to the size of the tumor itself:

$$\dot{V}(t) = \alpha \log\left(\frac{K}{V(t)}\right) V(t), \quad (3.3)$$

$$\dot{K} = -\lambda K + bV - dKV^{2/3} - eKg(t), \quad (3.4)$$

where the equation for K is obtained assuming spherical symmetry for the tumor and a reaction diffusion for the vasculature. In particular the term $V^{2/3}$ is used to described effects involving diffusion through the tumor surface. The term $g(t)$ is the effect of an antiangiogenic treatment ad it is modeled using PK-PD assumptions. In [144] the resulting model has 4 parameters and it is used to study the effects of antiangiogenic drugs from a quantitative standpoint, comparing the results with data of the tumor volume.

Several other models were proposed in the literature, based on the same principles. Aside for some study, properly detailed later on, ODE models are the only kind of models currently used in clinical applications: this is mainly due to their simplicity and their low computational cost, allowing to set up control and sensitivity problems at a reasonable cost.

Nevertheless, tumor growth is a phenomenon in which space effects cannot be neglected and play an important role. The tissue evolution in terms of morphogenesis and pattern formation (see [7, 55, 62, 56, 73, 120]) can not be described by integral quantities.

3.2.2 Discrete models

In discrete models (see [14, 75] for a review), cells are followed individually in their evolution: so one cell corresponds to one computational element. Discrete models are adequate to describe microscopic and mesoscopic scale phenomena such as carcinogenesis, in [128], competition and mutations effects. All these phenomena, fundamental in cancer development, are characterized by properties varying spatially on a scale comparable to the cell size. They become computationally unfeasible when treating complex *in vivo* systems, for which the number of cells may attain 10^{11} , and for which there is often no interest in following the path of a single cell.

Two kind of models were developed: the cellular automata models (see [4, 60, 119]), called lattice-based models and the agent models ([111]), usually referred as lattice-free models. A detailed review of these families and a comparison to continuous models is provided by [42, 13].

In cellular automata models cells are arranged on a lattice, in such a way that in each node there is at most one cell (or in certain cases group of cells, [96]). Different regular topologies can be implemented (see the book of Deutsch [56] for a general treatment) corresponding to different geometrical arrangements of interactions; in [96] cell locations are chosen randomly and Voronoi tessellation is applied to build the lattice.

At each node a number of states is associated: the state vector includes the cell position, its velocity and a set of biological variables, supposed to be significant for the evolution. The behavior of each cell is governed by local transition rules (modeling biochemical and mechanical processes), whose nature may be either deterministic or probabilistic. These rules determine the state of a cell as function of a certain set of neighborhood. A simple classical example (see the review of Roose [141]) consist in assigning three probabilities k_1, k_2, k_3 for the following events to occur: proliferation, quiescence (triggered by environmental conditions), or movement.

Examples and applications of a Lattice Gas Cellular Automaton (LGCA) model for the description of patterns arising in cellular systems are provided in [56]. In LGCA methods a variable cell density is accounted for, since more cells are allowed to occupy the same node. In each node a set of movement channels is defined (including the rest state), representing the possible momentum vectors of the cells. A sort of exclusion principle is proposed: cells may have the same position but not, at the same time, the same channel.

When cells divide, as consequence of a mitosis process, the daughter cell is placed in a free lattice point near the mother cell. This is in some sort artificial and unrealistic; as a matter of fact the geometrical constraints induced by the lattice oblige to introduce

some extra rule in the case that no place is available for the daughter cell. This is a weak point of cellular automata description (see [141]). Furthermore, some numerical artifacts may arise accordingly to the chosen topology, leading to unrealistic patterns. In spite of their schematic nature, they have been used in a wide variety of applications (see [110, 96]), because of their simplicity and ability to capture microscopic events or to represent molecular pathways.

More complicated from a mathematical and computational stand point, the agent based methods (see [111, 61, 163, 164]) are lattice-free. Cells are not constrained in fixed locations but they move in the space, according to mechanical laws. They are often described by rigid or elastic spheroids (see the work of Drasdo [60]). Mechanical cell-to-cell interactions are described by central potentials (see [42]), in such a way that both attraction and repulsion behaviors are represented. The mitosis is rendered in a more realistic manner and it occurs with a given rhythm. Several studies were performed, including the random cell movement (when a single cell is in liquid suspension it exhibits Brownian motion) and chemotactic effects ([62, 63]).

The behavior of the resulting growth is analyzed theoretically by statistical mechanics (For example through Langevin equations,[60]) and solved by means of Monte Carlo techniques. The models are able to reproduce accurately *in vitro* experiments like spheroids and monolayer growths. Drasdo (see [59]) proposed a coarse graining approach too. The main idea is to consider containers in which a maximum number of cells can enter (like in a packing problem). Equations are written through a path integral formulation; this approach is suitable for sparse phenotypes, but it does not describe well compact tumors.

Other approaches based on statistical mechanics are analyzed by Bellomo in [28]. In particular Boltzmann formulations are detailed; this is an interesting framework since mean field equations can be written, although cells behaves in a really different ways with respect to gas molecules, for what concerns collisions and reciprocal interactions.

A detailed approach were proposed by Rejniak in [137], for which cells are no longer modeled as simple elastic spheroids, but as continuous vesicles, separated one each other by elastic membranes. The cellular evolution is computed through an immersed boundary method and cell-to-cell interactions are imposed by means of potentials.

The agent models are expensive from a computational standpoint. Methods to reduce their cost were presented in [61], in which some rules are set up, governing a cellular automata model in such a way that it mimics accurately a reference agent based model. A key point, as outlined in [42], consists in translating the properties of agent based systems in continuous models, in order to apply their physical insight at a larger scale. However,

this task is hard from a theoretical standpoint and it is feasible in a limited number of cases; works in this sense can be found in [125, 88]. This inspired the development of a novel class of hybrid models, detailed in the end of this section.

3.2.3 Continuous models

In continuous type models the evolution of cell populations is described in terms of cellular density (*i.e.* number of cells per unit volume). These models were developed to represent tissue evolution at a macroscopic level. An exhaustive review is provided in [104].

Several models were proposed in the literature, ranging from reaction-diffusion models (which were the first spacial models to be developed, see [2, 45, 54, 79, 84, 148]), interface models ([98, 106, 107, 65]), mixture models (see, for a detailed overview [8, 18, 43, 51, 91, 133, 140, 33]).

In this section a general framework is presented, detailing the building blocks of continuous models and pointing out common features and differences between the approaches proposed in the literature.

The population dynamics of different cellular species is described through the continuity equations. Given a certain number of cellular phenotypes, their volumic densities being ϕ_i , and assuming that the specific mass for the i -th phenotype is constant in time, the mass conservation equation is:

$$\partial_t \phi_i + \nabla \cdot (J_i) = B_i - D_i + T_i, \quad (3.5)$$

where J_i is the flux function for the i -th phenotype, and B_i, D_i, T_i its birth, death and transition rates respectively. In all the models this equation states simply that in a given volume, the variation of the cell number of the i -th phenotype is due to a flux across the boundary of the volume itself or to some interaction or source terms (right hand side). In the work of Preziosi (see [131]) the Lagrangian mass conservation equation is derived, highlighting the contribution of the growth process in the tissue kinematics. Let us point out that in some continuous models (see [139, 140, 1, 64]) the cellular cycle is taken into account; a new independent extra variable, the age, is introduced, representing the time between two subsequent mitosis processes. These models are referred as age-structured models. In the following non-structured models are detailed, since they will be used for the present work.

In order to specify a model the nature of cells movement (*i.e.* J_i) has to be fixed, as well as the population dynamics; the latter consists in the relationships between one phenotype and the others and between one phenotype and the environment.

If J_i is directly linked to the volumic densities, the following law can be written:

$$J_i = -D^{(i)}\nabla\phi_i + \sum_k^{N_p} V_{ik}\phi_k, \quad (3.6)$$

where $D^{(i)}$ is the diffusivity tensor and V_{ik} the interaction matrix, and the model becomes a reaction diffusion model, as in [148, 54, 84]. Other laws give rise to non-linear diffusion models, as in [45, 79].

If, otherwise, the motion is rendered through a transport:

$$J_i = \mathbf{v}_i\phi_i, \quad (3.7)$$

where the vector field \mathbf{v}_i represents the velocity of the i -th phenotype. If the passive motion assumption, also called the constrained mixture assumption (see [140, 8]) is assumed, a unique vector field exists, such that it makes the tissue evolve ($\mathbf{v}_i = \mathbf{v}, \forall i$).

For the models characterized by transport phenomena, the mechanical nature of the velocity has to be investigated. The first hypothesis allowing to state a constraint on velocity is the saturation of the mixture, that is, in a given unitary volume, the sum of the volumic densities is unitary, *i.e.* :

$$\sum_i^{N_p} \phi_i = 1 \implies \nabla \cdot \mathbf{v} = \sum_i^{N_p} B_i - D_i + T_i \quad (3.8)$$

Since the sum of the transitions is zero, this law for the divergence simply states that the cellular process of mitosis acts as a volume source in the tissue, while the death is rendered by a volume sink. This is reasonable since when a mother cell divides duplicating its material, the two daughter cells occupy a greater volume, pushing the surrounding cells.

A law for the divergence is not sufficient to uniquely determine the velocity; at least a relation for the curl has to be fixed. In order to mechanically close the system several laws were proposed in the literature (see the review by Ambrosi [8] for a detailed derivation).

In general, momentum conservation for a continuum reads:

$$\partial_t(\phi_i\mathbf{v}) + \nabla \cdot (\phi_i\mathbf{v} \otimes \mathbf{v}) = \nabla \cdot \sigma_i + \phi_i\mathbf{b}_i, \quad (3.9)$$

where σ_i is the stress tensor for the i -th phenotype and \mathbf{b}_i is the body force acting on it. Constitutive equations must be added to this system in order to specify the mechanical nature of the tissue. Several hypothesis can be done: linear poroelastic models are developed in [142] to describe internal stress, anisotropic tissues are described in [48, 46], a viscoelastic behavior is detailed in [105, 132, 9, 139].

The tissue is often supposed to be in quasi-steady conditions (see [132]), so that the mechanics reduces to:

$$\nabla \cdot \sigma_i = 0, \quad (3.10)$$

which leads to a sort of viscoelastic Stokes dynamics.

Another simplification is derived under the assumption that the tissue behaves as a flow in a porous medium. In this case the momentum equation reduces to the Darcy law (see [8, 104]):

$$\mathbf{v} = -k\nabla\Pi, \quad (3.11)$$

where k is the permeability tensor and Π is the pressure, usually identified as the interstitial pressure, that represents a potential for the velocity. Adequate boundary conditions have to be set, according to the organ nature.

Another constitutive law is proposed by Cristini in [51], in which a thermodynamic argument is used to derive a Cahn-Hilliard system of equations for a mixture model. In this work a general framework is proposed and a study of non-linear instabilities is carried out in the case of a two phase mixture (namely the tumor tissue and water).

If phases ϕ_i are not diffused but they belong to subdomains, interface models are derived. In particular, conditions for the pressure Π are imposed on the tumor boundary and related to the interface curvature, see for instance [104, 107, 108, 74]. These models lead to non-linear instabilities and branching. Nevertheless in *in vivo* systems an identification of a tumor boundary can be difficult or even a impossible for some kind of cancer (especially for those of invasive nature).

In [133, 49] extra cellular matrix is taken into account for the dynamical description of the tissue.

Once the tissue mechanics is described, another element is fundamental to close the system and link the environmental conditions to the population dynamics: nutrients equations. Nutrients are potentially all the biochemical substances that determines, alter or regulate tumor growth. In [39] the effects of time delays on a nutrient-limited spheroid growth is described, while other works describe the effect of spatially distribution of nutrients on tumor shape (see the review by Lowengrub [104]).

The network of chemical signals interacting with a cell population is exceedingly complex. Classically for the sake of simplicity only few species are considered. Oxygen, glucose and H^+ ions are the most significant ones to be considered in continuous models.

Oxygen and glucose are responsible for the energetic path of the cells, its undergoing to hypoxia and so on, while H^+ concentration denotes the acidosis effects on the tissue, see [141]. In particular experiments have revealed that tumor is surrounded by a gradient

of acidity, influencing its capacity to attack the healthy tissue. Nutrients dynamics is usually rendered through reaction diffusion equations. Let c_k be the concentration of the k – *th* species in the tissue, its dynamics is governed by:

$$\partial_t c_k - \nabla \cdot (D_k(\phi_i) \nabla c_k) = C(\phi_i, c_k) + S(\phi_i, c_k), \quad (3.12)$$

where D_k is the diffusivity tensor that depends on the phase considered or on some morphological feature of the tissue (see for instance [148] for the motility and diffusivity estimation in grey and white matter in the brain), C is the consumption rate and S is a source term. Boundary conditions are imposed following some phenomenological consideration on the system.

When angiogenesis process is described (see [33, 13, 41, 47, 114]) factors promoting the vessels formation (like VEGF, as described in previous section), have to be taken into account. A lot of efforts are devoted to the description of this complex phenomenon, since it often represents the point after which tumor may reveal its malignancy, accelerating the invasion. The models proposed ranges from totally continuous models to hybrid discrete-stochastic models for vessel formation (see the work of Anderson[13] for a review).

Nutrients dynamics has to be linked to the population dynamics and in particular to mitosis (see [44]). The most simple non-linear relation providing such a feedback is the heviside function, representing a threshold:

$$B_i(\phi_j) = \nu_i H(c_k - \bar{c}_k), \quad (3.13)$$

where B_i is the mitosis rate and ν_i is the inverse of the mitosis time scale for the i – *th* phenotype, \bar{c}_k is the threshold; the relation states simply that if there is a sufficient nutrient uptake cells can proliferate, otherwise some transition to quiescence or apoptosis is going to happen.

Therapeutical effects may also be included (see [146, 139]); for systemic treatments, like chemotherapy, one or more nutrient equations have to be added and consequent effects on cell population investigated.

3.2.4 Hybrid models

Hybrid models try to combine the advantages of continuous and discrete models, see [12]. The aim is to take the intrinsic multiscale nature of tumor growth into account in a unique theoretical framework, describing phenomena occurring at very different space and time scales. As already mentioned, Othmer [125] derived continuous equations from

microscopic systems describing chemotaxis in bacteria. In the same spirit, but trying to avoid theoretical problems arising in different systems, in [34] a method is proposed such that macroscopic variables can be integrated as function of microscopic states even if their governing equations are not known *a priori* or they are difficult to be derived.

Two kind of hybrid models were proposed in the literature. The first one describes continuous fields evolution for some element of the model, such as nutrients and ECM, and discrete fields for the cells (see the work of Gerlee [81]). The cost of this kind of methods is often as high as that of discrete methods.

Other approaches were developed, trying to combine the two classes of methods in such a way that the cost is reduced, but microscopic behavior is taken into account in regions where it is more relevant. This is the key idea of the method proposed by Kim in [100]. In particular, only proliferating cells are represented at discrete levels, while quiescent and necrotic cells are represented continuously, as a mixture, as well as ECM and nutrients. The discrete method proposed is an agent lattice free method, cells are rendered as ellipsoids, they exchange forces such as contacts and drag due to adhesion. Forces exerted by cells on ECM are computed through an interpolation method. Stresses in the continuous media are modeled assuming a linear viscoelastic behavior. If quiescent cells start proliferating, a least square projection is performed and a consequent number of discrete individual created. When applied to a spheroid in avascular stage, this method allow to significantly decrease the computational cost (approximately by a factor 10).

Another kind of method, proposed by Bearer in [27] uses both continuous and discrete approaches to describe cell population evolution. In particular the two representations are used for all the phenotypes of the tumor. For the discrete cells an agent based method is defined. Cells are represented as zero dimensional entities, but the occupied volume is taken into account through a non-superposition constraint; chemotaxis, haptotaxis and forces are implemented in a classic way. Discrete cells and continuous phase exchange mass continuously: in particular when a region is hypoxic discrete cells are created and followed individually; their motion is mainly influenced by nutrients gradients. When a density threshold is exceeded discrete cells are reconverted to the continuous phase.

3.3 Toward realistic applications

Some works in the literature explored the possibility to use models to go toward realistic applications. A perspective is outlined in [134]. In this section a detailed review of these works is provided aiming at defining the context in which the present work is developed.

An important step in validating models is the comparison with experimental data. A first example in this sense is found in the work of Adam (see for instance [3]). A model describing the growth of a spheroid is calibrated via an algebraic inverse problem involving one parameter in order to fit experimental results concerning in particular the concentration of GIF (growth inhibitor factor) in spheroids. The same set of data were used to validate the non-linear diffusion model presented by Chaplain in [45]. In [79, 80] the effects of microenvironment and acidosis are studied and compared with some experiments, revealing the ability of *in silico* models to represent some spatial details like layer structures and pH gradients. The authors work also on data for breast cancer (ductal carcinoma). Other works were devoted to the comparison of experimental results; furthermore, in some of them, attempts were done trying to calibrate models for *in vivo* systems using parameters fixed using *in vitro* data. A review of these works is provided in [104, 141].

The applications concerning tumor growth are essentially aligned on three axes: the first one is *diagnosis*, the second one is *prognosis* and the third one is *treatment*. Diagnosis of pathologies relies on the detection of tumoral masses by means of medical imagery. Models can be exploited in order to act as a filter, showing elements which are normally not visible. An example of this is done in the case of brain tumors by Swanson (see [149]). Once a model is able to describe a certain pathology evolution, a prognosis becomes possible, showing its global behavior on a significant time scale (see [134, 89]).

Works are done aiming at describing the effect of therapy on the tumor evolution [146, 139, 140, 33, 145]. In these works some terms are added to the model describing untreated evolutions, so that the effects of drugs (as in [146, 145, 140, 33]) or that of irradiation therapies (see for instance [140]) can be taken into account. The ability in describing treatment by means of spatial models may be precious in order to evaluate therapy efficacy and, in perspective, to define better protocols. This was investigated mainly by ODE models, because the resulting problem is affordable from a computational standpoint. An example in this sense is detailed in [67], in which an ODE model is described, taking a Gompertzian growth into account, coupled with nutrient equations. The latter are augmented by suitable terms accounting for one or two chemotherapies. A control problem is set up as an optimization problem, for which cost functions are defined as a trade off between different clinical needs. For all the therapies, the idea is to minimize the injected dose (because of the collateral damages associated) while minimizing tumor size on a given time scale. The problem is targeted from a numerical standpoint by means of a multiple shooting method.

In [129] the theoretical study of an inverse problem concerning size-structured population is taken into account. The evolution of a population is described by means of a 1D PDE of the form:

$$\frac{\partial n(x, t)}{\partial t} + \frac{\partial n(x, t)}{\partial x} + B(x)n(x, t) = 4B(2x)n(2x, t), \quad (3.14)$$

where independent variables are the size (x) and the time (t), n is the cellular of individual, B is the birth rate. The equation model the population dynamics by considering a process of division of cells of size $2x$ into two cells of size x . This kind of model is studied in tumor growth to give a representation of metastasis process (see [24, 25]). In [129] the problem is to find $B(x)$ when noisy data are available concerning the division rate and the steady cellular density $N = n \exp(-\lambda t)$ (under the assumption of long time behavior, λ being a Maltus parameter associated to the steady state, see [129]). The problem is stated in a quasi-inversibility framework: let $N = N(B; \lambda)$ be the direct map corresponding to the equation, it is inverted by means of a regularization approach. In particular an approximate problem is solved and some theoretical estimates are proposed. In [58] the authors revisited the problem; some numerical technique are proposed and analyzed to solve the problem. In particular regularization approaches are compared to a filtering approach, revealing that spurious oscillations affecting the solutions may be reduced by properly combining these strategies.

An approach including therapy, described through PK-PD (*i.e.* Pharmaco-Kinetics, Pharmaco-Dynamics) models, in the description of tumor size-structured population calibrated via inverse problems is outlined in [24]. The authors study the mathematical properties of a model describing the metastasis process, where tumor growth is rendered by a Gompertzian model. Then, a coupling between this model and treatment is suggested. The mathematical properties of the inverse problems associated are investigated and some analytical estimates on parameters is found.

The present work is mainly devoted to inverse problems in tumor growth modeling, when data comes from medical images. The idea is to exploit as much as possible the amount of information available in clinical practice. In what follows a brief section explains the main kinds of medical imaging devices and then a review of works concerning image-based inverse problems is done.

3.3.1 Medical imaging techniques

In this section the main classes of medical imagery are reviewed. Medical imagery is the main source of information (in terms of quantity) concerning cancer pathologies. It is

a fundamental tool in clinical practice, in diagnosis, in treatment planning and control. Several kinds of imaging techniques exist, adapted to different anatomical parts of the body (and tumors).

CT-scans Classical tomography imaging based on X-rays (CT) has reached a fine depth on resolution, allowing to obtain 3D images with a precision of $1mm$ (*i.e.* voxel have edges of $1mm$ in length). The base process consist in three parts. In the first one a slice from a 3D volume is chosen. Then a projection is performed (rays produces shadow-like shapes on detectors) and finally the image is reconstructed by means of Radon's transform. More sophisticated filters (backup projection filtering) were set up, leading to a good noise rejection. It is used mainly for monitoring lungs, chest, liver (and biliary tree), kidney, pancreas and colon.

PET and SPECT The same reconstruction method, with some difference, is used in PET and SPECT imaging techniques. In PET scan (Positron Emission Tomography) some FDG (fluoro-2-deoxy-D-glucose), or other positron emitting products, is injected. Proliferating cells are normally characterized by a great consumption in glucose, so that they tend to accumulate it. A positron is emitted from FDG and when it annihilates with an electron, radiation is emitted and detected by a gamma ray camera. Unlikely, the resolution is low ($5mm$), that corresponds to the diffusion limit of positron before the emission of radiation. PET is used to detect metastasis (to discriminate between primary and metastasis) and, fused to CT allows to give estimates on tumor aggressivity. This estimate is called SUV index, defined in general as:

$$SUV = \frac{U}{(I/W)}, \quad [U] = kBq/mL, [I] = kBq, [W] = g, \quad (3.15)$$

where U is the uptake measured according to the emission, I is the total dose of radiation injected, W is the weight of the patient. SUV index is not uniquely defined and measured. Several criteria are possible. According to the definition the SUV is a field, depending on position ($U = U(x)$), in order to extract a scalar index the mean, the max or the min are used.

SPECT is a 3D version (using gamma rays) of radionucleotide imaging. The principle is that of CT scan, a radioactive isotope is injected, allowing to highlights in a better way certain parts of the organ. It is used in liver, neuro-oncology and in lymphoscintigraphy (*melanomas* or breast cancers).

MRI Magnetic Resonance Imaging (MRI) is based on a different physical principle, relying on proton spin. The classical Bloch formula for magnetization in a classical framework can be profitably used for image reconstruction. Its resolution is a bit lower compared to that of CT scan ($3mm$), but it allows to have different contrasts and flavors on the image and a better contrast. As a matter of fact, while in CT scan the only parameter determining the result is the tissue absorption of X-rays, in MRI three parameters play an important role: the so called free water density, the longitudinal relaxation time and the transverse relaxation time. It offers several advantages with respect to CT in monitoring soft tissues, its main drawback consists in difficulties to detect calcifications or bone tumor invasions. It is used for monitoring brain, spinal cord, muscles (good detection of *sarcomas*).

Current trends Other techniques are available, trying to catch more informations. The current trend is represented by functional imagery, in which molecular informations are included. The idea is that cancer origins are essentially molecular, and hence, mapping some significant molecular activity would result in a better understanding of the pathology state. A first example is DTI-MRI, which is able to provide, in addition to common informations, the diffusion tensor of water in each point of the domain.

A vast area of applied mathematics is devoted to the development of algorithms and methodologies for medical imagery. In particular different topics arise, corresponding to different practical needs: segmentation, registration, denoising and inverse problems in general. A comprehensive review of these problems can be found in [127].

3.3.2 Image-driven inverse problems

As expressed in [141, 42] the ability to calibrate models of different type to *in vivo* as well as *in vitro* evolutions is of great interest to the development of tumor growth modeling and the understanding of the mechanisms governing the pathology. One of the objectives is to investigate the use of models aiming at giving clinicians some useful information in different stages of clinical practice.

Continuous models are suitable for this task, because a large amount of information concerning the dynamics of the patient pathology comes from medical imagery and hence at the tissue level. As stated in the previous sections, a wide variety of macroscopic models were proposed in the literature. They all have one key feature in common: they are systems of coupled parametric PDEs.

In continuous-type models, microscopic scales and a part of mesoscopic scales are not directly modeled and represented. Thus, their effect is lumped into parameters, which describes proportionality between the fields involved. In order to simulate the evolution of a tumor, parameters have to be determined. In the literature the values of characteristic parameters are proposed, mainly concerning *in vitro* systems (see [104]). Let us point out that few parameters can be directly measured, instead, they have to be recovered from other measured quantities. This is due to the phenomenological nature of models and the fact that parameters often do not have a clear biological or physical meaning. Hence, parameters have to be identified.

Inverse problems are the mathematical tool intended to accomplish this task. A comprehensive review of mathematical results concerning inverse problems for different partial differential equations is done in [92]. Literature on inverse problems includes all kinds of PDEs: elliptic equations for problems of conductivity recovery in presence of electrostatic fields, contaminant source determination as example of convective-diffusive system of equations, wave scattering by unknown obstacles as the more treated case of hyperbolic problem (see [92]). There are two different strategies and frameworks to set inverse problems (see [21]): a deterministic or a probabilistic one. In the first one the inverse problem is often recast as the minimization of an error functional subject to some constraint while in the second one a bayesian approach is used. In this work we are mainly focused on a deterministic approach. However, some statistics and probability have to be considered in order to quantify and evaluate reliability and robustness in the presence of noise in the data and other kind of perturbations.

A first work in which images are used in order to calibrate models is done by Tracqui in [156]. Glioma growth is treated using a reaction diffusion model in which diffusion is isotropic. Parameters are found using an optimization method, comparing the area of the simulated tumor with the actual area measured on images.

A pioneering work in this sense is proposed by Hogeia in [89] in which a framework is proposed to set up an image-driven parameter estimation in the case of glioma growth. The goal of the work is twofold: first, improving non-rigid registration and extract valuable informations in order to build statistical anatomical atlases and, second, to be able to predict tumor growth for a specific patient. The model adopted is a coupling between a reaction-diffusion equation for the tumor cells density (similar to what described in [148]) and a linear elastic equation describing mechanical properties of the tissues. The equations are:

$$\frac{\partial c}{\partial t} - \nabla \cdot (D \nabla c) + \nabla \cdot (\mathbf{v}c) = \rho c(1 - c), \quad (3.16)$$

$$\nabla \cdot (\lambda \nabla \cdot X) + \mu (\nabla X + \nabla^T X) - \left[p_1 \exp \left(-\frac{p_2}{c^S} - \frac{p_2}{(2-c)^S} \right) \right] \nabla c = 0, \quad (3.17)$$

$$\mathbf{v} = \frac{\partial X}{\partial t}, \quad (3.18)$$

where c is cancer cell density, D is the diffusivity, taken as a scalar varying in white and grey matter (thus isotropic in the phases), \mathbf{v} is the velocity field, X is the lagrangian coordinate, ρ the division rate; the term in square brackets in Eq.3.17 represents a force exerted by the tumor on the tissue, and it is purely phenomenological; the parameters p_1, p_2, S are unknown. The elastic properties λ, μ and the diffusivity D evolve in time and in particular they are taken as passive scalar advected with velocity \mathbf{v} . The inverse problem is set up in a classical optimization framework. The L^2 norm between the images and the solution of the model is minimized with respect to the set (ρ, p_1, p_2) , subject to the constraint represented by the evolution equations, with a Tikhonov regularization (see [92, 21]) applied on the control set. Lamé coefficients λ and μ as well as diffusivities of white and grey matter are supposed to be known at the very beginning: their value is taken from the literature. The optimization is carried out with a classical adjoint-based technique. At each minimization step the adjoint problem is computed, providing the descent direction for the problem. This method was extensively studied on 1D testcases and compared to other methods; it was tested also on real data for one realistic case.

A similar work, enlightening a different strategy is proposed by Konukoglu in [102, 101]. Glioma growth is considered and the model used is similar to what is described in [89], but there is no transport for the tumor phase, so that there is no mechanical coupling, reducing the model to one reaction diffusion equation (Eq.3.16 without the conservation term). The solution of this equation is represented by a traveling wave, whose characteristic velocity reaches an asymptotic value. The system is well approximated by an eikonal equation of the form:

$$\nabla T(x)^T D(d_w, d_g) \nabla T(x) = \frac{4\rho T}{(4\rho T - 3)^2}, \quad T(x) = T_0, \quad x \in \Gamma, \quad (3.19)$$

where T is the time, T_0 is the initial value for T when x is in the initial tumor Γ , ρ is, as before, the growth rate of tumor cells; D is the diffusivity tensor, taken as isotropic, equal to $d_g I$ in the gray matter, to $d_w D_{water}$ in the white matter, where D_{water} is the diffusivity tensor of the water in the fibers, measured by means of DT-MRI. This is a four parameter model to be calibrated.

An error measure is introduced as the distance between the simulated contour $\Gamma(x, t_i)$ and the segmented contour of the image taken at the corresponding time. The inverse problem is hence reduced to an unconstrained minimization problem, solved by a Powell

quadratic programming algorithm (see, for instance [130]). An interesting point arising and discussed in this work is the non-uniqueness of the minimizer. Local minima are in general present in this kind of problems and even if the solution exists unique, there are usually infinitely many solutions which are able to fit the sequence of medical images with an error which is smaller or equal to the image resolution. In [102, 101] the non-uniqueness is due to the fact that the front speed allows to determine only the product ρD and not the two quantities separately. One parameter, ρ is fixed and the others are determined; this is an arbitrary choice. A perspective well explained by the authors consists in adding more measurements (even of different kind) to overcome the underdetermination.

A similar approach is developed by Swanson in [152], in which parameters of a diffusion models are calibrated by means of a level set methods, while assuming that the solution is a traveling wave. Once the model is able to describe the pathology evolution with a certain approximation several applications are possible. Among them in [150] the effect of surgical interventions is investigated.

In [22] the integration of data coming from functional imagery is taken into account. In particular the framework proposed integrates data coming from different PET, DT-MRI and conventional MRI.

Two models are analyzed: a modified logistic model, and a proliferation-apoptosis-migration model: both are one equation models describing the number of tumor cells of the population. The models can be modified by some additive terms accounting for therapy. Let us detail the second model, which is different from models usually set up and explain well the key ideas of this work. The number of cells in the i -th voxels (N_i) follows the dynamics:

$$\frac{dN_i}{dt} = p_i N_i - d_i N_i + k_{im} N_m, \quad (3.20)$$

where p_i is the proliferation rate, d_i the death rate and k_{im} is the fraction of the cells of the m -th voxels that enters into the i -th one. These function, as well as the initial value of N in each voxel have to be fixed in order to run a simulation of the system. The initial conditions, *i.e.* the number of cells in each voxel is computed using the ADC (Apparent Diffusion Coefficient) map. Some phenomenological relation taken from the literature is used to perform the calibration (see [22] for details). Proliferation rate is estimated via a linear mapping involving a special kind of PET imaging data. The SUV index is used to get some estimates for the cells death rate. Data coming from another kind of PET imaging, based on radioactive fluorine are used to compute the migration rate k_{im} . This work is an example of how different kind of informations can be integrated in the same model in order to set up an image driven analysis, exploring a promising direction.

A work on breast cancer is done in [78]. The simulation of tissues is carried out supposing a non-linear elastic behavior. The goal of the work is to understand, on one hand, tissue deformations caused by tumor and, on the other hand to evaluate impact of lampectomy on tissues. Medical MRIs are used to get the geometry needed to perform the simulations.

Chapter 4

Models and Computational Framework adopted

In this chapter the models used for this work are detailed followed by an accounting of the computational techniques adopted for the direct simulations. Then a preliminary analysis of the effect of parameters on the solutions of the direct models is presented. The last section of this chapter outlines the operations that have to be performed in order to use the medical images as data.

4.1 Two species Darcy-type model

In this section a simplified Darcy-type model is introduced, describing a three phases saturated flow in a porous isotropic non-uniform medium. This is the reference model for this work.

It is a parametric model that is simple and able to take the main physical features of tumor growth into account. In the literature, several complex models have been proposed [139, 140, 141, 43], describing age-structured populations as multi-species saturated flow including the modeling of the cell cycle. Compared to those models, the mathematical description proposed in the following is simpler and as a consequence it disregards certain biological mechanisms.

The dynamics of two different cellular species is considered, denoted by P and Q . The density P represents the proliferating cells (dividing cells, responsible for tumor growth) and Q is the density of necrotic cells that die because of lack of oxygen in the tissue. A passive motion assumption is made, so that the velocity field is equal for every cellular phenotype phase [139]. Under this hypothesis, the mass balance equations for P and Q are

$$\frac{\partial P}{\partial t} + \nabla \cdot (\mathbf{v}P) = (2\gamma - 1)P, \quad (4.1)$$

$$\frac{\partial Q}{\partial t} + \nabla \cdot (\mathbf{v}Q) = (1 - \gamma)P. \quad (4.2)$$

where the velocity \mathbf{v} models the tissue movement due to the increase of the tumor volume and γ is the hypoxia threshold, a scalar function of the oxygen concentration that is more precisely defined later on Eq. 4.10. If enough oxygen is available then $\gamma = 1$ and Eq. 4.1 describes the proliferation of tumor cells and the quantity of necrotic cells is constant thanks to Eq. 4.2. If there is a lack of oxygen, then $\gamma < 1$ and some proliferating cells die and enter the necrotic phase thanks to Eq. 4.2. The function γ is a purely phenomenological description of a complex biological process, and hence it has to be identified since it cannot be deduced from experiments.

The density of healthy cells is denoted by S and, since their metabolism is not as fast as the metabolism of proliferating cells, the equation for S reduces to an homogeneous transport equation, as explained in [139]:

$$\frac{\partial S}{\partial t} + \nabla \cdot (\mathbf{v}S) = 0. \quad (4.3)$$

An hypothesis of saturated flow (see [140, 8]) is assumed, that is $P + Q + S = 1$, at every point of the space domain and for every time. Summing up Eqs. (4.1), (4.2), (4.3) leads to an equation for the divergence of the velocity field, namely:

$$\nabla \cdot \mathbf{v} = \gamma P. \quad (4.4)$$

As already observed in the general outline of continuous models, this is equivalent to state that mitosis acts as volume source for the flow.

In order to mechanically close the system a Darcy-type law is stated, that describes quasi-steady flows in porous media, with a variable porosity:

$$\mathbf{v} = -k(P, Q)\nabla\Pi. \quad (4.5)$$

The scalar function Π plays the role of a pressure (or of the potential), and k is a porosity field, that is a function of P and Q . The most simple, phenomenological law is a linear mapping of the sum $(P + Q)$, so that we have:

$$k = k_1 + (k_2 - k_1)(P + Q), \quad (4.6)$$

where k_1 represents the constant porosity of the healthy tissue and k_2 is the porosity of the tumor tissue. Imposing Neumann conditions on the pressure field is equivalent, from a physical standpoint, to imposing that there is no mass leaving the domain. In order to have a well posed problem the equation for the divergence of the velocity is modified. In particular the divergence must be a zero average scalar quantity, so that:

$$\nabla \cdot \mathbf{v} = \gamma(C)P - \frac{\int_{\Omega} \gamma P \, d\Omega}{\int_{\Omega} (1 - Y) \, d\Omega} (1 - P - Q). \quad (4.7)$$

From a mechanical point of view this is equivalent to impose that the growth of the tumor causes a compression of the healthy tissue. Therefore the healthy tissue equation can be no longer considered an homogeneous transport equation.

After defining the mechanics of the system, the nutrient evolution has to be specified. In this case it reduces to a reaction-diffusion equation for the oxygen concentration. Other

nutrients are not taken into account. A quasi-steady state assumption is quite reasonable for the time interval of interest for this work (see [104]):

$$-\nabla \cdot (D(P, Q)\nabla C) = -\alpha PC - \lambda C, \quad (4.8)$$

where α is the oxygen consumption rate for the proliferating cells, λ is the oxygen consumption coefficient of healthy tissue and $D(P, Q)$ is the diffusivity. Again, the diffusivity can be written as a linear mapping of $P + Q$:

$$D = D_{max} - K(P + Q). \quad (4.9)$$

This phenomenological law reflects the fact that the diffusion of oxygen is different in the healthy or tumor tissues. According to the physics of the system, reflecting different clinical cases, Dirichlet or Neumann boundary conditions may be imposed for the oxygen field. For example, in order to mimic the presence of a blood vessel, the oxygen concentration is considered constant on the subdomain corresponding to the blood vessel. If homogeneous boundary conditions are imposed a source of oxygen have to be modeled according to the mechanisms that feed the tissues, otherwise the trivial (non physical) solution is found.

The hypoxia function γ simply states that, when the concentration of oxygen is under a certain threshold the cells become necrotic. The definition of γ is a regularization of the unit step:

$$\gamma = \frac{1 + \tanh(R(C - C_{hyp}))}{2}, \quad (4.10)$$

where R is a coefficient and C_{hyp} is the hypoxia threshold.

The model presented is a continuous type model derived from the mixture theory and it is a rather drastic simplification of those ones presented in the literature (see [140, 132]). This choice is motivated by the applications targeted. When a tumor is discovered it is already some millimeters in size and the propagation is essentially a macroscopic phenomenon, so that it is naturally described by continuous models.

The cell cycle is not directly represented but its effects are lumped into the γ function. Moreover, angiogenesis is not modeled. This is unrealistic since tumors that reach the size of some millimeters undergo to angiogenesis, which corresponds often to their transition to malignancy. Its effect may be rendered through the oxygen parameters and the efficacy of the model may be verified *a posteriori*. These simplification are necessary to solve inverse problem because of the scarcity of the available data. As stated, the objective is twofold: to give a reasonable description of the phenomenon and to define an affordable identification problem. Hence the model proposed is a compromise between these diverging objectives.

4.2 Regularized Darcy-type model

The model detailed in this section is a simplification of the model presented in previous one, intended to make inverse problems better conditioned. The starting point for the derivation consists in observing that nutrients do not appear directly in the population equations, but always biased by the hypoxia function γ . Moreover, since this model has to be inverted for our purposes, the steeper γ , the worse conditioned the problem. One possibility is to substitute the equation for nutrients with an equation for γ and performing some simplifications and further regularizations.

Let us derive the equation for γ by a change of variable (γ being an hyperbolic tangent, it is one-to-one):

$$\tilde{C} = R(C - C_{hyp}) \implies \tilde{C} = \frac{1}{2} \ln \left(\frac{\gamma}{1 - \gamma} \right). \quad (4.11)$$

The partial derivative of \tilde{C} with respect to γ is:

$$\frac{\partial \tilde{C}}{\partial \gamma} = \frac{1}{2\gamma(1 - \gamma)}. \quad (4.12)$$

Let us stress that γ is really close to 1 or to 0 on the most part of the domain. Its evolution equation is derived by applying the chain rule:

$$-\nabla \cdot \left(\frac{D(Y)}{2R\gamma(1 - \gamma)} \nabla \gamma \right) = -\alpha P \left[C_{hyp} + \frac{1}{2R} \ln \left(\frac{\gamma}{1 - \gamma} \right) \right] + f(Y, P, \gamma), \quad (4.13)$$

which is a nonlinear reaction-diffusion equation, in which $Y = P + Q$, as in the Darcy model presented above. Let us consider the three parts of this equation separately.

The non-linear diffusion coefficient $D(Y, \gamma)$ takes the following form:

$$D = \frac{1 - k_d Y}{2R\gamma(1 - \gamma)} \quad (4.14)$$

where k_d, R are two parameters. The diffusion has a minimum for $\gamma = 1/2$ and $D \rightarrow \infty$ for $\gamma \rightarrow 1$ or $\gamma \rightarrow 0$. These singularities for γ are responsible for the extremely bad condition number of the inverse problem. Instead of having an infinite diffusivity, let us assume that at $\gamma = 0$ or $\gamma = 1$ the diffusivity is:

$$D(Y, 0) = D(Y, 1) = c_0 D(Y, 1/2), \quad (4.15)$$

where c_0 is a parameter that defines the ratio between the maximum diffusivity, corresponding to $\gamma = 1$, $\gamma = 0$ and the diffusivity for $\gamma = 1/2$. The diffusivity is thus rewritten

in the following form:

$$D(Y, \gamma) = \frac{1 - \tilde{k}Y}{4(\gamma - \epsilon(c_0))(1 - \gamma + \epsilon(c_0))}, \quad (4.16)$$

where $\epsilon(c_0)$ is a scalar function of c_0 . This operation corresponds to translates the asymptotes of γ by a quantity ϵ : the next operation consists in ensuring that $0 \leq \gamma \leq 1$. A quadratic expression linking c_0 to ϵ is easily obtained. The term that corresponds to the nutrient consumption for the proliferating cells in Eq.4.13 becomes:

$$\mathcal{U} = -\alpha \left(C_{hyp} + \frac{1}{R} \ln \left(\frac{\gamma}{1 - \gamma} \right) \right) P. \quad (4.17)$$

In analogy to what is done before the same regularization is added, providing:

$$\tilde{\mathcal{U}} = - \left(\alpha_1 + \alpha_2 \ln \left(\frac{1/2(1 + 1/c_0)^{1/2} + (\gamma - 1/2)}{1/2(1 + 1/c_0)^{1/2} - (\gamma - 1/2)} \right) \right) P. \quad (4.18)$$

Let us observe that the consumption has a maximum for $\gamma = 1$, and this maximum is:

$$\tilde{\mathcal{U}}|_{\gamma=1} = - \left(\alpha_1 + \alpha_2 \ln \left(\frac{(1 + 1/c_0)^{1/2} + 1}{(1 + 1/c_0)^{1/2} - 1} \right) \right) P = -\alpha_1 P - \alpha_2 \ln(K)P. \quad (4.19)$$

The consumption computed for $\gamma = 1/2$ clarifies the physical meaning of α_1 :

$$\tilde{\mathcal{U}}|_{\gamma=1/2} = -\alpha_1 P. \quad (4.20)$$

The value for $\gamma = 0$ is important because it is supposed that $C = 0 \rightarrow \gamma = 0$ and thus the consumption computed in $\gamma = 0$ has to vanish:

$$\tilde{\mathcal{U}}|_{\gamma=0} = -(\alpha_1 - \alpha_2 \ln(K))P = 0 \iff \alpha_1 - \alpha_2 \ln(K) = 0. \quad (4.21)$$

This expression allows to eliminate one parameter as function of the other, recovering the same number of degrees of freedom as the original model.

The last term can be modeled in different ways, according to the physics of the system and the organ considered. In the present case a simple expression is assumed:

$$f = -Y\gamma \quad (4.22)$$

This is a linear consumption term for γ that aims at modeling a sort of overpopulation effect. For $Y = 0$, (*i.e.* in the healthy tissue) this term is zero.

The equation describing the evolution of γ has the following form:

$$\nabla \cdot \left(\frac{1 - \tilde{k}Y}{4(\gamma - \epsilon(c_0))(1 - \gamma + \epsilon(c_0))} \nabla \gamma \right) = \lambda_P \ln(Kg(c_0, \gamma)) P - \lambda_Y Y \gamma, \quad (4.23)$$

where the function $g(c_0, \gamma)$ is:

$$g(c_0, \gamma) = \frac{(1 + 1/c_0)^{1/2} + (2\gamma - 1)}{(1 + 1/c_0)^{1/2} - (2\gamma - 1)} \quad (4.24)$$

and $K = K(c_0)$ is:

$$K(c_0) = \frac{(1 + 1/c_0)^{1/2} + 1}{(1 + 1/c_0)^{1/2} - 1}. \quad (4.25)$$

Finally, $\epsilon(c_0)$ is:

$$\epsilon(c_0) = \frac{-1 + (1 + 1/c_0)^{1/2}}{2} \quad (4.26)$$

For sake of simplicity a more compact and manageable equation can be derived that mimics in a least square sense the behavior of the equation written above, keeping the properties imposed:

$$\nabla \cdot ((1 - KY)(\omega\gamma^2 - \omega\gamma + \sigma)\nabla\gamma) = (\lambda_P P + \lambda_Y Y)\gamma, \quad (4.27)$$

where ω, σ are parameters fixed according to the regularization length ϵ . For all the tests performed in the present work we have chosen $\epsilon = 2.5 \cdot 10^{-2}$, which implies $\omega = 35.40, \sigma = 9.76$. This modeling for $\gamma(x, t)$ suggests an interpretation: the hypoxia function acts like a triggering field for the growth and it represents the division velocity of a unitary volume of proliferating cells that at time t is in the position x . This characteristic velocity field is governed by a steady non-linear reaction-diffusion equation. Suitable boundary conditions are imposed according to the organ nature.

All the other equations for this model are kept identical with respect to the reference model presented in the previous section.

4.3 A one specie incompressible model

Another model was taken into account in the present work in order to compare the prediction results and to investigate how the models affect the identification procedure. The model briefly described in this section was presented and studied by Enault in [66].

It is a one specie incompressible model for tumor growth. The population of cancerous cells is named Y and follows the equation:

$$\dot{Y} + \nabla \cdot (\mathbf{v}Y) = cY, \quad (4.28)$$

where c is a constant parameter representing the growth rate for the tumor. A mechanical description for the velocity field is provided by the saturation between healthy tissue and tumor and by the Darcy assumption. In particular:

$$\nabla \cdot \mathbf{v} = cY, \quad (4.29)$$

and, then:

$$\mathbf{v} = (1 + \chi Y) \nabla \Pi, \quad (4.30)$$

where the permeability is represented by the function $k = (1 + \chi Y)$ and it is a linear function of Y , exactly as in the Darcy model. Π is the scalar potential. Boundary conditions are imposed according to the organ nature.

This model may be considered as a simplification of the Darcy model when several hypothesis are made: first, no nutrient dynamic is involved, the division ratio being a scalar constant parameter. This describe a tumor in steady environmental conditions. Second, there is only one cancerous phenotype, there is no population dynamics.

This system has only two scalar parameters (χ and c). It will be useful to determine which is the effect of the complexity on the ability to provide a realistic prognosis. A comprehensive analysis from a mathematical standpoint is found in [66].

4.4 Computational Framework

The numerical techniques adopted to perform all the direct simulations are detailed in this section. The numerical framework used is *eLYSe*.

The models described in the previous sections are in general systems of coupled elliptic and hyperbolic PDEs. In order to approximate their solutions two main ingredients are mandatory: a transport solver and a Poisson solver. The space discretization is done by means of a standard Finite Volume Methods (FVM) on cartesian MAC grids (see Fig.4.1.a). In particular, velocity is defined on cells interfaces, while pressure and other quantities, like densities and nutrient concentrations, (generically denoted by ρ in Fig.4.1.a) are known in the center of the cell, as usually done for incompressible Stokes problems. Linear interpolation is used, diffusivities and permeabilities, which enters in

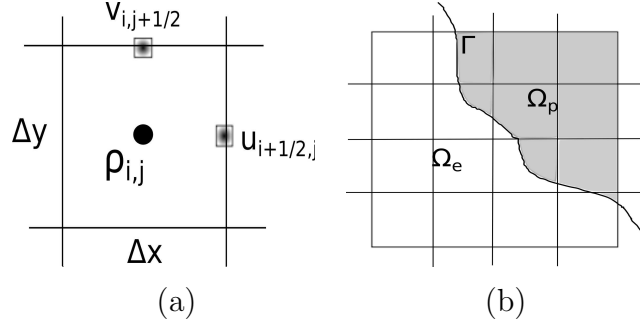


Figure 4.1: a) MAC discretization b) Penalization on cartesian grid

Poisson problems are computed at cells interfaces by means of the harmonic mean, in order to fulfill continuity requirements.

As example, the discretization of the two species Darcy-type model in 2D is briefly described. Let us first consider, the elliptic equations, describing Poisson problems for the nutrients concentration and for pressure. Elliptic operators are discretized within a penalization framework (see Fig.4.1.b), second order ghost fluid (see [82]) is used for different kind of boundary conditions. For the pressure field, the equation reads:

$$-\nabla \cdot (k(Y)\nabla\Pi) = \gamma P \quad x \in \Omega_p, \quad (4.31)$$

$$\Pi = 0 \quad x \in \Gamma = \partial\Omega_p, \quad (4.32)$$

where Ω_p is the domain in which pressure have to be integrated. The equation is discretized on the whole domain:

$$\begin{aligned} k_{i+\frac{1}{2},j} \frac{\Pi_{i+1,j} - \Pi_{i,j}}{\Delta x} \Delta y + k_{i,j+\frac{1}{2}} \frac{\Pi_{i,j+1} - \Pi_{i,j}}{\Delta y} \Delta x - k_{i-\frac{1}{2},j} \frac{\Pi_{i,j} - \Pi_{i-1,j}}{\Delta x} \Delta y + \\ - k_{i,j-\frac{1}{2}} \frac{\Pi_{i,j} - \Pi_{i,j-1}}{\Delta y} \Delta x + \frac{1}{\epsilon} \Pi_{i,j} \mathbb{1}_{\Omega_e} = -\gamma_{i,j} P_{i,j}, \end{aligned} \quad (4.33)$$

where k is the harmonic mean of the permeabilities computed at the corresponding cell interface, $\mathbb{1}_{\Omega_e}$ is the characteristic function of the domain Ω_e and $\epsilon = 10^{-10}$ is the penalization constant. The resulting linear system is solved by a preconditioned Krilov solver (GMRes) as implemented in PETSc libraries. In the case of parabolic equations, as in non-steady diffusion for nutrients, second order implicit Crank-Nicholson scheme is adopted.

Transport is computed through a classical WENO5 method, as proposed in [93], in order to limit mass loss effects. The divergence part of the conservation equations is taken into account as if it was a source for the transport equation, computed by means of an

exponential term. The resulting discretization scheme is not conservative. The divergence of the velocity being equal to the product between γ and P , a logistic equation is derived for the population. The whole method is updated in time using an explicit Runge Kutta mid point (second order accuracy), leading to a second order splitting of the operator. For P variable the semi-discretized equation (in time) is the following one:

$$P^{n+\frac{1}{2}} + \frac{\Delta t}{2} (\mathbf{v} \cdot \nabla P)^n = P^n + \frac{\Delta t}{2} (-P^n (\nabla \cdot \mathbf{v})^n + (2\gamma^n - 1)P^n), \quad (4.34)$$

$$P^{n+1} + \frac{\Delta t}{2} (\mathbf{v} \cdot \nabla P)^{n+\frac{1}{2}} = P^n + \Delta t \left(-P^{n+\frac{1}{2}} (\nabla \cdot \mathbf{v})^{n+\frac{1}{2}} + (2\gamma^{n+\frac{1}{2}} - 1)P^{n+\frac{1}{2}} \right). \quad (4.35)$$

The transport part has been kept on the left hand side, the other terms representing the forcing part of the equation.

Geometries are taken into account through a level set approach. For a comprehensive overview of the techniques we refer to [124]. For the present work level sets are taken as signed distance functions, computed with the PDE approach presented in [143]. In particular Level sets are used to initialize tumor according to a layer structure (it will be detailed later on), and to account for the organ geometry (in particular organs boundaries). Organ frontiers may induce different boundary conditions on different fields, according to the physical nature of interaction.

Parallelization (which is mandatory for 3D problems) is carried out using MPI and PETSc libraries.

4.5 Direct simulations

In this section the behavior of Darcy model with respect to parameters is investigated through direct simulations. For the 2D setting a realistic case is considered. Organ geometry is taken into account by means of level sets, tumor is initialized as it is seen in the first medical image. Details about the precise configuration are given further. 2D simulations were performed varying α , C_{hyp} , ξ , where ξ is the proportion of proliferating cells at $t = 0$, defined as:

$$\xi = \frac{\int_{\Omega} P(x, 0) dx}{\int_{\Omega} Y(x, 0) dx}. \quad (4.36)$$

Each parameter was varied in intervals spanning all the possible biological behaviors, *i.e.* ranging from a very aggressive exponential type growth, to a stable or shrinking tumor.

The following intervals of parameters were simulated for the Darcy model:

- $\alpha \in [0.5, 8.0]$,

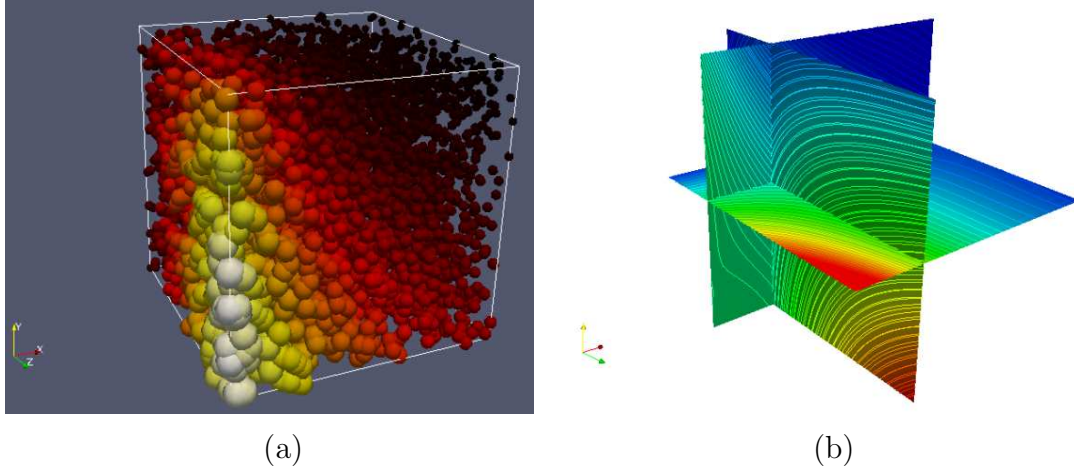


Figure 4.2: a) Direct simulations as function of three parameters (α, C_{hyp}, ξ) : sphere radius is proportional to the average tumor volume, color scale renders aggressivity (norm of the indicators). b) First indicator (f) plotted on three orthogonal slices and isocontours (30 lines between maximum and minimum).

- $C_{hyp} \in [0.2, 0.8]$ when $\max_{\Omega} \{C(x, t)\} = 1.0 \forall t$,
- $\xi \in [0.1, 0.9]$.

These intervals were uniformly sampled. The simulation time was taken, for all the simulations $T = 5$, which is an adimensional time such that, for the most aggressive tumor (*i.e.* $\alpha = 0.5$, $C_{hyp} = 0.2$, $\xi = 0.9$) tumor final volume is about four times the initial one. For all the simulation the porosity ratio was set as $\frac{k_2}{k_1} = 1.25$.

In order to evaluate the growth, three different indicators were considered. Their meaning and significance were discussed with medical doctors from Insitut Bergonié.

$$f = \int_0^T \int_{\Omega} \dot{Y}^2 dxdt, \quad g = \int_0^T \int_{\Omega} Y dxdt, \quad h = \int_0^T \int_{\Omega} \dot{P}^2 dxdt. \quad (4.37)$$

The first quantity (f) denotes the ability of tumor to invade organs, since it tells how fast it tends to increase its volume, in an average sense in $[0, T]$. g is the average of the tumor volume. Since the initial tumor is given and it is the same for all the simulations, g represents also how much the tumor has increased its volume. The last indicator reflects tumor aggressivity, its capacity to proliferate.

These quantities were plotted against the parameters values. In Fig.4.5.a) a plot is shown in which each sphere represent the result of one simulation. The sphere radius

is proportional to the average of the tumor volume, color scale is set according to the magnitude of the vector (f, g, h) . In Fig.??b) three slices were taken, on planes parallel to coordinate axis (*i.e.* when one parameter is kept constant). The plotted quantity (color scale and isocontours) is f .

This is in some sort a preliminary analysis, relying entirely on direct simulations and post processing. This analysis is good to understand the properties of the model solutions from a qualitative standpoint. Furthermore, in this work we tried to develop a reduced order approach based on POD technique. This imply the construction of a database, *i.e.* a collection of solutions varying the parameters. A good database is a trade off between the ability to represent a sufficiently broad variety of biological behaviors and that of rejecting impossible or improbable configurations. Such a preliminary investigation is helpful in building a good database.

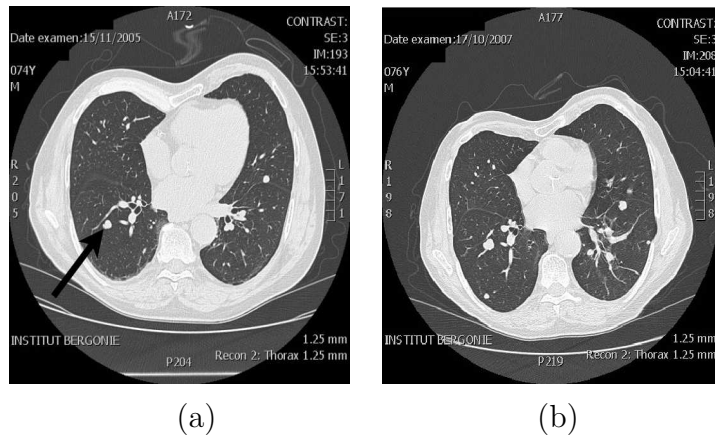
4.6 Dealing with medical images

When a sequence of images is provided by medical doctors, it is not ready to be used for inverse problems. Several stages are required in order to systematically solve the identification problems and get reliable results. In this work all these stages have been done by hand. Existing techniques have been considered and no novel methods have been investigated concerning image processing.

When bidimensional data are used the slice in which the tumor has the maximal area is chosen. This is, of coarse, an approximation. In this work tumors have been studied that were not too different from spheroids in shape, so that working with a section is not non realistic. Furthermore, this is close to what is done in clinical practice. Medical doctors are used to work on 2D slices instead of full 3D data, even when they are available. For all the treated cases the slice selected was that on which the tumor area was the larger among all the slices. Let us make an example of data, as they are generated by a CT scan (see Fig.4.6). There are several elements which are different in the two: first, the zoom is not the same. This is easy to infer (from thorax size for instance) and normally zoom data are available. Second, the tumor location with respect to the reference frame of the machine has changed. These images can not be used directly.

Two main stages are required before starting performing inverse problems: a segmentation and a registration processes.

A segmentation procedure isolates the tumor and the organ. Both elements are needed for the direct simulations to be performed. Images are segmented by a standard threshold



method. Realistic cases considered in this work uses CT scans of lungs as data. For this organ images are well contrasted and resolution is not too poor so that this segmentation method performs quite well. For other kinds of cancer this is more critical since tumor is diffused and thus a tumor boundary is not defined.

A registration step is mandatory. Indeed, direct simulations (and, as consequence, inverse problems) are performed in a fixed geometrical configuration, that is, the configuration corresponding to the first image of the sequence. Geometrical configuration means essentially organ shape and tumor position with respect to a fixed reference frame. Several elements make the configuration vary in a substantial way: patient is not in the same position when the successive scans are taken, machine may change and lungs undergo a high strain due to respiration or external constraints.

In order to overcome possible zoom change an homothety is applied. When not available, zoom ratio between images taken with different machines were approximated by measuring the distances between the *sternum* and the *vertebrae*, which is almost fixed, not affected by respiration or rigid movements. Rotations were fixed by a rigid registration approach. In order to refer tumor position to the same reference frame tumor baricenter were considered as fixed. This hypothesis is not ever realistic and the non-rigid registration based on optimal transport aims at relaxing it. However, for the most part of the metastases analyzed in the present work, rigid registration was a good choice.

Finally, images are recast in the desired resolution by means of a linear interpolation. In some of the cases a quadratic interpolation was used. Tumor density is normalized between 0 and 1, in such a way that compatibility with the models used is respected.

Chapter 5

Sensitivity Technique

In what follows a sensitivity framework (see [138] for details) for tumor growth modeling is described.

In the first section inverse problems for ODEs models are detailed. In particular, the model proposed by Simeoni in [109] is compared to the 0-D reduction of the Darcy type model. Inverse problems have been performed on several realistic cases.

In the second section an approximated sensitivity approach is proposed for PDEs models. Tests are commented on realistic datasets and some comparison with ODE models is established. A study on perturbations effect is done aiming at testing the stability and the reliability of the technique.

5.1 Sensitivity on ODE models

In this section a sensitivity approach is applied to ODE models. The goal is twofold: first, different ODE models are compared on several realistic cases and, second, general behavior of 0-D approaches is investigated and it will be compared to that of space approaches. Several works were devoted to inverse problems for ODE models (see [67]). Due to the simple nature of the equation, identifiability can be investigated in an analytical way (see for instance [116]). For generic PDE problems this task is exceedingly hard and out of reach.

5.1.1 A logistic-type model inspired by Darcy model

An ODE model derived from the two species Darcy model is set up. Let us briefly recall the PDE model presented in the previous chapter:

$$\begin{aligned}
\frac{\partial Y}{\partial t} + \nabla \cdot (\mathbf{v}Y) &= \gamma P, \\
\frac{\partial P}{\partial t} + \nabla \cdot (\mathbf{v}P) &= (2\gamma - 1)P, \\
\nabla \cdot \mathbf{v} &= \gamma P, \\
\mathbf{v} &= -k(Y)\nabla\Pi, \\
\nabla \cdot (D(Y)\nabla C) &= \alpha PC + \lambda C, \\
\gamma &= \frac{1 + \tanh(R(C - C_{hyp}))}{2}.
\end{aligned} \tag{5.1}$$

The dynamics of two species is described, the variables P and $Y = P + Q$ representing the proliferating and the total tumor cells densities respectively (the variable Q has

been substituted by the observable). The total lagrangian derivative of the population dynamics is derived by substituting the equation for the divergence of the velocity into the population equations, resulting in a coupled logistic dynamics. Neglecting the space effects the population dynamics of the 0–dimensional system reads:

$$\dot{Y} = \gamma P(1 - Y), \quad (5.2)$$

which represents a logistic type dynamics for the volume. The proliferating cells volume obeys the following dynamics:

$$\dot{P} = (2\gamma - 1)P - \gamma P^2, \quad (5.3)$$

that is again a logistic-type of dynamics. The function γ translates the environmental conditions: if the nutrient uptake is sufficient tumor proliferate, otherwise it dies. The nutrient dynamics that is taken into account is quite simple, consisting in only one species, let say the total quantity of oxygen that is available in the tumor neighborhood:

$$\dot{C} = (-\alpha P + \sigma \left(\frac{Y}{Y_0}\right)^{2/3})C, \quad (5.4)$$

where α is the consumption rate of the proliferating part of the tumor and σ represent the diffusivity rate of the oxygen, Y_0 represents the volume of the tumor as it is computed on the first scan. The initial condition for the overall amount of nutrients has been set as $C(0) = 1$. The exchange of nutrients is performed through the surface of the tumor (power 2/3 accounts for the surface); similar considerations are discussed in [144, 86]. Diffusivity has been fixed to $\sigma = 1$ for the performed tests.

The linking between the nutrients and the population dynamics is provided by an hyperbolic tangent, as for the Darcy-type model:

$$\gamma = \frac{1 + \tanh(10(C - C_{hyp}))}{2}. \quad (5.5)$$

The model was integrated by a second order Runge-Kutta mid point scheme. Sensitivity equations were derived exactly for this case. The control set reduces to $\alpha, C_{hyp}, P(0)$. The initial condition for P is the volume fraction of the tumor which is proliferating at $t = 0$.

The sensitivity system is derived for the proposed model. The following definitions are introduced:

$$Z_j^Y = \frac{\partial Y}{\partial c_j}, \quad W_j^P = \frac{\partial P}{\partial c_j}, \quad W_j^C = \frac{\partial C}{\partial c_j}, \quad W_j^\gamma = \frac{\partial \gamma}{\partial c_j}. \quad (5.6)$$

The equations, obtained by deriving the original system with respect to the control, reduce to:

$$\dot{Z}_j^Y = (W^\gamma P + \gamma W_j^P)(1 - Y) - \gamma P Z_j^Y, \quad (5.7)$$

$$\dot{W}_j^P = (2P - P^2)W_j^\gamma + [2\gamma(1 - P) - 1]W_j^P, \quad (5.8)$$

$$\dot{W}_j^C = \left[\frac{2}{3} \left(\frac{Y}{Y_0} \right)^{-1/3} Z_j^Y - \alpha W_j^P \right] C + \left[\left(\frac{Y}{Y_0} \right)^{2/3} - \alpha P \right] W_j^C + PC\delta_{c_j\alpha}, \quad (5.9)$$

$$W_j^\gamma = 4R\gamma(1 - \gamma)(W_j^C - \delta_{c_j C_{hyp}}), \quad (5.10)$$

where δ is 1 or 0 depending on whether the control element is present in the equation or not. The initial conditions are homogeneous for all the functions except for W_j^P , when $c_j = P_0$. The algorithm is straightforward: the direct model is integrated at iteration n , for a given set of control c_j^n . The error is computed with respect to the measured volumes (Im_i); then, the sensitivity system is simulated, and the error is projected on the sensitivity Z_j^Y , leading to the values of the descent direction. The gradient algorithm used for the tests on ODEs systems thus reads:

$$c_j^{n+1} = c_j^n + \beta \left(\sum_i^{N_o} \langle \mathcal{E}(x, t_i), Z_j^Y(x; t_i) \rangle_\Omega dx \right), \quad (5.11)$$

where c_j is the j -th element of the control set, N_o is the number of measures, \mathcal{E} is the error and β is the step, which is a constant parameter.

Let us describe some numerical details which are common to all the numerical tests performed.

The model being in adimensional unit for what concerns the time scale, the times at which data are taken need to be rescaled. As a matter of fact $0 \leq \gamma \leq 1$ that implies that the maximum growth rate for proliferating cell volume is 1. This means that:

$$\gamma = 1 \Rightarrow \dot{P} = P(1 - P) = \sup_\gamma \{P(\gamma, t)\}, \quad (5.12)$$

that is a logistic equation, whose solution represent the maximum growth rate for the tumor. This is a sort of compatibility condition, in the sense that the model can not represent tumors growing faster than this. All the treated cases are non-dimensionalized as follows:

$$\tau = 1.1 \frac{(t - T_{in})}{(T_{fin} - T_{in})}, \quad (5.13)$$

where τ is the simulation time, t is the real biological time, T_{in} and T_{fin} are the time at which the first and last datum are taken respectively.

Moreover, as already said, the model have been initialized from different initial points, in order to see if the method is robust enough and to evaluate the existence and the basin of attraction of local minima. The procedure of initialization is case dependent and it is the following one: several direct simulations are computed. Then, the parameters combination that allows a tumor to grow up to a factor 5 in volume is taken as the upper boundary for the parameters. The factor 5 is purely arbitrary but it is realistic for tumor observed in clinical practice. The lower boundary is the set of parameters that represents an almost steady tumor. Several initial points are chosen by uniformly sampling the parameter space between the upper and the lower boundary. For ODEs this is costless since a simulation takes only a second on a standard laptop.

The direct model was integrated by means of a second order explicit Adams-Bashfort (AB2) method, taking $N = 2500$ time steps. Stability and convergence of the results were checked.

The descent step is case dependent and it is chosen by tuning the algorithm in such a way that the highest step allowing to obtain a stable descent is found. A common step, which performs quite well for all the cases treated is $\beta = 10^{-4}$.

The stop criterion was based on both the average relative error on the fitting and the norm of the functional gradient at the $n - th$ iteration, defined respectively as:

$$\mathcal{E}_{rel} = \frac{1}{N_o} \sum_i^{N_o} \frac{(Y(t_i) - Im_i)^2}{Im_i^2}, \quad \Delta J = \frac{1}{\beta} \|c^{n+1} - c^n\|_2. \quad (5.14)$$

The stop on the relative error was taken as $\mathcal{E} \leq 10^{-2}$, while that of the 2-norm of the difference between the controls was $\Delta J \leq 10^{-4}$.

5.1.2 Realistic cases

In this part, the results of the proposed procedure are shown when realistic datasets are taken. Two datasets are used, corresponding to different tumors. The first one, BEN (see 5.1) represents measures taken from a brain tumor (Courtesy, CHU Bordeaux) by means of a conventional 3D MRI while FER (see 5.2) are volumes of a lung metastasis (primary tumor being in the tyroid, courtesy, Institut Bergonié), taken using 2D slices of a CT scan. What is under investigation is the ability of the model to fit the progression of the evolution.

The biological behavior of these tumors is quite different, so that fitting them with the same model would seem inappropriate. Nevertheless, parametric models can reasonably fit different behaviors. Furthermore, let us claim then in ODE models effects characterizing

Table 5.1: Data set and results for BEN case, Darcy-type model: 5 volumes measures are taken from 3D MRI, resolution 3.0mm.

<i>Month</i>	0	3.7	17.0	22.6	24
<i>Volume</i>	7.935	9.136	12.954	13.117	13.703
$\mathcal{E}_{2Im}(\%)$	0.0	0.10	0.26	1.0	3.0
$\mathcal{E}_{3Im}(\%)$	0.0	0.12	0.20	0.63	2.35
$\mathcal{E}_{4Im}(\%)$	0.0	0.15	0.26	0.50	2.0

Table 5.2: Data set and results for FER case, Darcy-type model: 5 volumes measures are taken from 2D scan, resolution 1.25mm.

<i>Month</i>	0	21	33	38	43
<i>Volume</i>	0.0235	0.033	0.049	0.061	0.073
$\mathcal{E}_{2Im}(\%)$	0.0	0.24	12.25	22.95	24.66
$\mathcal{E}_{3Im}(\%)$	0.0	3.95	0.47	6.56	5.48
$\mathcal{E}_{4Im}(\%)$	0.0	6.00	2.04	3.28	0.45

different physical and biological behaviors are flattened by the fact that only integral quantities are described (see [141]). The following test was performed: $\alpha = 1$ was treated as a parameter (in order to have a small control set, see [102]), C_{hyp} and $P(0)$ are the control. Let us remark that $P(0)$ is the fraction of proliferating cell volume over the total initial tumor volume ($0 \leq P(0) \leq Y(0)$). Using a small control lets us avoid as much as possible local minima and in this case is significant, since the amount of data is scarce. Having too many degrees of freedom would produce perfect interpolations, but not significant, since it will be equivalent to a polynomial interpolation of sufficiently high degree. In Fig.5.1 the results of the inverse problems are shown. The recovered parameters using four data are: $C_{hyp} = 0.86$ and $P_0 = 0.91$. This means that the tumor at the very beginning is almost entirely proliferating, but, since hipoxy threshold is high the system undergoes to a saturation. In particular the solid lines represent the direct simulation using the identified control set, the points represent the clinical measures; black circles represent data used for the identification while red squares are the data which have to be predicted. In Fig.5.1.a) the identification is performed using only two measures. This

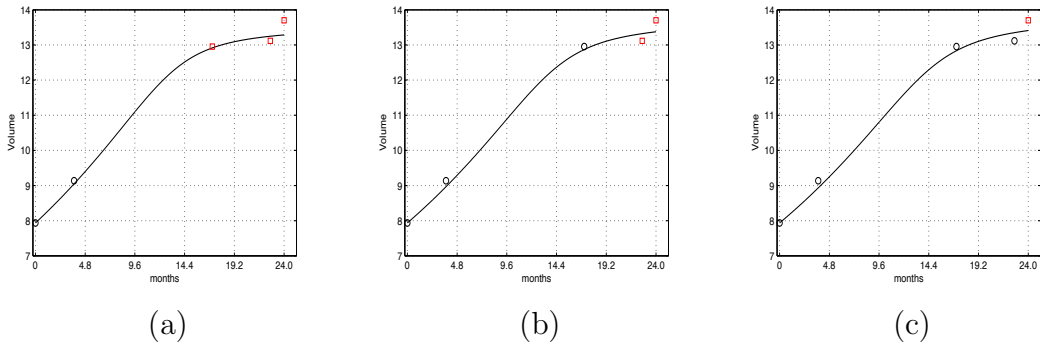


Figure 5.1: Identification for BEN case performed with a) 2 b) 3 c) 4 Data. Solid line represents the simulation results, black circles are the data used for the identification, red squares are the predictions.

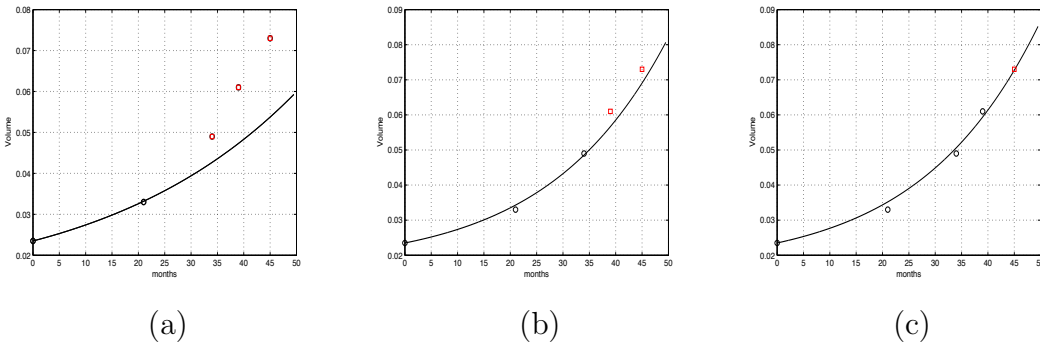


Figure 5.2: Identification for FER case performed with a) 2 b) 3 c) 4 Data

represents the minimal amount of information that is necessary in order to set up the inverse problem. Let us observe that the three fittings are very similar; increasing the number of data produces a least square effect on the fitting, that is, the model tends to fit worse the second point in order to decrease the total value of the quadratic error. Nevertheless the fitting is good since it allows to predict the global behavior of the tumor, even with two data. What is more important, for realistic applications, is the ability to predict correctly the first prediction point. In Fig.5.2 the same procedure was applied to FER case. The parameters recovered using four images are: $C_{hyp} = 0.35$ and $P(0) = 0.31$. In this case only one third of the tumor is proliferating and the hipoxya threshold is lower, so that the tumor is expected to grow in an exponential like manner. The fitting results are worse if compare to that of the BEN data set; in this case all the images are needed to obtain a fitting whose error is comparable with the machine tolerance for this tumor

Table 5.3: Data set and results for BEN case, Simeoni model: 5 volumes measures are taken from 3D MRI, resolution 3.0mm.

<i>Month</i>	0	3.7	17.0	22.6	24
<i>Volume</i>	7.935	9.136	12.954	13.117	13.703
$\mathcal{E}_{2Im}(\%)$	0.0	0.70	9.69	24.49	25.59
$\mathcal{E}_{3Im}(\%)$	0.0	0.71	1.74	13.97	14.43
$\mathcal{E}_{4Im}(\%)$	0.0	2.90	5.43	4.29	4.35

size. In particular a non-logistic behavior (increasing proliferation rate at $t \approx 32months$) is not well represented. Moreover the fitting of the second point become worse when four images are fitted.

The same tests were performed with the model proposed by Simeoni in [109]. Let us recall the model:

$$\dot{w} = \frac{\lambda_0 w}{\left[1 + \left(\frac{\lambda_0}{\lambda_1} w\right)^\psi\right]^{1/\psi}}. \quad (5.15)$$

For sake of brevity sensitivity equations are not reported; integration were performed with the same method. In Table 5.3 the results are reported. Simeoni model has three parameters, one ($\psi = 3.6$) is a regularization, which does not vary much (it may be considered a parameter). Thus, the number of control elements is equivalent to the one used for the Darcy-type model. The model proposed by Simeoni has a worse performance in fitting the BEN dataset. As a matter of fact, when 4 volumes are taken it has an average fitting error of 4.25%, greater than what obtained with the proposed Darcy-type model. In particular, when all the volumes data are taken the fitting of the second one becomes poor. The recovered parameters are: $\lambda_0 = 3.72$ and $\lambda_1 = 0.73$. In Fig.5.3 the fittings are shown when several volume data are taken. The dynamics described by the model is too simple in this case and does not allow a good representation of the saturation of the growth. In order to fit the points in a least square sense the model provide an almost linear fitting, which is not realistic.

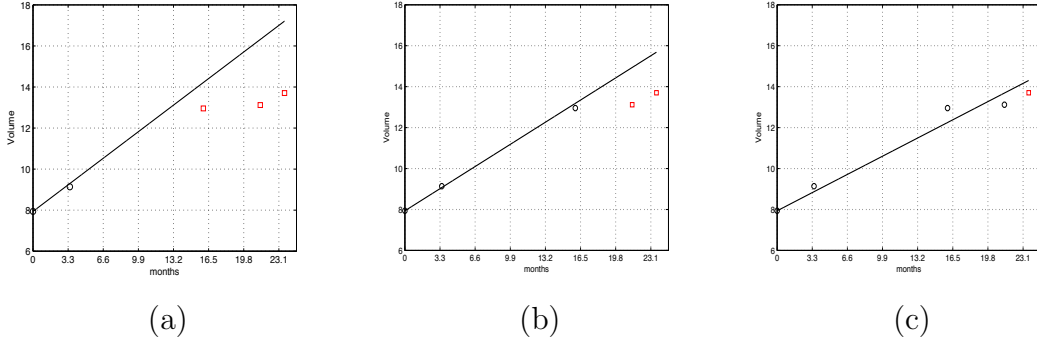


Figure 5.3: Identification in the BEN case performed with a) 2 b) 3 c) 4 Data and the Simeoni model

5.2 Sensitivity on 2D regularized Darcy-type model

A sensitivity approach is set up on the Darcy regularized model. Instead of considering exact sensitivity, an approximated sensitivity approach is set up in order to use only direct system integrations. This is less precise than the exact sensitivity approach described in the previous section, but it allows to build an easy parallelizable tool to solve the inverse problem.

Let us denote the solution of the direct simulation for the observable, at iteration n , with Y^n . Let us write the solution of the perturbed system with \tilde{Y}_j , which is the solution of the direct simulation when the j -th control element is perturbed, *i.e.* $\tilde{c}_j = c_j^n + \Delta c_j$, where $\Delta c_j / c_j^n = 5 \cdot 10^{-3}$. In the case that the control is zero, a small perturbation of 10^{-4} is taken as default value. The amplitude of the perturbations have to be chosen in such a way that the precision on the sensitivity is good (so the smaller the perturbation, the better the approximation), and that no cancellation errors affect the computation. Indeed, if the perturbation is too small, the solutions tends to be exactly the same (considering discretization errors), so that a zero sensitivity function would be recovered, or a sensitivity affected by numerical errors. At first order, the following relation holds:

$$Z_j \approx \frac{\tilde{Y}_j - Y^n}{\Delta c_j}. \quad (5.16)$$

The update step than consists in computing an approximated descent direction by projection of the error onto the approximated sensitivity and inject it into the optimization method.

Again, a gradient method were chosen as a first method:

$$c_j^{n+1} = c_j^n + \beta \left(\sum_i^{N_o} \langle \mathcal{E}(x, t_i), Z_j^Y(x; t_i) \rangle_{\Omega} dx \right), \quad (5.17)$$

where $\beta = 10^{-2}$ was the step used for the computations. A second choice of the method is a classical BFGS (see [122] for details), which will provide a faster convergence. In all the treated case the set of control is of small dimension, so that a low memory version is not necessary and matrix inversion may be done without a significant computational effort.

The starting point was chosen exactly with the same procedure used for the ODEs models: direct simulations were performed to select a range of parameters allowing to represent the admissible biological behaviors. Then, the parameters of the most aggressive and the quasi-steady simulations were chosen as upper and lower boundary.

The stop criterion was based, as done for the ODEs based inverse problems, on the average relative error on the fitting and the norm of the functional gradient at the $n - th$ iteration, defined respectively as: The stop on the relative error was taken as $\mathcal{E} \leq 10^{-2}$, that of the 2-norm of the difference between the controls was $\Delta J \leq 10^{-4}$.

5.2.1 Layer structure tests

The first set of tests were performed on a small size control set. The initial condition for the proliferating cells was parametrized by using the level set that describe the tumor boundary, as it is seen (and segmented) in the first image of the available sequence (*i.e.* for $t = 0$). Let us denote by $\phi(x)$ the implicit function whose zero isocontour coincides with the segmented boundary of the tumor. Then, the distribution for the proliferating cells reads:

$$P(x; 0) = P_0(x) = A \exp(-\delta\phi^2), \quad (5.18)$$

where A is the amplitude and δ is the steepness of the layer, that is, the inverse of its characteristic length. This condition is based on the well accepted hypothesis (confirmed also by experimental observations) that proliferating cells concentrates on the tumor boundary due to the presence of nutrients and better micro-environmental conditions. The other elements of the control set are the consumption rate of the proliferating cells (λ_P), that of the tumor tissue (λ_Y), the porosity ratio ($\chi = k_2/k_1$), the diffusivity coefficient (K). Thus, the control consisting in 6 parameters, 7 direct simulations are needed for each iteration of the descent algorithm.

Some constraints must be added to parameters in order to get admissible solutions. For the initial distribution of proliferating cells, it is important that $0 \leq A \leq 1$; moreover, $\delta \geq 0$, so that in the limit of a vanishing δ the distribution is uniform, but it is impossible to have a maximum of proliferating cells in the centre of the tumor. The porosity ratio must be a positive scalar ($\chi > 0$) for physical reasons. The penalization of the diffusivity have to satisfy $0 < K < 1$, in order to prevent that diffusivity is increased in the tumor region, which is unrealistic ($K > 0$) and to avoid an anti-diffusive behavior of γ ($K < 1$). An hypothesis concerns the consumption of γ : $\lambda_Y \leq 2 \cdot 10^{-2} \lambda_P$. A similar hypothesis is made for the non regularized Darcy model concerning the consumption of nutrients. These hypothesis were verified numerically. Let us suppose that c^n satisfy the constraints; it may happen that c^{n+1} does not: in this case the control at iteration $n + 1$ is modified such that the update fulfill all the requirements. In particular it is projected onto the constraint, the resulting update being on the constraint manifold. The constraint is, in this case, the boundary of the hypercube defined by the parameters intervals. So, if an update is such that, for example, $c_j^{n+1} > c_j^{max}$, then $c_j^{n+1} = c_j^{max}$.

This technique was tested first on a numerical testcase. In particular, a direct simulation was computed (parameters were randomly chosen) and taken as reference. A dataset of 12 images was recorded and used to validate the approach. The initial conditions for the tumor and the geometry were taken from a realistic case (called FER-II data set in the following). The computational domain was a square $[0, 8] \times [0, 8]$, the resolution 200×200 . Several tests were performed by changing the starting point and letting the algorithm evolve toward the solution according to the procedure described above. If the starting point coincides with the solution, the algorithm stay exactly in the solution. In all the other cases the error in L^2 norm was less than $2.5 \cdot 10^{-3}$. With 12 images no local minima were found even when the starting point was quite different to the solution (*i.e.* the fitting error greater than 20% in average, at the very first iteration of the algorithm).

After having validated the algorithm a realistic test was performed. Images were taken of a patient which has several metastases (primary tumor being in the thyroid).

In Fig.5.4 four scans covering an evolution over 45 months are presented. Even though this patient is affected by several metastasis, only the evolution of the one marked in Fig.5.4.a) will be studied here. Several tests were performed, varying the number of images used as input for the inverse problem. In particular, the tests with 2 and 5 images were performed. These allows to compare the behavior of PDEs models with that of ODE models and to understand if the chosen model is able to reproduce the growth dynamics in a satisfactory way.

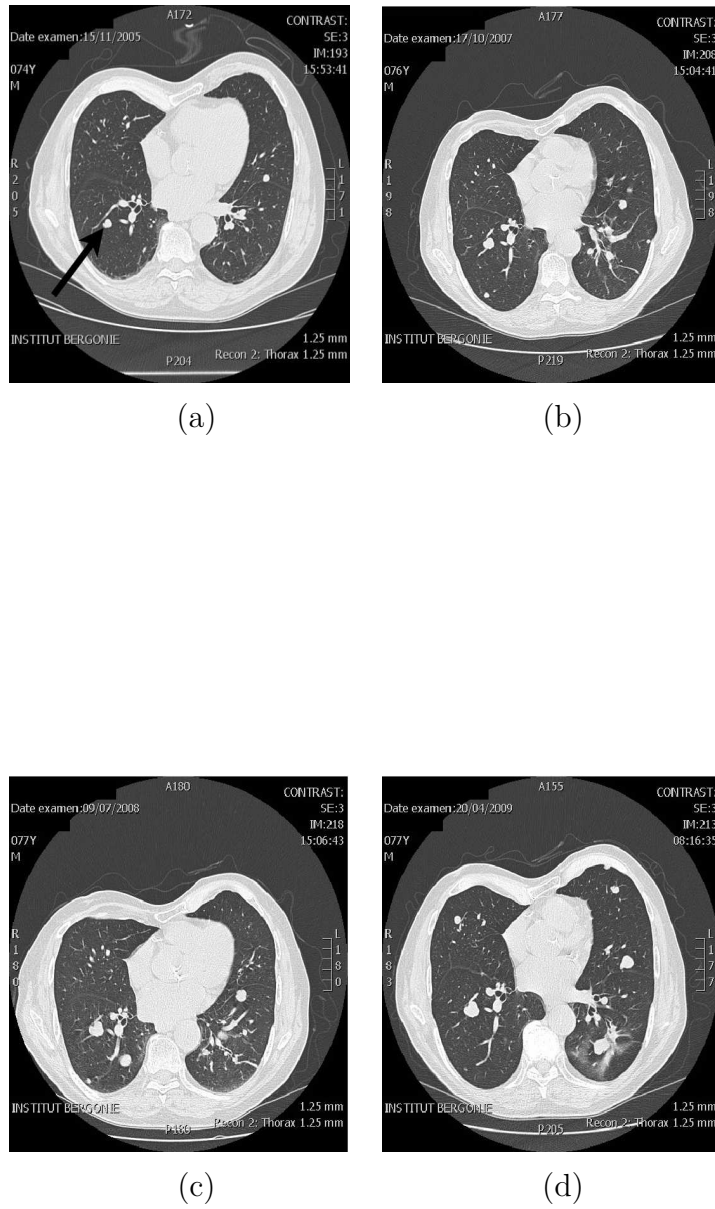


Figure 5.4: Scans: a) November 2005, b) October 2007, c) July 2008, d) April 2009

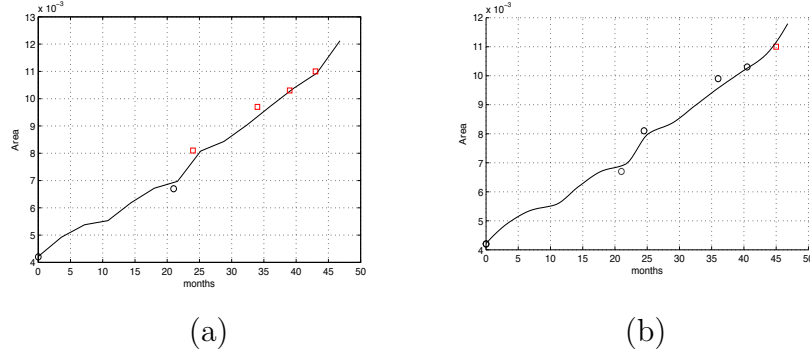


Figure 5.5: Curve of the evolution of the tumor area: identification with a) 2 images b) 5 images

Table 5.4: Data set and results for FER-II case, Regularized: 6 volumes measures are taken from 2D scans, resolution $1.25mm$.

<i>Month</i>	0	21.0	24.5	36.0	40.5	45.0
<i>Area</i>	4.2e-3	6.5e-3	8.1e-3	9.7e-3	1.03e-3	1.10e-3
$\mathcal{E}_{2Im}(\%)$	0.0	1.8	2.47	2.02	1.94	1.36
$\mathcal{E}_{5Im}(\%)$	0.0	1.8	1.23	3.03	0.48	1.09
$\ Y - Im\ _{2Im}$	0.0	0.22	0.24	0.35	0.31	0.24
$\ Y - Im\ _{5Im}$	0.0	0.22	0.24	0.33	0.29	0.22

The computational set up was the following one: the direct simulations were performed in a square domain $[0, 8] \times [0, 8]$ with a resolution of 200×200 . The final adimensional time was taken $T = 5$, that allows to represent the growth when $\max\{\gamma\} = \gamma|_{\partial\Omega_l} = 1$, where Ω_l is the lung boundary as it has been segmented in the first image of the sequence. For each direct simulation 20 frames of the growth are taken. The sensitivity technique was initialized in several points to avoid local minima and test convergence. The time needed to reach convergence for one sensitivity computation varies between 75 and 100 hours on one CPU.

The results in terms of volume are described in Fig.5.2.1. The curves are similar one each other, denoting that even with 2 images a good result is obtained. In Table 5.4 the errors are shown; the average error in volume (denoted by \mathcal{E}) when 2 images are considered is about 1.92% and it decreases to 1.53% when 5 images are used. The errors in L^2 norm are computed by the L^2 norm of the difference between the scan and the simulation at

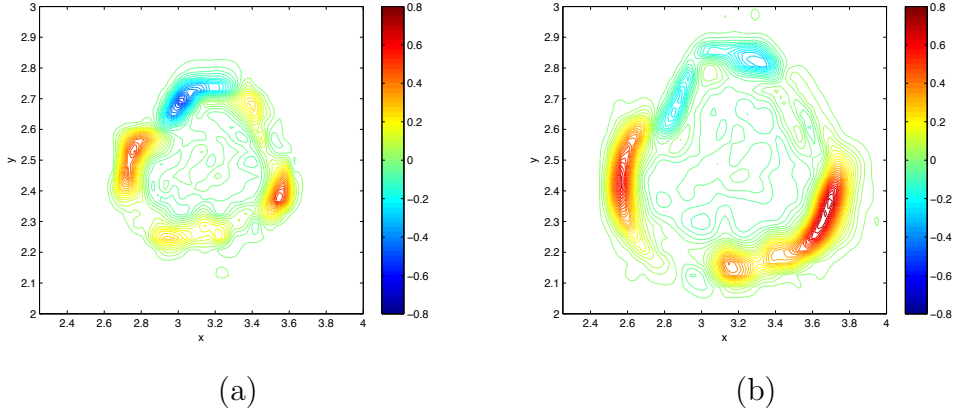


Figure 5.6: Contours of the difference between the scans and the simulation at time corresponding to a) the second image b) the last image. 40 isolines are plotted between the maximum and the minimum.

corresponding time, normalized by the L^2 norm of the scan. The trend when two or five data are used is practically the same, the values are not so different.

The space errors are investigated in terms of structures. In Fig.5.2.1 the difference between the scan and the simulated observable at corresponding time is shown when the identification performed with five images is considered. The contour plot are shown with 40 level lines between the minimum and the maximum. A zoom is represented in a window of coordinates $[2.25 - 4] \times [2 - 3]$. In Fig.5.2.1.a) error is represented with respect to the second scan, which was used for the identification, while in Fig.5.2.1.b) the error corresponding to the last image is plotted. The L^2 error is computed and normalized with the L^2 norm of the image. For the second scan it is 0.22 and for the sixth one 0.24. This is expected since the second scan was used for the identification procedure. However the difference is not too relevant. In particular the nature of the error is the same in the two cases: the differences are localized in a small region surrounding the segmented boundary, such that the error is more or less a zero average field. The volume is well captured, the recovered shape has still some errors.

The values of the recovered parameters when 5 images are used are the following ones: $\chi = k_2/k_1 = 5.377$, $K = 0.794$, $\alpha_N = 2.90$, $\alpha_S = 0.010$, $A = 0.9157$, $\delta = 75.5$. All the parameters have realistic values except for χ , which is too high (normal values are about 1.25). This is due to the fact that the error that affects the fitting is essentially concentrated on the tumor boundary. The Darcy model tends to regularize tumors, so that they tends to become less irregular while evolving. The mechanics of the system

is governed by the Darcy law. The divergence of the velocity play a major role in the evolution and control tumor volume. The vorticity, instead, influences the shape: its norm is induced by the parameter χ and it is different from zero in a small region surrounding tumor boundary. Increasing the value of χ diminishes the error on the shape. For higher values of χ the system could develop instabilities, which are not physical and prevent the inverse problem to be well conditioned.

Tests using 3 and 4 images were performed: the results are absolutely equivalent and thus, for sake of brevity, they are not reported.

An analysis is carried out on the sensitivity functions aiming at studying the properties of the obtained solutions. An analysis of the Hessian of the functional would require the computation of the adjoint system solution. Instead, we concentrate on the study of the property of the descent direction in correspondence of the numerical solution. It reads:

$$\frac{\partial J}{\partial c_k} = - \sum_i^{N_{Im}} \int_{\Omega} \mathcal{E}_i Z_k(x, t_i) d\Omega. \quad (5.19)$$

Using a Taylor development around the actual solution, the following is obtained:

$$\mathcal{E} = Im_i - Y(x, t_i) = Y(x, t_i) + \sum_j^{N_c} Z_j \Delta c_j - Y(x, t_i) + o(\Delta c_j^2). \quad (5.20)$$

This first order expansion is replaced into the expression for the descent direction, providing:

$$\frac{\partial J}{\partial c_k} \approx \sum_j^{N_c} \left(\sum_i^{N_{Im}} \int_{\Omega} Z_k Z_j d\Omega \right) \Delta c_j = \sum_j^{N_c} \langle Z_k, Z_j \rangle \Delta c_j, \quad (5.21)$$

that is, at first order, the descent direction is approximated by the product between the autocorrelation matrix of the sensitivities and a perturbation of the control. An analysis of the spectrum of the matrix tells us if there are directions in the control space that are not observable and that does not change the functional value in a significant way. Indeed:

$$\frac{\partial J}{\partial \mathbf{c}} \approx A \Delta \mathbf{c}, \quad \Delta \mathbf{c} = \sum_i^{N_c} a_i v^{(i)}, \quad (5.22)$$

where $v^{(i)}$ is the i -th eigenvector of A , the autocorrelation matrix of the sensitivities. Since eigenvectors form an orthonormal bases of the space a_i are uniquely defined and represents the projection of $\Delta \mathbf{c}$ on the i -th eigenvector. This expression is substituted

into the approximation of the descent direction, leading to:

$$\frac{\partial J}{\partial \mathbf{c}} \approx \sum_i^{N_c} a_i A v^{(i)} = \sum_i^{N_c} a_i \lambda_i v^{(i)}, \quad (5.23)$$

and λ_i is the i -th eigenvalues of A . if exist a $\lambda_i \approx 0$ this moving parallel to the i -th eigenvector does not make the functional vary at the first order. Conversely, this mean that the direction represented by the i -th eigenvector is not observable, there is no descent, so that the solution does not move in that direction, the parameter behaves more or less as a constant.

The analysis of the spectrum was performed and what follows was obtained: $\Lambda = \{1.10, 0.11, 8 \cdot 10^{-3}, 4 \cdot 10^{-4}, 2 \cdot 10^{-4}, 2 \cdot 10^{-7}\}$. The direction that corresponds to the higher eigenvalue is aligned with the direction that corresponds to the modification of the parameter that corresponds to the consumption of Y , which is constrained to be positive and not too high. The eigenvector corresponding to the smallest eigenvalue is aligned with the change in δ alone. This is probably due to the fact that the resolution of the layer is not sufficient, thus small changes in this parameter does not affect the simulation very much.

This computation may be used to precondition the descent and accelerate the converge. It is not as efficient as the knowledge of the Hessian but it may be helpful in accelerate the convergence.

5.2.2 Extending the control by harmonics

In order to see what the effect of the control set is on the solutions, a larger control set was tested, with the regularized Darcy model, exactly in the same conditions used for the tests shown in the previous section. We focus on the influence of the parameters determining the initial conditions: in this case harmonics are introduced as function of $\theta = atan(y/x)$. The expression for P_0 takes the following form:

$$P_0 = \left[\sum_{k=0}^{N_h} \alpha_k \cos(2\pi k\theta + \zeta_k) \right] \exp(-\delta\phi^2), \quad (5.24)$$

where α_k is the amplitude of the k -th harmonic and ζ_k its phase shifting. For the tests performed $N_h = 2$, so that 5 parameters describes the initial distribution for P . The constraint for the distribution has to be considered: there is no constraint for the phase shift. For the amplitudes the following must hold:

$$0 < \alpha_0 < 1, \quad (5.25)$$

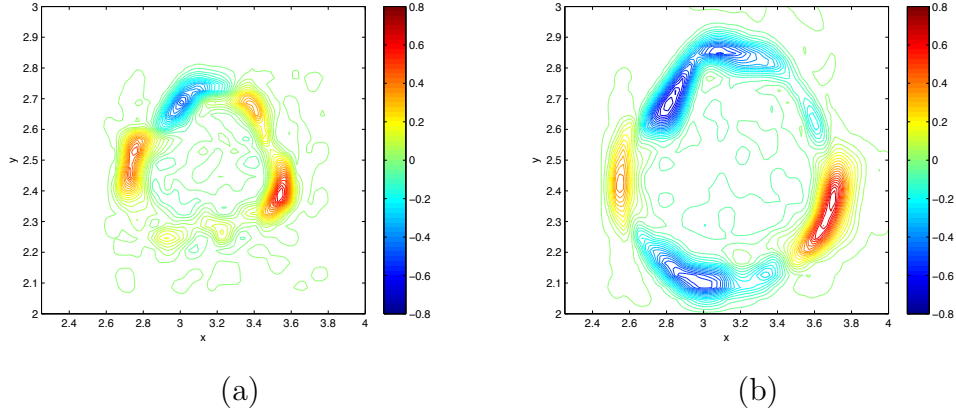


Figure 5.7: Contours of the difference between the scans and the simulation at time corresponding to a) the second image b) the last image. 40 isolines are used between the maximum and the minimum.

which means that the average of the amplitude of P_0 is in $(0, 1)$. Then, two conditions have to be satisfied:

$$\begin{aligned} \alpha_0 + \sum_{k=1}^{N_h} |\alpha_k| &< 1, \\ \alpha_0 - \sum_{k=1}^{N_h} |\alpha_k| &> 0, \end{aligned} \tag{5.26}$$

that is a sufficient condition for the proliferating cells density to be admissible. The test when 5 images are taken has been performed, since it represents the best possible fitting for the model, so that it tells us if a significant improvement is due to the use of an extended control.

In terms of volume there are no significant differences in the fitting, so that, for the sake of brevity the results will not be reported. Let us investigate, instead, the space error structure. The test was stopped when the same average error of the best fitting solution obtained with the layer structure control (see the previous section) was reached. In Fig.5.7 the zoom of the difference between the scan and the simulation is shown. The structure is slightly different, the characteristic dimension of the structures is different, they are smaller, and this is expected. Though, the same phenomenon highlighted in the previous section is observed, concerning the nature of the error; it does not change between an image used for the identification and the prediction. This is due to the regularizing character of the model used and to the fact that geometrical imperfections in the tissue

are not rendered.

The initialization of the optimization procedure was performed according to the procedure used for all the other tests, excepted for the harmonics, that were initialized to zero for all the tests.

Local minima appears with this extended control and the problem is more difficult to solve. In particular one solution corresponds to that obtained with the layer structure control (harmonics coefficients are null), the others have a modulation of the amplitude with the angle θ . The parameters values obtained are: $\chi = 3.30$, $K = 0.49$, $\alpha_N = 2.91$, $\alpha_S = 0$, $\alpha_0 = 0.5294$, $\delta = 38.74$, $\alpha_1 = 0.159$, $\zeta_1 = -0.676$, $\alpha_2 = -0.26$, $\zeta_2 = 1.36$. Let us remark that the ratio between permeabilities is decreased with respect to the layer structure control set and the diffusivity penalization too. This is the main effect and it is due to the presence of harmonics in the layer, that are able to render the shape in a slightly better way. The oxygen consumption rate does not change in a significant way, due to the fact that it influences the global behavior (the volume attained) and dynamics.

An analysis of the spectrum of the autocorrelation of sensitivities was performed in this case. The results are similar to those obtained with the layer structure control for what concerns the maximum and the minimum of the eigenvalues.

Extending the control with the regularized Darcy Model allows to have better performances in terms of shape recovery. The parameter describing the permeability ratio between the tumoral and the healthy tissue vary significantly with respect to the tests performed without harmonics. The other parameters are not affected so much. The drawback of extending the control in this direction is the appearance of local minima that make the system more difficult to deal with.

5.3 Testing other models

In this section some tests performed by adopting other models are detailed. First, the performance of the identification are investigated when the model proposed by Enault (see for instance [66]) is used. Let us briefly recall it:

$$\begin{aligned}\dot{Y} + \nabla \cdot (\mathbf{v}Y) &= cY, \\ \nabla \cdot \mathbf{v} &= cY, \\ \mathbf{v} &= (1 + \chi Y)\nabla\Pi.\end{aligned}\tag{5.27}$$

The parameter c is constant and represent the inverse of the characteristic time scale of the system, Y is the observable and χ is the permeability ratio.

Table 5.5: Data set and results for FER-II case, One specie incompressible model: 6 volumes measures are taken from 2D scans, resolution $1.25mm$.

<i>Month</i>	0	21.0	24.5	36.0	40.5	45.0
<i>Area</i>	4.2e-3	6.5e-3	8.1e-3	9.7e-3	1.03e-3	1.10e-3
$\mathcal{E}_{3Im}(\%)$	0.0	4.54	1.26	4.12	4.76	0.87
$\ Y - Im\ _{3Im}$	0.0	0.50	0.44	0.46	0.42	0.35

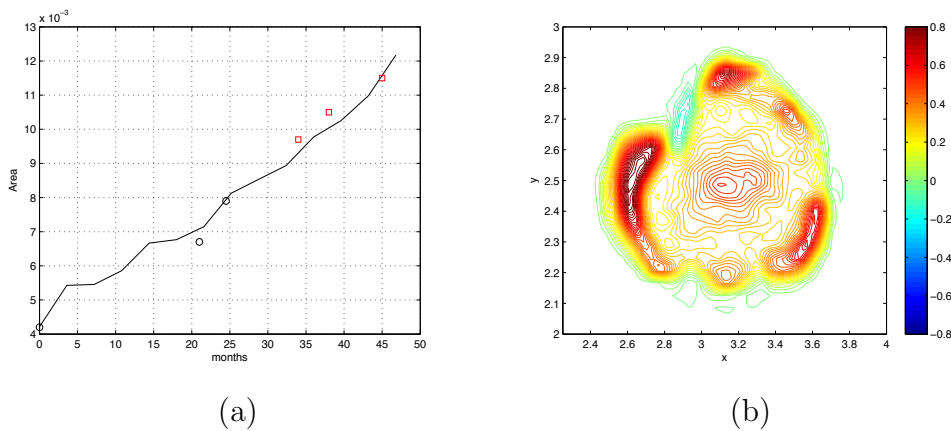


Figure 5.8: FER-II dataset analysis: a) Volume curve with respect to months b) Contours of the difference between scans and images for the first prediction, that is the fourth scan.

Let us describe the results obtained on the FER-II dataset when three images are used for the identification. The objective of this test is to see if a simple model, whose dynamics mimics the Darcy model, is able to take the main features of the propagation into account when a small control set is chosen. In particular two scalar parameters are set up: the proliferating rate (c) and the proportion of cancerous cells at the very beginning ($Y(0)$). The observable is taken as the characteristic function of Y . In Table 5.5 the results of the numerical experiments are shown. The model identified with three images has a greater error in fitting with respect to the Darcy model identified with two images. Indeed the average error in volume is about 3.11% with respect to the 1.92% obtained with the more complex model. The same trend in the errors may be observed in the L^2 errors, concerning the shape. In Fig.5.3.a) the volume curve is plotted. Again, the continuous line is the simulated evolution, the black circles represents the area of the scans used as data and the red squares are the measures that have to be predicted. The

curve confirms substantially what commented about the errors. The fitting is less good if compared to the one obtained using the Darcy model, but the growth process is well captured. Moreover, in spite of the use a very small control set, the main features of the propagation are represented and the errors have the same order of magnitude. This model may suffer in cases in which a plateau type of solution appears (as the model proposed by Simeoni), since there is no mechanism which can regulate or inhibit the growth.

In Fig.5.3.b) the difference between the fourth scan and the simulation is shown (40 contours lines are plotted between the maximum and the minimum). Peculiar structures localized around the tumor boundary appear, highlighting the fact that the shape is regulated approximately in the same way as in the more complex model. Thus, the complexity of the Darcy model acts on the dynamics, allowing to represents a wider range of growths. Little improvements are obtained on what concerns the representation of the shape.

Chapter 6

Residual Based Approach

In this chapter a residual based approach is presented, aiming at reducing the cost of the inverse problem. The proposed technique is based on the use of Proper Orthogonal Decomposition to build up a regularization for the inverse problem.

In the first section a summary of some preliminary tests are outlined: the goal is to show if and whether a residual based computation is effective. Then, the technique used for the model reduction is presented and the whole method detailed. In the following section some analytical tests are presented. The comparison with the sensitivity approach in the same numerical conditions is described and in the last section several realistic test cases are commented.

For all the study of the reduced order approach the two species Darcy model was used. It is recalled hereafter:

$$\begin{aligned}
\frac{\partial Q}{\partial t} + \nabla \cdot (\mathbf{v}Q) &= (1 - \gamma)P, \\
\frac{\partial P}{\partial t} + \nabla \cdot (\mathbf{v}P) &= (2\gamma - 1)P, \\
\nabla \cdot \mathbf{v} &= \gamma P, \\
\mathbf{v} &= -k(Y)\nabla\Pi, \\
\nabla \cdot (D(Y)\nabla C) &= \alpha PC + \lambda C, \\
\gamma &= \frac{1 + \tanh(R(C - C_{hyp}))}{2}.
\end{aligned} \tag{6.1}$$

Again, $Y = P + Q$ is the total density of tumor cells.

6.1 Preliminary inverse problems

The first inverse problems we solved are briefly presented. The objective is to study the possibility to rely on the residual of the equations to recover the unknown fields and parameters, thus transforming the inverse problem into an algebraic non-linear optimization. Several possibilities arise, the choices and the main results are discussed.

In particular the first inverse problem is a simple algebraic problem in which only a scalar is sought. Then, informations amount is decreased in order to approach realistic situations, in which, as already commented, it is scarce.

6.1.1 Identification of porosity

The first problem is the following one: identifying the porosity field $k(P, Q)$ knowing $P, Q, \gamma(C)$. If the unknown is simply the porosity field the solution can be computed

using a least square method with a Tikhonov regularization, that prevents numerical propagation of error due to singularities, i.e. zero velocity in certain domain regions.

Since the direct equations are used the time derivative of populations densities \dot{P}, \dot{Q} , see Eq.(4.1, 4.2) are needed.

The first choice is to use finite differences and so, supposing that two snapshots are given, sufficiently close in time, we write:

$$\dot{P} \approx \frac{P(t_1) - P(t_0)}{t_1 - t_0}, \quad \dot{Q} \approx \frac{Q(t_1) - Q(t_0)}{t_1 - t_0}. \quad (6.2)$$

Numerical tests were done in this configuration: one blood vessel sufficiently far from the tumor, Dirichlet boundary conditions for both the pressure field and the oxygen concentration. In such a configuration the system Eq.(4.1-2.19) can be written in the following manner:

$$\mathbf{v} \cdot \nabla P = (2\gamma - 1)P - \gamma P^2 - \dot{P}, \quad (6.3)$$

$$\mathbf{v} \cdot \nabla Q = (1 - \gamma)P - \gamma PQ - \dot{Q}, \quad (6.4)$$

$$\nabla \cdot \mathbf{v} = \gamma P, \quad (6.5)$$

$$\mathbf{v} = -k\nabla\Pi, \quad (6.6)$$

where the right hand side is known. For computational purposes the curl of the Darcy law is taken. The above system, denoting with w_1 and w_2 the right-hand side of the mass conservation equations (that we know since P, Q, γ are known), becomes:

$$(\partial_x P)V_x + (\partial_y P)V_y = w_1, \quad (6.7)$$

$$(\partial_x Q)V_x + (\partial_y Q)V_y = w_2, \quad (6.8)$$

$$\nabla \cdot \mathbf{v} = \gamma P, \quad (6.9)$$

$$k\nabla \wedge \mathbf{v} = \nabla k \wedge \mathbf{v}. \quad (6.10)$$

The first two equations being decoupled, the velocity field is computed directly. By using a least square method the following is found:

$$R_1^2 = ((\partial_x P)V_x + (\partial_y P)V_y - w_1)^2 \quad (6.11)$$

$$R_2^2 = ((\partial_x Q)V_x + (\partial_y Q)V_y - w_2)^2 \quad (6.12)$$

$$\overline{V_x}, \overline{V_y} = \arg \min \{ R_1^2 + R_2^2 + \alpha_1 (V_x^2 + V_y^2) \}, \quad (6.13)$$

where α_1 is the Tikhonov regularisation constant, chosen by the L-curve method. Once the velocity found, the porosity is solved in a similar manner.

The porosity field is reconstructed with an error that is smaller than 5%, in norm L^2 , for all the treated cases. The error is particularly low when potential or near potential flows $k \approx 1 + \epsilon(x, y)$, $\epsilon \ll 1$ are considered and when the system is identified in the first part of the avascular history, let us say at 10 – 20%. This is due to the fact that in this phase the mechanical aspects of the propagation, that are directly linked to porosity, are particularly important.

6.1.2 Simplified logistic-type model: identifying porosity and hypoxia function

In the second case porosity and hypoxia function γ are sought, the latter supposed to be constant. This is equivalent to identify the Darcy-type model with a simple logistic type model, similar to the one described in [38].

As in the previous case an approach based simply on the PDE system is possible. Let us assume that two subsequent snapshots of P and Q are given. This is sufficient to make the problem well defined. The system of equations to be solved is:

$$(\partial_x P)V_x + (\partial_y P)V_y = (2P - P^2)\gamma - (P + \dot{P}), \quad (6.14)$$

$$(\partial_x Q)V_x + (\partial_y Q)V_y = (-P - PQ)\gamma + (P - \dot{Q}), \quad (6.15)$$

$$\partial_x V_x + \partial_y V_y = \gamma P, \quad (6.16)$$

$$k \nabla \wedge \mathbf{v} = \nabla k \wedge \mathbf{v}, \quad (6.17)$$

The equations written above can be decoupled: the first three equations can be solved as done before using a least square method. The solution for the velocity field is thus injected into the curl of the Darcy equation to obtain the porosity. Several tests were performed in different numerical configurations: some numerical instability was found.

Indeed, an approach based simply on the described techniques is not always stable from a numerical point of view. Therefore there are cases in which the identification can not be performed directly using the PDEs system. Moreover, some tests were done in which the data amount was decreased, in order to approach realistic applications. The chosen observable was $Y = P + Q$ instead of P and Q . In these cases the problem results ill conditioned, preventing a residual based approach to be satisfactory. A regularization is looked for, such that the problem becomes affordable.

6.2 Regularization by Proper Orthogonal Decomposition

When the number of data decreases (the observable is only $Y = P+Q$) the inverse problem becomes more and more ill conditioned. In the literature regularization approaches are discussed in order to overcome this peculiar feature of inverse problems ([92, 21, 153, 95] for a comprehensive overview). In [153] the regularization process is studied in a statistical context, in [95] a discussion on regularization and model reduction effects is detailed. A polynomial chaos acceleration is commented in [112]. The regularization consists in looking for a solution in a different space (often of reduced dimension), in such a way that the resulting problem is better conditioned than the original one.

For the present work Proper Orthogonal Decomposition (POD) is used to set up a regularization for inverse problems. A detailed presentation of the technique is provided in [147, 90]. This approach was proposed for population dynamics in [165], and it is widely used in fluid mechanics to study the arising of coherent structures (see [90]), for model reduction (as in [32]) or in flow active control (see [161]).

Let us detail the Sirovich method for the POD decomposition. Given a solution $u(x, t; \pi_k)$, where π_k is the k -th parameter influencing the solution, a database of snapshots (N_s is their number) is built, consisting in the time frames collection of the simulated solutions. The i -th snapshot of the database is $u_i = u(x, t_i; \pi_k)$. The POD approach consists in looking for a basis ϕ_j , $j = 1, \dots, N_u$, where N_u is fixed, in such a way that the L^2 representation of u is maximized, that is:

$$\phi_i = \arg \min_{\tilde{\phi}_j} \left\{ \sum_k^{N_p} \int_0^T \int_{\Omega} (u(x, t; \pi_k) - \sum_j^{N_u} a_j(t, \pi_k) \tilde{\phi}_j(x))^2 dx dt \right\}. \quad (6.18)$$

The Sirovich hypothesis consists in stating that $\phi_j = \sum_h^{N_s} c_{jh} u_h$, that is, the modes are expressed as linear combination of the snapshots themselves. Introducing this into the minimization leads to an eigenvalue problem whose solution is:

$$\phi_j = \sum_h^{N_s} \frac{b_h^{(j)} u_h}{\lambda_j^{1/2}}, \quad (6.19)$$

where $b_h^{(j)}$ is the h -th component of the j -th eigenvector of the autocorrelation matrix

$$A_{ij} = \int_{\Omega} u_i u_j dx, \quad (6.20)$$

and λ_j the corresponding eigenvalue.

The representations of the variables that are not observed and that play a role in the dynamics of the models used for this work have been investigated. A database was built simulating the Darcy model in a squared domain. The growth of a tumor attracted by a blood vessel was simulated, varying the following parameters: $\chi = k_2/k_1$, $\eta = K/D_{max}$, α , C_{hyp} , λ . The domain is the square $[0, 8] \times [0, 8]$, the vessel is located at $x_0 = (3, 4)$, the tumor is initialized at the center. The vessel is simulated by a circle in which the oxygen concentration is fixed at $C_{bv} = 0.15$. More details on this testcase are provided in the following sections.

The database was built as follows: 576 simulations were done, taking 20 time frames each one. The parameters were varied in the intervals:

- $\chi = k_2/k_1$: $[0.50, 1.0, 1.5, 2.0]$, $k_1 = 1$ for all the simulations,
- $\eta = K/D_{max}$: $[0.10, 0.45, 0.80]$, $D_{max} = 2$ for all the simulations,
- α : $[0.1, 1.0, 3.0, 5.0]$,
- C_{hyp} : $[0.05, 0.045, 0.085, 0.125]$, $\max_{\Omega} \{C\} = 0.15$,
- λ : $[0.001, 0.1, 0.5]$.

For the Darcy-type model the unknowns are P, Y, C, γ, Π (or \mathbf{v}). There are two possibilities to build the regularization basis: the first one consists in extracting a unique vector basis, taking all the variables into account as components of the same vector field. The second one consists in looking for a separated expansion for each variable. This second option was chosen as the involved variables have different meanings and they are inhomogeneous from a physical standpoint. Let us show the POD eigenfunctions for the first modes of C and P for this testcase. For the other cases treated the POD eigenfunctions have a similar behavior and for the sake of brevity it will not be detailed. In Fig. 6.1.a (upper line) the first eigenfunction is shown, which is the average of the oxygen fields. The blood vessel is recognized. In the other modes the presence of the tumor becomes more evident: it induces some variations due to the consumption and its motion toward the blood vessel.

In Fig. 6.1 (lower line) the eigenfunction for the proliferating cell density are shown. They are compactly supported, since proliferating cells are, $\forall t \in [0, T]$. P is moving toward the blood vessel so the movement is rendered by the wavy structure. The higher the mode number the higher the wave number of the wave. The quantitative properties of representation of the modes have been investigated too. In Fig.6.2 the L^2 represen-

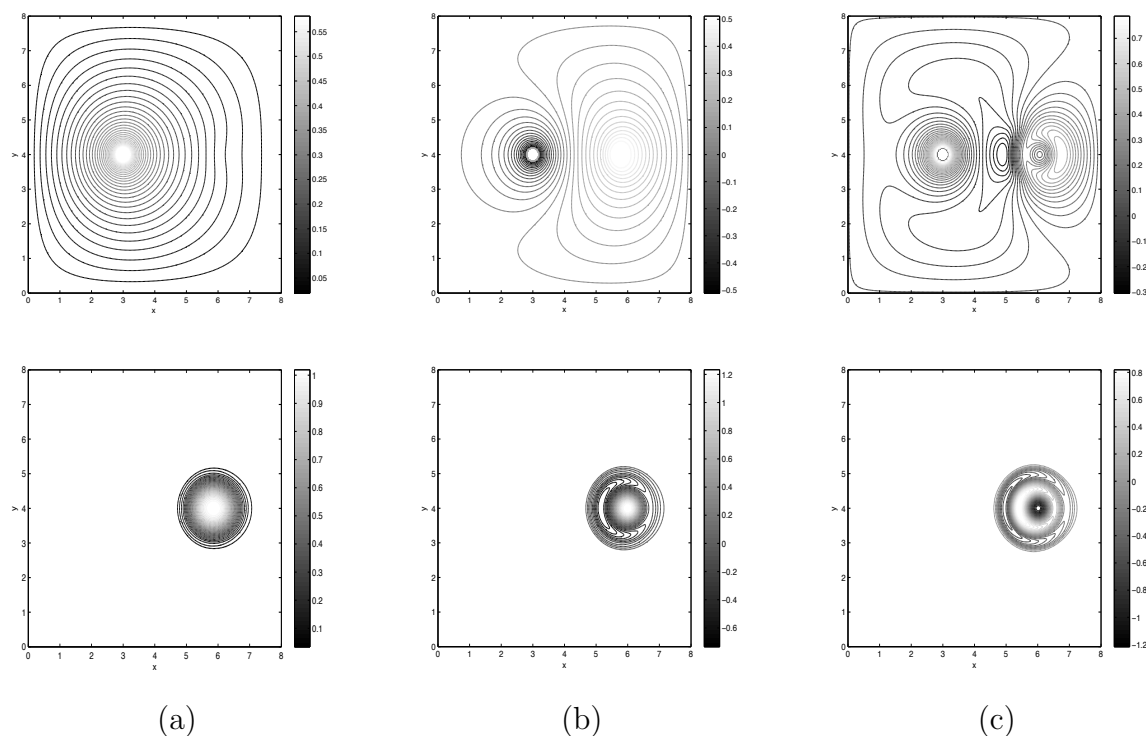


Figure 6.1: Eigenfunctions for the oxygen field (above) and for proliferating cells (below):
 a) First b) Second c) Third

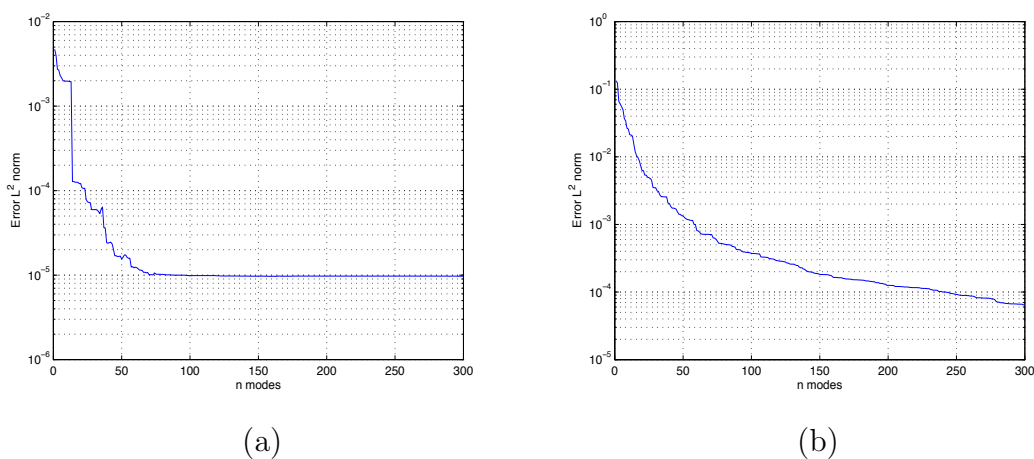


Figure 6.2: L^2 representation with respect to the number of used modes for a) oxygen and b) proliferating cells density; the database for the Darcy model was used.

tation error for the oxygen (a) and for proliferating cells density (b) is represented as function of the number of POD modes, when the setting presented in case I, detailed below, is adopted. A novel simulation, that does not belong to the database (initialized with random parameters) was performed and then L^2 error was computed when fields were reconstructed with an increasing number of POD modes. The error is quite similar between the two, but for oxygen it decreases faster. This is due to the fact that oxygen is governed by a diffusion equation, while proliferating cells evolve driven by a transport and their support evolves during the simulation. More POD modes are needed to take this non-global behavior into account for proliferating cells.

6.3 Reduced Order Technique

In this section the reduced technique is presented. It is composed by two stages: the *offline* and the *online* ones. The former consists in the construction of the database for a given case (*i.e.* a geometry, an initial tumor location and shape, a model) and in the extraction the POD basis for all the variables that are not observed. Then, in the *online* case, the expansion is injected into the equations and inverse problems is solved. In this section these passages are commented and the whole technique outlined.

Let us set up the reduced approach for the Darcy model; the observable evolution is governed by:

$$\dot{Y} + \nabla \cdot (Y \mathbf{v}) = \gamma(C)P. \quad (6.21)$$

the divergence of the velocity field obeys:

$$\nabla \cdot \mathbf{v} = \gamma(C)P - \frac{\int_{\Omega} \gamma P \, d\Omega}{\int_{\Omega} (1 - Y) \, d\Omega} (1 - Y), \quad (6.22)$$

where the expression relative to Neumann boundary condition for the pressure field was retained. In the case of Dirichlet boundary conditions the second term of the right hand side of this equation vanishes. The curl of the Darcy law reads:

$$k(Y) \nabla \wedge \mathbf{v} = \nabla k(Y) \wedge \mathbf{v}. \quad (6.23)$$

and the equation for the oxygen concentration field is written:

$$\nabla \cdot (D(Y) \nabla C) = \alpha PC + \lambda C. \quad (6.24)$$

The definition of the hypoxia function, γ , is unchanged.

The repeated index summation convention is used from now on. The observable is, again $Y = P + Q$, the non observed variables are expressed as combination of POD modes:

$$\begin{aligned} P &= a_i^P \phi_i^P & i = 1, \dots, N_P; \\ C &= a_i^C \phi_i^C & i = 1, \dots, N_C; \\ \gamma P &= a_i^{\gamma P} \phi_i^{\gamma P} & i = 1, \dots, N_{\gamma P}; \\ \mathbf{v} &= a_i^v \phi_i^v & i = 1, \dots, N_v, \end{aligned} \quad (6.25)$$

where $a_i^{(\cdot)} = a_i^{(\cdot)}(t)$ are scalar functions of time, $\phi_i^{(\cdot)} = \phi_i^{(\cdot)}(\mathbf{x})$ are functions of spatial coordinates.

The dimension of the empirical functional space, *i.e.*, the number of POD modes used to reconstruct the solution, is chosen such that if additional POD modes are included, the reconstruction of a given field does not vary up to a certain error value that, in this work, was fixed at 10^{-4} in L^2 norm.

Substituting these expressions in the system Eqs. (6.21) and (6.24) we obtain:

$$\dot{Y} + a_i^{(v)} \nabla \cdot (Y \phi_i^{(v)}) = a_i^{(\gamma P)} \phi_i^{(\gamma P)}, \quad (6.26)$$

$$a_i^{(v)} \nabla \cdot \phi_i^{(v)} = a_i^{(\gamma P)} \phi_i^{(\gamma P)} - \frac{\int_{\Omega} a_i^{(\gamma P)} \phi_i^{(\gamma P)} d\Omega}{\int_{\Omega} 1 - Y d\Omega} (1 - Y), \quad (6.27)$$

$$a_i^{(v)} k(Y) \nabla \wedge \phi_i^{(v)} = a_i^v \nabla k(Y) \wedge \phi_i^{(v)}, \quad (6.28)$$

$$a_i^{(C)} \nabla \cdot (D(Y) \nabla \phi_i^{(C)}) = \alpha a_j^{(P)} a_i^{(C)} \phi_j^{(P)} \phi_i^{(C)} + \lambda a_i^{(C)} \phi_i^{(C)}, \quad (6.29)$$

The hypoxia function γ , Eq. 2.21, is multiplied by P , in such a way that the product γP is:

$$a_i^{(\gamma P)} \phi_i^{(\gamma P)} = a_j^{(P)} \phi_j^{(P)} \frac{1 + \tanh(R(a_i^{(C)} \phi_i^{(C)} - C_{hyp}))}{2}. \quad (6.30)$$

System (6.26-6.29) is solved by minimization of the residuals under certain constraints that are introduced below.

The first one is linked to the fact that Eq. 6.29 is an homogeneous equation with respect to the coefficients $a_i^{(C)}$. This is due to the fact that, if the equation is in this form, non-homogeneous boundary conditions are imposed, or a source term describing some nutrients supply is added. Otherwise, one possible solution of the oxygen diffusion equation is the trivial one. Indeed, if $C_{hyp} < 0$ such a solution would be also a solution for the whole system Eqs. (6.26) and (6.30). In order to prevent the identification of a system with unphysical solutions we can proceed in two different ways. One consists in

discretizing the boundary conditions for oxygen, getting one scalar constraint, exactly as in the Petrov-Galerkin method. In the case of Dirichlet boundary conditions $C = C_0$ on $\partial\Omega_C$ where Ω_C is a blood vessel domain, one scalar equation is obtained of the form:

$$\sum_i \left(\frac{\sum_j b_j^i}{\lambda_i^{1/2}} \right) a_i^{(C)}(t) = 1, \quad \forall t. \quad (6.31)$$

Another option is to lift the solution and transform Eq. 6.29 into a non-homogeneous equation, with source terms. Both these approaches yield similar results in terms of inverse problem solution and hence in this work we simply lift the solution.

The system Eq.(6.26-6.29) can be solved by adopting two different strategies: performing a Galerkin projection, or using a least square technique. Performing a Galerkin projection implies to solve an inverse problem for a reduced order model, whose residual is orthogonal to the representation space. Dynamical approximations of such a model were investigated, finding that it captures the main physical aspects of propagation, but it is not always accurate. An alternative approach is to use a least square technique.

At a given time (say t_0), the snapshot $Y(t_0)$ and a subsequent snapshot $Y(t_1)$ are used to perform the computation of the time derivative. Let the residual of the l -th equation be R_l . We write $F = \sum_l R_l^2$ and

$$\left(a_i^{(\cdot)}(t_0), \pi_j \right) = \operatorname{argmin}(F) \quad (6.32)$$

where $a_i^{(\cdot)}$ are the expansion coefficients for the variables $P, C, \mathbf{v}, \gamma P$ and π_j are the parameters to be identified.

The second constraint to be imposed in the minimization results from the observation that, since in the inverse problem the equation for the variable P is not solved, the latter does not automatically satisfy: $0 \leq P \leq 1$ and therefore this is a constraint (fundamental for the population dynamics) to be imposed. To this end the residuals are penalized as follows:

$$\tilde{F} = F + c_1(\max\{a_i^{(P)}\phi_i^{(P)}\} - 1) + c_2(-\min\{a_i^{(P)}\phi_i^{(P)}\}) \quad (6.33)$$

where c_1, c_2 are positive numbers, set in such a way that penalization does not affect the stability of the procedure (in the present work $(c_1, c_2) \in [1.0, 2.5]e - 2$). The inverse problem finally takes the form of a non-linear algebraic optimization problem, that is solved using a Newton trust region method (see [87] for a Levenberg-Marquardt version applied to inverse problems).

In order to decrease the computational cost of the procedure a third constraint is imposed to define a feasible set of solutions. In particular, let $a_i^{(P)}(t_0)$ be the i -th POD

coefficient relative to the variable P evaluated at the time t_0 . The maximum and the minimum values reached by the coefficient $a_i^{(P)}(t)$ in the database can be calculated on the basis of the auto-correlation matrix of the variable. Indeed, the definition of the i -th POD mode implies that:

$$\phi_i^{(P)} = \frac{b_j^i P_j}{\lambda_i^{1/2}} \implies a_{ik}^{(P)} = \langle P_k, \phi_i^{(P)} \rangle = \frac{1}{\lambda_i^{1/2}} \langle P_k, b_j^i P_j \rangle \quad (6.34)$$

where $a_{ik}^{(P)}$ denotes the projection of the k -th snapshot of P on the i -th eigenvector.

From the definition of the eigenvector we finally obtain:

$$a_{ik}^{(P)} = \frac{1}{\lambda_i^{1/2}} \langle P_k, P_j \rangle b_j^i = \lambda_i^{1/2} b_k^i \implies \max_k \{a_{ik}^{(P)}\} = \lambda_i^{1/2} \max_k \{b_k^i\}. \quad (6.35)$$

The same holds for the minimum of the coefficient. Thanks to this relationship the interval of excursion I_k^{db} of the projection coefficients is estimated as follows:

$$I_k^{db} = [\min\{a_{ik}^{(P)}\}, \max\{a_{ik}^{(P)}\}]. \quad (6.36)$$

The solution is asked to be not too different from the simulations of the direct problem, since a database is built in which the biological behaviors of the variables are represented. Thus we restrict the admissible values of the POD coefficients to an interval I_k that is obtained from I_k^{db} by a stretching factor $1 + \delta$ where δ is a suitable positive number. In all the following simulations the value $\delta = 0.1$ was adopted. It should be noted that this choice still allows the procedure to identify solutions that are different with respect to the solution of the database. This procedure is repeated for all the variables included in the database.

6.3.1 Time interpolation

The hypothesis that two subsequent snapshots are close in time, or, in other words, that the time between two snapshots is small if it is compared with the characteristic evolution time of the phenomenon, is very optimistic. In order to relax this hypothesis, instead of using first order finite differences, that is equivalent to perform a linear interpolation between the snapshots, a different kind of interpolation is used. However, an higher order finite difference scheme, equivalent to a polynomial interpolation, would require a large number of snapshots. As an alternative, still assuming that only two images are available,

an additional hypothesis about the growth rate could be retained. Here, two cases are considered. In the case of exponential growth we write:

$$\dot{Y} \approx A \exp\{\zeta t\} + B \exp\{-\zeta t\} = f(\zeta), \quad (6.37)$$

where A, B are chosen in such a way that the two available snapshots are interpolated. One parameter, ζ , is free and enters the residual minimization process. The first equation of the system (6.21-6.24) becomes:

$$f(\zeta) + \nabla \cdot (a_i^{(v)} \phi_i^{(v)} Y) = a_i^{(\gamma P)} \phi_i^{(\gamma P)}. \quad (6.38)$$

In the case of a logistic-type growth we proceed in a similar way. We take

$$Y \approx AG(\omega, \sigma) + BG(-\omega, -\sigma) \quad (6.39)$$

where

$$G(\omega, \sigma) = \frac{\omega e^{\omega t}}{\omega - \sigma e^{\omega t}}. \quad (6.40)$$

As before A and B are adjusted such that the snapshots are interpolated. In this case, however, we are left with two free parameters (ω and σ) that are found within the residual minimization process.

6.4 Analytical testcases

In this section a synthetic validation of the technique is proposed. The identification of a Stokes-type flow using a Darcy-type model is described in two different physical situations. The aim of the tests commented in this section is twofold. First, it is a sort of emulation of realistic applications, in which a parametric model is used to describe the evolution of a more complex system, which may not obey the simple laws adopted. Second, this test highlights the possibility to apply inverse problems to build a hierarchy of models: if a simple model is able to recover the solution of a more complex one (with an acceptable error), it can be profitably used for realistic applications and preferred to the more complex one, since in general it is easier to deal with.

The equations describing a Stokes flow are the following ones:

$$\nabla \cdot \sigma + \nabla p = 0 \quad (6.41)$$

$$\sigma = \nu (\nabla \mathbf{v} + \nabla^T \mathbf{v}) \quad (6.42)$$

Table 6.1: Relative projection error as a function of the number of POD modes N_P and of the time instant considered T .

N_P	$T = 0$	$T = 5$	$T = 10$	$T = 15$
5	5.18e-2	9.64e-2	15.10e-2	15.68e-2
10	3.85e-2	5.12e-2	5.81e-2	9.13e-2
15	2.64e-2	3.62e-2	3.12e-2	4.45e-2
20	1.53e-2	2.38e-2	2.42e-2	3.51e-2
25	1.12e-2	1.44e-2	1.91e-2	2.52e-2

where ν is the kinematic viscosity, σ is the stress tensor, p is the pressure field. In order to perform the identification, two subsequent snapshots are taken from the numerical simulations of a Stokes-type flow. These snapshots are considered as if they were part of the evolution of a Darcy-type flow.

To solve the inverse problem the procedure described in the previous section is followed. To this end, a database of solutions of the Darcy-type flow is built, eigenfunction basis is extracted, the inverse problem is regularized and residuals are minimized. It is important that eigenfunctions are extracted from the simulations of the model used to performed the identification in order to approach what is done in realistic applications.

Let us point out that in the Stokes type flow the cellular species obey exactly the same population dynamics and what changes is the mechanical closure. As pointed out in [26] a viscoelastic flow in a two dimensional limit is well described by a Darcy-type law with a suitable definition of porosity. Thus, it is expected that 2D simplified Darcy model represents in a satisfactory manner all the main physical feature of the more complex Stokes-type flow. Nevertheless, there are also differences between the models, mainly due to the role of diffusivity.

As a preliminary test we investigate how the density of proliferating cells P determined using a Stokes mechanical closure is approximated by empirical eigenmodes obtained for a Darcy-type flow with the same initial conditions. The initial conditions and the computational set up is identical to that of the next section. We consider the L^2 relative projection error, see Table 6.1. This table shows that the relative projection error is acceptable and that it decreases with the number of modes and increases with time, as expected.

Next, we present the results of two different inverse problems, in which both the behavior of the oxygen concentration and the mechanical behavior of the healthy tissue

vary. In the first case the oxygen concentration on the boundary of the blood vessel is given, whereas in the second test case we assume that the oxygen is provided through the boundary of the computational domain and the value of the oxygen concentration on this boundary has to be identified. In the second test case we also impose a geometrical constraint corresponding to the fact that the tumor cannot leave the computational domain. This is done by modifying the boundary condition on the velocity, which in turn affects the dilatation rate and therefore the mechanics of all the tissues, including the healthy one. This is a model for the tumor growth inside an organ before the metastatic process.

6.4.1 Far blood vessel

The results of a first inverse problem are described. The tumor is a little spheroid that starts growing fed by a single blood vessel, of known position and source intensity. In particular, the computational domain is the box $\Omega = [0, 8] \times [0, 8]$, the tumor is initially located at $\mathbf{x}_t = (6, 4)$, the blood vessel at $\mathbf{x}_{bv} = (3, 4)$.

Dirichlet boundary conditions for both the oxygen and the pressure fields are imposed. In particular:

$$\Pi = 0 \text{ on } \partial\Omega, \quad C = 0 \text{ on } \partial\Omega, \quad C = C_0 \text{ on } \partial\Omega_C, \quad (6.43)$$

where Ω_C represents the domain of a blood vessel, and $C_0 = 0.15$.

In Fig.6.3 two snapshots of the solution of the Stokes-type flow for this case are represented. In Fig.6.3.a) the initial condition is plotted: at the right hand side the tumor (proliferating cell density is represented) is initialized as a little spheroid with an exponential distribution of proliferating cell density. The contour lines represents the isosurfaces of the oxygen concentration in the tissue. The same quantities are represented in Fig.6.3.b) for a subsequent time. Tumor has grown and it has started moving towards the blood vessel. Due to the oxygen consumption the tumor changes the oxygen distribution in the tissue.

In this case the system of equations defining the dynamics reduces to:

$$\dot{Y} + \nabla \cdot (a_i^v \phi_i^v Y) = a_i^{\gamma P} \phi_i^{\gamma P}, \quad (6.44)$$

$$a_i^{\gamma P} = \frac{1 + \tanh(R(a_i^c \phi_i^c - C_{hyp}))}{2}, \quad (6.45)$$

$$a_i^v \nabla \cdot \phi_i^v = a_i^{\gamma P} \phi_i^{\gamma P}, \quad (6.46)$$

$$k(Y) \nabla \wedge a_i^v \phi_i^v = \nabla k \wedge a_i^v \phi_i^v, \quad (6.47)$$

$$\nabla \cdot (D(Y) a_i^c \nabla \phi_i^c) = \alpha a_j^P a_i^C \phi_j^P \phi_i^C + \lambda a_i^C \phi_i^C. \quad (6.48)$$

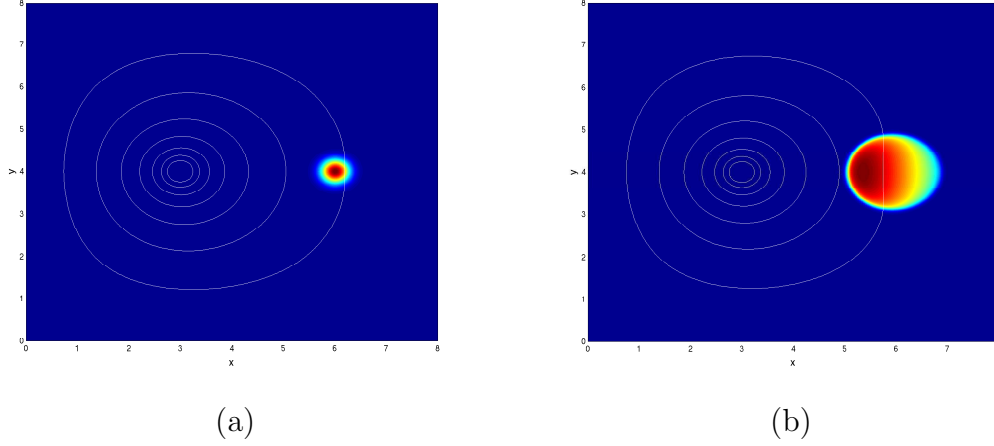


Figure 6.3: Solution of the Stokes-type flow in the case of a far blood vessel, at: a) $T=0$; b) $T=20$; contour lines represent oxygen concentration in the tissue.

Constraints to the oxygen field are imposed in order to prevent unphysical solutions to arise, as explained in the previous section. In order to close the procedure minimizing the residual of these equations, time derivative of Y is expressed as function of the snapshots. Linear interpolation, exponential interpolation and logistic interpolation are used. According to the sensitivity analysis on the representation properties of POD modes the following number of modes are used: for the variable P $N_P = 10 - 15$, for C $N_C = 5$, for \mathbf{v} $N_v = 30$, for γP $N_{\gamma P} = 10 - 15$.

Numerical results

In this section the numerical results of the procedure are discussed. Before analyzing the errors from a quantitative point of view the qualitative behavior of the obtained solution is described. In Fig.6.4 three snapshots taken from the two simulations are shown. The identification when $T = 5$ was performed using the second snapshot at $T = 10$. There are not a lot of differences between the images, all the stages of the growth being well represented. There are indeed no elements which discriminate in a definite manner the behaviors of the solutions. An error has to be defined to quantitatively evaluate the performance of the identification. The observable being $Y = P + Q$ a good choice is represented by the tumor volume and localization, that is, its center of mass position. The volume is:

$$V_Y(t) = \int_{\Omega} \mathbf{1}_Y d\Omega. \quad (6.49)$$

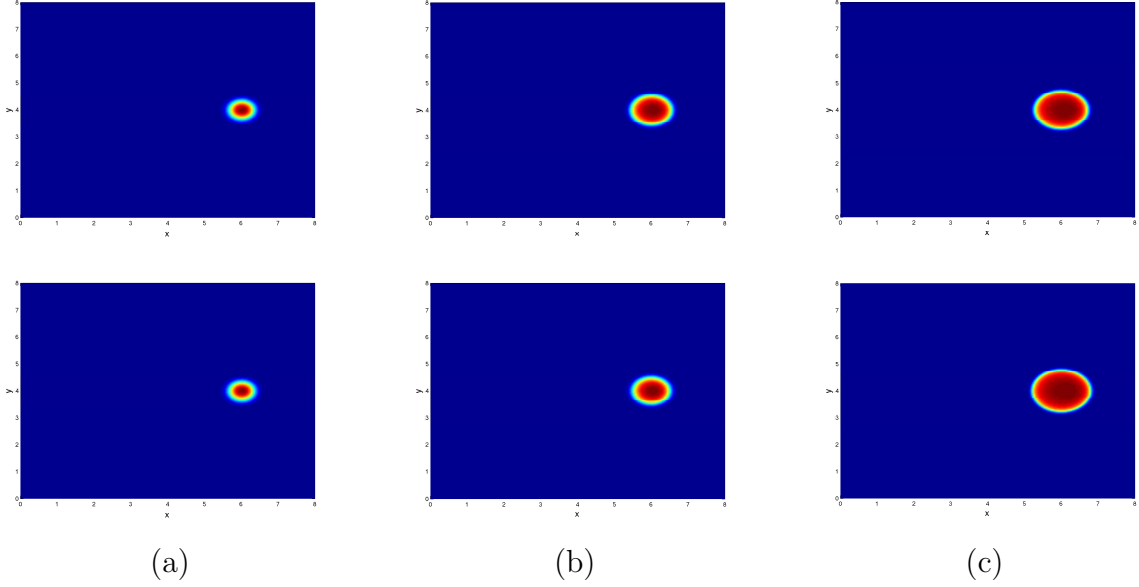


Figure 6.4: Tumor mass Y for the Stokes flow (upper row) and for the Darcy flow (below) : a) $T=5$ b) $T=10$ c) $T=15$; Color scale ranges from 0 (blue) to 1 (red)

Where $\mathbf{1}_Y$ is the characteristic function of the variable Y , so that the volume is the measure of the support of the tumor density. The position of the mass centre is:

$$\mathbf{x}_G = \frac{\int_{\Omega} \mathbf{1}_Y \mathbf{x} \, d\Omega}{\int_{\Omega} \mathbf{1}_Y \, d\Omega}. \quad (6.50)$$

The procedure to evaluate the error is straightforward: two snapshots of the Stokes type flow are taken and the identification using a Darcy-type flow is performed. Darcy flow system is simulated using the identified parameters and taking the first snapshot of the Stokes type flow as initial condition. The volume and the center of mass position are evaluated. If we denote as $V_Y^{(e)}$ and $x_G^{(e)}$ the volume and the center of mass position of the tumor in the Stokes-type flow, the relative errors are defined as follows:

$$\epsilon_V(t) = \frac{V_Y(t) - V_Y^{(e)}(t)}{V_Y^{(e)}(t)}, \quad (6.51)$$

$$\epsilon_X(t) = \frac{\left(X_G(t) - X_G^{(e)}(t)\right)^2}{\left(V_Y^{(e)}(t)\right)^{(1/2)}}. \quad (6.52)$$

The system is identified at different times, taking a different time interval between the snapshots. In Fig. 6.5.a) the relative error in volume is plotted, when the reference

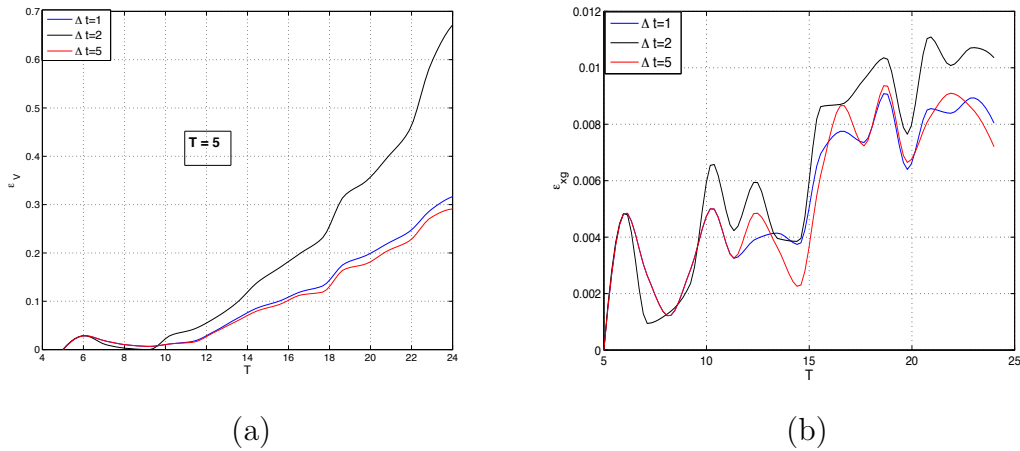


Figure 6.5: Relative error when identification time is $T=5$, with linear interpolation. a) volume error; b) centre of mass position error

snapshot is taken at $T = 5$, for linear interpolation, varying the time at which the second snapshot is taken. The error remains under the value of 0.1 for a large part of the time history of the simulation of the Darcy-type flow. All the identifications are practically equivalent. Let us investigate the property of approximation when the time interval is $\Delta t = 5$.

As a matter of fact in realistic applications the medical scans are performed at a somehow constant time rate. For example, if the first snapshot is taken at $T = 5$, the second one at $T = 10$, it is interesting to evaluate the error in $T = 15$, when the hypothetically third snapshot would be taken. According to this procedure, the error is under 10%.

In Fig. 6.5.b) the error on the centre of mass position scaled with the square root of the volume. We adopt this normalization in order to have a dimensionless error. In particular it is reasonable that the higher the dimension of the tumor the higher could be the absolute error in the centre of mass position. The relative error obtained represents the absolute error of the centre of mass position per unit length of the mean tumor radius.

All the simulations are equivalent and the error is particularly low, so that the transport approximation is rather good. This is true for all the performed simulations. Let us point out that the considered time scales are rather realistic. In the simulated time range the tumor volume is doubled.

In Fig. 6.6.a) the relative volume error is shown when $\Delta t = 5$ and interpolations are varied. The logistic one turns out to be less accurate for this case. This is probably

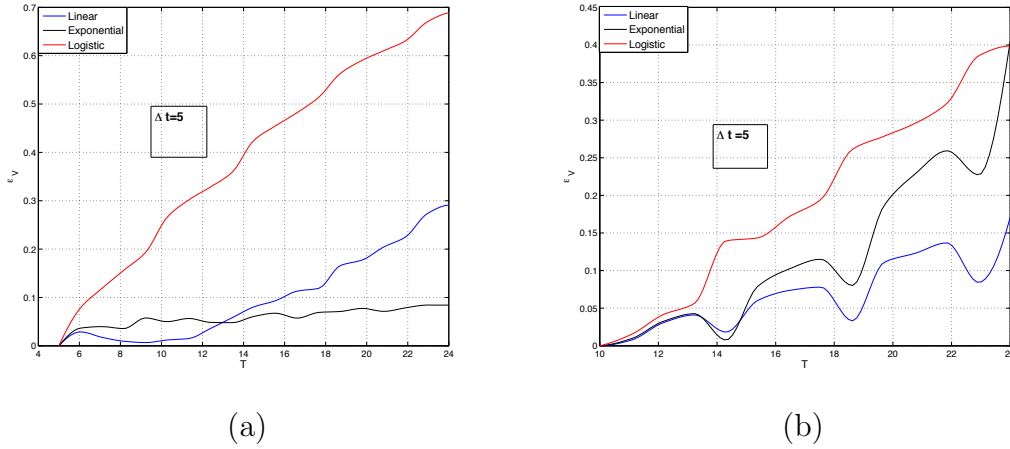


Figure 6.6: Relative volume error when $\Delta t = 5$, varying interpolations. a) $T=5$; b) $T=10$

due to the fact that the procedure is less stable from a numerical point of view, since in the logistic interpolation the time derivative is approximated adding two free parameters. At $T = 10$ the linear interpolation is better than the exponential one. On the contrary, when $T = 5$ the exponential interpolation provides a rather good approximation of the time derivative, so that the error remains under 0.1 for all the rest of the simulation. Let us analyze the error when $T = 10$ for both the interpolations, when we vary the time at which we take the second snapshot. In Fig .6.7 the three interpolations behave not so differently. The exponential one has a slightly better results for $\Delta t = 2$. When the identification is performed at $T = 10$, the error is small for a large part of the avascular history, but in general tends to grow faster with respect to the error made when the system is identified at $T = 5$. This is maybe due to the fact that the tumor has started moving towards the blood vessel so that the derivative can be no longer be well approximated by the derivative of an exponential type system.

When the Darcy type flow is simulated the initial condition for the Stokes type flow is used: this is equivalent to have an informations on the active part of the tumor. Thus, the computed error is solely due to the parameter reconstruction procedure and the differences between the models.

In other cases treated in the present work, initial conditions are identified. This turns out to be relevant for realistic applications, since it allows to have precious informations from a clinical standpoint. In particular, the distribution of the proliferating cells density can be approximated.

There is a sensitivity to the starting point for the Newton solver, due to the presence

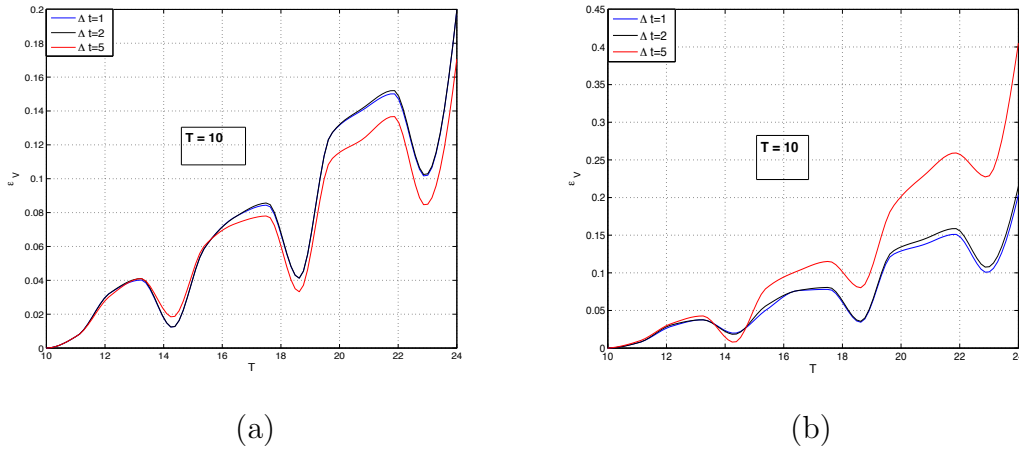


Figure 6.7: Relative volume error when $T = 10$, varying Δt with . a) Linear interpolation; b) Exponential interpolation

of local minima. One good criterion is to initialize the unknown POD coefficient in the following manner: a snapshot of Y is taken from the database, in such a way that the tumor size is comparable with that of the image, and a Galerkin projection of the initial conditions is done to find the coefficients. To evaluate the behavior of the procedure, several starting points were taken, randomly and according to the proposed criterion. After convergence, the lowest minimum was chosen as solution.

Irregular tumor shape

In this subsection the dynamics of an irregular tumor is identified, in the same configuration. The aim is to check if the procedure is robust enough to identify complex geometries. This is the main motivation for using a distributed model based on PDE.

In Fig.6.8 the solution of a Stokes flow (upper row) is compared with the solution of the Darcy flow when the identification procedure has been applied with an exponential type of interpolation. The initial tumoral distribution was taken from a scan image of a lung cancer (courtesy David Sarrut, Centre Léon Bérard, Lyon, France).

The solutions are similar, the procedure takes the effects of complex geometries into account, even if the models are quite different. As in the Stokes type flow some diffusivity acts. It is expected that the tumor boundary become less irregular as time increases, while in the Darcy-type flow there is no diffusivity.

As before, the error analysis is performed, the same qualitative and quantitative behavior is found with respect to the case of regular shapes. In particular the relative

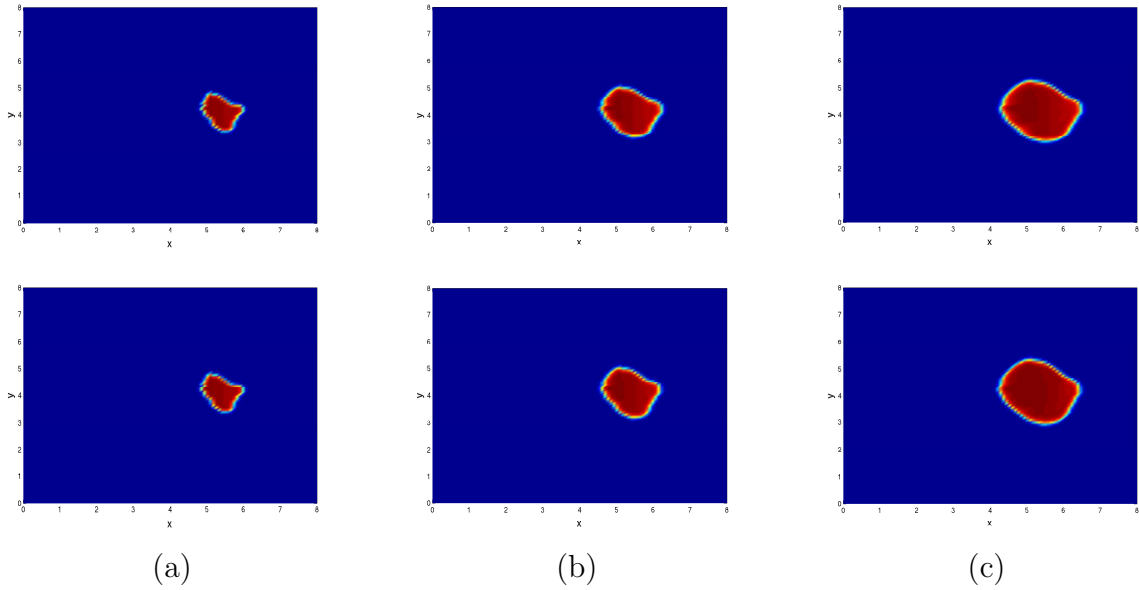


Figure 6.8: Tumor mass Y for the Stokes flow (upper row) and for the Darcy flow (below) : a) $T=5$ b) $T=10$ c) $T=15$

error stays under the value of 0.1 for a relevant portion of the avascular growth history, corresponding to the doubling of the tumor volume.

6.4.2 In vitro-like tumor: spherical growth

In this section the identification of an in vitro-like tumor growth is described; the tumor is, at the beginning, a little spheroid in the centre of the domain and the oxygen is provided by the boundary. Neumann boundary conditions for the pressure field and Dirichlet boundary conditions for the oxygen field are imposed. The oxygen concentration value at the boundary is taken as one of the unknowns of the inverse problem.

In Fig.6.9 the distribution of the proliferating cell density is plotted and the contour lines for the oxygen concentration; the solution at time $T = 0$ and time $T = 20$ is shown. A spherically symmetric growing process establishes, a necrotic core appears in the middle at the end of the numerical experiment, as expected in consequence of the symmetric setting.

The same procedure described in the previous section is utilized, regularizing on the variables that are not observed. In this case the oxygen field is lifted, in such a way that the boundary conditions are automatically satisfied by the POD modes expansion.

Let us note that, since the divergence of the velocity field is not merely equal to the

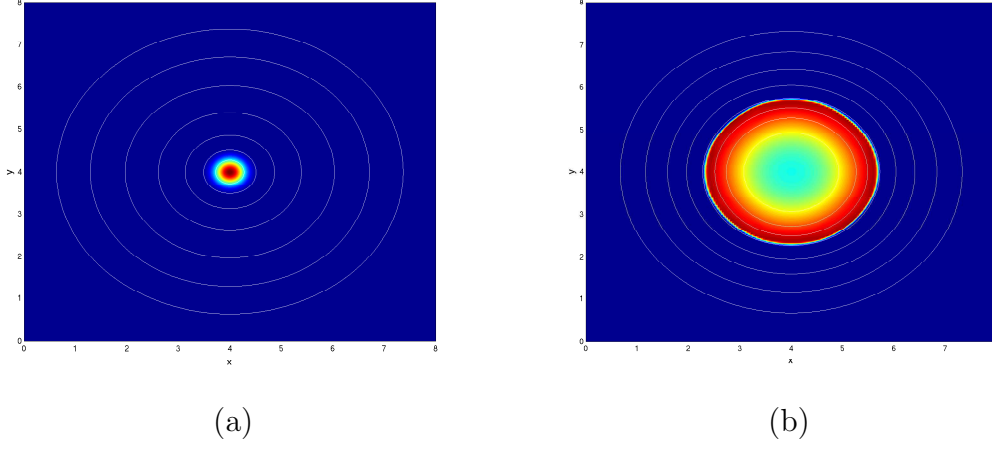


Figure 6.9: Solution of the Stokes-type flow in the case of a in vitro-like tumor at: a) $T=0$; b) $T=20$; contour lines represent the oxygen concentration levels

product γP , governing equations can no longer be decoupled, so that the residuals of all the equations together have to be minimized. Let $C^* = C - C_0$, where C_0 is the boundary value. The equation defining the inverse problem are, in this case:

$$\dot{Y} + \nabla \cdot (\mathbf{v}Y) = \gamma(C^*)P, \quad (6.53)$$

$$\gamma(C^*) = \frac{1 + \tanh(R(C^* + C_0 - C_{hyp}))}{2}, \quad (6.54)$$

$$\nabla \cdot \mathbf{v} = \gamma(C^*)P - \frac{\int_{\Omega} \gamma P \, d\Omega}{\int_{\Omega} 1 - Y \, d\Omega} (1 - Y), \quad (6.55)$$

$$k(Y)\nabla \wedge \mathbf{v} = \nabla k \wedge \mathbf{v}, \quad (6.56)$$

$$\nabla \cdot (D(Y)\nabla C^*) = \alpha P C^* + \lambda C^* + (\alpha P + \lambda)C_0, \quad (6.57)$$

In this way, a non homogeneous equation for the oxygen concentration is found, with a source term, and homogeneous boundary conditions. As in the previous case all the computations were performed using linear, exponential and logistic interpolation, with the same number of POD modes.

Numerical results

As done in the previous case, we look at the relative error of the volume and of the centre of mass position, when the time interval between two snapshots is varied, as well as the time at which the identification and the interpolation are performed.

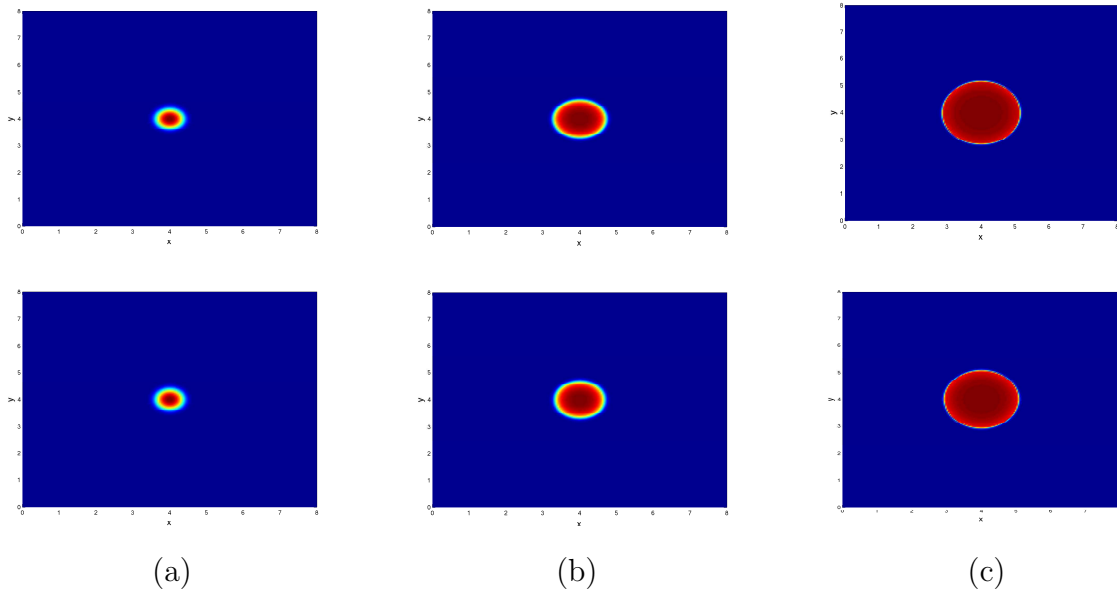


Figure 6.10: Tumor mass Y for the Stokes flow (upper row) and for the Darcy flow (below) : a) $T=5$ b) $T=10$ c) $T=15$

The qualitative behavior being reasonable, let us analyze quantitatively the error of the procedure for the present case. In Fig.6.11.a) the relative error of the volume is shown when a linear interpolation is used, varying the time at which the second snapshot is taken. The error remains smaller than 0.1 for a large portion of the remaining history. When the snapshots are close in time the linear interpolation is quite good.

The center of mass is fixed in all the simulations (a spherically symmetric growth is taking place) and the error of the center of mass position is expected to be very low, comparable with machine precision, since both the Darcy type flow and the Stokes type flow admit the spherically symmetric growth as solution. Indeed, this is confirmed by numerical experiments (see Fig. 6.11.b)). As done before, several interpolation rules are compared. In Fig. 6.12.a) the relative error of the volume is plotted when $\Delta t = 5$, the first snapshot taken at $T = 5$ and the interpolation is varied. The linear and the exponential interpolations are substantially equivalent, the error remaining under 10% for a large part of the avascular history. The logistic interpolation is less stable, as in the previous case, but in the end it allows the Darcy-type model to fit better the Stokes-type one. In Fig.6.12.b) the same error is shown when identification is performed at $T = 10$. In this case the error is larger, but the logistic interpolation reveals to be better than the others.

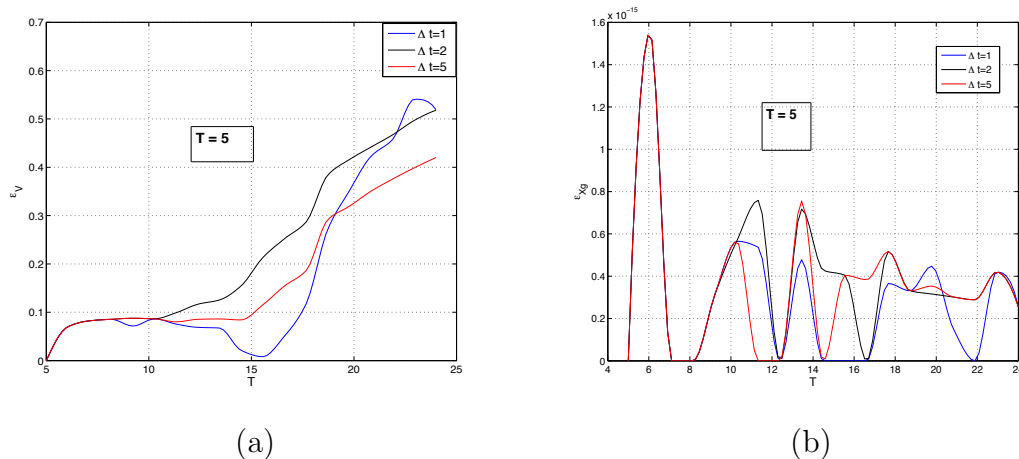


Figure 6.11: Relative error when identification time is $T=5$, with linear interpolation. a) volume error; b) centre of mass position error

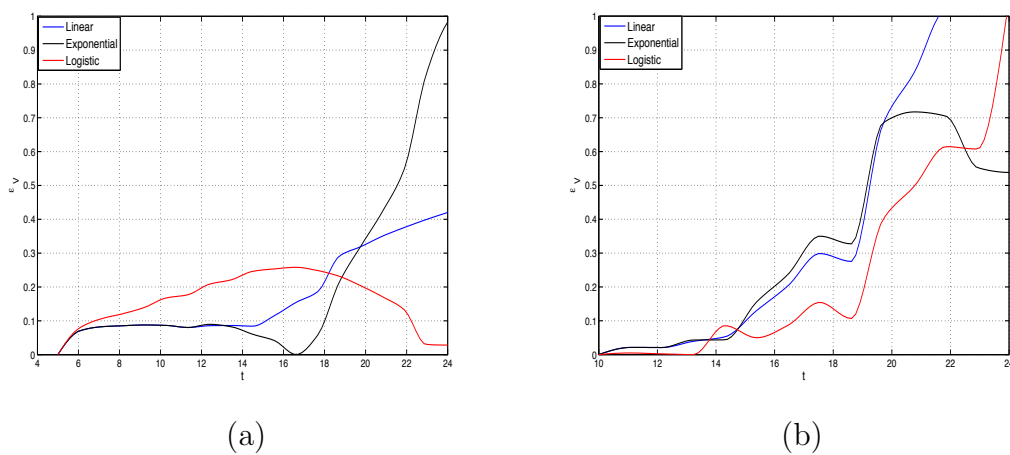


Figure 6.12: Relative volume error when $\Delta t = 5$, varying interpolations in the case: a) $T = 5$; b) $T = 10$

6.5 Comparison with Sensitivity

In this section a systematic comparison between the techniques proposed in this work is carried out. The same inverse problem is set up and solved, fixing all the ingredients: the model, the control set, the time scale and the data set. Let us point out that this setting may not be the best one, *i.e.* the setting allowing to obtain the smallest fitting error; here the objective is to compare the techniques in terms of computational cost, efficacy, accuracy and stability.

The chosen model is the regularized Darcy one, because of its simplicity. Dirichlet boundary conditions are imposed for both pressure and oxygen field. Geometry and data set are taken from FER-II case (see Sensitivity Chapter for details). The test consists in performing the identification when only the first two images are given, with both the techniques.

Two tests were performed: the first one with the layer structure control set, the second one by adding two harmonics.

6.5.1 Layer structure test

The control set consists in the parameters and in the initial distribution for the proliferating cell density. In this particular test the initial density distribution for proliferating cells is taken:

$$P(x, 0) = A \exp \{ -\delta \Phi^2 \}, \quad (6.58)$$

where Φ is the level set for the tumor, A the amplitude and δ the steepness. Let us point out that using this expansion oblige to revisit the reduced technique. No expansion for P is needed anymore, and hence there is no penalization of the functional, since the expansion satisfies by construction $0 \leq P(x, 0) \leq 1$. Only the modes for Π and γ are computed. The system of equations to be solved reduces to:

$$\dot{Y} + \nabla \cdot (k(Y)Y \nabla \phi_i^\Pi) a_i^\Pi = a_j^\gamma \phi_j^\gamma P(x, 0), \quad (6.59)$$

$$\nabla \cdot (k(Y) \nabla \phi_i^\Pi) a_i^\Pi = a_j^\gamma \phi_j^\gamma P(x, 0), \quad (6.60)$$

$$\nabla \cdot (D(a_k^\gamma \phi_k^\gamma, Y) \nabla (a_j^\gamma \phi_j^\gamma)) = (\lambda_P P(x, 0) + \lambda_Y Y) a_i^\gamma \phi_i^\gamma. \quad (6.61)$$

This system is solved at $t = 0$, taking the second image at $t = 0.3$. The time derivative is approximated by a logistic interpolation. The so obtained algebraic system is solved by means of a Newton trust region method. In this particular case it is equivalent to solve the reduced order model for the elliptic equations and to couple them with the

Table 6.2: Data set and results for FER-II case, fitted with the parameters identified by ROM: 6 volumes measures are taken from 2D scans, resolution $1.25mm$.

<i>Month</i>	0	21.0	24.5	36.0	40.5	45.0
<i>Area</i>	4.2e-3	6.5e-3	8.1e-3	9.7e-3	1.03e-3	1.10e-3
$\mathcal{E}_{Sens}(\%)$	0.0	1.8	2.47	2.02	1.94	1.36
$\mathcal{E}_{ROM}(\%)$	0.0	1.9	2.50	2.80	8.67	6.12
$\ Y - Im\ _{Sens}$	0.0	0.22	0.24	0.35	0.31	0.24
$\ Y - Im\ _{ROM}$	0.0	0.23	0.26	0.38	0.36	0.32

residual approximation for the observable. The system is cheap from the computational stand point, its solution taking only few minutes on a standard laptop. The system was initialized with several initial conditions in order to check the stability and the presence of local minima.

In Table 6.2 the errors are compared between the sensitivity approach (when two images are taken into account) and the reduced order model. The *ROM* performs quite well in terms of volume in the first part of the growth. For what concerns L^2 norms and in the second part of the growth sensitivity has substantially better results. The most relevant fact is that the two approaches show similar behavior in the very beginning (ROM is solved at $t = 0$). It is interesting that the reduced order model allows to get a correct solution on a time scale that is sufficiently large, *i.e.* on a scale comparable with the interval between two subsequent medical exams. In Fig.6.13 the fitting curves are shown, confirming essentially what commented about the errors. Let us remark that the two methods starts with exactly the same trend, so that the Reduced Order Model approach results in an approximation of the Sensitivity one in $t = 0$. The Error contours for the third image (*i.e.* the first prediction) are shown for the two methods in Fig.6.14. On the left, the result of the sensitivity is shown, the reduced order model is on the right. The differences between the two residuals are minimal, showing the ability of the reduced approach to mimic sensitivity. The error structure is the same and it is due to the control set and to the regularizing effect of the model, as previously commented.

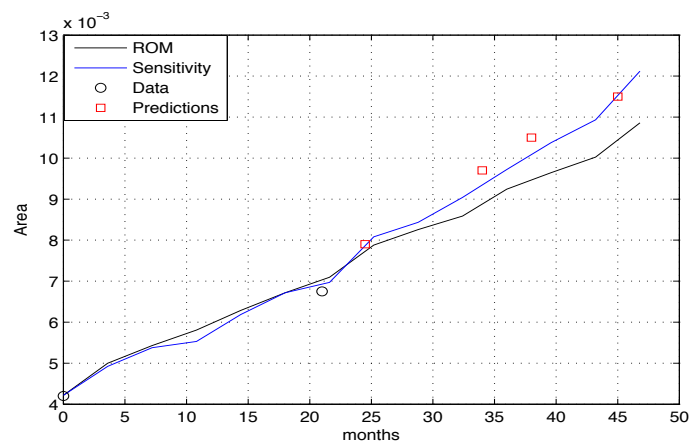


Figure 6.13: Area as function of time, for the Reduced Order Model (black line) and for the Sensitivity approach (blue line).

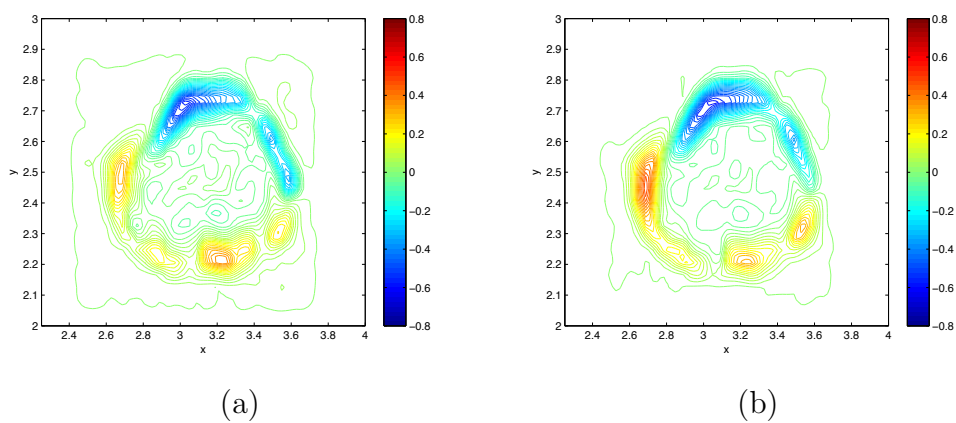


Figure 6.14: Difference between the third scan and the solution when the identification is performed by a) Sensitivity b) ROM

6.5.2 Extended control

The same comparison was carried out by adopting the control set extended by two harmonics. The problem is less stable from a numerical standpoint because of the appearance of more local minima. Constraints on the harmonics have been directly forced in the function of the residual computation for the Levenberg-Marquardt algorithm. Several reinitializations of the algorithm are needed to find the solution.

No significant improvement is observed with respect to the layer structure case. The residuals are similar to those observed with sensitivity and previously commented.

6.5.3 Costs and Summary

The techniques have a quite different philosophy and structure. The sensitivity approach is straightforward and it relies entirely on a functional minimization framework. Its cost is higher with respect to that of inverse problem and become important when 3D cases are considered, with a large control set. For a simple computation with a layer structure control set, in a 2D configuration, 2 days and a half are needed on one CPU.

The reduced order approach is divided into two phases: an *offline* and an *online* one. All the cost is concentrated in the offline stage. This stage for the moment has to be performed for each case treated, but it can be done when only one image is known (just to get geometry and the necessary conditions to perform direct simulations). Once more data are available (typically after three four months), the cost of the inverse problem is negligible (usually 15 minutes on a standard laptop). The technique is based on a residual formulation, which is less practical to deal with and to set up if compared to sensitivity, but costless.

6.6 Realistic tests

In collaboration with Institut Bergonié , we study thyroid cancer metastasis in lungs. We make the choice of keeping a two-dimensional setting. The main reason for that is computational feasibility, in the sense that computationally intensive identification procedures in clinical practice seem out of reach for the moment. Another motivation for this choice is that for practical reasons physicians tend to interpret the scans on the largest section of the lesion, even though three-dimensional data are available.

In what follows three different cases are treated, covering the spectrum of all the possible biological behaviors. For all, Darcy model was used for the identification. According

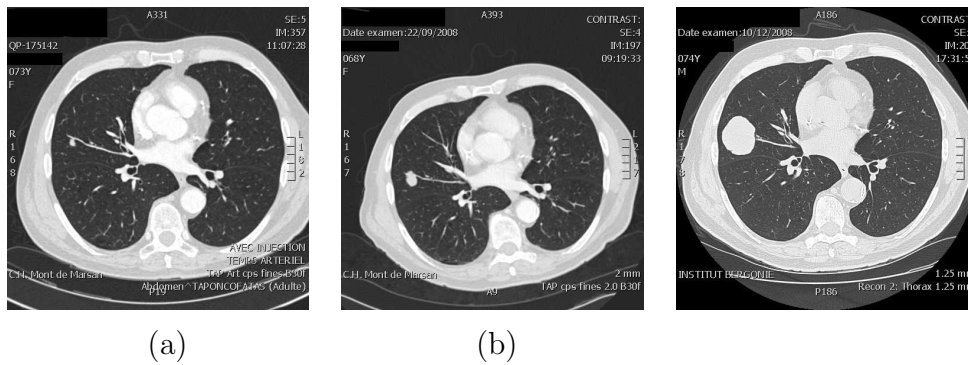


Figure 6.15: Fast growing tumor: scan at a) june 2008 b) september 2008 c) december 2008

to the sensitivity analysis on the representation properties of POD modes, the following number of POD modes was used: for the variable P , $N_P = 10$, for C , $N_C = 5$, for \mathbf{v} , $N_v = 30$ and for γP , $N_{\gamma P} = 10$.

6.6.1 Fast rate growth

As first case, an exponential fast growth is studied. In Fig.6.15 the evolution of a metastatic nodule is shown; the evolution takes about six months, the scans are taken at approximately constant rate. The problem is the following one: given the first two scans, we try to recover the third one, after having performed the parameters identification.

A database was build varying all the parameters in uniform intervals. The database consists in 128 simulations. For each one, 20 time frames are taken. The minimization takes about 20 minutes on one standard CPU. In Fig.6.16.a) the superposition of the simulation to the realistic geometry is shown, at the time corresponding to the third scan. The result is realistic, the volume not being too far from the measured one. The error is essentially a shape error. The model tends to regularize the shape, so that the simulated tumor is closer to a spheroid with respect to the real tumor. In order to prevent this error to arise two strategies are possible: the first one consists in modifying the model such that its dynamics is less regularizing and the second one consists in changing the control set.

In Fig.6.16.b) the volume curve is plotted with respect to days. There is a certain error in volume at the time corresponding to the third scan, but, in terms of time, it is about 15 days on a time interval of 6 months. For such a growth, featured by a high rate and a large final volume, not enough mechanics have been accounted for. As a matter of

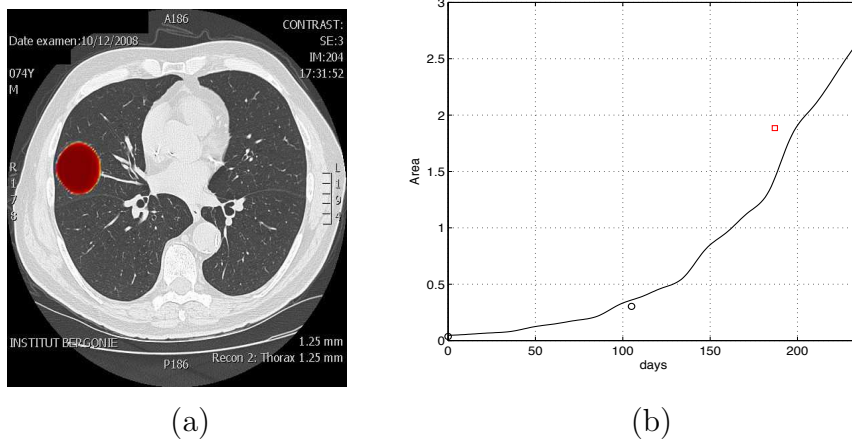


Figure 6.16: Results: a) Superposition of simulation and geometry b) Volume curve with respect to days

fact, tumor expansion causes some compression in the tissues and the constraints imposed by the thorax are not negligible.

6.6.2 Slow rate growth

The FER case is taken into account, presented in the chapter describing Sensitivity techniques. Though, the data set used is different (FER-I), essentially for historical reasons. When we started working on this case only a partial set was available, since it was, in some sort, a preliminary test. In what follows this test is reported. In the sections below a systematic comparison between the sensitivity and the ROM approaches is described, when both deal with the same data set, in the same conditions.

Using only the first two scans, we recover the parameters and the initial conditions that allow us to perform a forward simulation beyond the time corresponding to the second scan. Therefore, starting from the scan corresponding to October 2007 (see Sensitivity chapter for details), the growth rates obtained are actual model predictions.

In order to determine the POD modes, two databases were constructed by integrating in time the Darcy type model. The first database consists of 128 parameter configurations that result in growth rates of the order of the ones observed between the first and the second scan on a conventional time scale of 1. For each of the 128 configurations, 20 time snapshots were recorded. In order to check the stability of the identification with respect to the solution space sampling, a second database of 768 simulations was also built. Again

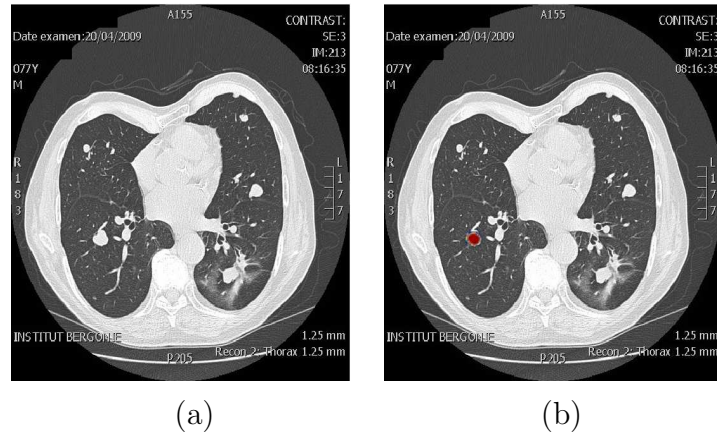


Figure 6.17: a) Fourth scan b) Simulation

20 time snapshots per simulation were considered. The results shown in the following do not significantly vary as a function of the database used.

Initially the proportion of proliferating cells is fixed to $P = 1$ on the tumor support, that is, at the beginning the tumor is totally proliferating. This value is of course not always realistic, but the results of the identification proved to be weakly dependent on this assumption.

In Fig.6.17 the simulated nodule growth are compared to the actual nodule size resulting from the scan of April 2009. The support of the Y distribution has approximately the same area as the real tumor. However, in the simulation the nodule is more isotropic than in reality.

In order to give a more quantitative evaluation of the results obtained we focus on the overall growth history. To this end, the predicted area of the tumor is compared to the actual one. In Fig.6.18 the solid line represents the simulation while the circles are the computed areas of the scans. The red squares are the prediction data. Let us point out that the procedure was carried out before that the last exam was performed by physicians. Similar results on area or volumes can be obtained by identifying ODE based models. Nevertheless, the present approach has the advantage of retrieving a precise spatial localization of the tumor as well as an indication of its cellular type and nutrient distribution.

We stress that only the first two scans were used in the identification. Nonetheless, the procedure is able to correctly detect the changes in trend at month 35, without having data near this point. The volume error on the fourth scan corresponds to 10 days on a time of 41 months, and, for the last exam, to 20 days over 45 months. This case shows what

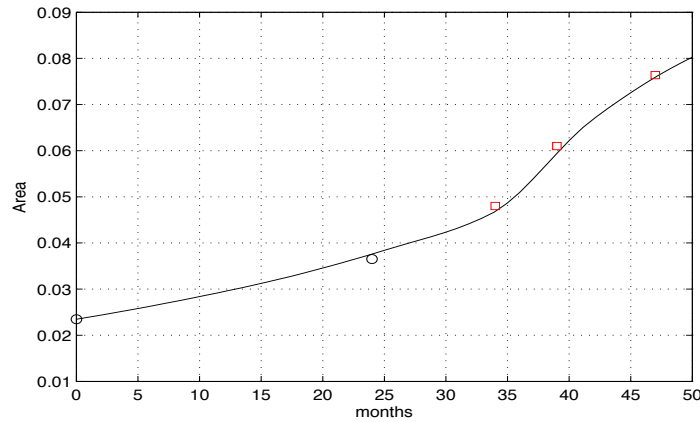


Figure 6.18: Area as function of time for the slow rate growth. Solid line represents the simulation results, black circles are the data used for the identification, red squares the predictions.

is the best result that can be obtained with the present technique. Having such a good prognosis power depends upon how good is the database (*i.e.* how close the simulations are to reality), how the logistic interpolation on Y affects the identification and, of course, how segmentation and data errors propagates through the whole process. In the next section a case is studied in which the reduced technique does not perform at best.

6.6.3 Two nodules

In this section the growth of two different metastatic nodules belonging to same patient are considered. Their evolution is shown in figure 6.19: the nodules exhibit different dynamics: while the first one is characterized by a rapid phase of growth followed by a plateau type of solution, the second one has a regular growth.

The problem, as before, is the following: we try to recover the third scan taking the first two images as data. The database used for the identification consists in 512 simulations for both the nodules, varying the parameters; 20 time frames per simulation were retained.

In Fig. 6.20.b) the volume curve is shown for the Nodule 2. The prediction is correct and it confirms substantially what obtained for the case discussed in the previous section. In Fig. 6.20.a) the prediction (in terms of volume) for the first nodule is shown. The identification is more difficult since two different growth patterns match the data with comparable residuals: the first one is an exponential type of growth (dashed blue line in

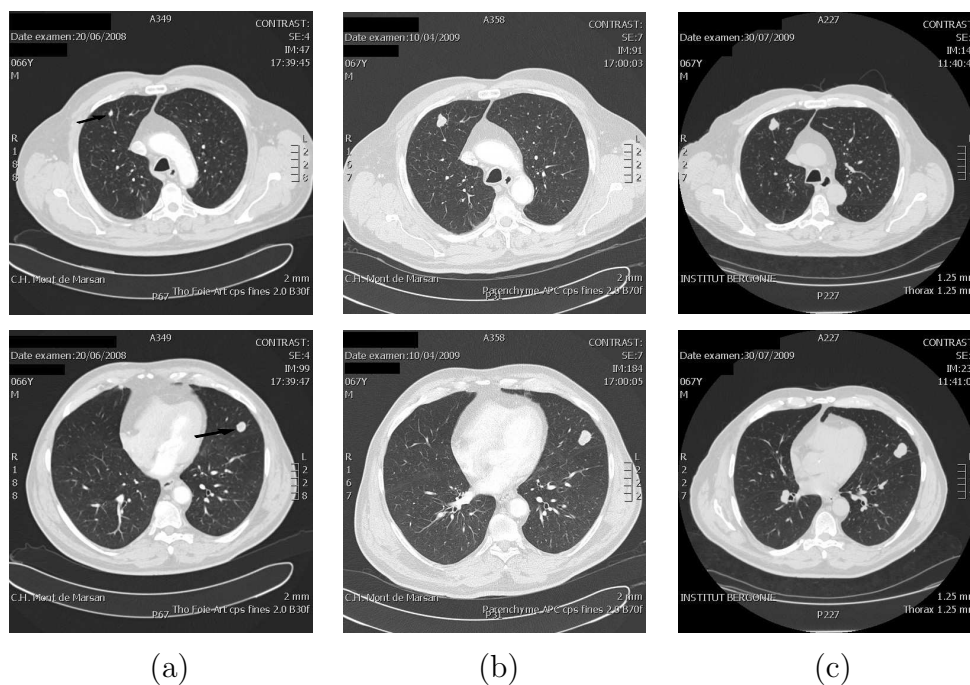


Figure 6.19: Nodule 1 (upper row) and Nodule 2 (lower row) at: a) June 2008 b) April 2009 c) July 2009

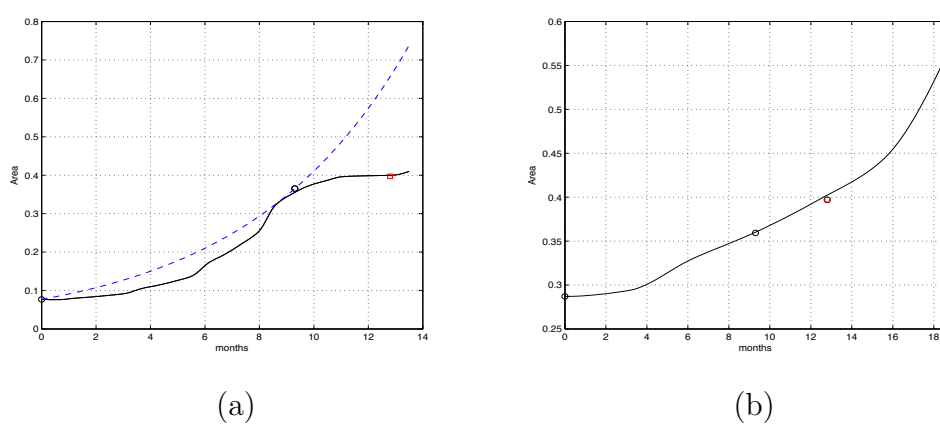


Figure 6.20: Volume curve for: a) Nodule 1 and b) Nodule 2.

the figure) and the second one is a plateau-type of evolution. The difficulty lies in the rapid growth of the nodule (its volume increased by a factor of 4): the configuration corresponding to the second image is too far from the first one and the approximation related to the derivative operator becomes poor. Thus, local minima for the functional have comparable values, two different families of solutions are possible. The correct curve has a residual norm smaller (so that it is actually well captured) than the exponential-type solution. However, in such a case, a third image is mandatory in order to get reliable predictions.

This case shows that the present technique is able to detect with a certain approximation different behaviors. Nevertheless there are certain reliability limitations linked to the relationship between the time scale on which the exams are performed and the proliferation speed of the tumor. A better set of data is needed when the volume ratio between the tumor volumes of two subsequent images attains a value of approximately 2.5.

These examples of application are clearly not conclusive from the view point of clinical relevance. An appropriate experimental protocol is under definition with our partners at Insitut Bergonié in order to systematically investigate the tumor growth prediction error.

Chapter 7

Optimal Transport

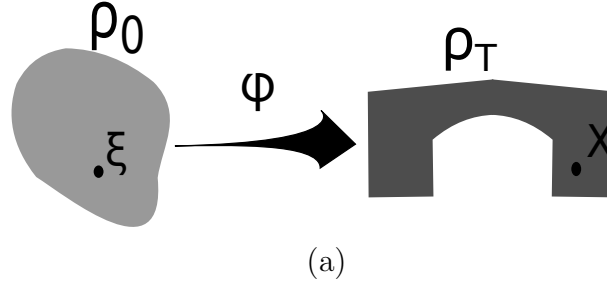


Figure 7.1: Conceptual scheme of Optimal Transport

7.1 Optimal transport theory

A part of this thesis is devoted to optimal transport theory and L^2 Monge-Kantorovich mass transfer. This section aims at introducing optimal transport and summarizing the main theoretical contributions on the subject.

Optimal transport is an ancient problem, formulated for the first time by Monge in 1781 (see [118] for the original formulation). It consists in looking for a transformation $x = X(\xi)$ (see Fig.7.1) allowing to re-arrange a density distribution from a starting $(\rho_0(\xi))$ to a final $(\rho_T(x))$ given configurations. Infinite many X exist that perform such a mapping but they are not all equivalent. A cost can be defined as a functional of the maps, the problem becoming to find a map that perform the density arrangement minimizing the cost ([118]). The formulation reads:

$$X(\xi) = \arg \min_{\tilde{X}} \left\{ \int_{\Omega_0} \rho_0(\xi) |\tilde{X}(\xi) - \xi|^p d\xi \right\}, \quad (7.1)$$

subject to the constraint:

$$\rho_0(\xi) = \rho_T(X(\xi)) \det(\nabla_{\xi} X), \quad (7.2)$$

where the cost defined in Eq.7.1 is called L^p transportation cost, and it is proportional to the density and the p norm of the displacement. The Eq.7.2 is the mass conservation equation expressed in lagrangian coordinates and it is called Jacobian equation. It supposes, in this form, that the mapping X is one-to-one. Details on this formulation and a generalization within a measure theory framework are found in [31, 30, 68, 157, 158, 11, 70].

The solution of the problem (*i.e.* the optimal $X(\xi)$) defines the p -Wasserstein distance between the densities $(\rho_0$ and $\rho_T)$. Uniqueness and regularity of solutions are analyzed in [70, 68].

This highly non-linear problem recently revived from a theoretical standpoint. Kantorovich in [97] proposed a weak formulation, defining a duality principle and highlighting

a linear nature for the problem in a product probability space. In particular, Monge-Kantorovich mass transfert is analyzed within a convex analysis framework. It is shown (see [68, 97] for details) that the weak problem can be formulated using a couple of convex functions; if, for instance, L^2 cost is assumed, they satisfy:

$$(\phi(\xi), \psi(x)) = \arg \min_{\tilde{\psi}, \tilde{\phi}} \left\{ \int_{\Omega_0} \rho_0(\xi) \phi(\xi) d\xi + \int_{\Omega_T} \rho_T(x) \psi(x) dx \right\}, \quad (7.3)$$

subject to the inequality constraint:

$$\psi(x) + \phi(\xi) \geq x \cdot \xi. \quad (7.4)$$

Another important contribution was given by Brenier polar decomposition theorem (in [35]), which is a generalization of Helmholtz (and de Rham) decomposition of vector fields. Given a vector field, it may always and uniquely be considered as the composition between an optimal mass transport and a divergence free mapping. The theorem was also proven by Gangbo in [76].

Polar factorization enlightened many relationships between optimal transport and partial differential equations (see [68, 10, 157, 158]). For instance, in [126], Wasserstein distance and, thus, optimal transport, is linked to the flow in porous media. The work of Otto contributed to show the possibility to study some PDEs evolution as gradient flow in a Wasserstein space (see [158] for a detailed comment of Otto's work).

Many connections arise with semi-geostrophic models used in meteorology and oceanography ([52, 53]). A first work in this sense, stating a variational formulation for incompressible Euler equations, is found in [19]. The interest of the approach proposed in [53] is twofold: first, by means of an analytic change of variable, Euler incompressible equations with semi-geostrophic terms are transformed in an optimal transport problem and, second, this allows to state a time boundary formulation for meteorological problems. Two configurations given, a flow is recovered uniquely, transporting the first into the final one.

Other physical applications concerns non-linear Born-Infeld theory for electromagnetism (see [37, 36, 50]). Interesting works treat collapsing sand piles ([69] for a details), representation of coalescence and fragmentation phenomena (in [162]), crowd motion (see [113]).

An important branch consists in using optimal transport in optimization problems (as, for instance, in [77]) and computer vision ([123]). In particular, some works in the literature ([85] among them) explored the possibility to use optimal transport as a non-rigid registration tool for medical imaging. This inspired the present work.

Optimal transport is treated from a numerical standpoint: after having analyzed the current approaches, a family of methods is proposed, exploiting the lagrangian structure of the problem. The aim is to use Monge-Kantorovich solvers as a tool for manipulating medical images, in a sort of pre-processing for inverse problems.

7.2 The L^2 Monge problem

In the original formulation Monge proposed the so called L^1 cost, that is, the cost is proportional to the mass and the displacement. In this work we focus on the numerical solution of the L^2 optimal mass transfer problem in \mathbb{R}^d , where d is the number of space dimensions. Let $\rho_0(\xi)$ and $\rho_1(x)$ be two non-negative scalar (density) functions with compact support Ω_0 and Ω_1 , respectively. We assume that

$$\int_{\Omega_0} \rho_0(\xi) d\xi = \int_{\Omega_1} \rho_1(x) dx = 1. \quad (7.5)$$

Let $x = X(\xi)$ be a smooth one-to-one map taking Ω_0 onto Ω_1 that verifies the jacobian equation

$$\det(\nabla_{\xi} X) \rho_1(X(\xi)) = \rho_0(\xi). \quad (7.6)$$

As a consequence, we have that $\forall \Omega \subseteq \Omega_0$

$$\int_{\Omega} \rho_0(\xi) d\xi = \int_{X(\Omega)} \rho_1(x) dx. \quad (7.7)$$

The jacobian equation (7.6) has many admissible solutions. Among all these mappings, the objective of this work is to describe a lagrangian method to find $X^*(\xi)$ such that

$$\int_{\Omega_0} \rho_0(\xi) \|X^*(\xi) - \xi\|^2 d\xi \leq \int_{\Omega_0} \rho_0(\xi) \|X(\xi) - \xi\|^2 d\xi \quad (7.8)$$

for all smooth one-to-one mappings $X(\xi)$. This functional measures the cost of the mass transport by a weighted square distance function. Other classes of optimal transport problems can be defined by introducing different norms instead of the above. We concentrate on the L^2 case because of its links with continuum mechanics [37] and since the solution of this problem finds applications in oceanography [53], shape optimization [77], computer vision [123] and image processing [136].

Mainly two classes of methods to solve this problem in realistic applications were proposed. One idea (see [16]) is to look for a mapping between the initial and final condition

by solving an appropriate partial differential equation up to steady state. The computational cost of this approach is that of finding the asymptotic solution of d transport equations. The main drawback is that, apart from accuracy, the convergence rate to the asymptotic solution may be poor. A different path is followed in [31], where a time-like variable is introduced and the space-time mapping between the initial and final mass distribution is found by a saddle point method that requires the solution of a Poisson problem in space and time at each iteration. The merit of the latter formulation is to show the links between the least action principle and the optimal mass transfer problem. From the computational view point, however, the time-like variable introduces additional unknowns to be solved for. In the next sections we will summarize the formulation at the base of these two approaches in order to introduce an alternative solution method where no partial differential equations are numerically solved to approximate the optimal map.

7.3 The Angenent-Haker-Tannenbaum (AHT) gradient flow

Let us recall a basic theoretical result on the L^2 optimal mass transfer problem (see [35],[68],[76]): there is a unique optimal map $X^*(\xi)$ characterized as the unique map transferring $\rho_0(\xi)$ to $\rho_1(x)$ which can be written as the gradient of some convex function $\Psi(\xi)$:

$$X^*(\xi) = \nabla_{\xi} \Psi(\xi); \quad (7.9)$$

in other words if we find a map that can be expressed as in the equation above and that satisfies equation (7.6), than this is the optimal map. Such a consideration is at the base of the AHT method [16].

In the following we recast AHT method in a continuum mechanics framework. Let $x = \mathcal{X}(\xi, t)$ be a smooth one-to-one mapping such that $\mathcal{X}(\xi, 0) = X_i(\xi)$ and let the initial map $X_i(\xi)$ satisfy the jacobian equation (7.6). The objective is to make this initial map evolve toward the optimal map by a gradient method, without altering the distribution $\rho_1(x)$.

Our plan is therefore to compute the variation of the cost functional

$$I = \int_{\Omega_0} \rho_0(\xi) \|\mathcal{X}(\xi, t) - \xi\|^2 d\xi, \quad (7.10)$$

with respect to t . To do so, we need some preliminary steps. We introduce the inverse mapping $\xi = Y(x, t)$, that, for given value of the parameter t and space coordinate $x \in \Omega_1$

retrieves the corresponding $\xi \in \Omega_0$. In other words $x = \mathcal{X}(Y(x, t), t)$ and hence

$$\nabla_{\xi} \mathcal{X} = (\nabla_x Y)^{-1}, \quad (7.11)$$

$$\partial_t Y + U \cdot \nabla_x Y = 0, \quad (7.12)$$

where $U(x, t) = \partial_t \mathcal{X}(\xi, t)$. If $\mathcal{X}(\xi, t)$ has to take Ω_0 onto Ω_1 , $\forall t \in \mathbb{R}^+$, then $\forall x \in \partial\Omega_1$ and $\forall t \in \mathbb{R}^+$, $U(x, t) \cdot n = 0$, where n is the normal to $\partial\Omega_1$. As an initial condition for the inverse map we take $Y(x, 0) = Y_i(\xi)$ with $Y_i(x) = X_i^{-1}(x)$. Let also assume that $x = \mathcal{X}(\xi, t)$ is mass preserving $\forall t \in \mathbb{R}^+$ so that

$$\det(\nabla_x Y(x, t)) \rho_0(Y(x, t)) = \rho(x), \quad (7.13)$$

and

$$\det(\nabla_x Y(x, 0)) \rho_0(Y(x, 0)) = \rho_1(x), \quad (7.14)$$

thanks to equation (7.11). On the other hand, mass conservation can also be written

$$\partial_t \rho + \nabla_x \cdot (\rho U) = 0, \quad (7.15)$$

with initial condition $\rho(x, 0) = \rho_1(x)$.

The derivative of the cost functional with respect to t is then

$$\begin{aligned} \partial_t I &= \\ & \frac{d}{dt} \int_{\Omega_0} \rho_0(\xi) [\|\mathcal{X}(\xi, t)\|^2 - 2\mathcal{X}(\xi, t) \cdot \xi] d\xi = \\ & \frac{d}{dt} \int_{\Omega_1} \rho_0(Y(x, t)) \|x\|^2 \det(\nabla_x Y(x, t)) dx - 2 \int_{\Omega_0} \rho_0(\xi) \partial_t \mathcal{X}(\xi, t) \cdot \xi d\xi = \\ & \frac{d}{dt} \int_{\Omega_1} \rho(x, t) \|x\|^2 dx - 2 \int_{\Omega_1} \rho(x, t) U(x, t) \cdot Y(x, t) dx. \end{aligned} \quad (7.16)$$

The vector field $Y(x, t)$ can be decomposed as the sum of a divergence-free vector field $Y_{\omega}(x, t)$ and the gradient of a scalar potential $\Phi(x, t)$, according to the classical Helmholtz decomposition. Hence, $\Phi = \Delta_x^{-1}(\nabla_x \cdot Y)$, $Y_{\omega} = Y - \nabla_x \Delta_x^{-1}(\nabla_x \cdot Y)$ and $Y_{\omega} \cdot n = 0$ on $\partial\Omega_1$. We now take

$$U = \frac{Y_{\omega}}{\rho}, \quad (7.17)$$

and as a consequence it follows that $\partial_t \rho = 0$, i.e., $\rho(x, t) = \rho_1(x)$. Then, in equation (7.16)

$$\frac{d}{dt} \int_{\Omega_1} \rho(x, t) \|x\|^2 dx = \frac{d}{dt} \int_{\Omega_1} \rho_1(x) \|x\|^2 dx = 0, \quad (7.18)$$

and

$$\begin{aligned}
 & \int_{\Omega_1} \rho(x, t) U(x, t) \cdot Y(x, t) \, dx = \\
 & \int_{\Omega_1} Y_\omega(x, t) \cdot Y_\omega(x, t) \, dx + \int_{\partial\Omega_1} \Phi(x, t) Y_\omega(x, t) \cdot n \, dx = \\
 & \int_{\Omega_1} Y_\omega(x, t) \cdot Y_\omega(x, t) \, dx.
 \end{aligned} \tag{7.19}$$

In summary, by taking $U(x, t)$ as in equation (7.17) an optimal descent direction is found for the minimization of I :

$$\partial_t I = -2 \int_{\Omega_1} Y_\omega(x, t) \cdot Y_\omega(x, t) \, dx, \tag{7.20}$$

together with an evolution equation for $Y(x, t)$

$$\partial_t Y + \frac{Y_\omega}{\rho_1} \cdot \nabla_x Y = 0, \tag{7.21}$$

such that the forward map $\mathcal{X}(\xi, t)$ satisfies

$$\det(\nabla_\xi \mathcal{X}(\xi, t)) \rho_1(\mathcal{X}(\xi, t)) = \rho_0(\xi), \tag{7.22}$$

$\forall t \in \mathbb{R}^+$. The minimum of the functional will be reached when $Y_\omega(x, t) = 0$, i.e., when $Y = \nabla_x \Phi$. Let us prove that this result on Y implies that $X^* = \nabla_\xi \Psi$. Indeed:

$$Y(x) = \xi = \nabla_x \Phi(x) \Rightarrow \xi = \nabla_\xi \Phi(X(\xi)) (\nabla_\xi X)^{-T}, \tag{7.23}$$

that, after multiplication by the Jacobian to both sides leads to:

$$\xi (\nabla_\xi X)^T - \nabla_\xi \Phi = 0. \tag{7.24}$$

The expression that follows is found by applying the properties of the derivative of scalar product of vector functions, assuming that Y is invertible:

$$\xi (\nabla_\xi X)^T = \nabla_\xi (\xi \cdot X) - X(\xi). \tag{7.25}$$

The expression for X is found by combining this relation with the Eq.7.24:

$$X = \nabla_\xi (\xi \cdot X - \Phi(X(\xi))), \tag{7.26}$$

thus, a function Ψ exists such that:

$$\Psi = \xi \cdot X - \Phi, \tag{7.27}$$

that is, Ψ is the Legendre transform of Φ , the two functions being a pair of convex conjugate functions. The converse is also true (see [158] for an extensive overview), that is, given a function Ψ convex almost everywhere such that $X = \nabla_{\xi}\Psi$, then Y exist such that $Y = X^{-1}$ and $Y = \nabla_x\Phi$ where Φ is the convex conjugate of Ψ .

The AHT approach to the solution of the optimal mass transfer problem is important because of its links with polar factorization of vector fields [35] and generalized Boussinesq equations [37]. However, from the numerical point of view it suffers from some drawbacks in that one should build $X_i(\xi)$ and this is not always an easy task. Moreover even when equation (7.12) is carefully integrated in time by a high order scheme, mass is not exactly conserved at the discrete level. Therefore if the initial map is far from the minimum and many gradient step iterations are needed, the error in mass conservation may be large. More recently, in [85], it was proposed to directly solve the minimization of (7.10) under mass conservation constraint, by a sequential quadratic programming approach. This method, however, leads to an optimization problem of the size of the spatial grid resolution.

7.4 Action minimization

In [30] it is shown that the optimal mass transfer problem is equivalent to the flow of a pressureless ideal compressible fluid. Consider a time-dependent density function $\rho(x, \tau)$ defined in \mathbb{R}^d such that

$$\rho(x, 0) = \rho_0(x) \tag{7.28}$$

and

$$\rho(x, T) = \rho_1(x). \tag{7.29}$$

The variable τ stands now for time and it plays a different role compared to the parameter t of the previous section. It can be shown (see [30]) that the optimal mass transfer problem is equivalent to the minimization with respect to $U(x, \tau)$ of the time integral of the kinetic energy (the action) associated to the transport:

$$J = \frac{1}{2} \int_0^T \int_{\mathbb{R}^d} \rho(x, \tau) \|U(x, \tau)\|^2 dx d\tau, \tag{7.30}$$

subject to equations (7.15), (7.28), (7.29).

Introducing a space-time lagrange multiplier $\psi(x, \tau)$, the Euler-Lagrange equations for the constrained minimum of J are

$$\partial_{\tau}\psi + U \cdot \nabla\psi = \frac{\|U\|^2}{2}, \tag{7.31}$$

$$U = \nabla\psi. \quad (7.32)$$

and because initial and final conditions are given for $\rho(x, \tau)$, no conditions are imposed on $\psi(x, \tau)$.

In [31], the action minimization problem under constraint is solved by the Uzawa algorithm. The main disadvantage of this approach is that the discretization of the additional time dimension is such that the size of the discrete problem is multiplied by N , if N is the size of the resolution in one space direction.

An important property of the optimal transport easily follows from this formulation. Indeed, an evolution equation for the potential can be obtained substituting equation (7.32) into equation (7.31):

$$\partial_\tau\psi + \frac{|\nabla\psi|^2}{2} = 0, \quad (7.33)$$

which is an Hamilton-Jacobi equation that describes a transport along straight lines. This can be seen by taking the gradient of the equation above to obtain

$$\partial_\tau U + (U \cdot \nabla)U = 0, \quad (7.34)$$

which shows that the velocity $U(x, \tau)$ is constant along a characteristic, i.e., the velocity is constant along rays in space and time. In fact, this means that if ξ is the lagrangian coordinate and $\mathcal{X}(\xi, \tau)$ the map between x and ξ at time τ , we have

$$U(\mathcal{X}(\xi, \tau), \tau) = V(\xi), \quad (7.35)$$

where $V(\xi)$ is the initial velocity. Deriving the above equation with respect to τ , we find equation (7.34).

7.5 Mass transport along straight lines

The plan is now to use a lagrangian representation of the density distribution to impose mass conservation. We consider a set of particles such that

$$\rho(x, \tau) \approx \sum_{j=1}^{N_p} c_j(t) \sigma(x - X_j(\tau)) \quad (7.36)$$

where N_p is the number of particles, X_j is the particle coordinate and $\sigma_j = \sigma(x - X_j(\tau))$ is a regularization of a Dirac mass satisfying

$$\int_{\Omega_\tau} \sigma(\xi) d\xi = 1, \quad (7.37)$$

where $\Omega_r \subset \mathbb{R}^d$ is the support of the regularizing kernel σ . Let $\Omega(\tau) = \bigcup_{j=1}^{N_p} \Omega_j(\tau)$, with $\Omega_j(\tau)$ the support of σ_j . We have that

$$\int_{\Omega(\tau)} (\partial_\tau \rho + \nabla \cdot (\rho \nabla \psi)) \, dx = \frac{d}{d\tau} \int_{\Omega(\tau)} \rho \, dx, \quad (7.38)$$

and substituting equation (7.36)

$$\frac{d}{d\tau} \int_{\Omega(\tau)} \rho \, dx = \frac{d}{d\tau} \int_{\Omega(\tau)} \sum_{j=1}^{N_p} c_j(\tau) \sigma_j \, dx = \sum_{j=1}^{N_p} \frac{d}{d\tau} \left(c_j(\tau) \int_{\Omega(\tau)} \sigma_j \right) \, dx, \quad (7.39)$$

which reduces to

$$\frac{d}{d\tau} \int_{\Omega(\tau)} \rho \, dx = \sum_{j=1}^{N_p} \partial_\tau c_j(\tau). \quad (7.40)$$

In the following we assume that

$$\partial_\tau c_j(\tau) = 0, \quad (7.41)$$

so that the mass conservation equation is identically satisfied. As a consequence, the time invariant quantity c_j can be interpreted as the mass of the j -th particle.

Let us now take

$$X_j(\tau) = \xi_j + V(\xi_j) \tau, \quad (7.42)$$

where ξ_j is the position of the particle at $\tau = 0$ and $V(\xi_j)$ is the initial velocity of the particle. This equation translates the fact that the velocity is constant along straight lines. Thanks to this assumption, equation (7.34) is identically satisfied.

7.5.1 Reconstruction of the initial condition

The discretization of $\rho(x, \tau)$ verifies the mass constraint by equation (7.41) and the particle trajectories $X_j(\tau)$ are such that $U(x, \tau)$ respects equation (7.34). We now choose the time-invariant coefficients c_j in such a way that the initial mass distribution $\rho(x, 0) = \rho_0(x)$ is approximated in a least-square sense.

Given $\rho(x, 0)$ on a regular cartesian mesh, a simple choice consists in placing the particles in the nodes where $\rho(x, 0) > \delta_0$, δ_0 being the smallest density that is considered. At the discrete level, the approximation problem is then formulated as an optimization problem for the c_j :

$$c_j = \arg \left\{ \min_{d_j} \sum_{k=1}^{N_g} \left[\rho(x_k, 0) - \sum_{j=1}^{N_p} d_j \sigma(x_k - X_j(0)) \right]^2 \right\}, \quad (7.43)$$

where N_g is the number of grid points where the error is evaluated. The particle initial positions $X_j(0) = \xi_j$ are given and coincide with the grid points where the density is above a certain threshold. Other more sophisticated choices, like for example adapting the particle distribution to $\rho(x, 0)$, can lead to better accuracy. However, if the initial position of the particles is given, the reconstruction of the initial density distribution always amounts to a quadratic optimization problem in the coefficients c_j that can be solved by a linear system. The computational cost of this step is negligible since the size of the problem is $N_p \times N_p$ and the number of particles is usually of the order of 10^3 to 10^6 , according to resolution and the number of space dimensions.

7.5.2 Potential velocity field and reconstruction of the final condition

The mass c_j of each particle is now determined from the approximation of the initial condition. The particles move along straight lines and the particle mass remains constant along these trajectories. Two conditions for the minimum of (7.30) are hence satisfied. We still have to enforce that the velocity field is potential and that the final condition on the density distribution is verified. In order to do so, we assume that the components of the velocity are expressed as centered finite differences in the respective directions of a scalar function whose values on the grid are ψ_l . Denoting by D_{jl} the elements of the discrete centered gradient operator, we have that the velocity of each particle is $V_j = \sum_{l=1}^{N_d} D_{jl} \psi_l$, where N_d is of the order of N_p . Next, an optimization problem with respect to ψ_l is solved to approximate the final mass distribution. We have

$$\begin{aligned} \psi_l = \arg \left\{ \min_{\Psi_l} \mathcal{E}(\Psi_l) \right\} = \\ \arg \left\{ \min_{\Psi_l} \sum_{k=1}^{N_g} \left[\rho(x_k, T) - \sum_{j=1}^{N_p} c_j \sigma(x_k - \xi_j - \sum_{l=1}^{N_d} D_{jl} \Psi_l T) \right]^2 \right\}. \end{aligned} \quad (7.44)$$

The gradient of the above function can easily be computed so that the numerical solution of this problem is solved by a steepest descent method or by quasi-Newton iterations.

Mollifying kernels $\sigma(\xi)$ with compact support can be used, although the support must be large enough to keep some desirable properties. In cases in which, for example, a fragmentation process takes place, or simply in cases in which the density supports at times $\tau = 0$ and $\tau = T$ have null intersection, compact support kernels with small enough

support may result in having $\partial\mathcal{E}/\partial\Psi_l = 0$ from the first optimization step because the error vanishes where the support of the kernel is non zero and vice versa.

In order to possibly speed up convergence toward the minimum, a penalization can be added to $\mathcal{E}(\Psi_l)$:

$$\mathcal{E}_p(\Psi_l) = \mathcal{E}(\Psi_l) + \beta \sum_j^{N_p} c_j \frac{\|\sum_{l=1}^{N_d} D_{jl}\Psi_l\|^2}{2}, \quad (7.45)$$

where $\beta \in \mathbb{R}^+$. The actual effect on convergence of the penalization term is studied in the numerical experiments hereafter.

In summary, in the discrete problem that we have formulated mass conservation, mass transport along straight lines and potential velocity field are exactly satisfied at the discrete level. The initial and final mass distribution are approximated in a least square sense. Of course, the problem solution is independent of T . We kept the notion of the time variable τ in case the intermediate states of the mapping are to be computed. This is an inexpensive task thanks to equation (7.42).

The code used for the numerical experiments presented below was written in C++. The code was conceived in an object oriented framework, the implementation is based on Standard Library only.

7.6 Preliminary numerical tests

In the following numerical experiments we use the gaussian kernel

$$\sigma(\xi) = \frac{1}{(\ell \sqrt{\pi})^d} \exp\left(-\frac{|\xi|^2}{\ell^2}\right), \quad (7.46)$$

where ℓ is the kernel characteristic length.

The first test is relative to a problem where the initial density distribution is uniform and the final one shows concentric compressions and rarefactions. The error in the initial and final density distributions is studied as a function of the discretization parameters. The other examples are aimed at analyzing the performance of the proposed solution method in more critical cases where density distributions with sharp boundaries are given or mass fragmentation phenomena occur. These cases are paradigmatic of situations that are encountered in medical imagery problems. The last two applications show results in this sense.

In all test cases the reconstruction of the final condition was attained by a constant step gradient descent method. The most computationally intense simulation, the two-dimensional mass splitting phenomenon, takes about 1 hour on a standard laptop. In

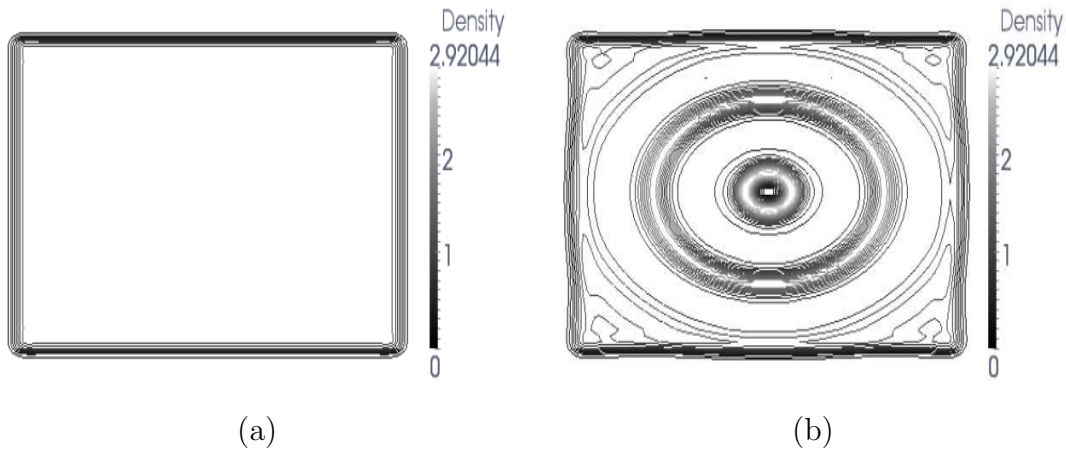


Figure 7.2: Density distribution at time a) $T=0$, b) $T=1$.

the next pictures, when isocontours are shown, 25 levels equally distributed between the minimum and the maximum value of the scale are drawn.

7.6.1 Recovering a wavy density distribution

The initial density distribution is $\rho(x, 0) = 1$ for $x \in [0, 1] \times [0, 1]$. We consider a velocity distribution

$$U(x, 0) = K \nabla(\sin(2\pi\omega\|x\|^2) \exp(-(\|x\|^2/\eta^2))),$$

where $K = 1.00e - 2$, $\omega = 4$ and $\eta = 0.25$. The initial density distribution and the velocity field are propagated in time according to equations (7.15) and (7.34). Once the density distribution at time $T = 1$ is found, we solve the optimal mass transfer problem. In Fig.7.2 the initial and final density distributions are represented. Rarefactions and compression zones can be identified according to the color scale. The space resolution of the figure is 200×100 . In this test case the resolution is intentionally not uniform.

Three different grid resolutions were considered, 100×50 , 200×100 , and 400×200 . For such resolutions, placing particles where density is larger than the density maximum divided by 1000, leads to the following number of particles: $1.25e3$, $5.00e3$ and $2.00e4$, respectively. The minimization of \mathcal{E} was stopped when the difference between the gradient norm of two subsequent iterations was less than $1.0e - 4$. The results are presented in tables 7.1, 7.2, 7.3.

First of all we remark that β has a reduced influence on the results. ϵ_T slightly decreases with β increasing, but then this effect is saturated. Of course ϵ_0 is independent

Table 7.1: Resolution 100×50 . ϵ_0 is the L^2 relative error on the initial density distribution, ϵ_T on the final. N_i is the number of iterations to minimize \mathcal{E} , *i.e.*, such that the gradient norm variation is below $1.0e - 4$.

ℓ	β	ϵ_0	ϵ_T	N_i
2.00 e-2	5.0 e-4	6.776 e-4	6.078 e-4	230
1.80 e-2	5.0 e-4	6.120 e-4	4.437 e-4	269
1.60 e-2	5.0 e-4	5.398 e-4	3.185 e-4	336
1.40 e-2	5.0 e-4	4.648 e-4	2.821 e-4	409
1.20 e-2	5.0 e-4	3.871 e-4	4.076 e-4	522
2.00 e-2	1.0 e-3	6.776 e-4	5.882 e-4	328
1.80 e-2	1.0 e-3	6.120 e-4	4.078 e-4	380
1.60 e-2	1.0 e-3	5.398 e-4	2.641 e-4	627
1.40 e-2	1.0 e-3	4.648 e-4	2.326 e-4	508
1.20 e-2	1.0 e-3	3.871 e-4	3.748 e-4	623
2.00 e-2	5.0 e-3	6.776 e-4	5.434 e-4	561
1.80 e-2	5.0 e-3	6.120 e-4	4.040 e-4	481
1.60 e-2	5.0 e-3	5.398 e-4	2.622 e-4	572
1.40 e-2	5.0 e-3	4.648 e-4	2.302 e-4	493
1.20 e-2	5.0 e-3	3.871 e-4	3.727 e-4	620

of β . We have that $\epsilon_0 \rightarrow 0$ as $\ell \rightarrow 0$, since in the limit case c_j equals the local value of the initial density distribution. Increasing the grid resolution, the number of particles increases and the error on the final resolution is systematically decreasing.

The error ϵ_T is not monotonically decreasing with the kernel length. There is a trade off between accuracy on the initial and final density distributions, depending on the ratio between the grid size and the kernel length. However, the optimal kernel length decreases with increasing grid resolution, as it should for consistency. No significant trend appears in the number of iterations except that in general the number of iterations increases as β does.

The values of $\left| \rho(x_k, T) - \sum_j^{N_p} c_j \sigma(x_k - \xi_j - V_j T) \right| / \rho(x_k, T)$ are shown in figure 7.3, when the resolutions used are 200×100 and 400×200 and $\ell = 1.00e - 2$, $\beta = 5.0e - 3$. The error is concentrated on the boundaries and in the higher density zones.

Table 7.2: Resolution 200×100

ℓ	β	ϵ_0	ϵ_T	N_i
1.40 e-2	5.0 e-4	3.979 e-4	2.633 e-4	173
1.20 e-2	5.0 e-4	3.729 e-4	1.675 e-4	177
1.00 e-2	5.0 e-4	3.249e-4	8.646 e-5	245
0.80 e-2	5.0 e-4	2.566 e-4	5.408 e-5	399
0.60 e-2	5.0 e-4	1.873 e-4	4.704 e-4	140
1.40 e-2	1.0 e-3	3.979 e-4	2.655 e-4	161
1.20 e-2	1.0 e-3	3.729 e-4	1.678 e-4	184
1.00 e-2	1.0 e-3	3.249e-4	8.852 e-5	236
0.80 e-2	1.0 e-3	2.566 e-4	5.703 e-5	393
0.60 e-2	1.0 e-3	1.873 e-4	4.859 e-4	142
1.40 e-2	5.0 e-3	3.979 e-4	2.673 e-4	189
1.20 e-2	5.0 e-3	3.729 e-4	1.768 e-4	196
1.00 e-2	5.0 e-3	3.249e-4	1.019 e-5	244
0.80 e-2	5.0 e-3	2.566 e-4	7.522 e-5	360
0.60 e-2	5.0 e-3	1.873 e-4	3.855 e-4	230

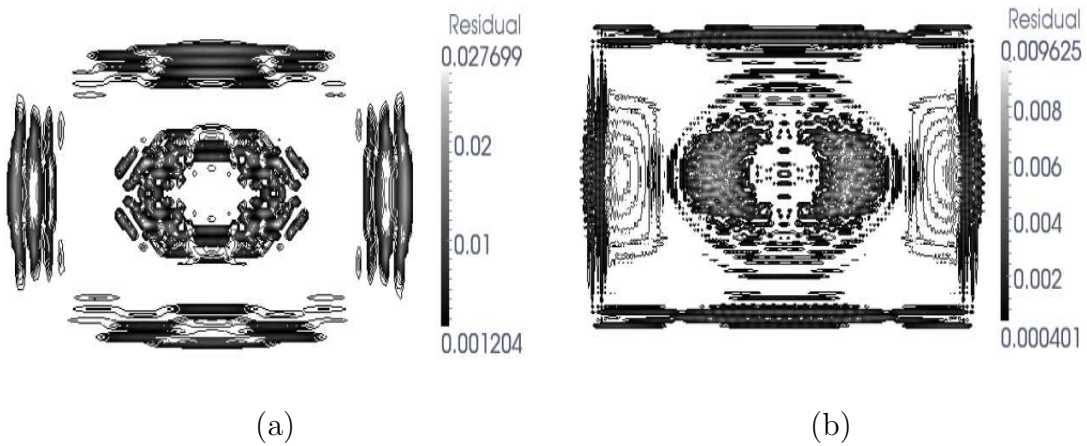
Figure 7.3: Relative error on the final density distribution. Resolution: a) 200×100 , b) 400×200 .

Table 7.3: Resolution 400×200

ℓ	β	ϵ_0	ϵ_T	N_i
1.00 e-2	5.0 e-4	8.288 e-5	3.737 e-5	230
0.85 e-2	5.0 e-4	7.108 e-5	2.754 e-5	204
0.70 e-2	5.0 e-4	5.921 e-5	3.420 e-5	307
0.55 e-2	5.0 e-4	4.790 e-5	9.985 e-5	390
0.40 e-2	5.0 e-4	3.573 e-5	2.704 e-4	193
1.00 e-2	1.0 e-3	8.288 e-5	3.821 e-5	219
0.85 e-2	1.0 e-3	7.108 e-5	2.770 e-5	213
0.70 e-2	1.0 e-3	5.921 e-5	3.517 e-5	326
0.55 e-2	1.0 e-3	4.790 e-5	9.998 e-5	410
0.40 e-2	1.0 e-3	3.573 e-5	3.004 e-4	195
1.00 e-2	5.0 e-3	8.288 e-5	3.975 e-5	250
0.85 e-2	5.0 e-3	7.108 e-5	2.821 e-5	245
0.70 e-2	5.0 e-3	5.921 e-5	3.519 e-5	278
0.55 e-2	5.0 e-3	4.790 e-5	1.021 e-4	334
0.40 e-2	5.0 e-3	3.573 e-5	4.455 e-4	227

7.6.2 Mass splitting: recovering a one-dimensional exact map

In this subsection we study the accuracy of the scheme proposed in a case where the exact map $X^*(\xi)$ is known. The difficulty is that the mass splits and that the initial and final densities are not uniformly differentiable, whereas the kernels used to represent the density distributions are uniformly differentiable. The initial density, of mass 1, is a hat function defined between -1 and 1. The final density distribution, of equal mass, is represented by two hat functions, symmetrically placed about the vertical axis and defined between -1 and 0, 0 and 1, respectively. The exact optimal map can be determined in this case by simply integrating the jacobian equation.

In Fig. 7.4 the results obtained with 80 grid points are contrasted to the exact solution. On the left, the initial density distribution, on the right the final one. In table 7.4 the results of the numerical solution are presented. In particular, we consider the error ϵ_T defined as before. Also, we consider the error ϵ_a , the L^2 norm of the difference between the exact solution and the result of the simulation, computed with an higher order quadrature. In this case it is possible to compute such an error since both the exact solution and the one resulting from the simulation are defined for all values between -1 and 1. Finally,

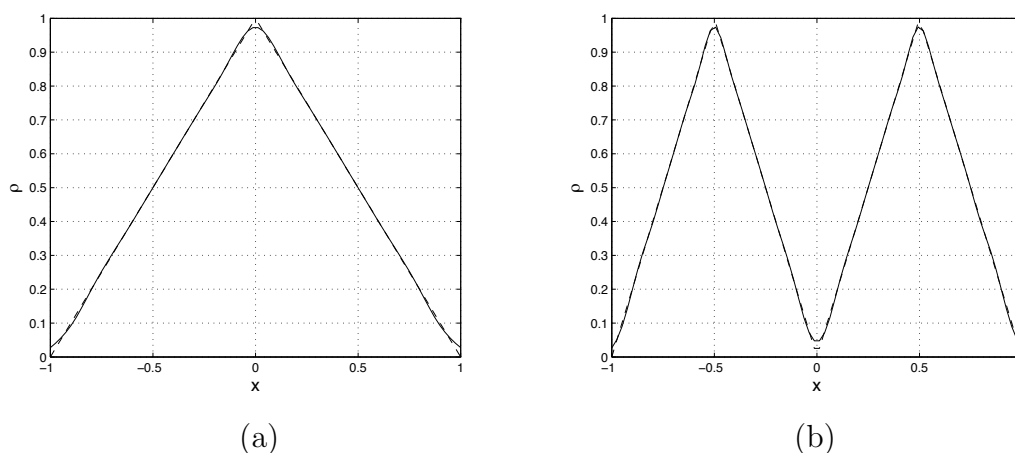


Figure 7.4: Density distribution at time a) $T=0$, b) $T=1$. The grid resolution is $N=80$.

we can compute E_{map} , the L^2 error between the exact map and the one obtained in the simulation. Since we actually compute the potential, this is a more stringent error since it is relative to a differentiated quantity. As before, the errors systematically decrease with increasing grid resolution. Also, the optimal kernel length decreases as the number of points increases.

7.6.3 Two-dimensional mass splitting

We investigate the two dimensional case of a final density distribution obtained using a potential that is just C^0 . The velocity field is discontinuous and hence the mass distribution is fragmented. In Fig.7.5 the density at time $T = 0$ and $T = 1$ are shown. At the beginning, the distribution is a normalized paraboloid. The potential from which the velocity field derives is $.01|x - 0.1 \sin(4\pi y) - 0.5|$.

The image is assigned on a 200×100 grid and the number of particles used is about $5e3$. The number of iterations for the algorithm to converge is approximately 1500. In Fig.7.6.a) the solution obtained by numerically solving the optimal transport problem is shown. All the details of the fragmentation process are correctly recovered. In Fig.7.6.b) the relative error on the final image in the case of 200×100 resolution is represented. The relative error is not concentrated along the singularity, but on the external boundary, since there the density values are close to 0.

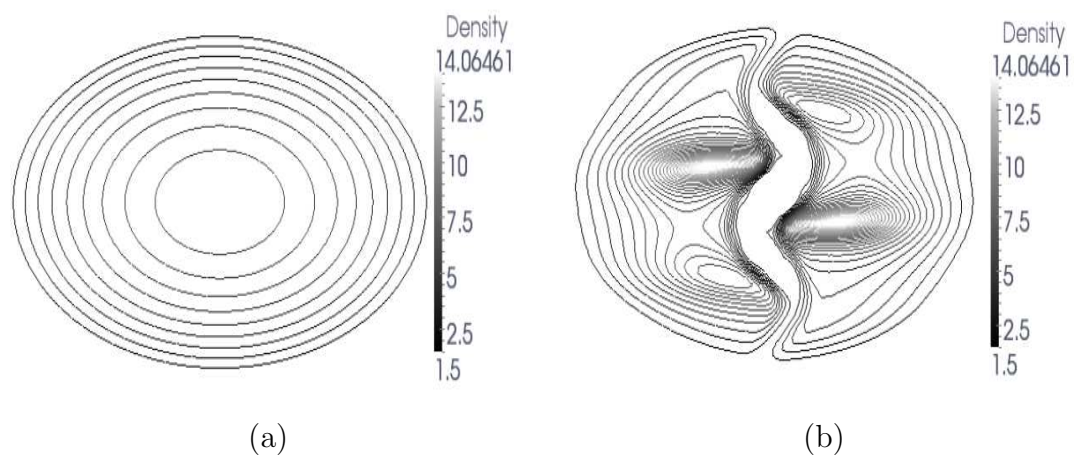


Figure 7.5: Reference density distributions, resolution 200×100 , at time a) $T=0$, b) $T=1$.

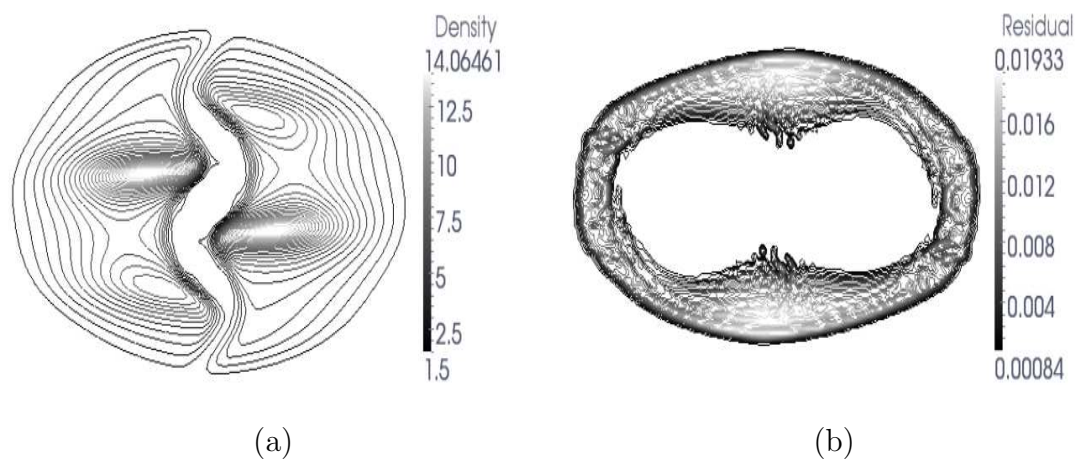


Figure 7.6: a) Density at time $T=1$ for the computed optimal solution b) relative error on the final image.

Table 7.4: N_p is the number of particles, ℓ is the kernel length, ϵ_T is the error computed on the actual grid, ϵ_a is the error computed with respect to the exact solution, and E_p is the error on the mapping, *i.e.*, on the gradient of the exact potential. The regularization was set to $\beta = 5e - 4$.

N_p	ℓ	ϵ_T	ϵ_a	E_{map}
10	2.00 e-1	1.74 e-2	8.30 e-2	1.16e-1
10	1.75 e-1	1.63e-2	8.44 e-2	1.14e-1
10	1.60 e-1	1.71 e-2	8.51 e-2	1.15e-1
20	1.60 e-1	1.52 e-2	3.39 e-2	0.92e-1
20	1.50 e-1	1.43e-2	3.10 e-2	0.91e-1
20	1.40 e-1	1.21 e-2	2.93 e-2	0.90e-1
40	1.15 e-1	1.00 e-2	1.60 e-2	0.79e-1
40	1.10 e-1	0.95e-2	1.51 e-2	0.77e-1
40	1.05 e-1	0.93 e-2	1.46 e-2	0.74e-1
80	8.50 e-2	8.91 e-3	9.98 e-3	0.55e-1
80	7.50 e-2	7.13e-3	8.41 e-3	0.51e-1
80	7.00 e-2	6.75 e-3	7.54 e-3	0.53e-1

7.6.4 Application to medical imagery

One possible application of optimal transport techniques concerns medical imagery and, in particular, non-rigid registration, see for example [136]. Image registration is the process of establishing a common geometric reference frame between two or more data sets possibly taken at different times.

Registration has a substantial recent literature devoted to it, with numerous approaches effective in varying situations, as described in [117]. These range from optical flow to computational fluid dynamics, to various types of warping methodologies. One class of methods is based on variational techniques, where the characterization of the desired transformation is embodied in the definition of the functional to be minimized. A mass preserving mapping that minimizes the distance may be of practical interest thanks to certain desirable properties: it is parameter free, symmetrical and the minimizer of the distance functional involved is unique. However, in the present context, image registration is used moreover as a challenging numerical illustration.

The first example discussed is relative to a thorax scan presenting lung noduli, while the second example is relative to the morphing of an image showing lung tissue attacked

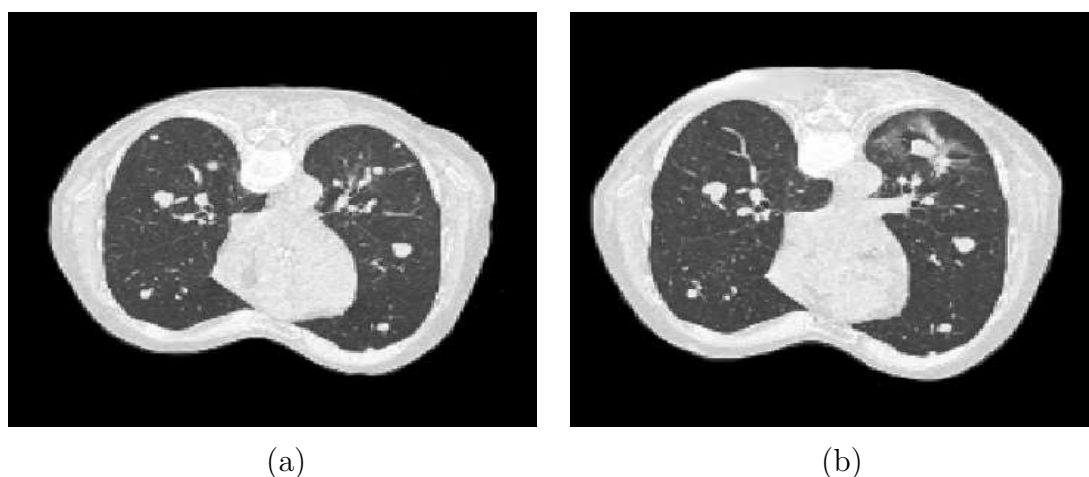


Figure 7.7: Thorax image scan at a) $T=0$, b) $T=1$ (corresponding to an evolution of six months); Courtesy Institute Bergonié, Bordeaux.

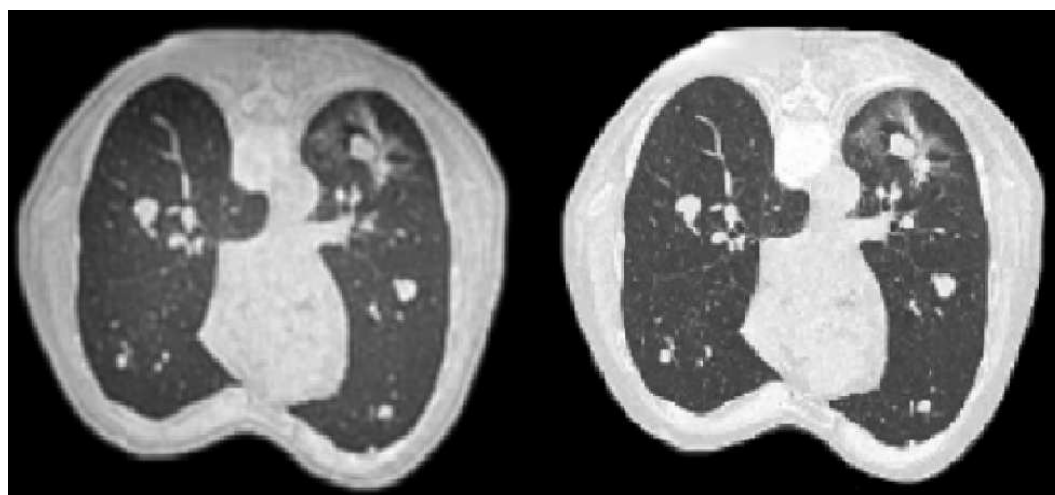
by cancer.

Thorax scan

In Fig.7.7 the initial and final thorax scans are shown. The objective is to find an optimal mapping between the two geometries. The images have a resolution of 200×200 and the number of particles used is approximately $2.0e4$. The number of iterations to reach convergence, due to the complexity of the geometry was 2500.

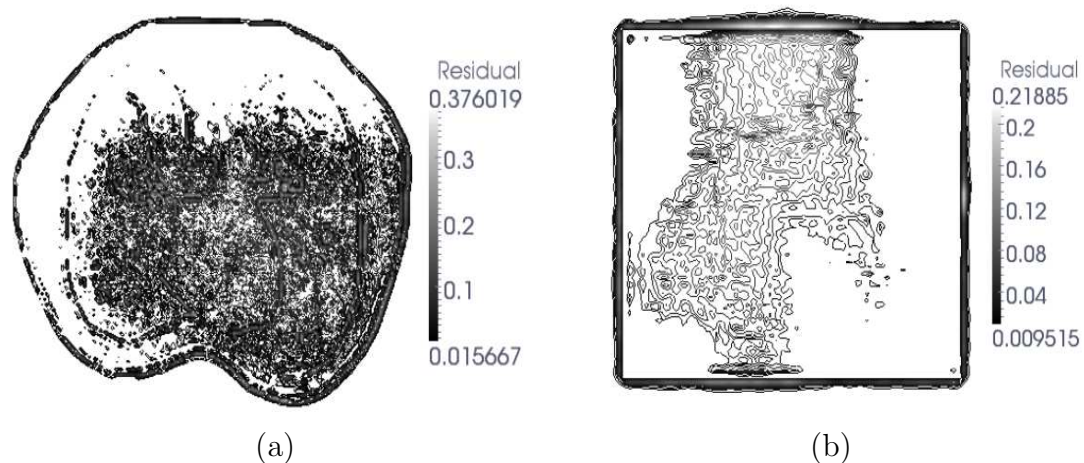
In Fig.7.8 the result of the computation is presented. On the left the solution obtained by applying the transformation to the first image is shown, on the right there is the actual scan. The main difference is in the normalization of grey scale: in order to perform a registration based on the optimal transport problem, the mass of the two density distributions must be the same and therefore the grey scale of the final image is modified so that it has the same “mass” of the initial image. Despite the complexity of the geometry, the agreement is quite good.

In Fig.7.9.a) the relative error on the final image is shown. It is higher in the region where there are sharp boundaries, as expected. The error is basically due to the gaussian kernel spreading sharp boundaries. In Fig.7.9.b) the potential of the transformation is shown.



(a)

Figure 7.8: On the left: optimal transport result at $T=1$; On the right the true image at the same time.



(a)

(b)

Figure 7.9: Residual of the final image in the case of a) Thorax non-rigid registration, b) Tissue mapping for a regressing tumor.

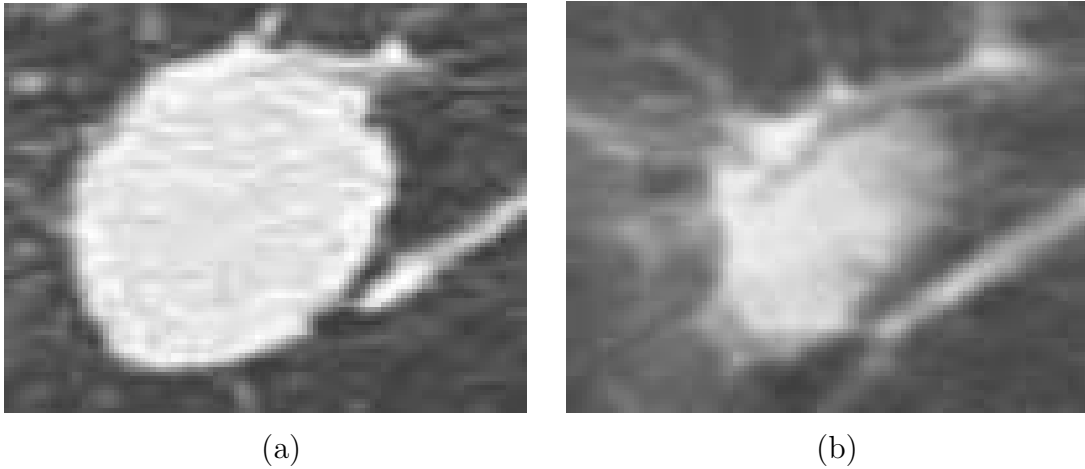


Figure 7.10: Tissue scan at a) $T=0$, b) $T=1$ (corresponding to an evolution of three months; Courtesy Institute Bergonié, Bordeaux).

Tissue morphing

A growing tumor can be associated to a certain displacement field. This field can be computed as the optimal plan that realizes the mapping between the scans. A portion of a lung scan representing tissue affected by cancer is considered and in Fig.7.10 two images are shown. The first image represents the original tumor ($T = 0$), which is then treated and its area decreases ($T = 1$). The space resolution of these images is 128×128 pixels, which is the original resolution of the scan. In Fig.7.11 the result of the optimal flow is compared to the actual image. The grey scale has slightly changed and this is due to the fact that the mass (the integral of the density over the domain) is decreased when the tumor is collapsed, so that a renormalization of the grey scale was necessary in order to enforce the mass conservation constraint. Apart from this, the agreement is good and no particular error structure emerges from the computation.

In Fig.7.9.b) the relative error with respect to the normalized image is shown.

7.6.5 A three-dimensional application

The objective of this section is to provide a discussion of the present approach computational viability to recover a non-trivial density distribution. Again, we take an example from medical imagery. The problem is to map a uniform mass distribution in a cube to a density distribution that corresponds to the magnetic resonance imaging (MRI) of a human head.

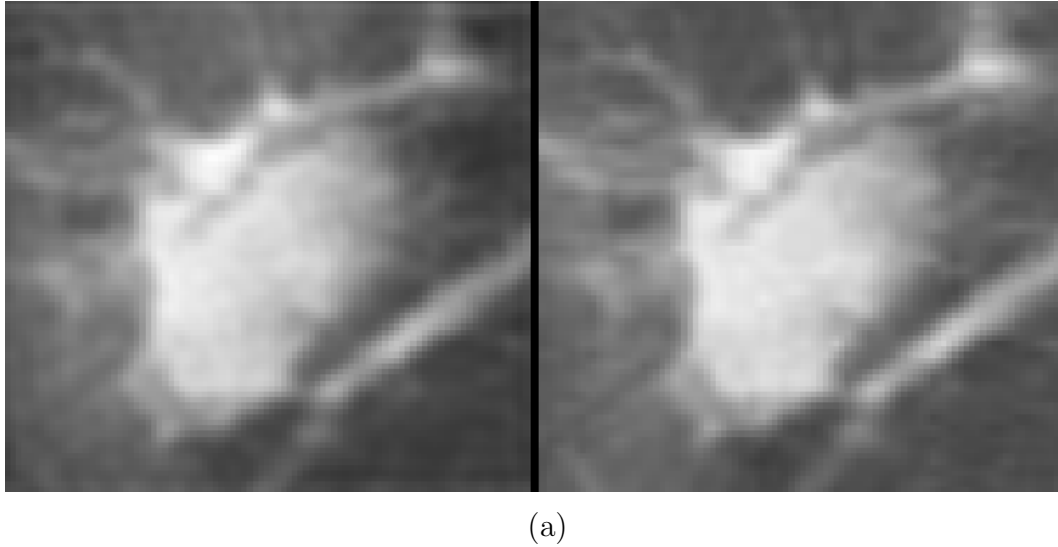


Figure 7.11: On the left: Monge result at $T=1$; On the right the true image at the same time.

Gaussian kernels evaluated on a sub-domain of 512 points and three different grid resolutions were employed: 15^3 , 30^3 and 60^3 . The simulations were stopped when the L^2 norm of the residual, as defined for the previous numerical tests, was divided by a factor 100 with respect to its initial value.

In Fig.7.12 the initial and final densities are represented at the highest resolution and in Fig.7.13 cuts in different planes of the same distribution show the complexity of the geometry to be recovered. In Fig.7.14 planes with the isocontours of the residual are represented, superposed to the solution. The residual is negligible everywhere except for some spots, corresponding to the sharpest details of the target distribution.

In table 7.6.5 we report the computational time per gradient iteration (T_{it}), and the number of gradient iterations (It). The computations were performed on a standard laptop computer. As before, N_p is the number of particles and β the penalisation. The kernel length is $\ell = 2e - 2$ for all the resolutions. If the number of particles is N_p and the grid points are N , using global kernels (kernels whose support is the whole domain) leads to a computational time per gradient iteration scaling with $N_p \times N \approx N^2$. But, as discussed, a simple truncated kernel evaluation leads to a linear scaling with N_p . This trend is indeed confirmed by the evolution of the computational time per iteration as a function of the number of particles in table 7.6.5. The AHT method [16] has also a computational cost per iteration which is proportional to N , whereas in the Uzawa method [31] the cost of one iteration scales more than linearly because the computation

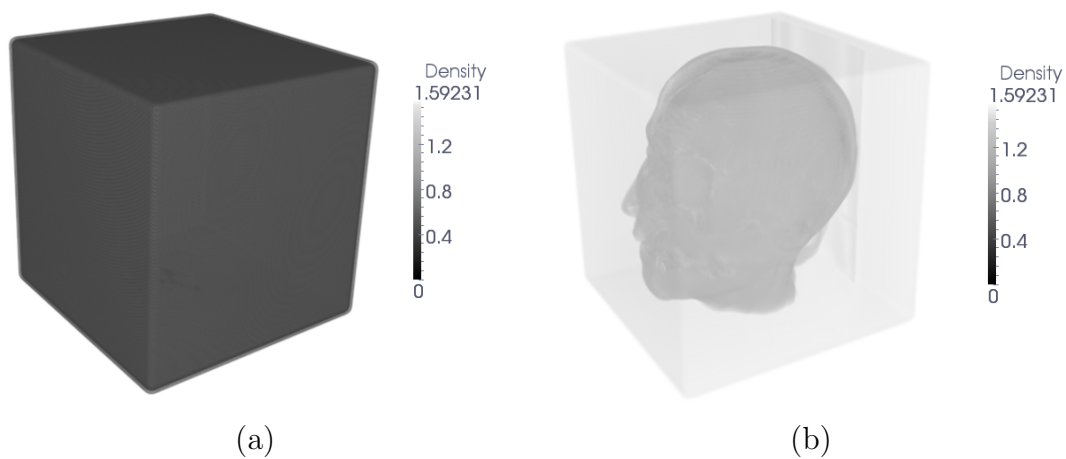


Figure 7.12: Density distribution at time a) $T=0$, b) $T=1$.

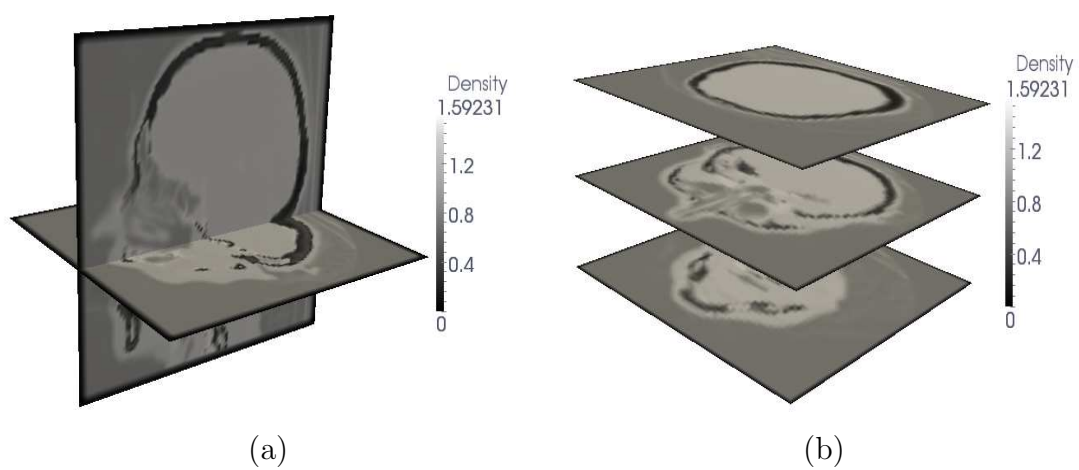


Figure 7.13: Slices of the final density distribution: a) XZ planes b) Z planes.

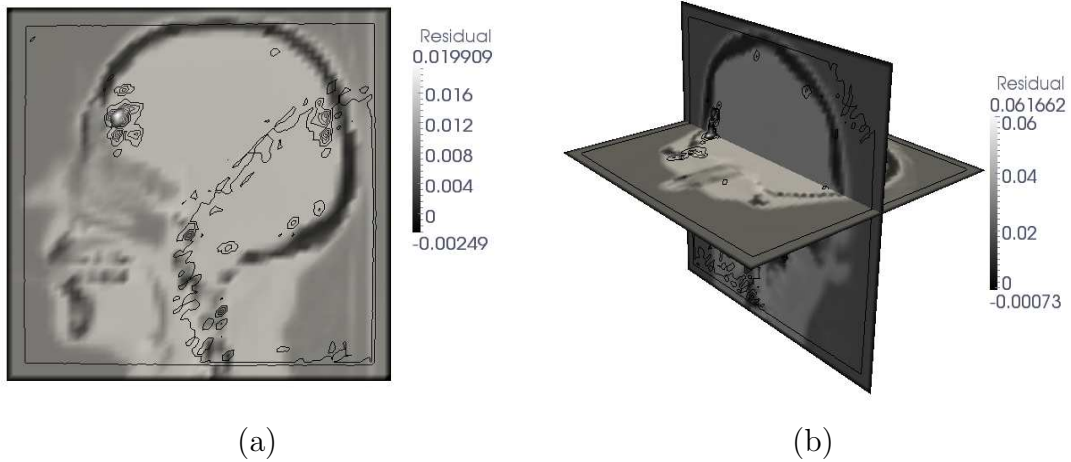


Figure 7.14: a) Contour lines of the residual distribution in the X plane; b) Contours of residual in YZ planes

N_p	β	T_{it}	It
15^3	1.2 e-3	1.2s	1000
30^3	2.4 e-4	9s	1100
60^3	1.6 e-4	72s	4000

of the gradient is obtained thanks to a fast Poisson solver in $d + 1$ dimensions.

Overall, the possible advantages of the present method reside mainly in the exact mass conservation and in the fact that N_p might be significantly smaller than N , since a particle is present only where mass is present. The actual computational bottle neck is rather linked to the number of gradient iterations to get to the minimum. However, this is a common issue to all methods based on optimization, *i.e.*, the AHT and the Uzawa scheme. Of course, a full discussion of this issue should involve the initial image, *i.e.*, how far from the solution the minimization starts, the width of the scale spectrum of the target image, and the actual minimization method employed. In this direction, a promising approach seems to be a multilevel optimization where the initial density distribution on a finer grid is obtained from the solution of a Monge problem on a coarser grid.

7.7 A preliminary investigation on the multilevel approach

In this section a multilevel acceleration of the proposed lagrangian method is introduced. The results on an artificial model problem are commented to support this preliminary analysis.

The idea is to exploit the solution on coarser grids to initialize the problem on finer ones. This is in some sort a preconditioning of the method. In particular it is efficient for all the cases in which the mapping solution of the optimal mass transport problem is characterized by low frequency displacements. The principle is that on coarser grids the scalar product between the particle kernel and the residual is larger (because the support of the kernel function is larger), allowing to recover large displacements in a better way.

For the moment, the technique has been implemented only on cartesian grids. The method on general non-structure grids is under development. The number of levels (N_l in the following) is *a priori* chosen. The original problem is defined on the finest grid, whose resolution is fixed (let us denote it by N_0 , number of quadrature points used). Then, the other levels are defined by considering half of the resolution in each space dimension, so that $N_{k+1} = \frac{1}{2^d} N_k$, where d is the space dimension.

The first step of the algorithm consists in applying a restriction operator to generate the problem to be solved of the coarser grid. In the present work a d -linear interpolation were adopted. A proper study on the influence of the restriction operator on the problem will be carried out in future.

Once the problem is solved at k level (*i.e.* the residual has been reduced of a certain factor), the potential or the velocity field are interpolated on the grid of the level $k - 1$, via a d -linear interpolation. This field is used as initial condition for the problem at $k - 1$ level.

An analysis of the computational cost is performed on a synthetic numerical example. Let us investigate the scaling of the multilevel approach and compare it to those one commented in the previous section for the original algorithm. The cost of a multilevel algorithm conceived in this way scales approximately as:

$$\mathcal{C} \approx \sum_k^{N_l} \frac{1}{2^{dk}} It_k, \quad (7.47)$$

where \mathcal{C} is the cost expressed in equivalent iterations on the finest grid (*i.e.* at the level 0), It_k is the number of iterations to converge at level k . The overall effective cost is

Table 7.5: Table representing the cost of the multilevel algorithm: the cost in equivalent iterations is shown for three different resolutions of the grid and as function of the number of levels adopted. The parameter $a_R^{(m)} = \frac{C_m}{C_0}$ quantifies the acceleration obtained when m levels are used for a problem originally formulated of a grid of resolution R^2 .

Levels	C_{256}	a_{256}	C_{128}	a_{128}	C_{64}	a_{64}
1	15600	1	12250	1	6000	1
2	5437.5	2.87	4321.5	2.84	2812.5	2.13
3	5062.5	3.08	3946.8	3.10	2550.0	2.35
4	5053.3	3.09	3937.8	3.11	2540.8	2.36

proportional to C via the number N of particles on the grid and the number of evaluations (and quadrature) for each particle.

The numerical test is proposed in a 2D setting. The computational domain in the square $[0, 1] \times [0, 1]$. Two densities are defined as follows:

$$\begin{aligned} \rho_0 &= 0.25 + \frac{R_0}{\int_{\Omega} R_0 dx}, \quad R_0 = \exp(-85(x_0^2 + y_0^2)), \\ \rho_T &= 0.25 + \frac{R_T}{\int_{\Omega} R_T dx}, \quad R_T = \exp(-100x_T^2 - 120y_T^2 + 150x_T y_T), \\ x_0 &= x - 0.45, \quad y_0 = y - 0.45, \\ x_T &= x - 0.55, \quad y_T = y - 0.55. \end{aligned} \tag{7.48}$$

These densities represent a translation (the norm of the gaussian centers displacement is $0.1\sqrt{2} \approx 14\%$ of the domain length) and a deformation of the gaussian function.

This problem was solved by the formulation presented in the above section, using d -linear kernels (*i.e.* the hat functions typically used in Finite Elements). The kernel length in this case is automatically given by the mesh size. The problem was discretized in three different resolutions, namely 64^2 , 128^2 , 256^2 and for each one the original method was compared to a 2, 3 and 4 grids approach. The computations were stopped, in all the numerical experiments, when the residual reached $1/50$ of its original value. The residual was normalized by the number of particles, so that it results an intrinsic quantity, allowing to better compare the simulations. The results are reported in Table 7.5. There are two main facts to be underlined. First, the multilevel, as it has been defined, produces an increasing acceleration with the number of the grid levels adopted. For the shown example, for all the resolutions, the acceleration obtained by means of a two grids approach is already good and there are not a lot of differences between the three and the four levels

computations. The maximum acceleration is a function of the resolution of the finest grid. In particular, when the original problem has a resolution of 128, it is maximum. This is problem dependent and it relies on the characteristic frequencies of the displacement field which is solution of the Monge problem. A second aspect to be described is the decreasing of the superlinearity of the algorithm. Let us consider the number of iterations when the classical algorithm is applied: with a resolution of 64^2 6000 iterations are needed, with 256 they mount to 15600, that is 2.6 times. When 4 grids are used, the ratio between the costs decreases to 1.98, because the problem is better conditioned.

Further investigations on the properties of the algorithm are under scrutiny. In particular the aim is to understand which elements of the problem affect the conditioning and which is the number of grids which allows to better solve it.

7.8 Application of Wasserstein distance to model reduction

In this section a possible application of the optimal transport tool presented above is introduced. The objective is to investigate the properties of Wasserstein distance when applied to model reduction. A classical tool in Reduced Order Modeling (ROM) is the Principal Component Analysis (PCA). In particular, in this work, POD (see [147]) was used in order to build a reduced dimension space describing fields involved in tumor evolution. In POD the L^2 representation of a given set of solutions is maximized, so that the L^2 distance between the reduced model and the database results minimized. The strategy based on L^2 norm has been widely studied and performs well when solutions are featured by a global behavior. On the contrary, when in physical systems structures are transported (let us think to a concentrated structure, like a vortices for examples), POD does not allow to give a satisfactory representation.

The key idea is to use the fact that the Wasserstein distance is naturally built by means of a transport to analyze systems in which transport plays a major role.

In what follows a technique is defined aiming at defining a representation that minimizes the Wasserstein distance between the reduced order model and a set of solutions of PDEs. A set of functions equipped with the Wasserstein distance is a metric space. In order to recast the analysis of the Wasserstein distances of this space into a principal component analysis framework (aiming at providing a reduced representation of it) an embedding is sought such that the metric space is approximated (at best) by an euclidean space. Indeed, the technique that allows to approximate a general distance with an eu-

clidean one is called multi dimensional scale embedding, and it may be found in [121]. In their article the authors use this tool to investigate the Wasserstein distances between phase spaces of time series described by ODEs.

Here, the purpose is to set up a similar tool to analyze partial differential equations solutions. Instead of considering the phase space, which would lead to exceedingly expensive computations, the time sampling of the solutions is used.

7.8.1 Technique definition

Let us suppose to have a database of densities, denoted by ρ_i , $i = 1, \dots, N_s$, such that:

$$\int_{\Omega \subset \mathbb{R}^d} \rho_i dx = 1, \quad \forall i = 0, \dots, N_s. \quad (7.49)$$

This hypothesis is necessary to study the densities in terms of optimal transport; it can be relaxed following the work of Benamou (see [29]). In this first study it is supposed to hold for the sake of simplicity.

The 2–Wasserstein distance (denoted by \mathcal{W}) between a couple of densities is thus defined as:

$$\begin{aligned} \mathcal{W}^2(\rho_i, \rho_j) &= \inf_{\tilde{X}} \left\{ \int_{\Omega} \rho_i(\xi) |\tilde{X}(\xi) - \xi|^2 d\xi \right\}, \\ \rho_i(\xi) &= \rho_j(\tilde{X}(\xi)) \det(\nabla_{\xi} \tilde{X}). \end{aligned} \quad (7.50)$$

This means that the squared Wasserstein distance is proportional to the density ρ_i and the square of the optimal displacement field. The optimal displacement is induced by the optimal mapping X^* , that, among all the change of coordinates $\tilde{X}(\xi)$ realizing the mapping between the densities i and j , minimizes the cost of Monge L^2 problem.

The Wasserstein distance squared is computed for all $i, j = 1, \dots, N_s$, so that $\frac{1}{2}N_s(N_s - 1)$ Monge problems are performed. Then, the following matrix is defined:

$$\mathcal{D}_{ij} = \mathcal{W}^2(\rho_i, \rho_j), \quad (7.51)$$

that is the matrix of the squared distances between the densities. This matrix has a particular structure: it is symmetric ($\mathcal{W}(\rho_i, \rho_j) = \mathcal{W}(\rho_j, \rho_i)$) and all the elements on the diagonal are zero because ($\mathcal{W}(\rho_i, \rho_i) = 0$), for the definition of distance. The i – th row of the matrix represents the distance between the i – th density and all the others. \mathcal{D} describes the densities as elements of a space equipped with the Wasserstein distance.

An embedding is sought, such that coordinates of the elements of the space are found with respect to the baricenter of the space, on the basis of their reciprocal distances. A standard technique is adopted. Let us define a projector J as follows:

$$J = I - \frac{1}{N_s} \mathbb{1} \mathbb{1}^T, \quad (7.52)$$

where $I \in \mathbb{R}^{N_s \times N_s}$ is the identity matrix and $\mathbb{1} \in \mathbb{R}^{N_s}$ is the column vector whose components are all 1. Given a vector v , the action of J on it consists in projecting it onto the space orthogonal to $\mathbb{1}$. The matrix embedding is defined as:

$$B = -\frac{1}{2} J \mathcal{D} J. \quad (7.53)$$

Then, B is decomposed via a singular value decomposition as follows:

$$B = USV^H, \quad (7.54)$$

where U and V are unitary matrices and S is the diagonal matrix whose entries are the singular values of B . Let us concentrate on the spectrum of B . It is proved that if the distance adopted is euclidean B is positive semi-definite. In this case a remarkable geometric interpretation is found. Wasserstein distance is in general not euclidean, so that negative eigenvalues appear. However, if we concentrate on the positive part of the spectrum, supposing that there are m positive eigenvalues, the following holds:

$$B \approx X \Lambda^+ X^T, \quad (7.55)$$

where $\Lambda^+ \in \mathbb{R}^{m \times m}$ is the matrix whose diagonal contains the positive part of the spectrum, $X \in \mathbb{R}^{N_s \times m}$ is the matrix whose columns are the eigenvectors corresponding to the positive eigenvalues. The components of the eigenvectors represent the coordinates of the points with respect to their baricenter. This completes multiscale embedding.

The eigenvectors have a different meaning in this context with respect to classical PCA. As stated, the embedding is performed with respect to a baricenter of the space, which is a density distribution whose properties will be further investigated in the following sections. The i -th component of the k -th eigenvector represents the weight of the i -th mapping (that transports the baricenter in the i -th snapshot) to build the optimal transport corresponding to the k -th eigenvalue. In the following we call k -th mode the k -th optimal transport, when a baricenter density is given. Conversely, when a base of mappings is taken in the space $\{v_1, \dots, v_k\}$, the mapping transporting the baricenter in the

$i - th$ snapshot is derived by summing the base mappings multiplied by the coordinates of the point representing the $i - th$ snapshot.

Roughly speaking, in POD the reduced space for the snapshots representation is built by means of the snapshots themselves, while in the proposed approach, due to the definition of Wasserstein distance, the representation of the snapshots is provided by means of a set of optimal transports that map a baricentral density into the snapshots. The space reduction is carried out in the space of the mappings.

7.8.2 Normalization of the embedding when a sampling of an optimal transport is considered

Let us suppose that the densities ρ_i are taken by uniformly sampling in time an optimal transport between ρ_0 and ρ_{N_s-1} . In this case, X_i , mapping ρ_0 into ρ_i is written by interpolation (see [30]):

$$X_i = \xi + i\Delta t \nabla_{\xi} \Phi(\xi), \quad (7.56)$$

where Δt is the sampling time. In this particular case, all the densities are aligned on a one dimensional subspace of the Wasserstein space, since they belong to the same optimal transport. Hence, we expect that only one eigenvalue of the matrix B is different from 0.

A property have to be investigated: if the number of samples is increased, the non-zero eigenvalue changes and tends to infinite with the number of the samples (*i.e.* with the dimension of \mathcal{D}). A normalization is introduced such that the eigenvalues tends to a finite value. Let us first compute the structure of the matrix of squared 2-Wasserstein distances for the case of an optimal transport. Let $\rho_0(\xi)$ be the first density.

The squared Wasserstein distance between the $i - th$ and the $j - th$ sample is thus:

$$\mathcal{D}_w^2(\rho_i, \rho_j) = \int_{\Omega_i} \rho_i(\eta) |X(\eta) - \eta|^2 d\eta, \quad (7.57)$$

where $X(\eta)$ is the optimal mapping between ρ_i and ρ_j . Using the properties of the mappings the elements of the matrix have the form:

$$\mathcal{D}_{ij} = \mathcal{W}^2(\rho_i, \rho_j) = \frac{C}{N_s^2} (i - j)^2, \quad (7.58)$$

where C is a constant, representing the squared Wasserstein distance (*i.e.* twice the kinetic energy) of the unique mapping linking all the snapshots. The time at which the last snapshot is taken is supposed to be $T = 1$.

Let us consider the matrix $\tilde{\mathcal{D}} = (i - j)^2$, $\tilde{\mathcal{D}} \in \mathbb{R}^{n \times n}$ and prove that: the associated embedding matrix B has only one zero eigenvalue, its value is $\lambda = \frac{n(n+1)(n-1)}{12}$.

First, the elements of B are computed using two standard results in finite series:

$$\sum_j^n j = \frac{n(n+1)}{2}, \quad \sum_j^n j^2 = \frac{n(n+1)(2n+1)}{6}. \quad (7.59)$$

By performing all the matrix vector products, exploiting the projector properties, the following is derived for B :

$$-(2B)_{ij} = (n+1)(i+j) - 2ij - \frac{(n+1)^2}{2} \Rightarrow B_{ij} = \frac{(n+1)^2}{4} + ij - \frac{(n+1)}{2}(i+j) \quad (7.60)$$

Let us introduce $k = \frac{n+1}{2}$. The expression for the entries of B can be recast as follows:

$$B_{ij} = k^2 - k(i+j) + ij \Rightarrow B_{ij} = (k-i)(k-j). \quad (7.61)$$

The relation written above states that B is the tensor product of a unique vector, whose components are $y_i = (k-i)$. This is sufficient to prove the first point. As a matter of fact:

$$Bv = \lambda v \Rightarrow yy^T v = \lambda v \Leftrightarrow \langle y, v \rangle y = \lambda v, \quad (7.62)$$

and only two possibilities arise:

1. $\lambda = 0 \Rightarrow \langle y, v \rangle = 0$ so that v belongs to the space orthogonal to y ,
2. $\lambda = \langle y, y \rangle$ and $v = y$.

This prove the first point. Let us compute explicitly the only non-zero eigenvalue. Again, the results on finite series are used, leading to:

$$\lambda_0 = \langle y, y \rangle = \sum_i^n (k-i)^2 = \frac{n(n+1)(n-1)}{12}. \quad (7.63)$$

The normalization condition for the generic $B \in \mathbb{R}^{N_s \times N_s}$ reduces thus to:

$$\mathcal{N} = \frac{(N_s+1)(N_s-1)}{12N_s}. \quad (7.64)$$

Let us define:

$$\overline{B} = \frac{B}{\mathcal{N}} = -\frac{6N_s}{N_s^2-1} JDJ, \quad (7.65)$$

and $\bar{\lambda}_{0,N_s}$ the only non zero eigenvalue associated to \bar{B} . The following property holds:

$$\lim_{n \rightarrow \infty} \lambda_{0,N_s} = \int_{\Omega_0} \rho_0(\xi) |\nabla_\xi \phi|^2 d\xi = \lambda_{0,N_s} \quad \forall N_s. \quad (7.66)$$

This property provides an interpretation for the eigenvalues of the embedding matrix. The only non-zero eigenvalue of the normalized embedding matrix \bar{B} approximates the squared Wasserstein distance of the displacement field, ($T = 1$ is supposed to hold).

The proposed normalization of the technique is useful not only in the particular case in which it has been derived. It is applied for numerical purposes when generic large systems are considered.

7.8.3 Baricenter of the space

In this section a property of metric spaces equipped with the Wasserstein distance is investigated. In particular, a baricenter is defined, *i.e.* a function (a density distribution) such that the sum of the 2–Wasserstein distance between it and all the other elements of the space is minimal. This is a mathematical property that holds independently from the technique proposed for the model reduction. Indeed, in the multiscale embedding the baricenter is implicitly defined. The baricenter obtained in that case (which is the origin of the euclidean space that approximates the Wasserstein one) is an approximation of the baricenter defined in this section. The interest in the computation of this particular function is that it represents the density distribution that, transported by a suitable combination of the base mappings (*i.e.* mappings which are the base of the euclidean space that approximates the Wasserstein one), approximates the snapshots.

In this section a characterization of the baricenter of the densities in the Wasserstein space is provided, by using basic results proved in the literature (see [68]). The result for the 2–Wasserstein distance is obtained; a generalization to p –Wasserstein distance is straightforward. The baricenter is defined as the element minimizing the sum of the squared distances with respect to the other points. The difficulty lies in the fact that the associated problem is a system of coupled variational problems:

$$\begin{aligned} X_i(\xi) &= \arg \min_{\tilde{X}} \left\{ \int_{\Omega_G} \frac{1}{2} \rho_G(\xi) |\tilde{X} - \xi|^2 - \lambda_i \left(\rho_G - \rho_i \det(\nabla_\xi \tilde{X}) \right) d\xi \right\}, \\ i &= 0, \dots, N_s - 1 \quad (i) \\ \rho_G(\xi) &= \arg \min_{\tilde{\rho}} \left\{ \int_{\Omega_G} \frac{1}{2} \tilde{\rho}(\xi) \sum_{i=1}^N |X_i - \xi|^2 - \sum_{i=1}^N \lambda_i (\tilde{\rho} - \rho_i \det(\nabla_\xi X_i)) d\xi \right\} \quad (ii). \end{aligned} \quad (7.67)$$

The first N_s problems describes the optimal mappings linking ρ_G to all the other densities, while the last one is the coupling problem, translating the definition of baricenter. The Euler-Lagrange equations are derived, according to [68].

For the first N_s problems the solution of the L^2 optimal mass transfer problem is recovered:

$$\rho_0(\xi) = \rho_i(X_i(\xi)) \det(\nabla_\xi X_i), \quad (7.68)$$

$$\nabla_\xi \lambda_i = (X_i - \xi) [\nabla_\xi X_i]^T. \quad (7.69)$$

This couple of equations defines a map between the initial condition ρ_G , whatever be, and the final density distribution ρ_i . A last Euler-Lagrange equation allowing to couple the problems and thus to determine ρ_G is obtained by making the variation with respect to $\tilde{\rho}$ vanish in Eq. 7.67.(ii). This leads to:

$$\sum_{i=1}^N \frac{1}{2} |X_i(\xi) - \xi|^2 - \lambda_i = 0. \quad (7.70)$$

In order to find a more explicit condition let us take the gradient of this expression:

$$\sum_{i=1}^N (X_i(\xi) - \xi) \cdot ([\nabla_\xi X_i]^T - I) - \nabla_\xi \lambda_i = 0. \quad (7.71)$$

Let us substitute Eq.7.69: the following result is obtained:

$$\sum_{i=1}^N X_i(\xi) - \xi = 0 \iff \sum_{i=1}^N u_i(\xi) = 0. \quad (7.72)$$

In each point of the space, the density $\rho_G(\xi)$ is such that the displacement fields associated to the mappings, summed up, are equal to zero. This system in every point of the space behaves as a N_s body system, ρ_G being implicitly a baricenter.

In the following sections some examples of applications of the proposed technique are detailed.

7.8.4 Ideal vortex scattering

In this section some numerical experiments are presented, concerning the study in terms of Wasserstein distance of the scattering of four ideal vortices in 2D. The detailed derivation of the equations governing the systems are found in [115].

Two couples of counter-rotating ideal vortices are initialized in the plane (their geometrical configuration is detailed below). The flow is incompressible and the vortices

being ideal, the vorticity is represented by four Dirac masses located in the vortices centers, so that the flow is irrotational almost everywhere. The potential field theory applies and the system may be reduced to an hamiltonian dynamical system describing the position of the centers in the plane. This case has been chosen because POD and standard techniques based on L^2 representation fails in giving a compact representation; the resulting number of modes is almost equal to the number of snapshots. Wasserstein distance provides, instead, an efficient compact representation.

Let us briefly present the governing equations. The domain is \mathbb{R}^2 , the four variables that determine the entire evolution of the system are $r_1, r_2, \theta_1, \theta_2$ and they are initialized as follows:

$$\begin{aligned} r_1(0) &= (l^2 + (1 + \beta)f^2)^{\frac{1}{2}}, \\ r_2(0) &= (l^2 + (1 - \beta)f^2)^{\frac{1}{2}}, \\ \theta_1(0) &= \arctan \left[\frac{(1 + \beta)f}{l} \right], \\ \theta_2(0) &= \arctan \left[\frac{(1 - \beta)f}{l} \right], \end{aligned} \tag{7.73}$$

where l, β, f are three parameters that determine the geometry of the system and the nature of the scattering. The cartesian coordinates of the vortices cores are linked to the variables as follows:

$$\begin{aligned} x_a &= r_1 \cos(\theta_1) & y_a &= r_1 \sin(\theta_1), \\ x_b &= r_2 \cos(\theta_2) & y_b &= r_2 \sin(\theta_2), \\ x_c &= r_1 \cos(\theta_1 + \pi) & y_c &= r_1 \sin(\theta_1 + \pi), \\ x_d &= r_2 \cos(\theta_2 + \pi) & y_d &= r_2 \sin(\theta_2 + \pi), \end{aligned} \tag{7.74}$$

The ODEs describing the evolution of the variables are:

$$\begin{aligned} \dot{r}_1 &= -\frac{2 \sin(2(\theta_1 - \theta_2))r_1 r_2^2}{\pi (r_1^4 - 2 \cos(2(\theta_1 - \theta_2))r_1^2 r_2^2 + r_2^4)}, \\ \dot{r}_2 &= -\frac{2 \sin(2(\theta_1 - \theta_2))r_2 r_1^2}{\pi (r_1^4 - 2 \cos(2(\theta_1 - \theta_2))r_1^2 r_2^2 + r_2^4)}, \\ \dot{\theta}_1 &= \frac{3r_1^4 - 2 \cos(2(\theta_1 - \theta_2))r_1^2 r_2^2 - r_2^4}{2\pi r_1^2 (r_1^4 - 2 \cos(2(\theta_1 - \theta_2))r_1^2 r_2^2 + r_2^4)}, \\ \dot{\theta}_2 &= \frac{r_1^4 + 2 \cos(2(\theta_1 - \theta_2))r_1^2 r_2^2 - 3r_2^4}{2\pi r_2^2 (r_1^4 - 2 \cos(2(\theta_1 - \theta_2))r_1^2 r_2^2 + r_2^4)}. \end{aligned} \tag{7.75}$$

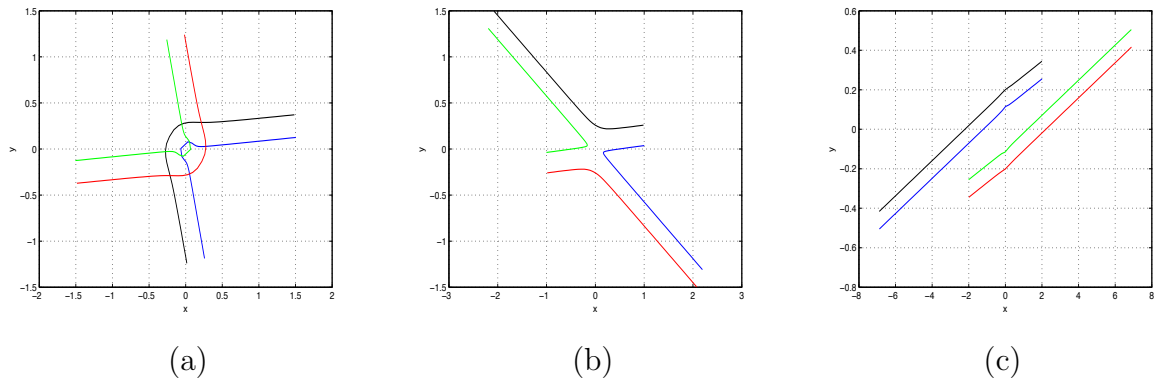


Figure 7.15: Three different scattering, trajectories of vortex cores for: a) $l = 1.5$, $\beta = 0.5$, $f = 0.25$ b) $l = 1.0$, $\beta = 0.75$, $f = 0.15$ c) $l = 2.0$, $\beta = 0.15$, $f = 0.30$

The equations of motion are integrated via an adaptive step fourth order Runge-Kutta scheme, in the time interval $[0, 2.5]$. The solution depends on the parameters initial values. In Fig.7.15, three different situations are represented. In Fig.7.15.a) a scattering is represented in which vortices keep their partner (the parameters used are: $l = 1.5$, $\beta = 0.5$, $f = 0.25$). When $l = 1.0$, $\beta = 0.75$, $f = 0.15$ vortices change their partner during the interaction and escape with the counter rotating vortex belonging to the other couple. In Fig.7.15.c) a weak interaction is represented, in which the couples simply move on (almost) straight lines (for $l = 2.0$, $\beta = 0.15$, $f = 0.30$).

Once the position of the vortices centers is known, the flow is obtained by the superposition of ideal vortex fields (velocity goes like $1/R$, where R is the distance to the centre). For a first analysis enstrophy is considered, so that the motion of four unitary Dirac masses is investigated. The Wasserstein distance has been computed by means of an exact combinatorial algorithm. For all the test 50 time frames were taken.

The embedding technique presented in the previous section were adopted. Some negative eigenvalues appear, due to the fact that the distance is not euclidean. They are small in modulus so that they are linked to some secondary feature of the evolution (in terms of Wasserstein distance). In Fig.7.16.a) the singular values of the embedding matrix are represented for the first case described. Only two eigenvalues are relevant in the approximation of the phenomenon. The corresponding eigenvectors are represented in a phase plane plot. The circles represent the components of the eigenvectors and can be associated to the time frames. Two directions emerges, that represent the optimal transports occurring before and after the interaction. The points which are not aligned represents the snapshots of the enstrophy configurations taken during the interaction.

7.8. APPLICATION OF WASSERSTEIN DISTANCE TO MODEL REDUCTION 171

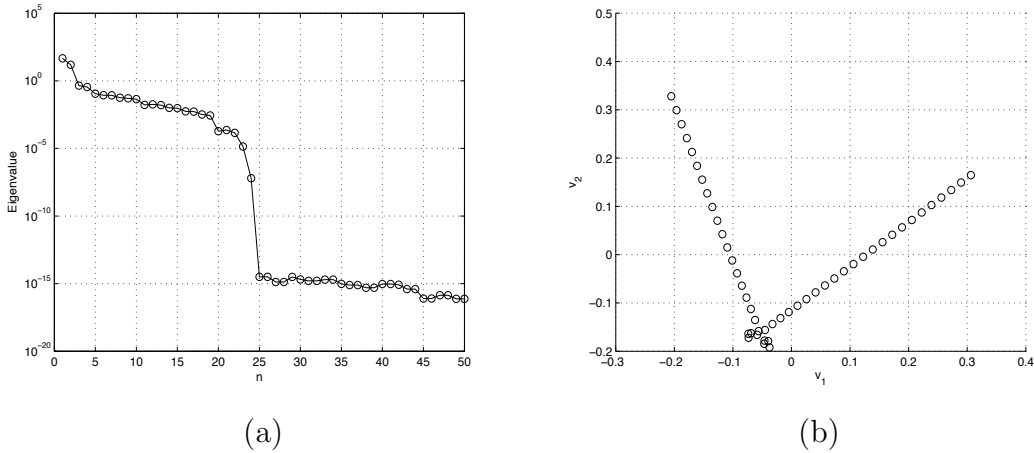


Figure 7.16: First case: a) the singular values of the embedding matrix in logarithmic; in b) the first two eigenvectors are represented in a phase plane plot.

The same analysis was performed for the cases b) and c) of Fig.7.15. Concerning the second case (see for instance Fig.7.17), the spectrum of the embedding matrix is similar to that obtained for the first case: two singular values emerges. Thus, the plot of the first two eigenvectors was done in a phase plane plot. As the vortex interaction is quite different, the resulting eigenvectors have a different configuration, but the optimal transport before and after the interaction may be recognized. The third case (see Fig.7.18) is different from the others. The interaction is very weak so that the resulting motion is practically an optimal transport. This third case may be considered as a perturbation of the analytical case analyzed in the previous section, in which the uniform sampling of a single optimal transport was used to derive a scaling relation for the eigenvalues. Indeed, in Fig.7.18.a) the plot of the singular values confirms that only one eigenvalue is important. The plot of the corresponding eigenvector in Fig.7.18.b) show that most of the snapshots are aligned, that is, they may be obtained by non-linear interpolation (*i.e.* by transport) of the baricentral density via a unique optimal transport. In this simple (and almost analytical) first examples, the comparison with the standard POD can be done conceptually in a very straightforward manner. The enstrophy is considered, which consists, as stated, in four Dirac masses. Thus, for the second and the third cases (Fig.7.15 b) and c)) the autocorrelation matrix (*i.e.* the matrix of scalar products of the snapshots) is the identity matrix. Hence, a lot of POD modes are necessary to reach the representation that is given by one or two modes built by the Wasserstein distance approach. For the first case (Fig.7.15.a)), the trajectories intersect, so that the autocorrelation matrix is not

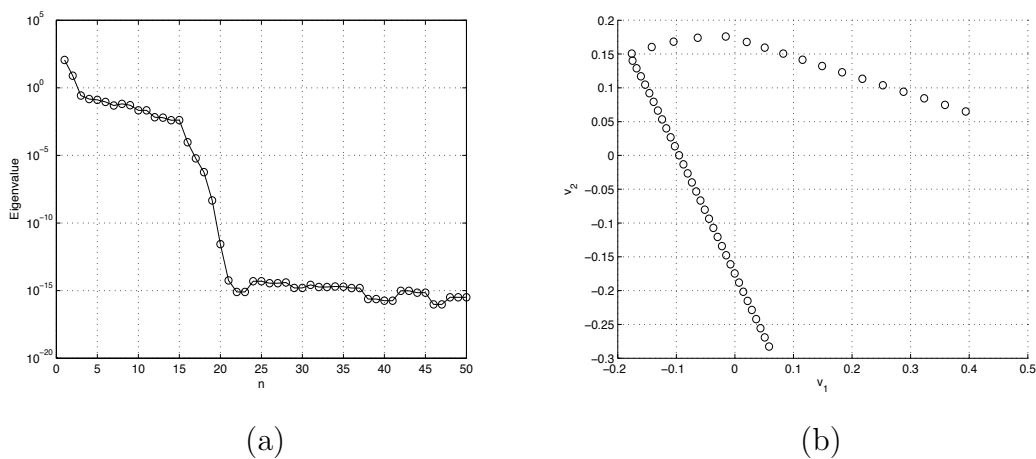


Figure 7.17: Second case: a) the singular values of the embedding matrix in logarithmic scale; in b) the first two eigenvectors represented in a phase plane plot.

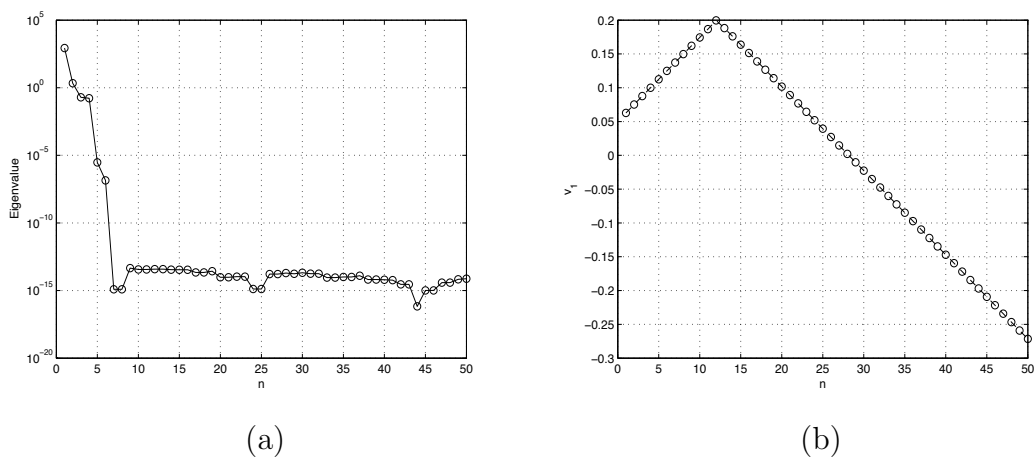


Figure 7.18: Third case: a) the singular values of the embedding matrix in logarithmic scale; in b) the first eigenvector

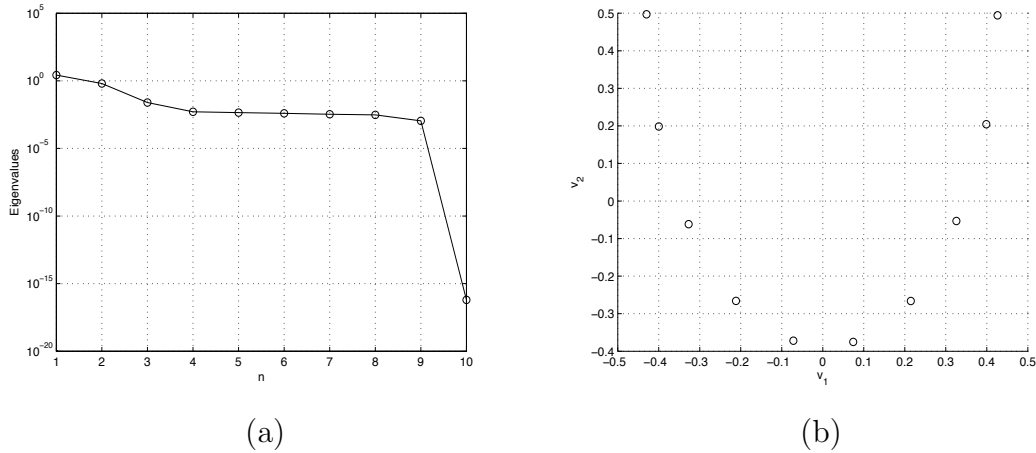


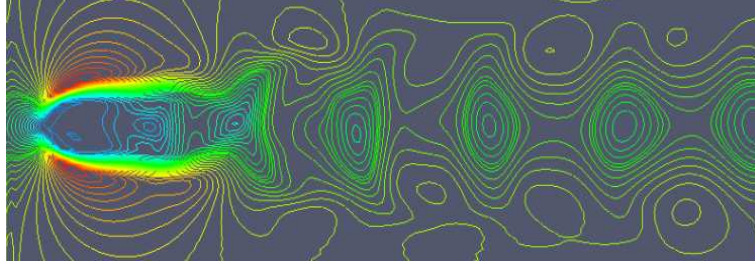
Figure 7.19: Kinetic energy of the flow around a circular cylinder: a) singular values in logarithmic scale b) phase plot of the first two eigenvectors

diagonal. However, few extradiagonal elements appear, so that, even in this case, a lot of POD modes are required.

7.8.5 2D cylinder vortex shedding

In this section the vortex shedding around a circular confined cylinder is analyzed. Several quantities may be studied. In order to give a complete analysis of the patterns arising (von Karman street) and to link the expansions for the mappings to incompressible Navier-Stokes equations at least two quantities are necessary (namely the two components of the velocity field u, v). In this preliminary study we concentrate on the ability to represent coherent structures and in particular to the possibility to have a good approximation in a reduced space. The kinetic energy of the flow is studied: it has been normalized in order to fulfill the mass constraint. Half a period of vortex shedding is considered of a flow computed at $Re = 200$.

A first analysis was performed taking 10 snapshots of the kinetic energy of the flow and computing the matrix of Wasserstein distances squared. The space resolution adopted was 200×100 , resulting in $2 \cdot 10^4$ collocation points. A multilevel algorithm was used with 4 grids and linear interpolation kernels. In Fig.7.19.a) the singular values of the embedding matrix associated to the problem is shown. The cascade has a smaller steepness with respect to those ones observed for the vortex scattering, but even in this case two eigenvalues may be retained, that provide a good approximation. In Fig.7.19.b) the phase



(a)

Figure 7.20: Baricentral density for the kinetic energy of the flow around a circular cylinder: isocontours, 30 lines between the maximum and the minimum

plot of the first two eigenvectors is shown, revealing a remarkable structure: the points are located on a circle. That means that, given two orthogonal base mappings ϕ_1, ϕ_2 the flow is well approximated by the transport of a baricentral density (localized in the centre of the circle) by the following mapping: $\Phi(t) = \cos(2\pi t)\phi_1 + \sin(2\pi t)\phi_2$, where $t \in [0, 1]$ is the time corresponding to a period.

This analysis suggests that three snapshots are sufficient to compute the baricentral density and two orthogonal base mappings. Three snapshots are taken at $t = 0, t = 0.25, t = 0.5$, equally distributed on half a period. In the following ρ_0 is the kinetic energy distribution at the very beginning, ρ_1 the kinetic energy at a quarter of period and ρ_2 that of at half a period. The optimal transport is computed by means of the multilevel algorithm, then, the obtained mapping is used to transport ρ_0 into the baricentral one, according to:

$$X_G = \xi + \frac{1}{2}\nabla_{\xi}\phi_{02}, \quad (7.76)$$

where the factor $1/2$ means that the collocation points are moved by half the displacement that allows to map ρ_0 into ρ_2 . Hence:

$$\rho_0(\xi) = \rho_G(X_g) \det(\nabla_{\xi}X_G). \quad (7.77)$$

In Fig.7.20 the baricentral density is shown, computed from the nonlinear interpolation between the kinetic energy distributions ρ_0 and ρ_2 . It is not perfectly symmetrical with respect to the x axis, and this is due to the fact that the considered snapshots have a slight asymmetry too. Let us remark that the baricentral density is not a configuration happening in the physical evolution of the system. However, the average position of the structures and the characteristic distance of the vortex in the weak may be inferred. In Fig.7.21 the base mappings are shown. The first mapping (Fig.7.21.a) has already

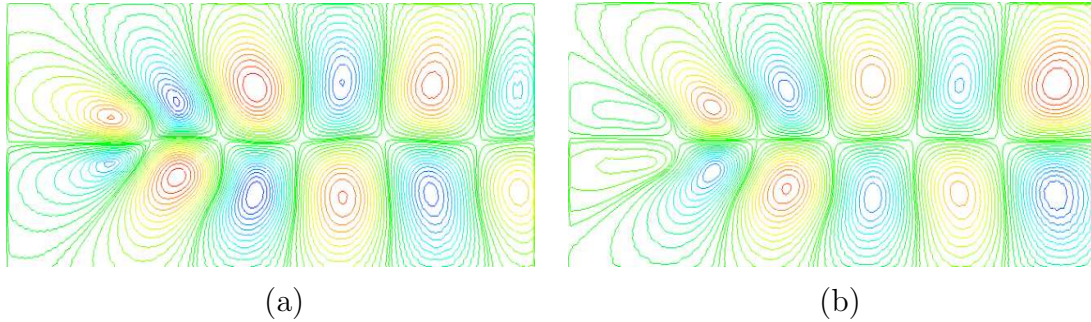


Figure 7.21: Isocontours of the base mappings: 30 lines between the maximum ($1.25e - 3$) and the minimum $-1.25e - 3$.

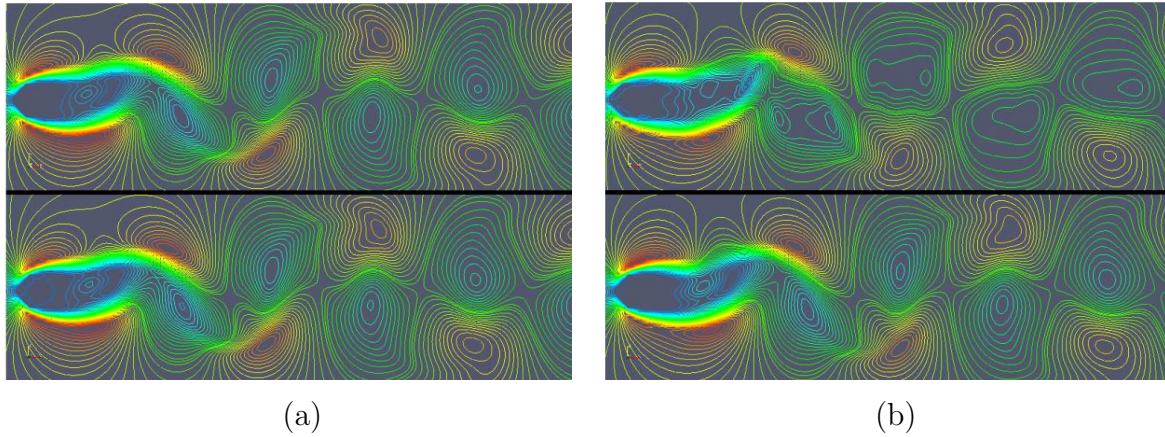


Figure 7.22: Isocontours (30 lines between the maximum and the minimum) of the reconstruction (upper line) and the simulation (lower line) for a) $t = 0$ and for $t = 1/8$

been computed to find the baricentral density. Once obtained, the mapping between the baricentral density and ρ_1 (*i.e.* the density located at a quarter of period) is computed providing automatically the mapping represented in Fig.7.21.b). The displacements fields (computed by taking the gradient of the potentials) are two sequences of alternated couples of sources and sinks, rendering the periodicity of the structures.

The approximation properties are investigated. In particular, given the base maps, the snapshots of the flow are reconstructed by transporting the baricentral density with the suitable displacement field, obtained by summing the mappings multiplied by $(\cos(2\pi t_i), \sin(2\pi t_i))$, where t_i is the position in the period of the $i - th$ snapshot.

Two cases are shown, corresponding to a good approximation and to a poor one. In Fig.7.22.a) the representation is shown for $t = 0$. In this case only the first mapping is used, and the snapshot has been used to build the base. This reflects in a very good

approximation. All the structures are represented correctly in terms of position and intensity. In Fig.7.22.b) the worst approximation is shown corresponding to the kinetic energy at $t = 1/8$, which is the farthest from the snapshots used to build the reduced space. Some errors appear concerning the position and the intensity of the structures. However, these errors are localized in the weak, the structures near the body are well captured. This is good if the local properties of the flow around the cylinder are of interest: for instance, if a representation of the forces acting on it is sought.

This first test is particular encouraging since it shows the possibility to give a sufficiently good approximation of the flow pattern using very little of information. The representation adopted is the minimal one, consisting in two modes computed using three snapshots. Adding a third mode and the informations coming from other snapshots will improve the representation.

Several possibilities arise concerning the model reduction strategy. Two perspective are currently under scrutiny: the first one is the enrichment of the reduced order model by means of global modes, resulting in an hybrid strategy: Wasserstein modes account for transport while global (POD) modes renders global behaviors. Moreover, a link between the potentials and the equations of the physics may be sought.

Chapter 8

Conclusions et Perspectives (français)

Dans ce chapitre on présente les conclusions de ce travail, ainsi que quelques perspectives et des questions ouvertes. D'abord on commente les résultats pour les problèmes inverses et ensuite ceux qui concernent les aspects numériques du transport optimal.

Problèmes Inverses Deux techniques ont été proposées dans cette thèse et les deux ont des résultats prometteurs, au sens qu'elles montrent qu'appliquer les modèles dans des cas cliniques n'est pas impossible.

Les avantages des modèles spatiaux par rapport aux modèles EDO est double: on donne une description des aspects spatiaux liés à la croissance et on pourrait espérer donner plus d'information aux médecins. Les tests effectués montrent que normalement les modèles EDP ont besoin de moins de données pour être calibrés. Le défaut principal des méthodes qui utilisent des modèles EDP est le coût computationnel. L'utilisation de la réduction de modèle est une avancée importante afin de rendre les méthodes EDP compétitives pour appliquer la technique cliniquement.

Un compromis entre la complexité des modèles et les données auxquelles on a accès est un élément clé pour la mise à point d'instruments basés sur des modèles phénoménologiques. Des modèles plus complexes ont un pouvoir prédictif supérieur, ils nous permettent notamment de donner une description de plus de phénomènes qui interviennent dans le processus de croissance, mais ils sont plus difficiles à calibrer. En particulier, si on n'a pas accès à beaucoup de données, ce qui est souvent le cas, le problème inverse est sous-déterminé. Les données utilisées dans le cadre de ce travail sont de CT sans, qui ont des bonnes propriétés de résolution et de contraste mais qui, en revanche, nous permettent de distinguer seulement entre tissu sain et tumorale. Par conséquent seulement des modèles très simples de croissance peuvent être utilisés.

Un autre élément qui joue un rôle primordial est le rapport entre les quantités modélisées et les mesures. Dans le cas présent une définition très simple d'observable a été adoptée, après une discussion avec les médecins. Rien ne garantit que ce choix (qui n'est pas unique) soit le meilleur. D'autres définitions d'observables pourraient être adoptées, qui donnent des meilleurs résultats. Une direction de recherche potentielle est constitué par l'inclusion dans l'ensemble des données de l'imagerie fonctionnelle. Celle ci permettrait d'avoir plus d'information concernant les tissus et d'utiliser des modèles plus complexes. Dans ce cas le rapport entre quantités modélisées et mesurées devrait être étudié avec beaucoup de soin.

Les résultats présentés doivent être jugés en considérant deux éléments : les erreurs dans les données et la variabilité du phénomène en jeu. Les scans ont une résolution

de 1.25mm, qui est comparable avec la taille des tumeurs dans la phase vasculaire. Les tumeurs analysées dans cette thèse ont une dimension qui est d'environ 5-6mm (mesurée sur le premier scan). Les erreurs (dues à la segmentation ou au bruit) pourraient influencer la précision des résultats de façon très significative. Une procédure standard au niveau de traitement de données est absolument nécessaire afin de pouvoir comparer les résultats des manière plus objective et systématique, même si les données sont dans des différents configurations géométriques.

Les mutations génétiques ainsi que phénomènes aléatoires qui influencent l'évolution de la tumeur de manière catastrophique ne peuvent pas être prévus. Comme on a commenté précédemment, la croissance tumorale est caractérisée par une grosse variabilité intra et inter-individuelle. Un objectif qui paraît raisonnable est d'estimer les volumes de la tumeur ainsi que les distributions spatiales des espèces proliférantes avec des erreurs de 10% sur une échelle de temps raisonnable, c'est-à-dire, correspondant à l'intervalle de temps entre deux examens cliniques successifs. Ce but a été atteint par les deux techniques présentés. Au niveau de volume les erreurs sont acceptables ; au niveau de forme les erreurs sont plus marquées et, cela, reste un point faible de la technique, parce que l'avantage des modèles spatiaux est de fournir potentiellement les informations sur la distribution spatiale du tissu tumoral. Il y a deux facteurs principaux qui déterminent ce résultats : le premier est l'ensemble de contrôle et le deuxième est le modèle. Les tests montrent que l'ensemble de contrôle a une influence sur le résultat, mais elle est limitée par rapport à celle du modèle. Le modèle utilisé permet de reproduire des comportements très variés. Ce qui n'est pas bien représenté est la complexité géométrique du tissu autour de la tumeur. En particulier, le tissu dans les poumons n'est pas isotrope, mais au moins localement orthotrope, suite à la présence de structures telles que les bronches ou d'autres inclusions aléatoires. Tous ces éléments géométriques ne sont pas déterminés a priori et ne peuvent pas être identifiés car le problème inverse serait sous déterminé. L'objectif serait, plutôt, d'arriver à les mesurer par des techniques d'imagerie fonctionnelle (DT-MRI, par exemple).

La façon de choisir les paramètres doit être discutée. En général dans les modèles phénoménologiques plusieurs paramètres apparaissent, qui décrivent les proportionnalités entre les différents champs qui caractérisent la croissance. Pour limiter l'effet des échelles spatiales et temporel et pour trouver des paramètres qui déterminent la croissance de façon intrinsèque, une version non-dimensionnelle est souhaitée. La technique de sensibilité permet de comprendre quels sont les paramètres qui influencent le plus l'évolution de la tumeur et ceux qui, en revanche, jouent un rôle mineur. Une analyse de la fonction-

nelle dans un voisinage de la solution permettrait de comprendre s'il y a des directions invariants dans l'erreur. Une façon efficace de choisir les paramètres fait en sorte que des vitesses non-dimensionnelles apparaissent (par exemple le rythme de division cellulaire, qui multiplie γ dans le modèle de Darcy), conformément au fait qu'on a des données d'une progression de la croissance. La rétroaction entre les concentrations des nutriments et la dynamique des populations est souvent modélisée par un effet de seuil. Le paramètre de seuil a une signification biologique claire, mais pourrait conduire à problèmes inverses mal conditionnés. La nature des équations influence les problèmes inverses : la longueur de diffusion des espèces chimiques dans le tissu n'étant pas significative, des modèles hyperboliques pourrait être envisagés. Les équations elliptiques nécessitent des conditions au bords, et souvent le bord que l'on peut choisir est la frontière de l'organe. Ce choix nous oblige à simuler tout l'organe, même si seulement une petite portion est attaquée par la tumeur.

L'approche de sensibilité est directe et facile à mettre en place. On peut utiliser différents modèles et plusieurs combinaisons d'observables. Ses défauts principaux sont le coût computationnel et la présence de minima locaux (liée à la formulation de minimisation). Les solutions obtenus par cette technique nous donnent beaucoup d'information. Si la valeur de la fonctionnelle est petite et la norme de la sensibilité est petite le fitting des données sera satisfaisant et stable pour des petites perturbations de l'ensemble de contrôle. Si la sensibilité n'est pas pratique dans tous les cas (par exemple pour les cas 3D), elle est un instrument puissant pour étudier les propriétés des solutions et les comparer avec celles que l'on peut obtenir par des approches réduites.

L'approche réduite proposée dans cette thèse est basée sur la POD. L'avantage principal est son faible coût computationnel. Le coût est entièrement concentré dans l'étape offline, mais cette étape peut être parallélisée de façon massive. L'introduction d'une base POD ne permet pas seulement de réduire le nombre d'inconnues mais aussi d'améliorer le conditionnement du problème. Contrairement à ce qui est fait couramment le système d'équations n'est pas projeté sur la base. La projection demande souvent une étape de calibration pour améliorer la représentation. On choisit plutôt d'écrire le résidu des équations aux instants de temps qui correspondent aux images. L'avantage est de transformer le problème inverse en un problème algébrique et de pouvoir le résoudre rapidement. Une perspective concerne la possibilité de mettre en place une approche hybride qui arrive à combiner les avantages des deux. Les résultats des problèmes inverses sont influencés par l'estimation des dérivés de l'observable. En particulier, cette approximation est produite par un estimateur qui prend la séquence d'observables et calcule les dérivés temporelles

aux temps correspondants. Dans les cas où les données sont très éloignées (i.e. quand le rapport entre les volumes de deux images est plus grand que 2.5 environ) l'estimation est mauvaise et elle a un effet de pollution sur les résultats. Le problème inverse identifie une configuration intermédiaire entre le modèle que l'on souhaite calibrer et l'estimateur qu'on utilise, c'est-à-dire, on identifie les paramètres du modèle (par exemple le modèle de Darcy) tels qu'il ait le comportement de l'estimateur. Cet effet est lié à la rareté d'informations.

Les résultats présentés dans la section Slow Growth sont en quelque sorte les meilleurs résultats qu'on peut espérer obtenir par une approche réduite. Dans ce cas, la base de données a été bien ciblée sur la croissance et la régularisation du problème inverse est très puissante. La solution du modèle calibré arrive à reproduire la croissance sur une échelle temporelle de deux ans environ, même si les approximations introduites sont très importantes. Dans les cas où le contrôle ne satisfait pas automatiquement certaines propriétés requises, celles-ci sont imposées par pénalisation. Cette technique est très simple à mettre en place mais introduit des paramètres qui doivent être fixés, ce qui rend la procédure un peu plus lente.

Le défaut principal des méthodes basées sur la minimisation est la présence de minima locaux. Ce phénomène devient dangereux lorsque plusieurs solutions arrivent à reproduire l'ensemble des données avec des résidus comparables. Dans ce cas le risque est de sous-estimer la croissance et des nouveaux examens cliniques seraient nécessaires afin de mieux comprendre la nature de la maladie.

Transport Optimal Au cours de cette thèse le transport optimal a été étudié afin de mettre en place une procédure de recalage non-rigide. Au-delà de cette motivation, des généralisations et d'autres applications ont été analysées et proposées.

On a étudié les aspects numériques du transport optimal. La difficulté est entièrement liée au fait que le problème est défini par des conditions au bord en temps. Une classe de méthodes qui utilisent la structure lagrangienne du problème a été proposée et validée par des cas test variés. Un soin particulier a été porté à la robustesse, afin d'arriver à reproduire les champs de déplacement dans des configurations critiques du point de vue de la mécanique des milieux continus, telles que la fragmentation ou la coalescence de la masse.

La perspective principale liée à la technique est l'approche multi-niveau qui permet d'accélérer de façon remarquable la vitesse de convergence. Cette approche permet aussi d'utiliser des noyaux à support compacte, caractérisés par un faible coût d'évaluation et

de quadrature. Une autre perspective est liée à l'utilisation des maillages non-structurés, qui permettraient de concentrer les points de quadrature où le résidu est plus élevé.

L'outil de recalage non-rigide fourni des champs de déplacement réguliers dans la plus part des cas. Néanmoins il y a des systèmes physiques ou biologiques pour lesquels les simplifications introduites par le transport optimal ne sont pas acceptables. La croissance tumorale en fait partie, car en général la tumeur grossit et la masse n'est pas conservée. Une normalisation de l'échelle de gris a été souvent proposée dans la littérature, mais elle est artificielle. Une perspective concernant l'utilisation du transport optimal pour analyser des systèmes dans lesquels la masse n'est pas conservée est proposée dans [29].

Le travail sur le transport optimal se conclut par une perspective concernant l'utilisation de la distance de Wasserstein en réduction de modèle. L'objectif principal de cette partie est de comprendre si on peut donner une représentation réduite efficace des systèmes physiques où les phénomènes de transport dominant. Le choix qui a été fait pour ce travail préliminaire est d'utiliser la distance de Wasserstein en cherchant quand même de se remettre dans un cadre d'analyse en composantes principales, grâce à une opération de scaling multidimensionnel. Les résultats obtenus sur des cas test artificiels sont prometteurs.

Le problème théorique principal que l'on doit prendre en considération concerne le fait qu'une base de données de densités ayant toutes la même masse doit être construite. Dans les système EDP il y a parfois des quantités qui sont conservés, mais il est important d'arriver à analyser des solutions quelconques. La perspective proposée dans [29] semble être une possibilité concrète de résoudre ce problème.

Chapter 9

Conclusions and Perspectives

In this chapter the conclusions of the present work, some perspective and open questions are presented. First, a discussion on inverse problems is outlined, followed by some comments on optimal transport.

Inverse problems For what concerns inverse problems, two techniques were presented, both providing encouraging results, in the sense that they suggest that attacking realistic applications is not out of reach. Let us analyze in detail the main contributions and the problems encountered.

The advantage of the using of space models with respect to ODEs is twofold: the space character of the phenomenon is taken into account, which allows us to provide, for the considered cases, useful informations to clinicians (like for instance the identification of the active part of the tumor); second, the systems based on PDEs usually requires less data to capture the dynamics, since more elements are described concerning the evolution (usually, two, three data are sufficient to get a relatively reliable prediction). The main disadvantage of PDEs based approaches is their computational cost. The setting up of reduced order model may tackle this problem and it is important to make PDEs based tools competitive for realistic applications.

The balancing between the complexity of the model and the available data is the key element for the setting up of tools based on phenomenological models. Complex models have the advantage of rendering more complex dynamics, which translates in a better prediction power, but they are more difficult to calibrate. In particular, if the data amount is scarce (which is often the case), they make the related inverse problems under-determined. A trade off might be chosen. In the present work the considered data were scans, which have a good resolution and contrast properties but they only show two phenotypes: tumor and healthy tissue, without any other kind of information. Only simple models may be calibrated starting from these data.

Another key point is represented by the relationship between modeled and observed quantities. A very simple definition of observable were adopted (after a discussion with medical doctors), which is reasonable, but does not guarantee that better (and more sophisticated) choices might be made. A promising direction of research is represented by functional imagery, which make more informations available concerning the tissue nature. The models that might be used with such an amount of data would be more complex and this could improve substantially the predictions. The link between quantities shown by functional imagery and the modeled ones would need to be investigated more carefully.

The obtained results have to be judged considering two elements: the errors in the

data and the variability of the phenomenon. Scans have a resolution of 1.25mm, which is comparable with the typical size of avascular tumors. The tumors analyzed in this work have, in the first image of the sequence, a size that does not exceed 5 – 6mm. Errors (segmentation, noise, etc.) might affect the precision of the results in a very significant manner. A standard procedure for measuring quantities, segment images and registrate them is mandatory. It is fundamental to improve the results, since it allows to set up an objective basis to quantitatively and systematically compare the results. Moreover, it makes comparison between several clinical case possible even if exams were performed on different machines and in different conditions.

Mutations and random phenomena that influences tumor behavior in a catastrophic way can not be predicted. As said, tumor has an enormous inter and intra individual variability. A reasonable goal is to estimate with an error less that 10% the volume and the main features of the tumor on a time scale comparable with that of the clinical exams. This has been reached, for the cases considered, by both the techniques presented in this work. In general, they manage to capture the dynamics of the growth even when two or three data are used. The volume is well represented while the shape is reconstructed with a larger error. This is still a weak point, since the advantage of space models is in their ability to represent space features of the growth. There are two main causes of this error: the control set and the model. The control set may influence, as proved, the result of the identification, but it does not influence the predictions as much as the model does. The model adopted allows to recover a wide range of dynamical behaviors. Globally, all the considered growths could be reasonably represented. The lack is in the geometric representation of the tissues. In particular, for lungs, the tissue is not, locally, uniform and isotropic. Bronchia induces, at least, an orthotrope structure. Random inclusions and fibered structures affects the evolution and can not be *a priori* determined or identified (the problem would be under-determined). The goal is, instead, to measure them, using for example DT-MRI.

Parametrization of the models has to be discussed. In general phenomenological models have different constants and parameters that appears and play an important role in the dynamics. In order to bypass the effect of the space and time scales, a non-dimensional version of the models would have to be written. This would help finding parameters which intrinsically determines the growth, allowing a more straightforward comparison between different cases. Furthermore, sensitivity helps finding which parameters influences more the solutions and which not. In particular, it highlights the most important directions of descent for the error functional. A more significant parametrization would be such that

non-dimensional velocity appears, like the rate of division (*i.e.* a constant that multiplies γ in the two species Darcy model), and so on. This is conformal to the use of a sequence of data showing a progression of the growth. The feedback between the nutrients and the population dynamics is often rendered by a threshold. Using the threshold value as a parameter may be dangerous (it may induce a bad conditioned behavior), but, on the other hand, is meaningful. The equations nature affects also the inverse problems precision. As seen, the diffusion length of chemical species in the tissue is not so relevant, so that a model based on hyperbolic equations might be proposed. Elliptic equations require boundary conditions to be impose on the organ boundary (it is the more natural boundary to be chosen); this oblige us to consider the entire organ for the simulations even if only a small part of it is involved in tumor dynamics, resulting in an extra cost from a numerical standpoint.

The sensitivity approach is straightforward and it may be easily set up based on different models and observables sets. Its main drawbacks are the computational costs and the presence of local minima (due to the functional minimization approach). However, the results provide a lot of informations concerning the obtained numerical solution. If the value of the functional is low and the norm of the sensitivity is low, the result is the resulting fitting will be good, even if perturbations in the parameters are added. As a matter of fact the definition of sensitivity (and its physical meaning) guarantees us that if it is small in norm the difference between a solution and the solution obtained when small perturbations are added in the control set is small. If it is not practical for all the cases (3D) due to its cost, it is a powerful tool to investigate the properties of the solutions and to compare them with those obtained by reduced order techniques.

The reduced order model proposed in this work is based on POD. The main advantage is the low computational cost carachterizing the online stage. The offline stage may be easily parallelized. The effect of POD does not only affect the cost by reducing the number of unknowns, but improve substantially the conditioning of the problem, regularizing it. One of the main causes of illness of inverse problems is the effect of higher frequencies. A regularization eliminate or control their effect, accelerating the convergence. Contrary on what is currently done, the system of equations is not projected onto the basis. The projection on the basis need often a calibration procedure to be set up, since the representation of the dynamics results poor. Instead, a residual minimization is sought. The main advantage is due to the fact that the algebraic problem is solved rapidly, the main disadvantage consists in the fact that it is more difficult to formulate the residual problem and to deal with it when more than two images are taken into account or different set of

models or kinds of observables are considered. A promising perspective in this sense is the setting up of an hybrid approach potentially combining the advantages of a sensitivity approach with those of the reduced order methods.

The results of the reduced approach are mainly influenced by the approximation of the derivative of the observable. It is made by an estimator taking the sequence of the images in input. When few images are available and the tumor has grown fast, that is when tumor volume ratio between two subsequent images exceeds 2.5, a bad estimation has an effect of pollution of the results. The inverse problem identify an intermediate configuration between the Darcy model and the estimator, that is, it identify the parameters of the Darcy model such that it behaves like a logistic one, for example (if logistic estimator is adopted). This is the effect of the scarcity of the informations.

The results presented in the section Slow Growth, concerning FER-I data set are in some sort the best result that may be obtained by means of the reduced approach proposed. In that case the database represented very well the dynamics of the growth, resulting in a powerful regularization. The identified dynamics fitted the real data providing a reasonable prognosis on a time scale of two years, inspect of the simplifications introduced.

In the proposed residual based approach penalizations should be added to the functional according to the control set in order to impose some constraints. This introduces free parameters to be set, which might decrease the rapidity of obtaining the results and makes the procedure less friendly.

The main problem affecting inverse problems is the presence of local minima. This becomes dangerous when divergent predictions fits the data set with comparable residuals. If more solutions fit well the data, the risk being to under-estimate the growth, novel exams should be done, in order to discriminate between the solution and to understand whether the growth is aggressive or not.

Optimal Transport In the present work optimal transport were investigated to set up a non-rigid registration tool and possible estimators of quantities appearing in tumor models. In spite of these first motivations, possible generalizations and applications to other contexts were analyzed and proposed.

The numerics of the optimal transport was studied. The difficulty lies entirely in the fact that transport is formulated as a boundary value problem, instead of a common initial value problem. A family of methods exploiting the remarkable lagrangian formulation of optimal transport were proposed, whose cost scales like the other methods proposed

in the literature. The technique was validated by several examples and demonstrated robust, allowing to represent collapsing and fragmentation phenomena (which requires a weak formulation) or to recover non-trivial three dimensional configurations. The main perspective concerning the numerics is the study of the multilevel technique, that proved to significantly speed up the convergence. In particular the aim is to use a multilevel approach with a compact kernel representation, which is featured by a low cost of evaluation and quadrature. Another direction of research consists in using non-structured meshes, adapted on the residual in order to diminish it more rapidly where it is higher. This, combined with a multilevel approach, might improve substantially the quality and the rapidity of the computation, opening the possibility to use optimal transport in several realistic applications.

When used as non-rigid registration tool it furnishes reasonable registration displacement fields in most of the situations. However, there are cases, like for example tumor growth, in which mass is not preserved, so that merely rescaling grey scale in sort that mass is conserved between the configuration is artificial and not realistic. This is what is currently done in the literature and it has been tested in this work. Mass sources can be taken into account by following the work of Benamou ([29]) or by considering suitable changes of variables.

The use of Wasserstein distance to set up model reduction strategy was investigated. The objective is to provide a representation of the advection of concentrated structures (which is not well represented by conventional PCA strategies) exploiting the properties of Wasserstein distance. A multidimensional scale embedding was used to introduce a principal component analysis framework based on Wasserstein distance. The proposed technique was applied to different numerical testcases, leading to promising results. Other tests are mandatory and they will be carried out in future. The main open question concerns the balancing of the data. Indeed, optimal transport needs, in order to be set up, that the density distributions are of equal mass. When considering PDEs, only a relatively small set of problems is fully determined by conserved quantities. In general the functions obtained by sampling the solutions are not balanced. One possibility, to be further investigated, might consist in adapting what detailed in [29] to the technique proposed in the current work.

Bibliography

- [1] L.M. Abia, O. Angulo, and J. Lopez Marcos. Age-structured population models and their numerical solution. *Ecol. Modelling*, 188:112–136, 2005.
- [2] J.A. Adam. A simplified mathematical model of tumor growth. *Math. Biosci.*, 81:229–244, 1986.
- [3] J.A. Adam. A mathematical model of tumor growth: Iii. comparison with experiments. *Math. Biosci.*, 86:213–227, 1987.
- [4] T. Alarcón, H. Byrne, and P.K. Maini. A cellular automaton model for tumor growth in inhomogeneous environment. *J.Theor. Bio*, 225:257–274, 2003.
- [5] B. Alberts, A. Johnson, J. Lewis, and M. Raff. *Molecular Biology of the Cell*. Garland Science, Taylor and Francis, 5th edition edition, 2008.
- [6] D. Ambrosi, F. Bussolino, and L. Preziosi. A review of vasculogenesis models. *Comput. Math. Methods Med.*, 6:1–19, 2005.
- [7] D. Ambrosi, A. Duperray, V. Peschetola, and C. Verdier. Traction pattern of tumor cells. *J. Math. Biol*, 58:163–181, 2009.
- [8] D Ambrosi and L. Preziosi. On the closure of mass balance models for tumor growth. *Math. Models Methods Appl. Sci.*, 12:734–754, 2002.
- [9] D. Ambrosi and L. Preziosi. Cell adhesion mechanisms and elasto-viscoplastic mechanics of tumors. *Mech. Model. Mechanobiol.*, 8:397–413, 2009.
- [10] L. Ambrosio. Lecture notes on optimal transport problem. Technical report, Scuola Normale Superiore, Pisa, 2000.
- [11] L. Ambrosio. Evolution problems in spaces of probability measures. *Physica D*, 239:1446–1452, 2010.

- [12] A.R.A. Anderson. A hybrid mathematical model of solid tumor invasion: the importance of cell adhesion. *Math. Med. Biol.*, 22:163–166, 2005.
- [13] A.R.A. Anderson and M. Chaplain. Continuous and discrete mathematical models of tumor-induced angiogenesis. *Bull. Math. Biol.*, 60:857–900, 1998.
- [14] A.R.A. Anderson, M. Chaplain, K. Rejniak, and J. Fozard. Single-cell based models in biology and medicine. *Math. Med. Biol.*, 25:185–186, 2008.
- [15] M. Andreeff, D.W. Goodrich, and H.P. Koeffler. Cell proliferation and differentiation. In *Cancer Medicine*. Holland-Frey, 7th edition edition, 2006.
- [16] S. Angenent, S. Haker, and A. Tennenbaum. Minimizing flows for the monge-kantorovich problem. *SIAM J. Math. Anal.*, 35:61–97, 2003.
- [17] R.P. Araujo and D.L.S. McElwain. A history of the study of solid tumor growth: the contribution of mathematical modelling. *Bull. Math. Biol.*, 66:1039–1091, 2004.
- [18] R.P. Araujo and D.L.S. McElwain. A mixture theory for the genesis of residual stresses in growing tissues: I. a general formulation. *SIAM J. Appl. Math.*, 65:1261–1284, 2005.
- [19] V.I. Arnold and B. Khesin. *Topological methods in hydrodynamics*. Springer, 1998.
- [20] S. Astanin and A. Tosin. Mathematical model of tumor cord growth along the source of nutrient. *Math. Model. Nat. Phenom.*, 2:153–157, 2007.
- [21] R.C. Aster, B. Borchers, and C.H. Thurber. *Parameter estimation and inverse problems*. Elsevier, 1st edition, 2005.
- [22] N.C. Atuegwu, J.C. Gore, and T.E. Yankeelov. The integration of quantitative multi-modality imaging data into mathematical models of tumors. *Phys. Med. Biol.*, 55:2429–2449, 2010.
- [23] D. Balding and D.L.S. McElwain. A mathematical model of tumor-induced capillary growth. *J. Theor. Biol.*, 114:53–73, 1985.
- [24] D. Barbolosi, A. Benabdallah, F. Hubert, and F. Verga. Mathematical and numerical analysis for a model of growing metastatic tumors. *Math. Biosci.*, 218:1–14, 2009.

- [25] D. Barbolosi, F. Verga, A. Benabdallah, F. Hubert, C. Mercier, J. Ciccolini, and C. Faivre. Modélisation du risque d'évolution métastatique chez les patients supposés avoir une maladie localisée. *Oncologie*, 2011.
- [26] G. Bayada, L. Chupin, and S. Martin. Visco elastic fluid in a film domain. *Quarterly of applied mathematics*, 65:625–651, 2007.
- [27] E.L. Bearer, J.S. Lowengrub, Y.L. Chuang, H.B. Friboes, F. Jin, F.M. Wise, M. Ferrari, D.B. Agus, and V. Cristini. Multiparameter computational modeling of tumor invasion. *Cancer Res.*, 69:4493–4501, 2009.
- [28] N. Bellomo, A. Belloquid, and E. de Angelis. The modelling of immune competition by generalised kinetic (Boltzmann) models: review and research perspective. *Math. Comput. Modeling*, 37:65–86, 2003.
- [29] J.-D. Benamou. Numerical resolution of an unbalanced mass transport problem. *Math. Model. Num. Analysis*, 37:851–868, 2003.
- [30] J.-D. Benamou and Y. Brenier. A computational fluid mechanics solution to the Monge–Kantorovich mass transfer problem. *Numerische Mathematik*, 84:375–393, 2000.
- [31] J.-D. Benamou, Y. Brenier, and K. Guittet. The Monge–Kantorovitch mass transfer and its computational fluid mechanics formulation. *International Journal for Numerical methods in fluids*, 40:21–30, 2002.
- [32] M. Bergmann, C.H. Bruneau, and A. Iollo. Enablers for robust pod models. *Journal of Computational Physics*, 228:516–538, 2009.
- [33] F. Billy, B. Ribba, O. Saut, H. Morre-Trouilhet, T. Colin, D. Bresch, J.P. Boissel, E. Grenier, and J.P. Flandrois. A pharmacologically based multiscale mathematical model of angiogenesis and its use in investigating the efficacy of a new cancer treatment strategy. *J. Theor. Biol.*, 260:545–562, 2009.
- [34] K.A. Bold, Y. Zou, I.G. Kevrekidis, and M.A. Henson. An equation-free approach to analyzing heterogeneous cell population dynamics. *J. Math. Biol.*, 55:331–352, 2007.
- [35] Y. Brenier. Polar factorization and monotone rearrangement of vector-valued functions. *Communication in Pure and Applied Mathematics*, 64:375–417, 1991.

- [36] Y. Brenier. Optimal transportation of flows and nonlinear electromagnetism. In *ESAIM Proceedings*, 2007.
- [37] Y. Brenier. Optimal transport, convection, magnetic relaxation and generalized Boussinesq equations. *Journal of NonLinear Science*, 19:547–570, 2009.
- [38] G. F. Brunton and T. E. Wheldon. The gompertz equation and the construction of tumor growth curves. *Cell. Tissue. Kinet.*, 13:455–460, 1980.
- [39] H. M. Byrne. The effect of time delays on the dynamics of avascular tumor growth. *Math. Biosci.*, 144:83–117, 1997.
- [40] H. M. Byrne, T. Alarcón, M.R. Owen, S.W. Webb, and P.K. Maini. Modeling aspects of cancer dynamics: A review. *Phi. Trans. R. Soc.*, 364:1563–1578, 2006.
- [41] H. M. Byrne and M.A.J. Chaplain. Mathematical models for tumor angiogenesis: Numerical simulations and nonlinear wave solutions. *Bull. Math. Biol.*, 57:461–486, 1995.
- [42] H. M. Byrne and D. Drasdo. Individual-based and continuum models of growing cells populations: a comparison. *J. Math. Biol.*, 58:657–687, 2009.
- [43] H. M. Byrne and L. Preziosi. Modelling solid tumor growth using the theory of mixtures. *Math. Med. Biol.*, 20:341–366, 2003.
- [44] M.A.J. Chaplain. Avascular growth, angiogenesis and vascular growth in solid tumors: the mathematical modelling of the stages of the tumor development. *Math. Comput. Model.*, 23:47–87, 1996.
- [45] M.A.J. Chaplain, D.L. Benson, and P.K. Maini. Nonlinear diffusion of growth inhibitory factor in multicell spheroids. *Math. Biosci.*, 121:1–13, 1994.
- [46] M.A.J. Chaplain and G. Lolas. Mathematical modeling of cancer invasion of tissue: dynamic heterogeneity. *Networks Heterogen. Media*, 1:399–439, 2006.
- [47] M.A.J. Chaplain, S.R. McDougall, and A.R.A. Anderson. Mathematical modeling of tumor-induced angiogenesis. *Ann. Rev. Biomed. Eng.*, 8:233–257, 2006.
- [48] A. Chauviere, T. Hillen, and L. Preziosi. Modeling cell movement in anisotropic and heterogeneous tissues. *Networks Heterogen. media*, 2:333–357, 2007.

- [49] A. Chauviere, L. Preziosi, and T. Hillen. Modeling the motion of a cell population in the extracellular matrix. *Discrete Contin. Dyn. Syst.*, B (Suppl.):250–259, 2007.
- [50] G. Crasta and A. Malusa. A variational approach to the macroscopic electrodynamics of anisotropic hard superconductors. *Archive for Rational Mechanics and Analysis*, 192:87–115, 2009.
- [51] V. Cristini, X. Li, J.S. Lowengrub, and S.M. Wise. Nonlinear simulations of solid tumor growth using a mixture model: invasion and branching. *J. Math. Biol.*, 58:723–763, 2009.
- [52] M. Cullen and W. Gangbo. A variational approach for the 2-Dimensional semi-geostrophic shallow water equations. *Archive for Rational Mechanics and Analysis*, 156:241–273, 2001.
- [53] M. Cullen and R.J. Purser. A duality principle in Semi-geostrophic theory. *Journal of Atmospheric Sciences*, 44:3449–3468, 1987.
- [54] E. de Angelis and L. Preziosi. Advection-diffusion models for solid tumors evolution *in vivo* and related free boundary value problem. *Math. Models Meth. Appl. Sci.*, 10:379–407, 2000.
- [55] T.S. Deisboeck, M.E. Berens, A.R. Kansal, S. Torquato, A.O. Stemmer-Rachamimov, and E.A. Chiocca. Pattern of self-organization in tumor systems: complex growth dynamics in a novel brain tumor spherical model. *Cell Proliferation*, 34:115–134, 2001.
- [56] A. Deutsch and S. Dormann. *Cellular Automaton Modeling of Biological Pattern Formation*. Birkäuser, 2005.
- [57] A. d’Onofrio. A general framework for modeling tumor-immune system competition and immunotherapy: Mathematical analysis and biomedical inferences. *Physica D*, 208:220–235, 2005.
- [58] M. Doumic, B. Perthame, and J.P. Zubelli. Numerical solution of an inverse problem in size-structured population. *Inverse problems*, 25:045008, 2009.
- [59] D. Drasdo. Coarse graining in simulated cell populations. *Adv. Complex Systems*, 8:319–363, 2005.

- [60] D. Drasdo and S. Hoehme. Individual-based approaches to birth and death in avascular tumors. *Math. Comput. Modeling*, 37:1163–1175, 2003.
- [61] D. Drasdo and S. Hoehme. A single scale based model of tumor growth in vitro: monolayers and spheroids. *Phys. Biol.*, 2:133–147, 2005.
- [62] D. Drasdo and S. Hoehme. On the role of physics in the growth and pattern of multicellular systems: What we learn from individual cell-based models? *J. Stat. Phys.*, 128:287–345, 2007.
- [63] D. Drasdo, R. Kree, and J.S. McKaskill. Monte-carlo approach to tissue cell populations. *Phys. Rev. E*, 52:6635–6657, 1995.
- [64] J. Dyson, E. Sanchez, R. Villela-Bressan, and G. Webb. An age and spatially structured model of tumor invasion and haptotaxis. *Discrete Contin. Dyn. Syst.*, B 8:45–60, 2007.
- [65] C.M. Elliot and S. Luckaus. A generalized diffusion equation for phase separation of a multi-component mixture with interface free energy. *Inst. Math. Appl.*, 887, 1991.
- [66] S. Enault. *Modélisation de la propagation d’une tumeur en milieu faiblement compressible*. PhD thesis, ENS Lyon, 2010.
- [67] M. Engelhart, D. Lebedez, and S. Sager. Optimal control for selected cancer chemotherapy ode models: A view on the potential of optimal schedules and choice of objective function. *Math. Biosci.*, 229:123–134, 2011.
- [68] L.C. Evans. Partial differential equations and Monge–Kantorovich mass transfer. Technical report, University of California, Berkeley, 1997.
- [69] L.C. Evans and M. Feldman. Fast/slow diffusion and collapsing sandpiles. *Journal of Differential Equations*, 137:166–209, 1997.
- [70] A. Figalli. Existence, uniqueness and regularity of optimal transport maps. *SIAM J. Math. Anal.*, 39 (1):126–137, 2007.
- [71] J. Folkman, J. Heymach, and R. Kalluri. Tumor angiogenesis. In *Cancer Medicine*. Holland-Frey, 7th edition edition, 2006.

- [72] A. Friedman. A hierarchy of cancer models and their mathematical challenges. *Discrete Cont. Dyn. Syst.*, B 4:147–159, 2004.
- [73] A. Friedman and F. Reitich. On the existence of spatially patterned dormant malignancies in a model for the growth of non-necrotic vascular tumors. *Math. Models Methods Appl. Sci.*, 11:601–625, 2001.
- [74] A. Friedman and F. Reitich. Analysis of a mathematical model for the growth of tumors. *J. Math. Biol.*, 4:262–284, 2009.
- [75] J. Galle, G. Aust, G. Shaller, T. Beyer, and D. Drasdo. Individual cell-based models of the spatial temporal organization of multicellular systems-achievements and limitations. *Cytometry*, 69 A:704–710, 2006.
- [76] W. Gangbo. An elementary proof of the polar factorization of vector-valued function. *Archive for Rational Mechanics and Analysis*, 128:381–399, 1994.
- [77] W. Gangbo and V. Oliker. Existence of optimal maps in the reflector-type problems. *ESAIM COCV*, 13:93–106, 2007.
- [78] M. Garbey and G. Zouridakis. Modeling tumor growth: from differential deformable models to growth prediction of tumors detected in pet images. *Eng. Med. Biol.*, 3:2687–2690, 2003.
- [79] R.A. Gatenby and E.T. Gawlinski. A reaction-diffusion model of cancer invasion. *Cancer Res.*, 56:5745–5753, 1996.
- [80] R.A. Gatenby, E.T. Gawlinski, A.F. Gmitro, B. Kaylor, and R.J. Gillies. Acid-mediated tumor invasion: a multidisciplinary study. *Cancer Res.*, 66:5216–5223, 2006.
- [81] P. Gerlee and A.R.A. Anderson. An evolutionary hybrid cellular automaton model of solid tumor growth. *J. Theor. Biol.*, 246:583–603, 2007.
- [82] F. Gibou, R.P. Fedkiw, L.T. Cheng, and M. Kang. A second-order-accurate symmetric discretization of the poisson equation on irregular domains. *J. Comput. Physics*, 176:205–227, 2002.
- [83] B. Gompertz. On the nature of the function expressive of the law of human mortality, and on a new mode of determining the value of life contingencies. *Phil. Trans. of R.S.*, 115:513–585, 1825.

- [84] H.P. Greenspan. Models for the growth of solid tumor by diffusion. *Stud. Appl. Math.*, 51:317–340, 1972.
- [85] E. Haber, T. Rehman, and A. Tannenbaum. An efficient numerical method for the solution of the L^2 optimal transfer problem. *SIAM Journal on Scientific Computing*, 32:197–211, 2010.
- [86] P. Hahnfeldt, D. Panigraphy, J. Folkman, and L.R. Hlatky. Tumor development under angiogenic signaling: A dynamical theory of tumor growth, treatment response, and postvascular dormancy. *Cancer Res.*, 59:4770–4775, 2001.
- [87] M. Hanke. A regularizing levenberg-marquardt scheme, with applications to inverse groundwater filtration problems. *Inverse Problems*, 13:79–95, 1997.
- [88] H. Hatzikirou, L. Brush, and A. Deutsch. From cellular automaton rules to an effective macroscopic mean field description. *Acta Phys. Polonica B.*, 3(2):399–416, 2010.
- [89] C. Hogue, C. Davatsikos, and G. Biros. An image-driven parameter estimation problem for a reaction-diffusion glioma growth model with mass effect. *J. Math. Biol.*, 56:793–825, 2008.
- [90] P. Holmes, J.L. Lumley, and G. Berkooz. *Turbulence, coherent structures, dynamical systems and symmetry*. Cambridge University Press, 1st edition, 1996.
- [91] J.D. Humphrey and K.R. Rajagopal. A constrained mixture model for growth and remodeling of soft tissues. *Math. Mod. Methods Appl. Sci.*, 12:407–430, 2002.
- [92] V. Isakov. *Inverse problems for partial differential equations*. Applied Mathematical Sciences. Springer, 1st edition, 2010.
- [93] G.S. Jiang and C-W. Shu. Efficient implementation of wheighted eno schemes. *J. Comput. Phys.*, 126:202–228, 1996.
- [94] A.F. Jones and B.D. Sleeman. Angiogenesis-understanding the mathematical challenge. *Angiogenesis*, 9:127–138, 2006.
- [95] J. Kaipio and E. Somersalo. Statistical inverse problems: Discretization, model reduction and inverse crimes. *Journal of Computational and Applied Mathematics*, 198:493–504, 2007.

- [96] A.A. Kansal, S. Torquato, G.R. Harsh, E.A. Chiocca, and T.S. Deisboeck. Cellular automaton of idealized brain tumor growth dynamics. *BioSystem*, 55:119–127, 2000.
- [97] L.V. Kantorovich. On the transfer of masses. *Doklady Akademii Nauk SSSR*, 37:227–229, 1942.
- [98] E. Khain and L.M. Sandler. Generalized Cahn-Hilliard equation for biological applications. *Phys. Rev. E.*, 77:051129, 2008.
- [99] E.C. Khon. Invasion and metastasis. In *Cancer Medicine*. Holland-Frey, 7th edition edition, 2006.
- [100] J.S. Kim, M.A. Stolarska, and H.G. Othmer. A hybrid model for tumor spheroid in vitro: Theoretical development and early results. *Math. Methods Appl. Sci.*, 17:1773–1798, 2007.
- [101] E. Konukoglu. *Modeling glioma growth and personalizing growth models in medical images*. PhD thesis, STIC, University of Nice - Sophia Antipolis, 2009.
- [102] E. Konukoglu, O. Clatz, B.H. Menze, M.A. Weber, B. Stieltjes, E. Mandonnet, H. Delingette, and N. Ayache. Image guided personalization of reaction-diffusion type tumor growth model using modified anisotropic eikonal equations. *IEEE TMI*, 29(1):77–95, 2010.
- [103] H. Levine, S. Pamuk, B.D. Sleeman, and M. Nielsen-Hamilton. Mathematical modeling of capillary formation and development in tumor angiogenesis: penetration into the stroma. *Bull. Math. Biol.*, 63:801–863, 2001.
- [104] J.S. Lowengrub, H.B. Friboes, F. Jin, Y.L. Chuang, X. Li, P. Macklin, S.M. Wise, and V. Cristini. Nonlinear modelling of cancer: bridging the gap between cells and tumours. *Nonlinearity*, 23:1–91, 2010.
- [105] B.D. MacArthur and C.P. Please. Residual stress generation and necrosis formation in multi-cell tumor spheroids. *J. Math. Biol.*, 49:537–552, 2004.
- [106] P. Macklin and J.S. Lowengrub. Evolving interfaces via gradient of geometry-dependent interior poisson problem: Application to tumor growth. *J. Comput. Phys.*, 203:191–220, 2005.

- [107] P. Macklin and J.S. Lowengrub. An improved geometry-aware curvature discretization for level set methods: Application to tumor growth. *J. Comput. Phys.*, 215:392–401, 2006.
- [108] P. Macklin, S. McDougall, A.R.A. Anderson, M.A.J. Chaplain, V. Cristini, and J.S. Lowengrub. Multiscale modeling and nonlinear simulation of vascular tumor growth. *J. Math. Biol.*, 58:765–798, 2009.
- [109] P. Magni, M. Simeoni, I. Poggesi, M. Rocchetti, and G. de Nicolao. A mathematical model to study the effects of drugs administration of tumor growth dynamics. *Math. Biosci.*, 200:127–151, 2006.
- [110] D.G. Mallet and L.G. de Pillis. A cellular automata model of tumor-immune system interactions. *J. Theor. Biol.*, 239:334–350, 2006.
- [111] Y. Mansuri, M. Kimura, J. Lobo, and T.S. Deisboeck. Emerging patterns in tumor systems: simulating the dynamics of multicellular clusters with an agent-based spatial agglomeration model. *J. Theor. Biol.*, 219:343–370, 2002.
- [112] Y. M. Marzouk and H. N. Najm. Dimensionality reduction and polynomial chaos acceleration of bayesian inference in inverse problems. *Journal of Computational Physics*, 228:1862–1902, 2009.
- [113] B. Maury and J. Venel. A mathematical framework for a crowd motion model. *Comptes Rendu Mathematiques*, 346:1245–1250, 2008.
- [114] S.R. McDougall, A.R.A. Anderson, and M.A.J. Chaplain. Mathematical modeling of dynamic adaptive tumor induced angiogenesis: clinical applications and therapeutic targeting strategies. *J. Theor. Biol.*, 241:564–589, 2006.
- [115] V.V. Meleshko and M.Y. Konstantinov. *Vortex Dynamics and chaotic phenomena*. World Scientific Publishing Company, 1st edition, 2002.
- [116] N. Meshkat, M. Eisenberg, and J. DiStefano. An algorithm for finding globally identifiable parameter combinations of non-linear ode models using groebner bases. *Math. Biosci.*, 222:61–72, 2009.
- [117] J. Modersitzki. *Numerical methods for image registration*. Oxford University Press, 1st edition, 2004.

- [118] G. Monge. Memoire sur la theorie des deblais et des remblais. *Histoire de l'Academie des Sciences de Paris*, 1781.
- [119] J. Moreira and A. Deutsch. Cellular automaton models of tumor development: a critical review. *Adv. Complex Syst.*, 5:247–267, 2002.
- [120] J. Murray and G. Oster. Cell traction models for generation of pattern and form in morphogenesis. *J. Math. Biol.*, 33:489–520, 1984.
- [121] M. Muskulus and S. Verduyn-Lunel. Wasserstein distances in the analysis of time series and dynamical systems. *Physica D*, 240:45–58, 2011.
- [122] J. Nocedal and S.J. Wright. *Numerical Optimization*. Operations Research. Springer, 2nd edition, 2010.
- [123] P. Olver and A. Tannenbaum. *Mathematical Methods in Computer Vision*. Springer – Verlag, 2004.
- [124] S. Osher and R. Fedkiw. *Level Set Methods and Dynamic Implicit Surfaces*. Applied Mathematical Sciences. Springer, 2003.
- [125] H.G. Othmer and A. Stevens. Aggregation, blowup, and collapse: the abc's of taxis in reinforced random walks. *SIAM J. Appl. Math.*, 57:1044–1081, 1997.
- [126] F. Otto. Viscous fingering: an optimal bound on the growth rate of the mixing zone. *SIAM J. Appl. Math.*, 57:982–990, 1997.
- [127] N. Paragios, J. Duncan, and N. Ayache, editors. *Biomedical Image Analysis: Methodologies and Applications*. Springer, 1st edition, 2011.
- [128] A.A. Patel, E.T. Gawlinski, S.K. Lemieux, and R.A. Gatenby. A cellular automaton model of early tumor growth and invasion: The effects of native tissue vascularity and increased anaerobic tumor metabolism. *J. Theor. Biol.*, 213:315–331, 2001.
- [129] B. Perthame and J.P. Zubelli. On the inverse problem for a size structured population model. *Inverse problems*, 23:045008, 2007.
- [130] M. Powell. Unconstrained optimization by quadratic approximation. *Math. Progr. B*, 92, 2001.

- [131] L. Preziosi. *Cancer Modeling and Simulation*. Mathematical and Computational Biology. Chapman and Hall/CRC, 2003.
- [132] L. Preziosi, D. Ambrosi, and C. Verdier. An elasto-visco-plastic model of cell aggregates. *J. Theor. Biol.*, 262:35–47, 2010.
- [133] L. Preziosi and A. Tosin. Multiphase modeling of tumor growth and extracellular matrix interaction: mathematical tools and applications. *J. Math. Biol.*, 58:625–656, 2009.
- [134] V. Quaranta, A.M. Weaver, P.T. Cummings, and A.R.A. Anderson. Mathematical prognosis of cancer: the future of prognosis and treatment. *Clin. Chim. Acta*, 357:173–179, 2005.
- [135] J.C. Reed. Apoptosis and cancer. In *Cancer Medicine*. Holland-Frey, 7th edition edition, 2006.
- [136] T. Rehman, E. Haber, G. Pryor, J. Melonakos, and A. Tannenbaum. 3D nonrigid registration via optimal mass transport on the GPU. *Medical Image Analysis*, 2009.
- [137] K. Rejniak. An immersed boundary framework for modeling the growth of individual cells: an application to early tumor development. *J. Theor. Biol.*, 247:186–204, 2007.
- [138] W. Rheinboldt. On the sensitivity of solutions of parametrized equations. *SIAM J. Numer. Anal.*, 30:305–320, 1993.
- [139] B. Ribba, T. Colin, and S. Schnell. A multiscale mathematical model of cancer, and its use in analyzing irradiation therapies. *Theor. Biol. Med. Modelling*, 3:7, 2006.
- [140] B. Ribba, O. Saut, T. Colin, D. Bresch, E. Grenier, and J.P. Boissel. A multiscale mathematical model of avascular tumor growth to investigate the therapeutic benefit of anti-invasive agents. *J. Theor. Biol.*, 243:523–541, 2006.
- [141] T. Roose, S.J. Chapman, and P.K. Maini. Mathematical models of avascular tumor growth. *SIAM Rev.*, 49:179–208, 2007.
- [142] T. Roose, P.A. Netti, L.L Munn, Y. Boucher, and R. Jain. Solid stress generated by spheroid growth using a linear poroelastic model. *Microvascular Res.*, 66:204–212, 2003.

- [143] G. Russo and P. Smereka. A remark on computing distance functions. *J. Comput. Phys.*, 163:51–67, 2000.
- [144] R.K. Sachs, L.R. Hlatky, and P. Hahnfeldt. Simple ode models of tumor growth and anti-angiogenic or radiation treatment. *Math. comp. mod.*, 33:1297–1305, 2001.
- [145] S. Sanga, J.P. Sinek, H.B. Friboes, M. Ferrari, J.P. Fruehauf, and V. Cristini. Mathematical modeling of cancer progression and response to chemotherapy. *Expert Rev. Anticancer Ther.*, 6:1361–1376, 2006.
- [146] J.P. Sinek, S. Sanga, X. Zheng, H.B. Friboes, M. Ferrari, and V. Cristini. Predicting drug pharmacokinetics and effect in vascularized tumors using computer simulation. *J. Math. Biol.*, 58:485–510, 2009.
- [147] L. Sirovich. Low dimensional description of complicated phenomena. *Contemporary Mathematics*, 99:277–305, 1989.
- [148] K.R. Swanson, E.C.Jr. Alvord, and J.D. Murray. A quantitative model for differential motility of gliomas in grey and white matter. *Cell Proliferation*, 33:317–329, 2000.
- [149] K.R. Swanson, E.C.Jr. Alvord, and J.D. Murray. Virtual brain tumors (gliomas) enhance the reality of medical imaging and highlight inadequacies of current therapy. *Br. J. Cancer*, 86:14–18, 2002.
- [150] K.R. Swanson, E.C.Jr. Alvord, and J.D. Murray. Virtual resection of gliomas: effect of extent of resection on recurrence. *Math. Comput. Model.*, 37:1177–1190, 2003.
- [151] K.R. Swanson, C. Bridge, J.D. Murray, and E.C.Jr. Alvord. Virtual and real brain tumors: using mathematical modeling to quantify glioma growth and invasion. *J. Neuro. Sci.*, 216:1–10, 2003.
- [152] K.R. Swanson, R. Rostomily, and E.C.Jr. Alvord. A mathematical modeling tool for predicting the survival of individual patients following resection of glioblastoma: a proof of principle. *Br. J. Cancer*, 98:113–119, 2008.
- [153] L. Tenorio. Statistical regularization of inverse problems. *SIAM Review*, 43:347–366, 2001.

- [154] A. Tosin. Multiphase modeling and qualitative analysis of the growth of tumor cords. *Networks Heterogen. Media*, 3:43–84, 2008.
- [155] A. Tosin, D. Ambrosi, and L. Preziosi. Mechanics and chemotaxis in the morphogenesis of vascular networks. *Bull. Math. Biol.*, 68:1819–1836, 2006.
- [156] P. Tracqui and M. Mendjeli. Modelling three dimensional growth of brain tumors from time series of scans. *Math. Model. Meth. Appl. Sci.*, 9:581–598, 1999.
- [157] C. Villani. *Topics in optimal transportation*. American Mathematical Society, 1st edition, 2003.
- [158] C. Villani. *Optimal Transport, old and new*. Springer-Verlag, 1st edition, 2009.
- [159] Z. Wang, L. Zhang, J. Sagotsky, and T.S. Deisboeck. Simulating non-small cell lung cancer with a multiscale agent-based model. *Theor. Biol. Med. Model.*, 4:50, 2007.
- [160] J.P. Ward and J.R. King. Mathematical modeling of avascular tumor growth. *IMA J. Math. Appl. Med. Biol.*, 14:36–69, 1997.
- [161] J. Weller, E. Lombardi, and A. Iollo. Robust model identification of actuated vortex wakes. *Physica D*, 238:416–427, 2009.
- [162] G. Wolansky. On time reversible description of the process of coagulation and fragmentation. *Archive for Rational Mechanics and Analysis*, 193:57–115, 2008.
- [163] L. Zhang, C.A. Athale, and T.S. Deisboeck. Development of a three dimensional multiscale agent-based tumor model: simulating gene-protein interaction profiles, cell phenotypes and multicellular patterns in brain cancer. *J. Theor. Biol.*, 244:96–107, 2007.
- [164] L. Zhang, Z. Wang, J.A. Sagotsky, and T.S. Deisboeck. Multiscale agent-based cancer modeling. *J. Math. Biol.*, 58:545–559, 2009.
- [165] Y. Zhang, M. A. Henson, and Y. G. Kevrekidis. Nonlinear model reduction for dynamic analysis of cell population models. *Chemical engineering science*, 58:429–445, 2003.